Dissertation zur Erlangung des Doktorgrades der Fakultät für Chemie und
Pharmazie der Ludwig-Maximilians-Universität München

Nanostructures for Watersplitting Applications

Michael Beetz

aus

Fürth, Deutschland

2023

Erklärung

Diese Dissertation wurde im Sinne von § 7 der Promotionsordnung vom 28. November 2011 von Herrn Prof. Dr. Thomas Bein betreut.

Eidesstattliche Versicherung

Diese Dissertation wurde eigenständig und ohne unerlaubte Hilfe bearbeitet.

München, den 23.11.2023 ....
Michael Beetz

Dissertation eingereicht am: 08.08.2023

1. Gutachter:	Prof. Dr. Thomas Bein
2. Gutachter:	Prof. Dr. Achim Hartschuh
Mündliche Prüfung am:	21.11.2023

If you want to find the secrets of the universe, think in terms of energy, frequency and vibration.

— Nikola Tesla

Abstract

With today's ever increasing demand for green and renewable energy, hydrogen arose as a promising candidate as energy carrier for the future. Since its application is widespread from the use as a basic chemical up to the generation of power in fuel cells, the demand for green hydrogen will increase in the future.

This thesis presents multiple projects, which allow the efficient conversion of power with or without the energy of the sunlight to efficiently produce hydrogen. All approaches shown emphasize sustainability with respect to the used materials or strongly reduce the use of rare and non-abundant materials. The synthesized materials were extensively studied for their performance and stability by various physical analytical techniques, such as (photo)electrochemistry, X-ray diffraction, X-ray photoelectron spectroscopy or electron microscopy.

In the first chapter, the corrosion and dissolution of a highly active photoelectrocatalyst ($\mathrm{Mo{:}BiVO_4}$) was investigated. A protection strategy using an ultra-thin niobium doped titania layer with an additional oxygen evolution co-catalyst ($\mathrm{Fe_xNi_{1-x}O}$) was established to supress the parasitic dissolution processes and even increase the activity to unprecedented photocurrents under harsh electrochemical conditions.

The second chapter describes another promising application of niobium doped titania as protective layer on lithium doped copper oxide as a photocathode device. Photocorrosion, in this case, was observed under operating conditions, when brought in contact with water. In-depth electron energy loss spectroscopy studies allowed the observation of the corroded species and verification of our protection layer approach.

In the third chapter, a multistep synthesis procedure for microporous conductive oxide particles, loaded with Ir nanoparticles as highly active electrocatalyst for water oxidation, is described. The use of the rare active catalyst Ir was minimized by a homogeneous coating of the complete inner and outer surface of the porous scaffold particles. The loading of those particles was monitored and calculated using scanning transmission electron microscope electron tomography data combined with the microparticles' size distribution from dynamic light scattering.

The fourth chapter presents another novel route for supported $\mathrm{IrO_2}$ catalysts for the oxygen evolution reaction in proton exchange membrane electrolyzers. Carbon soot was used as a nanostructured template, which was homogenously coated by niobium-doped titania in an atomic layer deposition process. After loading with $\mathrm{IrO_2}$ as an oxygen evolution catalyst for dark electrolysis, the prepared devices showed very low overpotentials while using a very low iridium mass loading.

In the fifth chapter the influence of vanadium as a dopant in nickel oxide based nanocatalysts was investigated. It could be shown that small amounts of vanadium(III) ions ($< 5\,\%$) inhibit the

phase transformation from α-$Ni(OH)_2$ to the less electrochemically active β-$Ni(OH)_2$ phase. This results in an overall increased oxygen evolution reaction activity of vanadium-doped nickel oxide.

Chapter 6 and 7 made use of high resolution electron tomography reconstructions of silver-doped gold nanostars. Since plasmonic responses of such particles strongly depend on their morphology, such as, shape, number of branches and size, a synthesis allowing very precise control of those properties was developed. The plasmonic response of those synthesized gold nanostars was analysed and compared to computational simulations. In the end, the simulations were further refined using electron tomographic reconstructions from real-world particles.

In conclusion, this thesis deals with the challenges of today's energy conversion applications, and provides possible solutions for efficient water-splitting using a mininum amount of noble metals or rare-earth materials. It also demonstrates that precise control of nanostructures and detailed investigations of their morphology and shape are key factors to overcome limitations and further increase the understanding of energy conversion processes.

Contents

1 Introduction

1.1 Hydrogen as an Energy Carrier in Today's Society

Today's increasing energy demand is primarily met by fossil-based fuels, leading to detrimental environmental impacts such as the greenhouse effect, ozone layer depletion, acid rain, and pollution.[1] To address the urgent need to limit global warming to 1.5 degrees Celsius,[2,3] a global strategy for full decarbonization must be developed.[4] While the German government focuses on a green and sustainable energy future,[5,6] sustainable energy conversion technologies from renewable sources remain limited.[7]

Hydrogen is considered a promising energy carrier for the future due to various reasons. It offers a more sustainable alternative to traditional fuels like oil and gas as it can be generated from diverse sources (e.g. renewables, nuclear, oil, natural gas, and coal)[8–11] and produced through different methods such as electrolysis or steam reforming. This enables the sustainable and abundant production of hydrogen. Moreover, hydrogen possesses unique properties that make it suitable for various applications, including electricity generation in fuel cells with zero carbon emissions and only water as a by-product. Hydrogen can also be utilized for large-scale energy transportation and storage. Despite technical barriers, advancements have been made, paving the way for hydrogen to become a viable and widespread energy source in the future.

While hydrogen currently represents a small fraction of global energy use,[12] its significance is growing rapidly, especially in the transport sector. However, the adoption of hydrogen as a transport fuel faces challenges related to refueling infrastructure, particularly the safe and practical implementation of pressurized hydrogen cylinders.[13] To overcome this limitation, various technologies are being developed, such as PEM fuel cells that offer high efficiency and can be integrated into vehicles. Provided filling station networks can be established at a reasonable rate.[14] Additionally, research is ongoing to optimize fuel cell design and explore alternative approaches like using metal hydrides for hydrogen storage in vehicles.[15–17] However, these technologies are still in early stages and require further development before becoming viable alternatives.

The use of hydrogen has the potential to decarbonize multiple sectors, including freight logistics, industrial heating, chemicals, and agriculture, leading to reduced emissions and improved air quality.[18] Hydrogen can be produced from a wide range of domestic and renewable energy sources, making it an inherently clean fuel that is carbon neutral throughout its life cycle.[10,19–22] Moreover, hydrogen can address the challenge of variable output from renewable sources by storing energy in large pressurized tanks or as liquid organic hydrogen carriers.[23–25] As hydrogen scales up, it is expected to become a cost-effective option for energy storage spanning from days to months.[26] The existing infrastructure for hydrogen distribution can also be utilized for transporting hydrogen-based fuels in rural and remote areas.[12]

While the efficient and economical production of hydrogen currently faces challenges, future economies of scale and technological advancements are expected to substantially reduce production costs.

1.1.1 Hydrogen as an Energy Carrier

Hydrogen is predominantly found bound in chemical compounds like water or hydrocarbons, making it necessary to produce hydrogen from primary energy sources. However, environmentally friendly hydrogen production faces numerous challenges. The most common method, steam reforming, contributes to carbon dioxide emissions and does not reduce fossil fuel usage.[27,28]

To achieve environmentally friendly hydrogen production, hydrogen must be generated from non-fossil fuel resources using non-fossil-based energy, such as solar or wind power, to obtain hydrogen from water. The hydrogen pathway consists of three steps: hydrogen production, transport/storage, and usage.[29] However, none of these steps currently rival fossil fuels in terms of reliability, performance, and cost.[30] For example, polymer electrolyte membrane (PEM) water-electrolysis (under acidic conditions), a method for hydrogen generation, relies on expensive and rare noble metals as catalysts. Hydrogen is often transported as a cryogenic liquid or in pressurized containers, but the density at 300 bar can limit practical applications with vehicle ranges beyond 500 km.[31,32] Fuel cells, used for converting hydrogen back to electricity, are expensive to produce and require platinum, a rare noble metal.

While hydrogen as a primary energy carrier still faces obstacles in everyday applications, many of these challenges can be mitigated through mass production. Improvements in water electrolysis can be achieved by using common, non-noble catalyst materials or reducing the reliance on noble-metal-based catalysts. Additionally, direct solar energy can be utilized in photoelectrochemical water splitting to reduce the external energy required for the process.

Enhancements in hydrogen transport and storage can be made through the use of more dense storage forms like liquid organic hydrogen carriers (LOHC), enabling easy absorption and release of hydrogen via hydrogenation and endothermal dehydrogenation of aromatic organic compounds.

Furthermore, hydrogen can be utilized as a base chemical in various large-scale industries. For instance, it can be employed in the Fischer-Tropsch synthesis to produce synthetic fuels (synfuels) or in steelmaking processes as a substitute for coal and natural gas, facilitating the direct reduction of iron ore to crude steel.

These examples highlight the potential applications of green hydrogen, from generation to utilization, in effectively reducing carbon dioxide emissions and mitigating environmental impacts.

1.1.2 Hydrogen Production

As already mentioned, hydrogen can be produced by a variety of processes, including already well-established techniques and new and upcoming processes. Hydrogen is a sustainable and environmentally friendly energy carrier. The production pathway and the primary source of energy that is used to generate hydrogen has to be discussed and influences the footprint of hydrogen generation on our environment.
Hydrogen is often referred to by colors indicating its origin and the primary used energy source for production:

- white: White hydrogen refers to naturally generated hydrogen such as in magma degassing, decomposition of organic matter or radiolysis of water, to name just a few.[33]
- red: High temperature catalytic splitting of water can be performed in nuclear power plants.[33–35]
- turquoise: In methane pyrolysis, a non-polluting industrial process converts natural gas (methane) to hydrogen and solid carbon by the use of heat and catalysts. The produced solid carbon can be used industrially or used for landfilling.[33]
- brown: Brown or black hydrogen is produced by gasification (with water) of brown or black coal, respectively. Thereby, carbon-rich materials are converted into hydrogen and carbon dioxide, which is released into the atmosphere.[33]
- gray: Gray hydrogen describes hydrogen extracted from natural gas by steam reforming, releasing emissions into the atmosphere.[33]
- blue: Blue hydrogen stems from gasification of coal or steam reforming of natural gas. The difference to gray or brown hydrogen is that all emissions are captured and stored and not released into the environment, making this kind of hydrogen effectively environmental friendly.[33,36,37]
- green: Green hydrogen is refered to as hydrogen that was produced without the emission of carbon dioxide or other greenhouse gases. Its production is defined as sustainable and the primary energy source used for hydrogen generation is renewable, such as, wind or solar power. Green hydrogen can also be produced using waste biomass.[33,36]

It becomes apparent that only selected types of hydrogen production such as for green or blue hydrogen will enable a complete fossil fuel phase-out in today's society.

1.1.3 Usage of Hydrogen

With hydrogen having the ability to be a clean fuel that, when produced from environmentally friendly primary energy sources, and when avoiding greenhouse gas emissions, it can easily replace fossil-based hydrogen in industrial processes.[38–40] Especially, in oil refining, steel- or ammonia production, where hydrogen is already used in large quantities, the potential for emission reduction is enormous.

Also when used in fuel cells, hydrogen allows for the clean generation of power for a wide range of applications. Fuel cells in electric cars would allow for the full decarbonization of the transport sector. Also, carbon-based fuels with high energy density, which are still needed for aerial vehicles, could be provided as *synfuel*, produced from green hydrogen.[41,42]

In buildings, hydrogen can be used for heating in hydrogen boilers or in fuel cells. Another approach investigated is blending of green hydrogen into existing gas networks to reduce the overall carbon-footprint of the heating process.[43]

In power generation, hydrogen is one of the most promising options for storage of renewable energies. A temporary oversupply of energy can be directly used for electrolysis of water to produce green hydrogen, which can be subsequently stored as a pressurized gas, converted into commodity chemicals or used for production of *synfuels*.

1.2 Synthesis Pathways of Hydrogen

Already well-established synthesis pathways for hydrogen such as coal gasification or natural gas reforming often use energy primarily provided by fossil fuels. Therefore, new synthesis pathways, which can be easily integrated using renewable energy ressources, have to be developed. Especially, water electrolysis, high-temperature electrolysis, photoelectrochemical water splitting or biomass gasification are currently investigated, just to name a few.

1.3 Theory of Water Splitting

Water splitting, in general, describes the chemical reaction in which two water molecules are split into two hydrogen- and one oxygen molecule, according to the following equation:

$$2\,\mathrm{H_2O} \longrightarrow 2\,\mathrm{H_2} + \mathrm{O_2}$$

The overall water splitting reaction is an endothermic process and therefore needs a minimum energy of $\Delta G = 237.2\,\mathrm{kJ\,mol^{-1}}$ and $\Delta E^0 = 1.23\,\mathrm{V}$ to take place. Water splitting pathways are differentiated by how the required energy is provided:

A rather direct approach is found in the so-called dark electrolysis, where water is split into oxygen and hydrogen using an electric current. Since electrical energy is more valuable than other types of energy, it is desired to minimize the usage of electrical energy and use other forms of energy, such as heat. In theory, at 2500°C water undergoes thermolysis and no additional electrical current is required. However, since these temperatures are not suitable for industrial applications, a mixture of both variants can be used. High-temperature electrolysis operates between 100°C and 850°C and increases the efficiency of the water splitting reaction compared to common dark electrolysis.

Photoelectrochemical water splitting, sometimes referred to as "artificial photosynthesis", uses harvested light to perform the water splitting reaction on a semiconductor's surface. Since the sun's light can be directly used, this approach is seen as one of the most promising ones, in terms of the use of renewable energies.

Photocatalytic water splitting achieves both partial reactions of the water splitting process on a single material/electrolyte interface, which is directly submerged into water or an electrolyte.

Other methods, such as radiolysis or nuclear-thermal water splitting, are also discussed as a possible way for hydrogen production, at the cost of nuclear radiation and nuclear contamination of the environment.

1.3.1 Dark Water Electrolysis

Especially in proton-exchange membrane (PEM) water electrolyzers the oxygen evolution reaction (OER) plays a crucial role, since the kinetics of this partial reaction and instabilities of the used catalyst materials still remain challenging. Most PEM electrolyzers, today, use cost-intensive iridium based materials on the anode side for effective and catalytically active water oxidation. However, those materials are prone to dissolution under operating conditions of the OER. Therefore, the low abundance and high-costs of Ir-anodes requires the minimization of the used iridium at maximized water splitting activities, which makes a deep understanding of the kinetics and mechanisms inevitable.

Kinetic parameters, such as the Ir dissolution, can be in-situ monitored using electrochemical methods or ICP-MS.[44–46]

1.3.2 Photoelectrochemical Water Splitting

Efficient water splitting can be achieved with the help of the sun's light by exploiting a semiconductor's properties to convert light into electrical energy. Here, the semiconductor absorbs photons with a higher or equal energy than the corresponding band gap to excite electrons from the condudction band (CB) to the valence band (VB), leaving behind positively charged vacancies, often referred to as "holes".

Since the water splitting reaction is an endothermic reaction with a required energy of $\Delta G = 237.2\,\mathrm{kJ\,mol^{-1}}$ and $\Delta E^0 = 1.23\,\mathrm{V}$, the required energy is ideally provided by sunlight. The ideal semiconductor would be able to absorb the maximum amount of incident light over the total spectral range of the light source and convert its harvested energy completely into excited electrons, which are used for water oxidation and reduction, in the end. The overall water splitting reaction can be divided into two half reactions, the so called hydrogen evolution reaction (HER) and the oxygen evolution reaction (OER). In the ideal case, a photoanode should provide one oxygen molecule per 4 incident photons and a photocathode should provide one hydrogen molecule per 2 incident photons, respectively. However, in reality a semiconductor does not always convert one photon to one electron/hole pair, nor is the charge separation guaranteed for long enough times to take part in one of the half reactions.

$$2\,\mathrm{H_2O(l)} \longrightarrow 2\,\mathrm{H_2(g)} + \mathrm{O_2(g)} \tag{1.1}$$

$$2\,\mathrm{H^+} + 2\,\mathrm{e^-} \longrightarrow \mathrm{H_2} \tag{1.2}$$

$$2\,\mathrm{H_2O} \longrightarrow \mathrm{O_2} + 4\,\mathrm{H^+} + 4\,\mathrm{e^-} \tag{1.3}$$

A semiconductor that is in contact with an electrolyte, equilibrates with the redox potential of the electrolyte. At illumination with photons with greater or equal energy than the band gap of the semiconductor, electron-hole pairs are generated. Therefore, those electrons are excited from the valence band to the conduction band, leaving vaccancies, the so-called holes, in the valence band. At a photoanode, these positively charged holes accumulate at the surface to the electrolyte and oxidize water to oxygen in the OER (see eq. 1.3). On the other hand, the generated electrons reduce water at the cathode to hydrogen in the so called HER (see eq. 1.2). To generate oxygen in this process, the energy of the valence band of the photoanode has to become more positive than the oxygen evolution potential. For hydrogen evolution, the position of the conduction band has to be more negative than the hydrogen evolution potential. The optimum water splitting reaction should take place using a photoanode and photocathode in tandem configuration, as shown in figure 1.1

In the case of a n-type semiconducting material, which is in contact with an electrolyte, the FERMI level of the surface lies close to the conduction band, but above the FERMI level of the surface towards the electrolyte. To achieve an equlbrium, electrons will move towards the surface of the semiconductor and therefore bending the conduction and valence bands until they align with the surface states. In the case of a p-type semiconductor, band bending occurs in the other direction upon removing electrons from the surface and therefore also bending the conduction and valence bands until energetic equilibration is reached.[47,48] Band bending allows for alignment of the band structure of a semiconductor, which is in contact with an electrolyte, in such a way that electrons can be transfered via the semiconductor-electrolyte interface. This allows for effective charge separation of photogenerated electrons or holes by prevention of charge accumulation at the surface.

Surface states caused by surface reactions, dangling-bonds or unpaired electrons can cause new electronic states at the semiconductor-electrolyte interface and hinder or favor effective charge transport across the interface.[49]

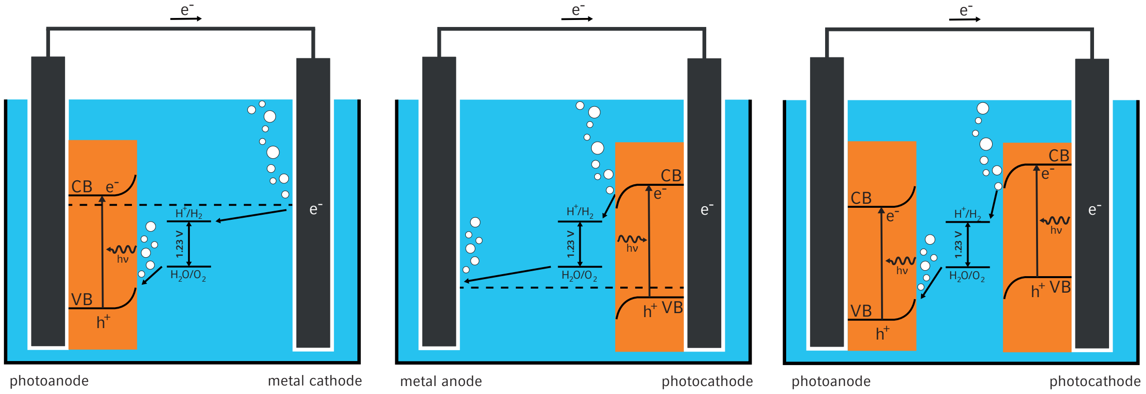

Figure 1.1: Energy diagrams of photoelectrochemical water splitting of a a) photoanode with counterelectrode, b) photocathode with counter electrode and c) photoanode and photocathode in tandem cell configuration.

A semiconductor's properties, suitable for water splitting can be characterized by various parameters, such as the incident photon to current efficiency (IPCE) or the charge transfer efficiency. IPCE measurements allow one to determine the ratio of a resulting current density to the incident photon flux I_0. This correlation can also be described as the product of the charge transfer efficiency η_{trans}, the light harvesting efficiency η_{LH} and the hole separation efficiency η_{sep} by the following equation:

$$\mathrm{IPCE} = \frac{j_{cur}}{I_0 \cdot q} = \eta_{LH} \cdot \eta_{trans} \cdot \eta_{sep} \tag{1.4}$$

The charge transfer efficiency η_{trans} can be determined experimentally using the transient current response when switching the light from the on to the off state and vice versa. Thereby, η_{trans} is defined as the ratio of the steady state current j_{ss} to the instantaneous current j_0 when switching on the light source.

$$\eta_{trans} = \frac{j_{ss}}{j_0} \tag{1.5}$$

1.3.2.1 Corrosion in PEC Water Splitting

Resulting currents in PEC water splitting have to be interpreted very carefully since most of the commonly used characterization techniques do not allow any interpretation of the source of those currents. Beside the desired water splitting reaction, side reactions such as dissolution–, corrosion– or redox-processes can occur and lead to measured "photocurrents" which do not stem from the actual water splitting reaction but from those side reactions. Further, those currents are often parasitic and lead to either the formation of catalytically less active material or to less overall material on the electrode, resulting in massive performance losses over time. Therefore, when judging a materials' performance in photoelectrochemical devices, durability, reliability and robustness are key factors next to the overall water splitting performance.

The device degradation behaviour can be impacted by external factors, like irradiation intensity, applied potential, pH of the electrolyte or ion concentrations in the electrolyte. By variation of these parameters to more suitable ones for the respective materials, the degradation can be slowed down or even completely hindered. For example, suitable pH values and potentials can be extracted from POURBAIX-diagrams.

However, some experimental circumstances or industrial applications may require special conditions, to overcome the above discussed corrosion mechanism; additional strategies, such as protective layers, the application of co-catalysts or the use of sacrificial agents can be used to increase the stability and performance of a PEC catalyst material.

1.3.2.2 Stability in Water Splitting Applications

One major limitation to overcome in PEC water splitting is to achieve a highly active and stable PEC reaction. Since PEC water splitting is often conducted in strongly acidic or basic environments at high applied potentials, corrosion and dissolution processes that affect the stability of the used material are quite common. Therefore, protection strategies for achieving stable interfaces without blocking the charge transport have to be developed.

A semiconductors' stability under PEC conditions depends on the self-reduction Φ_{red} and self-oxidation Φ_{ox} potentials relative to $E(H_2O/H_2)$ for the cathode and $E(O_2/H_2O)$ on the anode.

A material is becoming unstable when Φ_{red} is below $E(H_2O/H_2)$ or Φ_{ox} is above $E(O_2/H_2O)$. In contrast, when the self-oxidation/reduction values are placed in between the material's conduction band and the $E(H_2O/H_2)/E(O_2/H_2O)$, respectively, the stability strongly depends on the branching ratios k_{HER} and k_{OER} of the water splitting reaction and the competing corrosion reaction as a side reaction. The branching ratio can be improved using a relevant co-catalyst which improves the charger transfer kinetics of the HER or OER and therefore reduces the undesired side reactions.

Stability can be further enhanced by using nanostructured geometries, which benefit from short travel distance from the place of generation to the place of use for minority charger carriers, which can improve charger transfer kinetics.[50,51] However, nanostructured materials reveal a relatively high surface to the electrolyte which increases non-light driven dissolution processes. As an example: Si, one of the most commonly used photoelectrodes, forms an oxide (SiO_2) or silicic acid (H_2SiO_3) on its surface when exposed to strongly acidic electrolytes, which leads to degradation or deactivation of the device. More stable semiconducters, such as metal oxides possess a high intrinsic stability towards strongly acidic or basic environments at the cost of relatively low PEC performance compared to other semiconducting materials. This implies that the ideal PEC water splitting electrode would possess the acitivity of a non-oxide semiconductor combined with the stability of a metal oxide semiconducting material. In principle, devices with such a behavior can be manufactured by application of a thin metal oxide protection layer on a highly active photoabsorbing semiconductor. One of the most commonly used protective layer is TiO_2, since its Φ_{red} and Φ_{ox} are very negative and very positive, respectively and therefore result in a very limited dissolution behavior, which makes TiO_2 an effective material as a protection layer.[52–55]

For example, 10 nm TiO_2 protection layers were reported to impart outstanding stability to previously unstable photoanodes or cathodes.[56–59]
The charges created under illumination in a semiconducting material drive the catalytic reactions at the semiconductor/electrolyte interfaces. Thus, the transport of the charges through a protective layer is essential to maintain the maximum photocurrents of such a device.

1.3.2.3 Oxygen Evolution Co-Catalysts

Further stability improvements of a PEC device can be achieved by increasing the effectiveness of the water splitting reaction itself. Since corrosion currents stem from side-reactions, which are at least as favoured as the water splitting reaction under operating conditions, those can be reduced by facilitation of the water splitting reaction.

In practice, a suitable co-catalyst for water oxidation or reduction, such as Pt, IrO_2 or RuO_2, in the form of nanostructured materials can be used to favour the water splitting reaction at the catalyst/electrolyte interface. Since the materials mentioned above are quite expensive and rare materials, the search for cheaper and catalytically active materials is still ongoing. For dark water oxidation, $\mathrm{Fe_xNi_{1-x}O}$ is an intensively investigated catalyst due to its activity, abundance, low-overpotential and an easily applied material with significant stability.

Moreover, the combination of a PEC device with an applied co-catalyst has attracted increasing interest in the last years.[60–65] Since the electron-hole pairs generated via illumination are not used for the water splitting reaction directly but rather transferred to the more stable co-catalyst to undergo the oxidation or reduction half-reaction, the photoabsorbing semiconductor is protected and isolated from parasitic side reactions, which can lead to an increase in livetime and overall photoelectrochemical activity.[66–68]

1.4 Nanostructured Materials

Nanomaterials have gained interest due to their tunable physical, chemical and electrical properties in contrast to their bulk material counterparts. In general, nanomaterials are defined by their dimensions of the overall shape or internal porous structure being in a range of 1 – 1000 nm in at least one dimension. 1 nm represents 10^{-9} m in length. Depending on their size, composition and morphology nanomaterials exhibit various different properties which allow the use in a broad range of applications. Those primary attributes allow the precise tuning of physicochemical characteristics, such as wettablity, melting point, electrical and thermal conductivity, catalytic activity, light scattering and absorption.

With nanomaterials, being produced by physical or chemnical processes, biological species or anthropogenic activities, they are omnipresent in our environment. Naturally occuring nanomaterials can be found in the hydrosphere, atmosphere or lithosphere and are usually a product of erosion, grinding processes by wind, earth movement or vulcanic activities. One of the first known and famous natural nanomaterials, is the group of zeolites. Zeolites are microporous aluminosilicates originally discovered by the mineralogist A. Cronstedt in 1756. He realized that when heating the unknown mineral in a flame the rocks seem to "boil". He concluded that water inside of a zeolite was not bound chemically but rather simply included inside the structure and escapes those cavities when heating up. Further, the dehydrated zeolites allowed the absorption of gases, such as ammonia, carbon dioxide, as well as alcohol. Those fundamental properties were further investigated by J. W. McBain who coined the term "molecular sieve". Today, over 40 different naturally occuring zeolite frameworks are known. However, synthetic zeolites with over 200 additional topologies have been discovered until today.

1.4.1 Synthesis of Nanostructured Materials

Control over the synthesis and its parameters for nanoparticles or nanostructured materials is the key for targeted adjustments in a material's properties at the nanometer scale. Composition, particle size, shape, structure (crystalline/amorphous), and the particles' size distribution yield unique physical properties of a nanostrucutred material. Two fundamental factors, such as the large surface to volume ratio and quantum confinement effects are the main reasons for their special properties. For exampole, a semiconductor's bandgap strongly depends on the size, shape, composition and crystallinity of a material. Therefore, a precise control of those parameters allows one tune the bandgap to desired energies for an application.

In general, two very different pathways can be used for fabricating nanostructured materials. One of them is the so-called top-down strategy which involves the breaking down of a bulk material into nanosized particles or objects. The other one is the so-called bottom-up approach, which refers to the build-up of a material from the bottom (atom-by-atom) or by self-assembly of molecular precursor molecules. While the top-down approach starts from the bulk material and involves cutting, etching or grinding processes to break down and miniaturize the material to nanoparticles, the bottom-up approach uses small molecules or atoms and uses them as basic building blocks to produce larger structures (still at the nanometer scale) of the desired size or complexity.

A general approach for a crystalline metal oxide nanoparticle synthesis is the colloidal sol-gel chemistry. Typically precursors, such as metal alkoxides are used to produce the "sol", which forms a colloidal solution by gradual hydrolysis or polycondensation of the precursor molecules to a "gel"-like phase. Removal of the supernatant can be done by centrifugation, sedimentation, dialysis or phase-separation. Often a thermal treatment is performed afterwards to increase the stability and crystallinity of the product. The resulting small and stable nanoparticles usually exhibit BROWNIAN motion and therefore form stable nanoparticle suspensions, which can be used for further applications. Due to their small volume and high surface area, nanoparticles produced by a "sol-gel" approach often tend to agglomerate. Stabilization of the individuale particles can be achieved by surface modification using sterically demanding or repelling ligands, such as oleic acid or oleylamine.

Thin films of nanoparticles can be produced combining the sol-gel approach with other known thin-film techniques, such as spin-coating, dip-coating or spray-coating.[69–73]

1.4.1.1 Spin-Coating

In the case of spin-coating, the "sol" is applied to the center of the substrate, which is spun at up to 10.000 rpm to spread the material by centrifugal force. Depending on the rotation speed, viscosity and concentration of the precursor solution the resulting thin film varies in thickness. Excess fluid is spilled off the edges due to the centrifugal force. A subsequent heating step of the applied layer is often done to drive the reactions to the desired product phase. needed for the nanoparticle formation in the thin-layer. Spin-coating is a highly versatile technique employed in various applications, particularly in the controlled thin-film preparation of different materials. One prominent example is the fabrication of silica nanoparticles thin-films on a substrate.[74,75] Furthermore, spin-coating enables easy and controlled preparation of two-dimensional nanoparticle thin films in general, as highlighted by Hong *et al.*.[76] It is also frequently utilized as a coating or loading technique to achieve uniform distribution of nanoparticles onto other materials, as shown in the studies conducted by Alvarado *et al.*[77], Krogman *et al.*[78], and Yildiz *et al.*.[79]

Typical examples, where spin-coating is widely used is, for example, the controlled thin-film preparation of silica nanoparticles or preparation of thin-film membranes from polymers or organic framework materials, such as metal-organic-framework or covalent organic framework materials. Thereby spin-coating produces homogeneous thin films.

1.4.1.2 Dip-Coating

The dip-coating technique allows, similar to spin-coating, for the production of thin films on a substrate. First, the substrate is immersed into the precursor solution ("sol"). When withdrawing the substrate at a constant speed, a thin layer of the precursor solution is deposited on the substrate. The speed of withdrawing defines the deposited layer thickness of the coating. When the substrate is fully pulled out, the excess liquid is drained from the surface. This approach also usually needs a subsequent heating step for full phase/nanoparticle formation in the applied layer.

1.4.1.3 Spray-Coating

Spray-coating forces a precursor solution, which is accelerated by a carrier gas, through a converging-diverging DE LAVAL type nozzle to produce a finely dispersed aerosol with droplets sized a few micrometers. The high throughput of the nozzle allows for a homogenous application of the precursor solution on a substrate. Using spray-coating allows for the application of thick layers or large areas in comparison to, e. g., spin-coating.

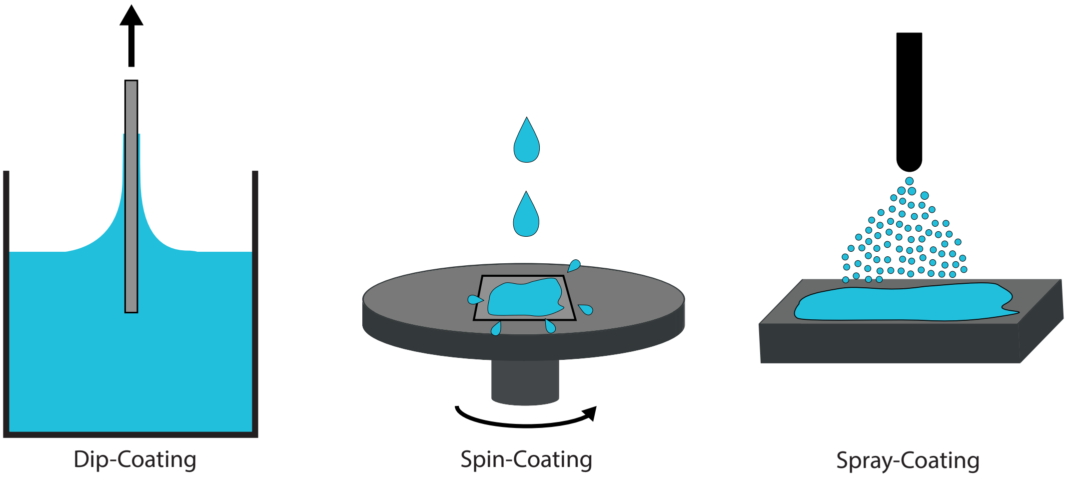

Figure 1.2: (From left to right) **Dip-coating:** A substrate is immersed in a liquid/precursor solution and slowly pulled out of the solution, leaving a thin precursor film on the substrate's surface. **Spin-coating:** A substrate with applied precursor solution is spun to evenly spread the solution on the substrate by centrifugal forces. **Spray-Coating:** A thin nozzle is used to evenly distribute a precursor solution (using a carrier gas) onto a substrate.

1.5 Plasmonic Resonance Energy Transfer

The field of plasmonics is revolutionizing the way we interact with our environment by creating novel devices and systems that can be tuned to specific optical frequencies or wavelengths. However, in order to realize the full potential of these systems it is often necessary to tailor their response to a specific environment. For example, biomedical sensors must be able to detect a single molecule of a particular substance at a specific location in the human body, but to achieve this they must tune the response of the sensor so that only molecules of that substance are detected while rejecting those from other molecules and particles that are also found in the body. By designing structures that can sense and respond to particular frequencies of light, it is possible to create systems that can perform functions such as chemical sensing, biomolecular sensing, and molecular detection.[80–84]

In order to design these sensors one has to understand the fundamentals of how light interacts with materials and how the properties of the material change as the frequency of the light changes. Metal nanoparticles are well suited to this task because they are able to be engineered to exhibit a variety of properties such as color or electrical conductivity that make them useful for a wide range of applications in electronics, optics, and energy conversion. One such application is the creation of "plasmonic nanostar" antennas, which are analogous to conventional antennae used in wireless radio communications. By manipulating the shape and size of the nanoparticles and also their surrounding environment, we can control the interactions between the nanoparticles and the surrounding medium in a way that allows us to achieve tailored plasmonic response to specific wavelengths of incident light.[84]

Nanostar antennae's properties are extremely sensitive to their shape and 3D morphology, which is why detailed information about their three-dimensional shape and thickness is becoming increasingly needed within and outside of scientific communities for fundamental research purposes. Many techniques have been utilized in the past to obtain this information including scanning electron microscopy (SEM), transmission electron microscopy (TEM), confocal laser scanning microscopy (CLSM), etc. However, these techniques often provide only two-dimensional images which do not provide an accurate representation of the underlying structure. Advanced imaging techniques such as electron tomography allow us to obtain 3-D representations of internal and external structures and have become an invaluable tool for researchers studying nanoscale objects.[84]

1.6 Electron Tomography

Electron tomography (ET) is a powerful technique that allows for the visualization of the overall three-dimensional morphology of nanoparticles and nanostructures. This technique can produce high-resolution images and three-dimensional information about the external as well as the internal structure of very small objects and particles. It can be used to determine the precise shape and size of objects as well as their chemical composition at a scale of tens of nanometers.[85]

This technique has become an indispensable tool in the field of materials science, enabling researchers to gain crucial insights into the structure and composition of nano-objects at the atomic scale. By providing detailed information about a material's size, thickness, composition, and shape, this technique allows for precise tailoring of the properties of nanostructured materials, which is essential for designing materials with specific functionalities. Precise tailoring of these properties are crucial in designing nanostructured materials for energy conversion (e.g. "nanostar antennae"[84]) or energy storage such as batteries and supercapacitors, as well as in display devices such as quantum-dot OLEDs.[86,87]

In materials science, electron tomography is a widely used technique that involves the acquisition of a set of images from a scanning transmission electron microscope, which are typically taken under high-angle annular darkfield conditions. The resulting dataset comprises a collection of projection images of a nano-sized sample, captured from multiple angles. However, before these images can be used in the electron tomographic reconstruction process, several pre-processing steps are required, such as image alignment, background subtraction, and data conversion. These steps must be performed prior to the use of electron tomographic algorithms (e.g., weighted backprojection[88–91], simultaneous iterative reconstruction techniques[92,93], or discrete algebraic reconstruction techniques[94–96]) to generate a three-dimensional tomographic reconstruction.

1.7 Motivation

This thesis deals with the developement, tuning and characterization of various nanostructured materials, especially suitable for sustainable and green energy conversion applications such as PEM electrolysis, photocatalytical water splitting and plasmonic light harvesting. The focus of the projects presented here was the minimization of usage of rare-earth or noble metal materials while maintaining maximum efficiency and catalytic activity. The main challenge was to find ways to reduce the usage of noble metals and also to tune the performance of materials using earth-abundant elements by nano-structuring or creating nano-sized layers. Especially corrosion mechanisms were investigated and prevented using nano-sized protective layers.

The work presented in this thesis comprises several aspects such as: (i) the synthesis of oxide-based nano-materials from earth-abundant elements and their study as catalytically active materials in photoelectrochemical water splitting, and (ii) the synthesis and study of corrosion mechanisms of known catalytically active materials with applied protective layers for optimization of the photoactivity and stability under harsh operating conditions.

All the materials discussed here show excellent performance in terms of their electrochemical properties, as well as favorable structural and morphological definition. They have thus been developed as promising candidates for clean energy conversion applications.

1.7.1 Challenges in Photoelectrochemical Water Splitting

Photoelectrochemical water splitting (PEC) is a process where water molecules are split into hydrogen and oxygen using light and possibly an applied potential. It was first proposed as a mechanism for splitting water in the 1950's but has since seen much interest as a viable alternative for the production of clean fuel and basic chemicals for the chemical industry.[97–102] However, despite being attractive in terms of cost and sustainability, there are a number of challenges associated with PEC that need to be addressed before it can become a reality on a large scale:

One of the main challenges that needs to be addressed is the development of low-cost catalysts for the water splitting reaction. There are many different catalysts that could be used. For example, noble metals and semiconductors, but they are still very expensive to produce and are only really effective under very specific conditions. In order for PEC to become commercially viable, it is important to develop a catalyst that is both inexpensive and effective within a wide range of conditions. Another challenge that needs to be overcome in the development of a large-scale

PEC catalyst is the efficient utilization of solar energy to drive the reactions. Solar energy is abundant and cheap but is harvested at relatively low efficiencies by conventional photovoltaic cells (which convert light into electricity), meaning that a significant amount of the energy is lost in the form of heat. In order to use solar energy efficiently, it is necessary to find a way to increase the rate of photogeneration in the cell in order to increase the overall efficiency of the process. And finally, in order to make PEC truly sustainable and cost-effective, we need to develop ways to overcome the issue of greenhouse gas emissions associated with the production of hydrogen from fossil fuels.

With that in mind, chapter 3 discusses molybdenum-doped bismuth vanadate ($\mathrm{Mo{:}BiVO_4}$), which is used as a catalyst for photoelectrochemical water oxidation. In this work the influence of doping levels and various kinds of protective layers on the stability and photoelectrochemical characteristics of the photoanode were studied. Long-term stability measurements under continuous irradiation and under typical operational conditions showed that coated electrodes are very stable over several days. By varying the thickness and type of the coating it was possible to optimize the material properties and stability to obtain the best photocatalytic activity and stability. The presence of a thin layer (2 nm) of a water oxidation co-catalyst ($\mathrm{Fe{:}NiO_x}$) further enhanced the catalytic activity of the $\mathrm{BiVO_4}$ nanostructured film.

Chapter 4, in contrast, investigates the photoelectrochemical water splitting behavior on the cathode side, using copper oxide-based cathodes. It could be shown that under operating conditions those electrodes suffer from degradation in form of conversion of the photoelectrochemically active Cu(II)O to the inactive $\mathrm{Cu(I)_2O}$. A protective layer of niobium-doped titanium dioxide on top of the electrode was found to improve the activity and stability after multiple hours of these electrodes by suppressing the degradation of the active species. This was achieved by limiting the uncontrolled growth of copper oxide on the surface of the electrode. In addition, the thickness of the niobium-doped layer was found to be an important parameter for the activity and stability of the electrode since thicker layers lead to a decrease of electrochemical activity while thinner layers lead to higher oxygen evolution rates but a shorter lifetime of the electrode.

1.7.2 Challenges in PEM Electrolysis

PEM electrolysis is another promising technology for the generation of hydrogen gas and oxygen from water, which uses only an applied potential to drive the water splitting reaction. Because of the simplicity of this process, there has been considerable interest in its application as a means of generating hydrogen on an industrial scale. However, there are several demands on catalytically active materials that must be overcome if this technology is to be adopted for commercial purposes. Some of the major challenges associated with the use of PEM electrolysis catalysts for the production of hydrogen include the following:

- Good kinetics of the water-splitting reaction.
- A stable and durable catalyst material is required that can be used repeatedly without serious degradation of the activity and stability.
- The system must operate at high pressures, temperatures and currents to achieve a high rate of production and to maximize the efficiency of the process.

Those demands are crucial for the efficient and cost-effective production of hydrogen. Currently, used materials such as platinum and iridium are expensive and have a negative impact on the economic viability of the process. The search for alternatives or a significant reduction of the used amount is therefore a high priority for the industry.

The following projects were focused on the minimization of used noble metals (especially reduction of Ir-content) or replacement of any noble metals with alternative such as vanadium-doped nickel oxides, while achieving the maximum activity as a electrocatalytically active material.

The electrocatalytic performance for dark PEM electrolysis applications of iridium oxide nanoparticles applied at antimony-doped tin oxide micro particles was studied in chapter 5. A new synthesis for a direct deposition of iridium oxide nanoparticles on porous tin oxide micro-spheres was developed and the synthesized particles were characterized for their electrochemical performance and stability. The effective Ir-loading of those particles was determined using HAADF STEM electron tomography in combination with DLS and EDX elemental mapping measurements.

In chapter 6, another approach for the preparation of highly active oxygen evolution catalysts is presented, which uses carbon-templated conductive oxides as a support for a highly electrochemically active IrOx layer. The support structures were prepared using soot nanoparticles as a template for ALD deposition of niobium-doped titanium oxide. A thin but highly catalytically active IrOx coating was obtained by ALD on the surface of the support material. The prepared catalysts were also investigated in detail using a scanning electron microscope (SEM) and a high-resolution transmission electron microscope (TEM) in order to determine the structure of their surface. Finally, the catalytic activity of the supported catalyst was tested by performing electrochemical measurements in aqueous media using different potentials. The results of the study indicate that the fabricated materials can be used as efficient catalysts for electrolytic water splitting.

In conclusion, this thesis presents a comprehensive investigation of the development, tuning, and characterization of various nanostructured materials for sustainable and green energy conversion applications. The projects showcased in this work aim to minimize the use of rare-earth and noble metal materials while maintaining maximum efficiency and catalytic activity. The findings presented in this thesis show that the developed materials are promising candidates for clean energy conversion applications, with excellent performance in terms of their electrochemical properties, efficiency and stability. Through the research on PEC water splitting and PEM electrolysis, this work contributes to the growing body of knowledge on sustainable energy technologies and paves the way for future research in this area.

Bibliography

[1] T. N. Veziroglu. In J. W. Sheffield & Ç. Sheffield, editors, *Assessment of Hydrogen Energy for Sustainable Development*, NATO Science for Peace and Security Series, 9–31 (Springer, Dordrecht), **2007**.

[2] J. Tollefson. *Nature*, **2018**. *562*(7726), 172–173.

[3] A. V. Karmalkar & R. S. Bradley. *PLOS ONE*, **2017**. *12*(1), e0168697.

[4] *A sustainable future for the European Cement and Concrete Industry: Technology assessment for full decarbonisation of the industry by 2050*. **2018**.

[5] P. Mair. *German Politics*, **2001**. *10*(2), 99–116.

[6] R. Beveridge & K. Kern. *Renewable Energy L. & Pol'y Rev.*, **2013**. *4*, 3.

[7] D. Akinyele & R. Rayudu. *Sustainable Energy Technologies and Assessments*, **2014**. *8*, 74–91.

[8] P. P. Edwards, V. Kuznetsov & W. I. David. *Philosophical Transactions of the Royal Society A: Mathematical, Physical and Engineering Sciences*, **2007**. *365*(1853), 1043–1056.

[9] J. O. Abe, A. Popoola, E. Ajenifuja & O. Popoola. *International Journal of Hydrogen Energy*, **2019**. *44*(29), 15072–15086.

[10] M. Balat. *International journal of hydrogen energy*, **2008**. *33*(15), 4013–4029.

[11] B. Gaudernack & S. Lynum. *International journal of hydrogen energy*, **1998**. *23*(12), 1087–1093.

[12] I. Staffell, D. Scamman, A. V. Abad, P. Balcombe, P. E. Dodds, P. Ekins, N. Shah & K. R. Ward. *Energy & Environmental Science*, **2019**. *12*(2), 463–491.

[13] S. Nilsen, H. S. Andersen, G. Haugom & H. Rikheim. In *The 1st European Hydrogen Energy Conference & Exhibition (EHEC)*. **2003** .

[14] C. Wang, S. Wang, L. Peng, J. Zhang, Z. Shao, J. Huang, C. Sun, M. Ouyang & X. He. *Energies*, **2016**. *9*(8), 603.

[15] B. Sakintuna, F. Lamari-Darkrim & M. Hirscher. *International journal of hydrogen energy*, **2007**. *32*(9), 1121–1140.

[16] B. P. Tarasov, P. V. Fursikov, A. A. Volodin, M. S. Bocharnikov, Y. Y. Shimkus, A. M. Kashin, V. A. Yartys, S. Chidziva, S. Pasupathi & M. V. Lototskyy. *international journal of hydrogen energy*, **2021**. *46*(25), 13647–13657.

[17] A. Schneemann, J. L. White, S. Kang, S. Jeong, L. F. Wan, E. S. Cho, T. W. Heo, D. Prendergast, J. J. Urban, B. C. Wood *et al.* *Chemical reviews*, **2018**. *118*(22), 10775–10839.

[18] G. S. Seck, E. Hache, J. Sabathier, F. Guedes, G. A. Reigstad, J. Straus, O. Wolfgang, J. A. Ouassou, M. Askeland, I. Hjorth *et al.* *Renewable and Sustainable Energy Reviews*, **2022**. *167*, 112779.

[19] A. Sgobbi, W. Nijs, R. De Miglio, A. Chiodi, M. Gargiulo & C. Thiel. *international journal of hydrogen energy*, **2016**. *41*(1), 19–35.

[20] D. Gielen, E. Taibi & R. Miranda. *International Renewable Energy Agency (IRENA)*, **2019**.

[21] J. Andrews & B. Shabani. *International journal of hydrogen energy*, **2012**. *37*(2), 1184–1203.

[22] C. J. Quarton, O. Tlili, L. Welder, C. Mansilla, H. Blanco, H. Heinrichs, J. Leaver, N. J. Samsatli, P. Lucchese, M. Robinius *et al.* *Sustainable energy & fuels*, **2020**. *4*(1), 80–95.

[23] S. Muyeen, R. Takahashi & J. Tamura. *Electric Power Systems Research*, **2011**. *81*(5), 1171–1179.

[24] F. Barbir. *Solar energy*, **2005**. *78*(5), 661–669.

[25] S. Bennoua, A. Le Duigou, M.-M. Quéméré & S. Dautremont. *international journal of hydrogen energy*, **2015**. *40*(23), 7231–7245.

[26] H. Council. **2020**.

[27] A. Karle. *Elektromobilität: Grundlagen und Praxis* (Carl Hanser Verlag GmbH Co KG), **2020**.

[28] A. M. Ranjekar & G. D. Yadav. *Industrial & Engineering Chemistry Research*, **2021**. *60*(1), 89–113.

[29] R. B. Gupta. *Hydrogen fuel: production, transport, and storage* (Crc Press), **2008**.

[30] J. Kurtz, S. Sprik & T. H. Bradley. *International Journal of Hydrogen Energy*, **2019**. *44*(23), 12010–12023.

[31] M. Hurskainen & J. Ihonen. *International Journal of Hydrogen Energy*, **2020**. *45*(56), 32098–32112.

[32] M. Reuß, P. Dimos, A. Léon, T. Grube, M. Robinius & D. Stolten. *Energies*, **2021**. *14*(11), 1–17.

[33] A. Kusoglu. *The Electrochemical Society Interface*, **2021**. *30*(4), 44.

[34] J. Pinilla, R. Utrilla, R. Karn, I. Suelves, M. Lázaro, R. Moliner, A. García & J. Rouzaud. *International Journal of hydrogen energy*, **2011**. *36*(13), 7832–7843.

[35] X. Wu & K. Onuki. *Tsinghua science and Technology*, **2005**. *10*(2), 270–276.

[36] M. Noussan, P. P. Raimondi, R. Scita & M. Hafner. *Sustainability*, **2021**. *13*(1).

[37] H. C. Lau. In *International Petroleum Technology Conference* (OnePetro), **2021** .

[38] S. van Renssen. *Nature Climate Change*, **2020**. *10*(9), 799–801.

[39] K. Oshiro & S. Fujimori. *Applied Energy*, **2022**. *313*, 118803.

[40] F. Cuevas, J. Zhang & M. Latroche. *Engineering*, **2021**. *7*(6), 715–718.

[41] L. Reyes-Bozo, C. Fúnez-Guerra, C. Sandoval Yanez & G. Schaffeld. In *26. Interdisziplinäre Wissenschaftliche Konferenz Mittweida*, 002 (Hochschule Mittweida), **2021** 183–186.

[42] T. Takeshita & K. Yamaji. *Energy Policy*, **2008**. *36*(8), 2773–2784.

[43] J. Ogden, A. M. Jaffe, D. Scheitrum, Z. McDonald & M. Miller. *Energy Policy*, **2018**. *115*, 317–329.

[44] J. Ranninger, S. J. Wachs, J. Möller, K. J. Mayrhofer & B. B. Berkes. *Electrochemistry communications*, **2020**. *114*, 106702.

[45] S. O. Klemm, A. A. Topalov, C. A. Laska & K. J. Mayrhofer. *Electrochemistry Communications*, **2011**. *13*(12), 1533–1535.

[46] O. Kasian, S. Geiger, K. J. Mayrhofer & S. Cherevko. *The chemical record*, **2019**. *19*(10), 2130–2142.

[47] Z. Zhang & J. T. Yates Jr. *Chemical reviews*, **2012**. *112*(10), 5520–5551.

[48] Y. Jiao, A. Hellman, Y. Fang, S. Gao & M. Käll. *Scientific reports*, **2015**. *5*(1), 1–8.

[49] J. A. Turner. Energetics of the semiconductor-electrolyte interface, **1983**.

[50] M. G. Walter, E. L. Warren, J. R. McKone, S. W. Boettcher, Q. Mi, E. A. Santori & N. S. Lewis. *Chemical Reviews*, **2010**. *110*(11), 6446–6473.

[51] A. Standing, S. Assali, L. Gao, M. A. Verheijen, D. van Dam, Y. Cui, P. H. L. Notten, J. E. M. Haverkort & E. P. A. M. Bakkers. *Nature Communications*, **2015**. *6*(1).

[52] S. Cao, Z. Kang, Y. Yu, J. Du, L. German, J. Li, X. Yan, X. Wang & Y. Zhang. *Advanced Energy Materials*, **2020**. *10*(9), 1902985.

[53] J. Zheng, Y. Lyu, R. Wang, C. Xie, H. Zhou, S. P. Jiang & S. Wang. *Nature Communications*, **2018**. *9*(1).

[54] M. Beetz, S. Häringer, P. Elsässer, J. Kampmann, L. Sauerland, F. Wolf, M. Günther, A. Fischer & T. Bein. *Advanced Functional Materials*, **2021**. *31*(45), 2011210.

[55] Z. Tian, P. Zhang, P. Qin, D. Sun, S. Zhang, X. Guo, W. Zhao, D. Zhao & F. Huang. *Advanced Energy Materials*, **2019**. *9*(27), 1901287.

[56] Y. W. Chen, J. D. Prange, S. Dühnen, Y. Park, M. Gunji, C. E. Chidsey & P. C. McIntyre. *Nature materials*, **2011**. *10*(7), 539–544.

[57] B. Mei, T. Pedersen, P. Malacrida, D. Bae, R. Frydendal, O. Hansen, P. C. Vesborg, B. Seger & I. Chorkendorff. *The Journal of Physical Chemistry C*, **2015**. *119*(27), 15019–15027.

[58] T. Moehl, J. Suh, L. Severy, R. Wick-Joliat & S. D. Tilley. *ACS applied materials & interfaces*, **2017**. *9*(50), 43614–43622.

[59] A. Didden, P. Hillebrand, B. Dam & R. Van De Krol. *International Journal of Photoenergy*, **2015**. *2015*.

[60] N. Rozman, P. Nadrah, R. Cornut, B. Jousselme, M. Bele, G. Dražić, M. Gaberšček, Š. Kunej & A. S. Škapin. *International Journal of Hydrogen Energy*, **2021**. *46*(65), 32871–32881.

[61] D. Wang, R. Li, J. Zhu, J. Shi, J. Han, X. Zong & C. Li. *The Journal of Physical Chemistry C*, **2012**. *116*(8), 5082–5089.

[62] L. Mao, H. Liu, S. Liu, Q. Ba, H. Wang, L. Gao, X. Li, C. Huang & W. Chen. *Materials Research Bulletin*, **2017**. *93*, 9–15.

[63] G. Ge, M. Liu, C. Liu, W. Zhou, D. Wang, L. Liu & J. Ye. *Journal of Materials Chemistry A*, **2019**. *7*(15), 9222–9229.

[64] A. K. Patra, V. Amoli, A. K. Sinha & D. Kim. *ChemCatChem*, **2020**. *12*(8), 2315–2323.

[65] X. Hu, Y. Li, X. Wei, L. Wang, H. She, J. Huang & Q. Wang. *Advanced Powder Materials*, **2022**. *1*(3), 100024.

[66] S. Bai, W. Yin, L. Wang, Z. Li & Y. Xiong. *RSC advances*, **2016**. *6*(62), 57446–57463.

[67] Z. Liu, J. Zhang & W. Yan. *ACS Sustainable Chemistry & Engineering*, **2018**. *6*(3), 3565–3574.

[68] D. Chen, Z. Liu, Z. Guo, W. Yan & Y. Xin. *Journal of Materials Chemistry A*, **2018**. *6*(41), 20393–20401.

[69] P. B. Koli, K. H. Kapadnis, U. G. Deshpande, B. pandurang More & U. J. Tupe. **2020**.

[70] D. Roy, M. Basu & S. Paul. In *Journal of Physics: Conference Series*, volume 1579 (IOP Publishing), **2020** 012007.

[71] A. Khadher, M. Farooqui, M. Mohsin & G. Rabbani. *J. Adv. Sci. Res*, **2016**. *7*, 1–8.

[72] S. Bhatia, N. Verma & R. Bedi. *Results in physics*, **2017**. *7*, 801–806.

[73] Q. Luo. In *Solution Processed Metal Oxide Thin Films for Electronic Applications*, 109–140 (Elsevier), **2020**.

[74] D. Xia & S. Brueck. *Journal of Vacuum Science & Technology B: Microelectronics and Nanometer Structures Processing, Measurement, and Phenomena*, **2004**. *22*(6), 3415–3420.

[75] D. Xia, D. Li, Z. Ku, Y. Luo & S. Brueck. *Langmuir*, **2007**. *23*(10), 5377–5385.

[76] Y.-K. Hong, H. Kim, G. Lee, W. Kim, J.-I. Park, J. Cheon & J.-Y. Koo. *Applied Physics Letters*, **2002**. *80*(5), 844–846.

[77] J. A. Alvarado, A. Maldonado, H. Juarez & M. Pacio. *Journal of Nanomaterials*, **2013**. *2013*, 167–167.

[78] K. C. Krogman, T. Druffel & M. K. Sunkara. *Nanotechnology*, **2005**. *16*(7), S338.

[79] Z. Yildiz, A. Atilgan, A. Atli, K. Özel, C. Altinkaya & A. Yildiz. *Journal of Photochemistry and Photobiology A: Chemistry*, **2019**. *368*, 23–29.

[80] L.-Y. Hsu, W. Ding & G. C. Schatz. *The journal of physical chemistry letters*, **2017**. *8*(10), 2357–2367.

[81] J. Li, S. K. Cushing, F. Meng, T. R. Senty, A. D. Bristow & N. Wu. *Nature Photonics*, **2015**. *9*(9), 601–607.

[82] X. Liu, Y. Zhang, A. Liang, H. Ding & H. Gai. *Chemical Communications*, **2019**. *55*(76), 11442–11445.

[83] J. Hu, M. Wu, L. Jiang, Z. Zhong, Z. Zhou, T. Rujiralai & J. Ma. *Nanoscale*, **2018**. *10*(14), 6611–6619.

[84] T. V. Tsoulos, S. Atta, M. J. Lagos, M. Beetz, P. E. Batson, G. Tsilomelekis & L. Fabris. *Nanoscale*, **2019**. *11*(40), 18662–18671.

[85] J. Frank *et al. Electron tomography* (Springer), **1992**.

[86] T. Inoue, T. Kita, O. Wada, M. Konno, T. Yaguchi & T. Kamino. *Applied Physics Letters*, **2008**. *92*(3), 031902.

[87] P. A. Midgley, M. Weyland, T. J. Yates, I. Arslan, R. E. Dunin-Borokowski & J. M. Thomas. *Journal of microscopy*, **2006**. *223*(3), 185–190.

[88] M. Radermacher. *Electron tomography: methods for three-dimensional visualization of structures in the cell*, **2006**. 245–273.

[89] M. Heyndrickx, T. Bultreys, W. Goethals, L. Van Hoorebeke & M. N. Boone. *Scientific Reports*, **2020**. *10*(1), 18029.

[90] C. MessaoudiI, T. Boudier, C. O. S. Sorzano & S. Marco. *BMC bioinformatics*, **2007**. *8*(1), 1–9.

[91] R. M. Mersereau & A. V. Oppenheim. *Proceedings of the IEEE*, **1974**. *62*(10), 1319–1338.

[92] J. Trampert & J.-J. Leveque. *Journal of Geophysical Research: Solid Earth*, **1990**. *95*(B8), 12553–12559.

[93] A. C. Kak & M. Slaney. *Principles of computerized tomographic imaging* (SIAM), **2001**.

[94] K. J. Batenburg & J. Sijbers. In *2007 IEEE International Conference on Image Processing*, volume 4 (IEEE), **2007** IV–133.

[95] A. H. Andersen & A. C. Kak. *Ultrasonic imaging*, **1984**. *6*(1), 81–94.

[96] K. J. Batenburg & J. Sijbers. *IEEE Transactions on Image Processing*, **2011**. *20*(9), 2542–2553.

[97] L. J. Minggu, W. R. W. Daud & M. B. Kassim. *International journal of hydrogen energy*, **2010**. *35*(11), 5233–5244.

[98] Z. Chen, H. N. Dinh, E. Miller *et al.* *Photoelectrochemical water splitting*, volume 344 (Springer), **2013**.

[99] Y. Yang, S. Niu, D. Han, T. Liu, G. Wang & Y. Li. *Advanced Energy Materials*, **2017**. *7*(19), 1700555.

[100] E. Miller. *Energy & Environmental Science*, **2015**. *8*(10), 2809–2810.

[101] T. Hisatomi, J. Kubota & K. Domen. *Chemical Society Reviews*, **2014**. *43*(22), 7520–7535.

[102] A. G. Hufnagel, H. Hajiyani, S. Zhang, T. Li, O. Kasian, B. Gault, B. Breitbach, T. Bein, D. Fattakhova-Rohlfing, C. Scheu *et al.* *Advanced functional materials*, **2018**. *28*(52), 1804472.

2 Characterization and Techniques

Nanoparticles and nanostructured materials provide strongly morphology dependent properties, mainly based on their size and shape. Characterization of those is often difficult since devices and techniques with high precision are required and data interpretation can be difficult due to quantum effects.

With nanostructured materials often having features smaller than the wavelength of visible light conventional light microscopes are not able to resolve those at the nanometer scale. X-ray or Electron microscopy techniques, such as, scanning electron microscopy and transmission electron microscopy are used to retreive material dependend properties, such as, elemental compositions and oxidation states of nanostructured materials.

Electrochemical characterization also requires the use of high precision instrumentation and measurement setups, since photoelectrochemical corrosion currents can be as low as a few pico amperes and have to be measured precisely over a long period of time.

2.1 Electrochemical Analysis Techniques

Potentiostatic, galvanostatic, as well as, MOTT-SCHOTTKY-analysis experiments were performed using a AUTOLAB PGSTAT302N potentiostat in a 3-electrode setup with H_2/Pt as reference electrode.

2.1.1 Cyclic Voltammetry

Cyclic voltammetry (CV) is a common electrochemical analysis method used for characterization of faradaic and capacitive processes. In a 3-electrode setup, consisting of a working electrode (WE), counter electrode (CE) and reference electrode (RE), a potential is cyclically sweeped between two fixed vertex potentials at a fixed scanspeed dE/dt and applied between the WE and CE, with respect to the CE. As a result, the recorded currents J_{WE} of the working electrode in relation to the applied potentials E_{WE} are plottet and form the so-called cyclic voltammogram. Since any occuring redox processes under the applied potential have a electron exchance as a consequence, those processes are seen in an increasing current at the WE. Capacitive currents J_{cap}, which describe the accumulation and dissipation of charges at a surface are also seen in cyclic voltammetry and can give information about the electrochemical surface areas or about the rearrangement of ions at the double layer.[1]

The universal oxidation or reduction reaction, occuring on an electrode can be described by the following reaction equation:

$$\mathrm{A} \pm \mathrm{e} \rightleftharpoons \mathrm{B} \tag{2.1}$$

Thereby, among other factors, the standard rate constant k^0 for converting A to B, the diffusion coefficients and the scanning rate determine the expressed peak height in the voltammogram.

2.1.2 Chronoamperometry and Chronopotentiometry

For simulation of operating conditions a electrode can be operated at a fixed potential (chronoamperometry (CA)) or at a fixed current (chronopotentiometry (CP)) while recording the current or the applied potential over time, respectively. While in electrocatalysis often CP is used to observe the overpotential of a reaction over time, stability measurements in photoelectrochemistry are often performed as CA analysis. Using CP at various current densities allows for the determination of the TAFEL-slope and exchange current densities of an electrode.

Further, CA and CP can be related to the electrocatalytic activity of a material, since the water splitting reactions are irreversible and non-diffusion limited processes. A decrease of the measured currents in CA or an increase of the overpotential in CP indicate a decline in water splitting currents and reduced catalytic activity.

2.1.3 Electrochemical Impedance Spectroscopy

Electrochemical Impedance Spectroscopy (EIS) uses the impedance of a system, which is the ratio of voltage or potential to an alternating current (AC) system, to gain information about the resistance or capacitance of multi-interface electrochemical devices. Such a device can be a photoelectrode immersed in an electrolyte, for example. Current and voltage in an AC system are strongly related to each other, since one causes the other, periodic waves of those parameters have the same frequency. The constant time shift between those waves is called the phase shift Φ. In the BODE and NYQUIST plots the total impedance Z can be expressed by using Z as the length of a vector and Φ as the angle, with, real part of the impedance Z', plotted on the X achsis, and the imaginary part Z'' on the Y axis. (see fig. 2.1)[2–5]

The impedance can be measured by application of a fixed potential wave with known frequency, the so-called NYQUIST-frequency, to the system and recording the resulting current wave. Z, Z', Z'' and Φ can be calculated from the recorded data.[6]

The relation of current to the applied potential in the case of an AC system and the resulting impedance is shown in the following equations:

$$\text{Potential: } E_t = E_0 \cdot \sin(\omega \cdot t)$$
$$\text{Current: } I_t = I_0 \cdot \sin(\omega \cdot t + \Phi)$$
$$\text{Impedance: } Z(\omega) = \frac{E_t}{I_t} = Z_0 \frac{\sin(\omega \cdot t)}{\sin(\omega \cdot t + \Phi)}$$

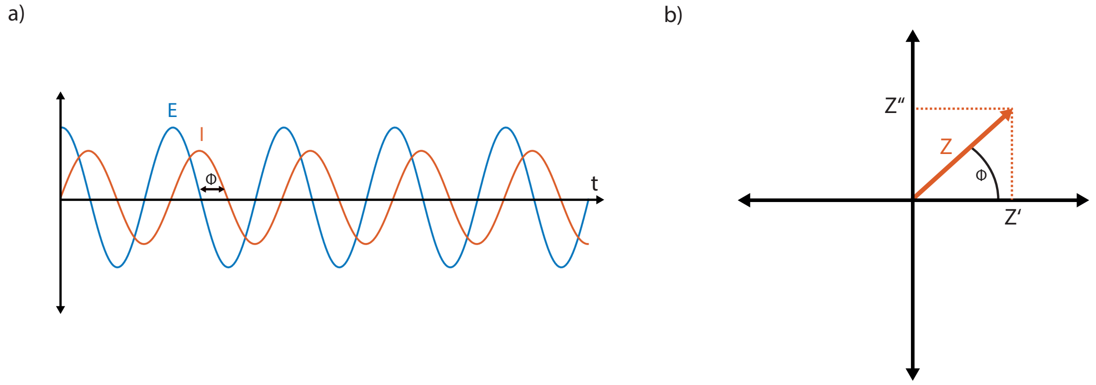

Figure 2.1: a) Periodic waves of a potential E and the resulting current I, used in EIS. Φcorresponds to the phase shift. b) Impedance Z in vector representation with Z'' at the abscissa and Z' shown on the ordinate with Φas angle between Z' and Z''.

2.2 X-Ray Diffraction

The atomic and molecular structure of a crystal is commonly determined using X-ray diffraction (XRD). An incident beam of X-rays diffracts on the periodic structure of a crystal into specific directions. The angles and intensity distribution of the diffracted beams produce a reciprocal three-dimensional picture of the electrons density within the crystal. Interpretation of the data allows one to determine information, such as, crystal lattice distances, atomic positions and atomic disorder.

The advantage of XRD is the rapid and non-destructive analysis of a known or unknown material. Crystal and phase analysis experiments were performed using a Bruker D8 X-ray diffractometer and STOE diffractometer, both using Cu-Kα radiation.

2.2.1 Theory

X-rays are generated inside a vacuum tube by interaction of fast electrons, extracted from a heated cathode with a metal target, such as, copper or molybdenum. Upon impact, the electrons excite the inner-shell electrons of the target material into the vacuum state, creating electron gaps that are subsequently replenished by higher-shell electrons, emitting characteristic photons with discrete energies. A monochromator or filter allows for the selection of one of these characteristic wavelengths to radiate towards the sample. Usually Cu-Kα or Mo-Kα with a wavelength of 1.54433 Å and 0.713543 Å are selected, respectively.[7,8]

Since crystal lattice distances are of the same magnitude as the wavelength of the produced X-rays, diffraction according to the BRAGG-equation occurs. The BRAGG-equation[9] describes the relationship of the used wavelength λ with the angle of incidence θ_B and the crystal lattice spacing d. Higher order diffractions are taken into account by an integer n in the BRAGG-equation:

$$n \cdot \lambda = 2d \cdot \sin(\theta) \tag{2.2}$$

At angles θ fullfilling the BRAGG-equation[9] constructive interference of the X-ray beam occurs, which results in intensities proportional to the square of the wavefunction at the angle of the diffracted beam, resulting in a material-specific diffraction pattern, which can be compared to a database (e g. ICSD by FIZ Karlsruhe or the OCD).

Information about crystallite sizes and domains can be extracted from reflection broadening of the pattern. While large and defectless crystalls generate sharp and distinct reflections in the XRD, small and defect-rich crystallites result in broad and less-distinct reflexes. This behavior can be described by the SCHERRER-equation, where the average size of a crystal domain d can be determined from the full width at half-maximum (FWHM) of a reflection at the corresponding angle θ and the used wavelength λ:[10]

$$d = \frac{K\ \lambda}{\mathrm{FWHM}\ \cos(\theta)} \tag{2.3}$$

Whereby K, the SCHERRER-constant, is set to 0.9 for most cases.

2.3 Electron Microscopy

Especially in nanoscience, the size of synthesized nanoparticles is usually 100 nm or less in diameter and therefore in a range where conventional optical microscopy does not provide enough spatial resolution to resolve those structures. The spatial resolution is limited by the so-called ABBE-limit, which describes a microscope's maximum resolution as a function of the used wavelength and the smallest used numerical aperture. The ABBE diffraction limit[11], where two minimum resolvable distances are distinguishable, is given by the following equation:

$$d = \frac{\lambda}{2\ n\ \sin(\theta)} = \frac{\lambda}{2\ \mathrm{NA}} \tag{2.4}$$

To overcome this limitation, RUSKA and KNOLL developed the first electron microscope in 1932, providing the basis for the developement of high-resolution microscopy down to the picometer scale until today.

2.3.1 Scanning Electron Microscopy

Scanning electron microscopy (SEM) allows for the topographical and morphological investigation of a sample. Electrons with an energy of about 1 to 40 keV are generated in the electron gun by applying a high-voltage to a heated filament, coated with a Schottky-material, in the case of a Schottky-field-emitter. The extracted electrons are further accelerated and focused towards the sample by a condensor lens system and various apertures. A scanning generator scans the electron beam over the sample's surface, where the interaction of the electron beam with the atoms in the sample generates secondary electrons, characteristic X-rays, Auger-electrons, backscattered electrons and Bremsstrahlung.[12,13]

Secondary electrons can be used for imaging by correlation of the beam position to the current, caused by those electrons in an Everhart-Thornley detector.[14] This type of detector consists primarily of a scintillator and is located inside the specimen chamber of the SEM. A positive voltage at the detector attracts the low energy secondary electrons and converts them to light using the scintillator inside the detector. A photomultiplier amplifies the signal and uses it as intensity signal of the corresponding pixel in the image.

Backscattered electrons, which typically possess higher energies than secondary electrons, can be detected by applying a high negative voltage to the detector to deflect low energy electrons such as secondary electrons. The signal corresponds to the backscattered electrons and can be used for Z-contrast imaging or backscattered electron diffraction.

Characteristic X-rays, generated by the interaction of the primary electron beam (see fig. 2.2) with the sample gives information about a sample's composition using energy dispersive X-ray (EDX) spectroscopy. EDX is an analytical technique that provides elemental compositions and chemical characterization of the sample. Its principle relies on the interaction of a primary electron with an inner-shell electron in an atom of the sample. The high-energy incoming electron excites an inner-shell electron to the vacuum state leaving an electron vacancy. The recombination of this vacancy from a higher state takes place under emission of an X-ray photon with an energy corresponding to the energy difference of the shells involved in recombination. Since all these energy transisitions are characteristic for the element and its electronic shells, the photon energy can be attributed to the elemental composition. EDX spectrometers are usually equipped with a silicon drift detector, which allows for direct determination of the incoming photon's energy to the generated electron-hole pairs upon interaction of a photon with the detector.

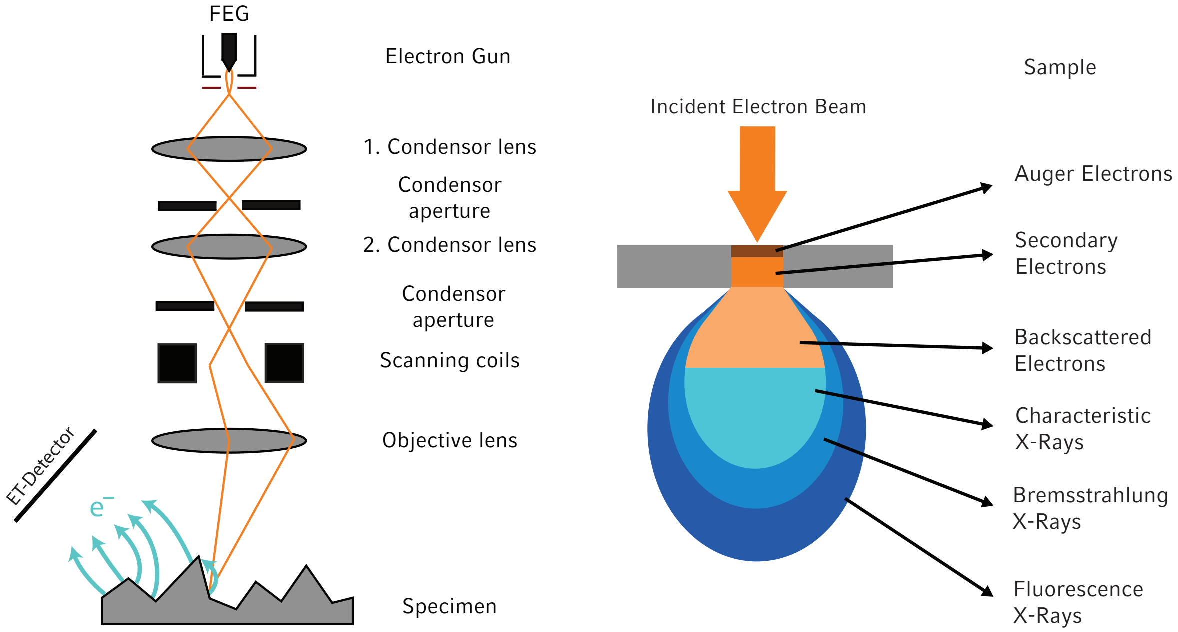

Figure 2.2: Left: Scheme of a scanning electron microscopes. Free electrons are generated in the electron gun and accelerated towards the specimen. Multiple condensor lens systems and apertures focus the electron beam onto the sample. The scanning coils deflect the beam and therefore allow to scan the beam over the sample. Right: Interaction volume of the incident electron beam with the sample generating AUGER-, secondary, backscattered electrons and characteristic X-rays and fluorescence.

2.3.2 Focused Ion Beam Microscopy

Focused ion beam (FIB) microscopy[15–17] is closely related to SEM with the difference that a FIB setup uses a focused beam of ions instead of electrons. The highly accelerated ions possess a higher momentum and therefore stronger interactions with the sample, compared to electrons, used in the SEM. This allows the FIB to be used for imaging, etching and deposition and is therefore commonly used to prepare thin TEM lamellae of a sample.[18]

FIB systems today are usually incorporated in dual beam devices, which include an SEM and a FIB in one device. The most common type of a FIB microscope uses Ga^+ ions, which are extracted by means of high electric fields from a heated gallium metal source and accelerated towards the sample in the form of a finely focused beam of ions. Low beam currents can be used for imaging, while high beam currents allow for site specific milling or etching.

On impact of the ions onto the sample, the sample's atoms are ablated in the form of neutral or secondary ions. Additionally, secondary electrons originating from this process are generated and can be used for imaging purposes. FIB images are usually sensitive to grain orientation and material contrast.

In contrast to SEM, FIB causes (partial) destruction of the specimen. The high energy gallium ions sputter atoms from the sample's surface and therefore allow the precise milling on the nanometer scale of the sample. This allows the FIB to be used for machining at the micro/nanometer scale of a wide range of materials.

Ion beam-induced deposition of metals, such as platinum, or carbon can be achieved by introducing precursor gases into the vacuum chamber where the gas adsorbs onto the sample. On interaction with the ion beam the gas decomposes to generate the corresponding solids, which are therefore deposited on the sample where the ion beam was located. This gas-assisted deposition can be used to apply a protective layer for further etching processes, or to fuse nanoparticles or a FIB lamella to a manipulator.

2.3.3 Transmission Electron Microscopy (TEM)

To get high resolution images of nanoscale materials, common light microscopy is not suitable. In 1932 Ruska and Knoll[13] built a microscope which used highly accelerated electrons instead of light.[13] These electrons allow for imaging at atomic resolution with today's high resolution TEM instruments, as the Abbe-limit describes the maximum resolution in dependence of the wavelength of the used irradiation. The transmission electron microscope (TEM) offers deep insights into the sample's properties like crystal structure, orientation, morphology or elemental composition. Several different detectors or spectroscopes can be further attached to the microscope. They can be used to get detailed information about the material's composition, band gaps or oxidation states. This section discusses some details about the setup and the functionality of a TEM and the most commonly used operating modes.

2.3.3.1 Setup of a Transmission Electron Microscope

The setup of a TEM can be compared to the setup of a typical optical light microscope. A sample area is illuminated by an electron beam which is accelerated towards the sample. The electrons penetrate and interact with the samples' material. The electrons are detected below the sample in transmission.

Free electrons are emitted from a cathode via thermal or field emission and accelerated by an electrical field towards the sample. In the case of thermal emission, the emission current density J is given by the Richardson-equation ($J \sim T^2 \cdot e^{-\frac{\phi}{k_B T}}$)[19] which describes the dependency of J on the work function of the metal ϕ and the temperature T. The most common thermal emitter materials are tungsten (W) or lanthanum hexaboride (LaB_6) due to the high melting point of W (3422 °C)[20] or low work function of LaB_6 ($\phi(LaB_6) = 2.3 - 2.4\,eV$)[21]. Field emission guns (FEG) require very strong electric fields ($\sim 10^9\,Vm^{-1}$) on sharp tungsten tips. Due to the strong field, the work function of the material is lowered and bent such that electron-tunneling into the vacuum occurs. The current density J for FEGs can be described by the FOWLER-NORDHEIMER equation ($J \sim e^{-\frac{k\phi^{3/2}}{|E_{el}|}}$)[22], where k is a constant dependent on the material, ϕ is the work function and E_{el} is the electric field strength. A FEG supplies a high brightness electron beam at narrower energy widths in comparison to the thermionic emitters. The so called "SCHOTTKY" emitter[23] combines the principles of thermionic and field emitters and benefits from higher intensities at the cost of energy width and brightness.[24]

The generated electron beam is focused by the condensor lens system, which controls the intensity and convergence of the beam by an electro-magnetic deflection of the electrons due to a generated inhomogeneous electromagnetic field. The sample thickness should be in the range of ~100 nm for the electrons to be able to pass through. The image of the sample is projected onto the image plane of the objective lens and is further magnified by intermediate and projector lenses to form the final image on the screen. Alternatively, the diffraction pattern in the back focal plane of the objective lens can be magnified and focused on the screen. Optionally a selected area diffraction (SAD) aperture can be inserted into the beam path at the position of the projected image plane of the objective lens to only allow electrons of a specific area of the sample being used for generation of the diffractiton pattern. A schematic setup of the image generation in the TEM can be seen in fig. 2.3.

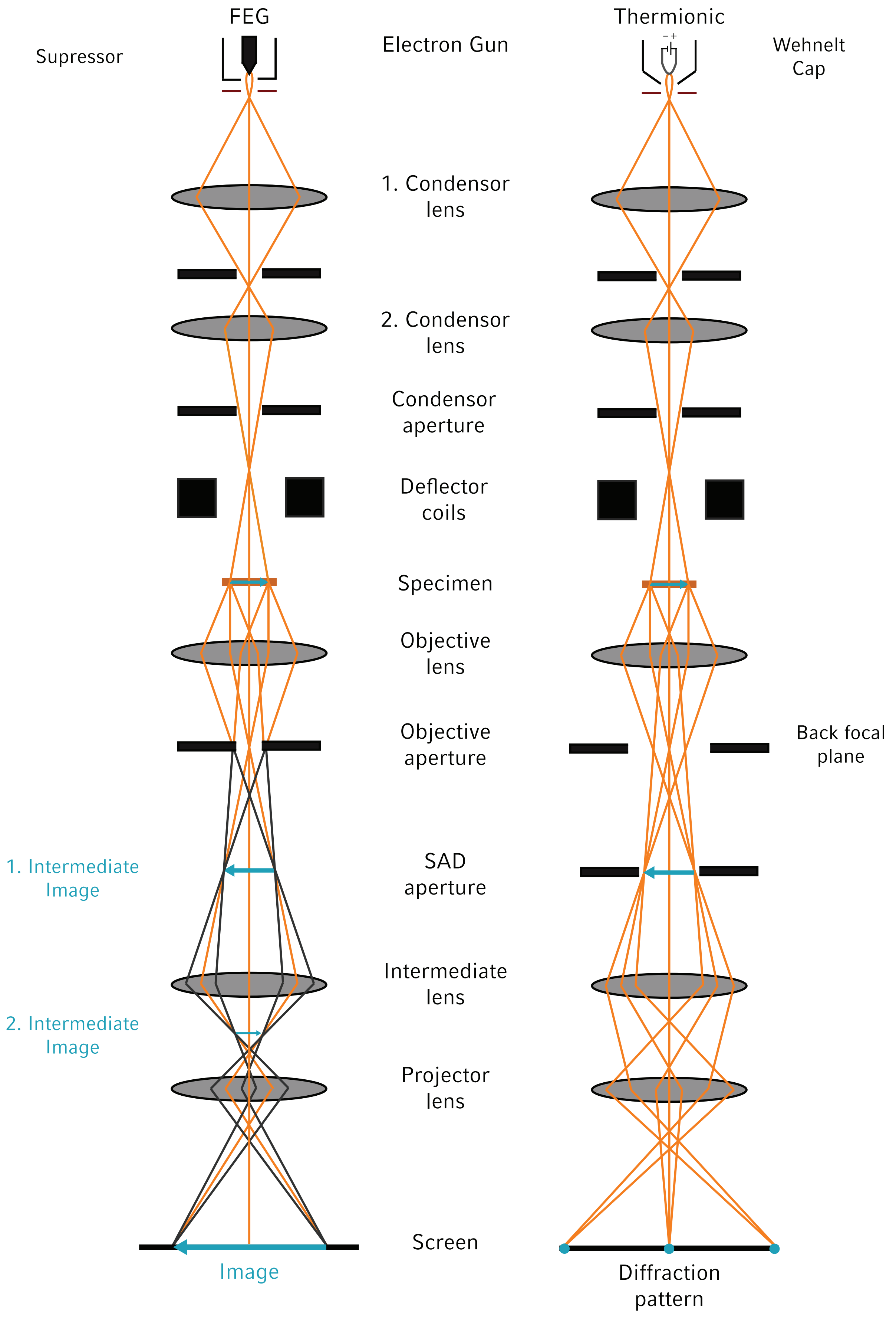

Figure 2.3: Schematic setup of a TEM with beam path [25]. **Left:** TEM equipped with a FEG as electron source. The projector lens system focuses a magnified image of the sample on the screen. **Right:** TEM equipped with thermionic gun. The projector lens system focuses the diffraction pattern on the screen.

2.3.3.2 Electron Diffraction

Crystalline samples can be characterized by their diffraction pattern. The diffraction pattern results from constructive interference of electrons on crystal lattice planes. The scattering of the electrons can be compared to the scattering in the double-slits-experiment with light. Electrons can be described as waves due to the wave-particle duality and hence they are capable of constructive and destructive interference depending on the path differences and the corresponding phase shift of the wave. Constructive interference occurs for BRAGG angles θ_B when the path length difference δs is a multiple integer (order of diffraction k) of the wavelength λ. Thereby, the scattering angle θ is twice θ_B. This dependence is described by the BRAGG equation, which can be seen in eq. 2.5.[26,27]

$$k \cdot \lambda = 2d \cdot \sin(\theta_B) \tag{2.5}$$

As a result, the lattice plane spacings d_{hkl} can be directly calculated from the BRAGG equation.[9] The intensities of the diffraction spots, the distances between the spots and the symmetry of the pattern are characteristic for a crystalline material phase.

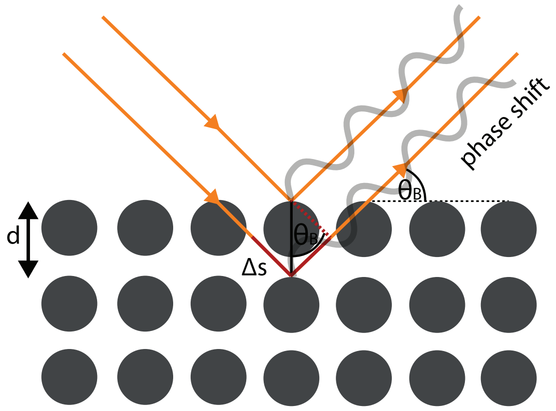

Figure 2.4: BRAGG diffraction on crystal lattice planes. The BRAGG angle θ_B depends on the lattice plane distance d and the wavelength λ.

2.3.3.3 Bright Field and Dark Field Imaging

In bright field mode (BF) an aperture is placed in the back focal plane of the objective lens, blocking the diffracted beams selectively. This results in an enhanced contrast and strongly scattering parts of the sample appear dark in the image. A detailed interpretation of the contrast can be difficult due to the simultaneous occurrence of different contrast-forming phenomena. Alternatively, the objective aperture can be positioned around distinct diffraction spots of the diffraction pattern. Only sample regions which contribute to this diffraction spot appear bright in the image, a so called dark field (DF) image.

2.3.3.4 Scanning Transmission Electron Microscopy (STEM)

A TEM which operates in scanning mode uses a strongly convergent electron beam which is raster-scanned over a specified sample area. Transmitted electrons are detected by various STEM detectors below the sample. An image is generated by correlation of the beam position with the measured signal. STEM detectors consist of multiple ring detectors which allow the direct detection of signals at different scattering angles. The bright field detector records electrons scattered in forward direction up to an angle of around $10-25\,\mathrm{mrad}$ ($\theta < 10 - 25\,\mathrm{mrad}$). The annular dark field detector is a ring detector with a hole in the middle. Depending on the magnificaton of the diffraction pattern (camera length), it detects electrons scattered into an angular range with a minimum and maximum. In annular dark field mode, this angular range is set to approximately $25 < \theta < 50\,\mathrm{mrad}$. Higher scattering angles with $\theta > 30\,\mathrm{mrad}$ (RUTHERFORD scattering) can be detected by further increasing the camera length, thereby a high-angle annular dark-field (HAADF) signal is obtained. In HAADF-STEM, the image contrast is directly depending on the atomic number Z (Z-contrast) due to the increased RUTHERFORD scattering probability with increased Z.[25] STEM is particulary suitable for analytical techniques such as energy dispersive X-ray (EDX) and electron energy loss spectroscopy (EELS).[28,29]

2.3.4 Spectroscopy Methods

Spectroscopic methods in electron microscopy usually include energy dispersive X-ray spectroscopy (EDX) and electron energy loss spectroscopy (EELS). Both methods use interactions of the incident electron beam with the samples' material to gain additional information about the sample such as elemental composition, oxidation states, phonon excitations, inter- and intra-band transitions, plasmonic resonance or inner shell ionization.

2.3.4.1 Energy Dispersive X-Ray Spectroscopy

Energy dispersive X-ray spectroscopy (EDX) also referred to as EDS uses the interaction of the primary electron beam and the sample. If the incident electrons provide enough energy to excite an inner-shell electron creating an electron hole, a higher-energy shell electron replenishes the hole and releases the difference between the higher-energy and lower-energy shell in form of a photon (X-ray) with a discrete wavelength. The resulting photons are characteristic of the difference in energy between the two shells and the type of element.[30]

Detecting the energy and the number of the generated characteristic X-rays allows the determination of presence and abundance of a specific element. This is usually done using silicon drift detectors with attached PELTIER cooling systems. The energy of an incident photon is measured by the amount of ionization in the detector material. In high-purity silicon with PELTIER cooling the amount of generated electron-hole pairs is directly proportional to the incident photon energy and therefore offers an easy way for X-ray detection at high count rates and high energy resolution.

2.3.4.2 Electron Energy Loss Spectroscopy

In electron energy loss spectroscopy (EELS) electrons from the incident electron beam are inelastically scattered by the samples' material. The loss in energy by the scattering process can be measured by an electron spectrometer.[31]

Detection of the energy loss requires a filter and a magnetic prism, which focuses equal-energy electrons onto a point in the detector plane. The spatial read-out of the camera features the EEL spectrum.

In the EEL spectrum the energy range with energy losses smaller than 50 eV is referred to as the low-loss region, while higher energies are referred to as core-loss region. The zero-loss peak, which is the most dominant feature in the EEL spectrum, describes the electrons, that passed through the sample without loosing energy, while the low-loss region features information such as sample thickness or band gaps. The core-loss region shows element-specific features such as information about oxidation states or elemental compositions.

EELS can be used as complementary method to EDX, since elements overlapping in the EDX usually don't overlap in the EEL spectrum and vice versa.

EELS can further be used to measure a sample's thickness. Since the plasmonic region in the EEL spectrum is mainly depending on the mean free path of electrons, traveling through the material and the sample thickness, the thickness can be estimated from the sum peak at the plasmonic region and the mean free path λ_p for each element present.

In this thesis a THERMO FISHER SCIENTIFIC / FEI Helios G3 UC scanning electron microscope with a resolution of 0.6 nm/px and a THERMO FISHER SCIENTIFIC / FEI Titan Themis 80–300 with a resolution of < 90 pm was used for high resolution TEM, STEM and tomography experiments. A THERMO FISHER SCIENTIFIC / FEI Tecnai G2 operating at 200 kV and equipped with a TVIPS CCD camera was used for initial and standard investigations.

2.3.5 Electron Tomography

Tomography, in the common sense, describes the reconstruction of a 3D object from multiple 2D projections at different angles. The reconstruction is performed by a combination of various mathematical processes like the RADON transformation, image convolution or the SIRT algorithm. Relevant processes used in this thesis are explained in the following.

2.3.5.1 Radon Transformation and Reprojection

In the context of tomography, a projection is referred to as an image which represents a 3D object in 2D seen from a specific perspective angle. In theory, a projection of an object is generated by a set of parallel rays penetrating the object and hitting a projection plane orthogonally.[32] The pixel's intensity on the projection plane results from the sum of the intensities of the incident rays hitting the plane in the pixel area. The rays' intensity is dependent on the interactions within the material during the penetration. A geometrical illustration of the formation of projections for the case of a 2D and a 3D object is shown in fig. 2.5(A) and (B) respectively. The mathematical description of this projection is given by the so called RADON transformation.

The RADON transformation is named after JOHANN RADON, an Austrian mathematician, who provided a mathematical description for a projection of an object at a specific angle.[33] It is mainly used in tomographic techniques and returns a parallel projection (forward projection) of the object along a radial line at a specified angle.[34]

In the case of a 2D object, the transformation is realized by line integration over the object's function $b(x, y)$ multiplied with a transformation kernel δ. In this case, δ represents the DIRAC-δ

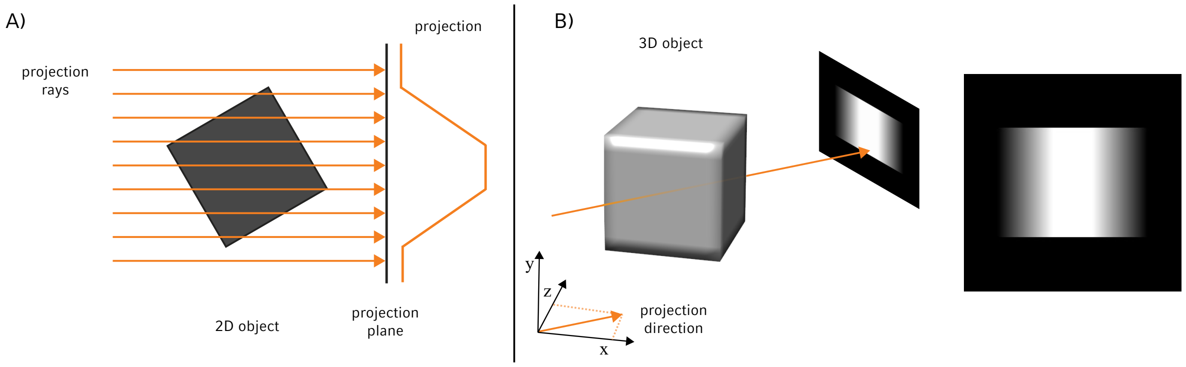

Figure 2.5: A) Schematic illustration of projection rays penetrating an object (cube). The resulting projection is the sum of the intensity of each projection ray hitting the projection plane in the pixel area. B) RADON transformation of a 3D cube results in a 2D projection of the cube.

"function". δ does not fulfill the criteria of a function in the traditional sense but is merely an assignment of values at various points:[35,36]

$$\delta(n) = \begin{cases} 0, & n \neq 0 \\ +\infty, & n = 0 \end{cases} \tag{2.6}$$

δ is often approximated with the unit momentum function, which can be described as a Gaussian with zero width and infinite height.[34,37] The total area of the spike in the origin, according to the normalization integral is one:

$$\int_{-\infty}^{\infty} \delta(n)\mathrm{d}n = 1 \tag{2.7}$$

In the case of the RADON transformation, the δ-function is used as transformation kernel with the linear equation of a projection ray in the argument. Multiplication of $b(x, y)$ with δ causes a summation of all values of $b(x, y)$ which are located on the projection ray.[38] Hence, the RADON transformation $\mathcal{R}$ can be described as function r of b at the angle φ, the position vector $x^T = \begin{pmatrix} x \\ y \end{pmatrix}$, the line distance from the origin u and $e_\varphi = \begin{pmatrix} \cos(\varphi) \\ \sin(\varphi) \end{pmatrix}$:[38]

$$r(u, \phi) = \mathcal{R}\{b(x, y)\} := \int_{-\infty}^{\infty} \int_{-\infty}^{\infty} b(x, y)\delta(x^T \cdot e_\varphi - u)\mathrm{d}x\mathrm{d}y \tag{2.8}$$

Fig. 2.6 shows a schematic illustration of the RADON transformation. The shown projection ray (orange vector) penetrates the object (gray) and hits the projection plane. The added intensities of all rays can be seen as 2D projection of the object on the projection plane.

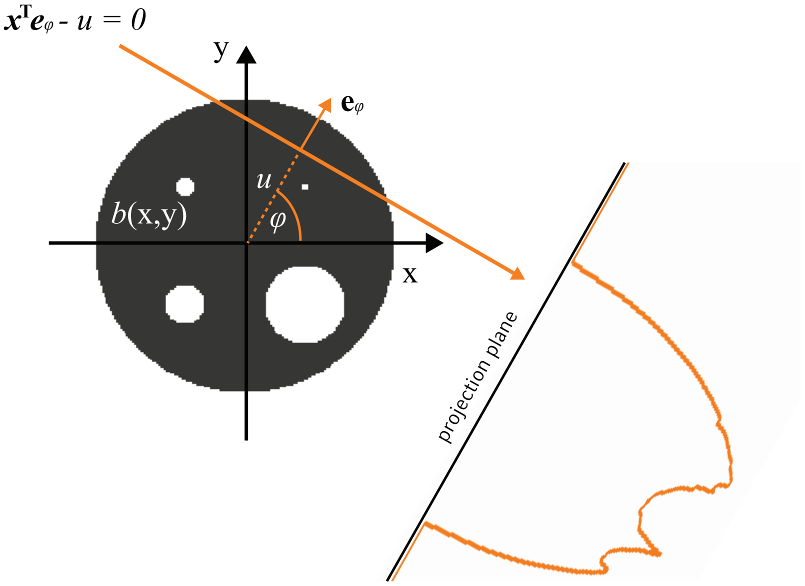

Figure 2.6: Geometrical illustration of the Radon transformation. All intensities of $b(x, y)$ are added up to a pixel on the projection plane if they are located on a projection ray $(x \cdot e_\varphi - u)$.

The inverse Radon transformation or retransformation $\mathcal{R}^{-1}$, which returns the backprojection of the transformed data, can be obtained by mathematical conversion:[39]

$$b(x,y) = R^{-1}\{r(u,\varphi)\} = \frac{1}{2\pi^2}\int_{0}^{\pi}\int_{-\infty}^{\infty}\frac{1}{(x^T e_\varphi - u)}\frac{\partial r(u,\varphi)}{\partial u}\mathrm{d}u\mathrm{d}\varphi \tag{2.9}$$

In theory, a reconstruction of an object can be obtained by the inverse Radon transformation. However, the full set of line integrals has to be known which is not possible in most tomographic techniques due to a limited number of projections and acquisition angles. In practice, the retransformation is done algorithmically by an even distribution of the projections' intensities over the whole length of the volume interpolated to a cartesian grid. This principle is used in most common tomographic techniques like the weighted backprojection (WBP)[40] or filtered backprojection[41].

2.3.5.2 Reconstruction Algorithms

Tomographic techniques include a variety of different algorithms used for a 3D reconstruction from projections. This section introduces three commonly used algorithms: The algebraic reconstruction technique (ART), the simultaneous iterative reconstruction technique (SIRT) and the discrete algebraic reconstruction technique (DART). These algorithms differ with respect to their suitability for different objects, computing time and quality of reconstruction.

2.3.5.3 ART

Because of limitations in acquisition setups, projections from certain angular ranges are not accessible in many cases. This often results in inaccurate or imperfect reconstructions. The problem was tackled by GORDON *et al.* who rediscovered the idea of an algebraic reconstruction technique[42] whose fundamental principles were already provided in 1937 by STEFAN KACZMARZ.[43] The goal is the recovery of the density function of an object from its forward projections (RADON transformations) at a limited range of angles and number of projections.[44] ART supplies a numerical solution for the reconstruction of an object estimating a transformation vector in a system of linear equations:

$$Wa = p \tag{2.10}$$

In the case of a 2D reconstruction, W is the density matrix containing the weight a voxel j contributes to a ray i. The elements of W are referred to as w_{ij}. w_{ij} is usually the length or the part of the volume the ray i penetrates the cell j. p is a vector containing the measured projection values and a a vector containing the values of the object per cell. Using this, the set of linear equations can be expanded to:[45]

$$\begin{aligned} w_{11}a_1 + w_{12}a_2 + \cdots + w_{1N}a_N &= p_1 \\ w_{21}a_1 + w_{22}a_2 + \cdots + w_{2N}a_N &= p_2 \\ &\vdots \\ w_{M1}a_1 + w_{M2}a_2 + \cdots + w_{MN}a_N &= p_M \end{aligned} \tag{2.11}$$

Here M and N are the lengths of the vectors p and a respectively. Due to limited computation power large systems cannot be solved analytically for a. Numerical solutions like ART-1[43], multiplicative ART[46] or ART-3[47] were developed for fast and accurate solutions of those systems. They are based on cyclic estimations of the solution with modification of a.

The following equation shows the update statement for a of an iteration i:[45,48,49]

$$a^{(i)} = a^{(i-1)} + \frac{p_i - \langle a^{i-1}, \mathbf{w}_{i,:} \rangle}{\langle \mathbf{w}_{i,:}, \mathbf{w}_{i,:} \rangle} \mathbf{w}_{i,:} \tag{2.12}$$

Let $\mathbf{w}_{i,:} = (w_{i1} \;\; w_{i2} \;\; \ldots \;\; w_{iN})^T$ be the transposed i-th ($i \in \{1, \ldots, M\}$) row of W.

Hence, W can be written as: $W = \begin{pmatrix} \mathbf{w}_{1,:}^T \\ \mathbf{w}_{2,:}^T \\ \vdots \\ \mathbf{w}_{M,:}^T \end{pmatrix}$. The update equation for the next iteration uses the residual, shown in the numerator, of the last iteration $a^{(i-1)}$ to update $a^{(i)}$.

All cells j being penetrated by the ray i and having a weight $w_{ij} \neq 0$ are updated in $a^{(i)}$.

The initial guess $a^{(0)}$ is arbitrary but should be as close as possible to the solution for fast convergence. Convergence is reached when the equation $Wa = p$ is satisfied. As convergence criterion the mean squared error (MSE) of $a^{(i)}W$ and p_i is commonly used. Due to inconsistencies in the set of equations introduced by approximations used for a ART usually suffers from salt and pepper noise.[48] These noise effects can be reduced by using relaxation parameters and constraining operators. Nevertheless, this results in much longer convergence and computing times in return.[42,50]

2.3.5.4 SIRT

In 1972, GILBERT *et al.* independently developed an algorithm similar to ART (see 2.3.5.3), called the simultaneous iterative reconstruction technique. In contrast to ART, SIRT updates $a^{(k-1)}$ to $a^{(k)}$ after all N computations. The update equation for SIRT can be expressed as:[45]

$$a_j^{(k)} = a_j^{(k-1)} + \frac{1}{\sum_{i=1}^{M} w_{ij}} \sum_{i=1}^{M} \frac{w_{ij} r_i^{k-1}}{\sum_{h=1}^{N} w_{ih}} \tag{2.13}$$

With r_i^k as the residual vector from the previous iteration: $r_i^k = (p - Wa^{(k)})$.[45] The elegance of this expression becomes more clear when written in matrix-vector notation. Two diagonal matrices $R \in \mathbb{R}^M$ and $C \in \mathbb{R}^N$ are defined which contain the inverse of the sum of the columns and rows of the weighting matrix. This compensates for the number of rays hitting each cell and the number of cells that are hit by each ray: $r_i = 1/\sum_{j=1}^{N} w_{ij}$ and $c_i = 1/\sum_{i=1}^{M} w_{ij}$. Taking this into account the update equation can be simplified to:[45]

$$a^k = a^{k-1} + CW^T Rr^{k-1} \tag{2.14}$$

The SIRT approach usually leads to better looking, less noisy reconstructions than the ones computed by ART. Fast convergence, easy implementation and high quality reconstructions nowadays make SIRT a widely used technique for reconstruction in almost all tomographic processes.[51,52]

2.3.5.5 DART

The discrete iterative reconstruction technique (DART) is an approach combining the elements of discrete and continuous tomography. It was developed by Batenburg *et al.* in 2011.[53] DART basically consists of alternating SIRT and segmentation steps providing low-noise, high quality reconstructions with fast convergence. DART is applicable for objects having a limited number of fixed scattering densities (material values) and assumes that most of the errors in the reconstruction are located near the boundary of the object to the vacuum. Hence, all non-boundary voxel values are fixed to a discrete material value z or in the case of vacuum to 0. The choice of material value depends on a previously set threshold, the segmentation parameter. Thereby, z depends on the material density, the background and the acquisition parameters. With most of the voxels being fixed to the correct value, the new estimation for the boundary voxels will be much more accurate in the next SIRT iteration. Alternating these two steps repeatedly leads to fast convergence in the sense of the MSE between projection and reprojection. Nevertheless, wrongly determined and assigned material values will lead to over- or underestimation of the object.

All tilt series used for tomographic reconstructions in this thesis were recorded using the Thermo Fisher Scientific / FEI Titan Themis 80-300 transmission electron microscope, operating at 300 kV in STEM HAADF mode. As sample holder a Fischione tomography holder capable of tilt angles up to 80°C was used. The reconstructions were done iteratively using TomoJ for image alignment and subsequently alternating SIRT and DART until the standard deviation of the reprojectons of the reconstruction was minimized.

2.4 Volumetric Sorption Analysis

2.4.1 Nitrogen Sorption

Sorption methods are a common way to characterize porous materials. Materials' properties such as pore volume, specific surface area and pore size distribution can be estimated from nitrogen sorption experiments.[54,55] Sorption, in general, can be classified in absorption and adsorption. The absorption process refers to the penetration of a substance into the solid (porous) material whereas adsorption describes the process of an attachment of molecules onto the material's surface. Materials that are capable of adsorption are called "adsorbent", while the substance which gets adsorbed is called "adsorbate". The adsorption methods can be further classified in two subcategories, on the one hand the physisorption and on the other hand the chemisorption. During chemisorption, the adsorbate changes the material chemically by a reaction of the adsorbent with the adsorbate. In the case of the physisorption process, the adsorbate forms just weak interactions such as van-der-Waals forces and can be easily removed again reducing the pressure.

In a typical nitrogen sorption experiment, a known amount of sample is outgassed at elevated temperatures and reduced pressures to remove impurities, left-over solvent or adsorbates. For the experiment, the sample is usually cooled down to the boiling point of the adsorbate (77 K for nitrogen (N_2)). The temperature is kept constant during the acquisition of the isotherm.

The IUPAC (International Union of Pure and Applied Chemistry) classifies the isotherms into six major types, denominated isotherms type I through VI (see fig. 2.7). Each type of isotherm is characteristic for a certain class of material.[54] Depending on the pore diameter the pores can be classified into micro-, meso- and macropores. The most common model for the description of gas adsorption in porous materials was developed by Brunauer, Emmett and Teller in 1938 (BET theory).[56] They based their model on a number of assumptions like a dynamic equilibrium of adsorption and desorption, an energetically homogeneous surface with no favored adsorption sites, and the absence of lateral interactions between the adsorption layers. Even though these assumptions are not always fulfilled, the BET model can be applied in good approximation for a large variety of materials.

In this work nitrogen sorption measurements were performed on a Quantachrome Instruments – Autosorb-1 at 77 K.

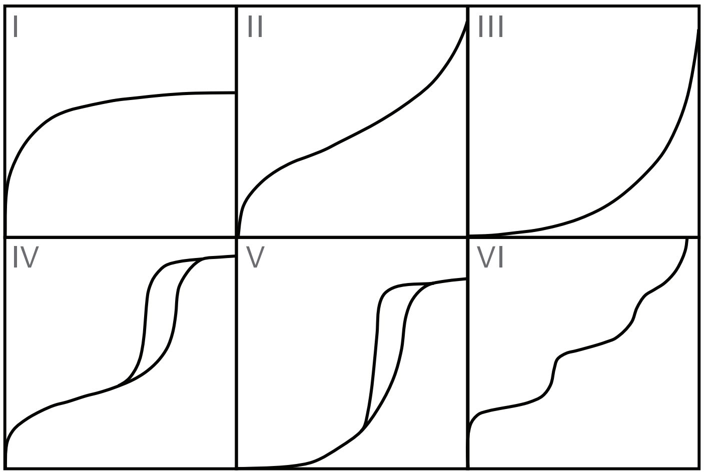

Figure 2.7: The six major types of isotherms, according to IUPAC. Type **I**: microporous material (monolayer adsorption); Type **II**: non- or macroporous materials (high adsorption enthalpy); Type **III**: non- or macroporous material (low adsorption enthalpy); Type **IV**: mesoporous material (high adsorption enthalpy); Type **V**: mesoporous material (low adsorption enthalpy); Type **VI**: nonporous, uniform material (layer-by-layer adsorption). Adapted from Sing *et al.* [54]

2.5 Photoelectrochemical Analysis

Photoelectrochemical analysis involves the study of the interplay between light and electric current at the surface of a material. It enables the determination of critical parameters such as photoelectrochemical efficiency, charge carrier dynamics, and photoresponse characteristics. In a typical three-electrode setup, the analysis employs a working electrode, a reference electrode, and a counter electrode, immersed in an electrolyte solution. When illuminated, the photons excite the photoelectrochemically active material, initiating photoelectrochemical processes that can be monitored and quantified.

One of the key aspects of photoelectrochemical analysis is the determination of photoelectrochemical efficiency, which quantifies the effectiveness of a thin film or nanoparticle-based photoelectrode in converting light energy into electrical energy. Efficiencies are often evaluated through measurements of photocurrent density, open-circuit potential, fill factor, and power conversion efficiency. These parameters reflect the ability of the film or nanoparticles to generate and transport charge carriers, as well as their ability to harvest light. Understanding the charge carrier dynamics and transport properties of thin films or nanoparticles is crucial for optimizing their photoelectrochemical performance. Techniques such as transient absorption spectroscopy [57], time-resolved photoluminescence spectroscopy [58,59], and impedance spectroscopy [2,60,61] provide insights into charge carrier generation, recombination, and transport processes. These measurements help to evaluate the photoelectrochemical mechanisms and behavior of nanoparticles, leading to deeper insights and improvements in device performance.

2.5.1 Mott-Schottky Analysis

Mott-Schottky analysis [62–64] is a valuable electrochemical technique employed within photoelectrochemical analysis to investigate the electronic properties and charge transport behavior of materials, including nanoparticles. This analysis offers insights into the surface charge accumulation and depletion phenomena under an applied potential, and can be used to determine the carrier concentration and flat band potential of a semiconductor material.

The analysis is based on the Mott-Schottky equation [62], which describnes the relationship between the capacitance of the space charge region (CSC), the applied potential (V), the semiconductor properties, and the carrier concentration (N) of the material. The Mott-Schottky equation is shown in the following:

$$\frac{1}{C^2} = \frac{2}{\epsilon\epsilon_0 A^2 e N_d}(V - V_{fb} - \frac{k_B T}{e}) \tag{2.15}$$

Here, C refers to the capacitance of the space charge region, e represents the elementary charge, ϵ is the relative permittivity of the material, A the area, ϵ_0 is the vacuum permittivity, N_d denotes the dopant concentration, V represents the applied potential, and V_{fb} signifies the flat band potential.

To conduct a Mott-Schottky analysis, electrochemical impedance spectroscopy (EIS) [2,65,66] measurements are used. EIS involves the application of an alternating current signal to the interface between the semiconductor and the electrolyte, enabling the measurement of resulting impedance. By analyzing the impedance data, the capacitance of the space charge region can be determined.

The obtained impedance data are then utilized to generate a Mott-Schottky plot by plotting $\frac{1}{C^2}$ as a function of the applied potential. The slope of the plot provides crucial information about the carrier concentration, while the intercept on the potential axis yields the flat band potential. Mott-Schottky analysis facilitates the understanding of doping levels, carrier density, and the predominant charge carrier type (electrons or holes) within the semiconductor material. It is particularly useful for investigating surface properties and evaluating the effectiveness of surface modifications or coatings on the photoelectrochemical performance of thin films or nanoparticles.

In summary, Mott-Schottky analysis is a powerful tool within photoelectrochemical analysis, enabling to gain insights into the electronic properties of semiconductors and photoelectrochemically active materials.

2.6 Optical Spectroscopy

2.6.1 Raman Spectroscopy

Raman spectroscopy is based on the Raman effect, which was first described by C. V. Raman in 1928. Raman spectroscopy has become a powerful technique for the characterization of materials. The Raman effect describes the excitation of a dipole oscillation by light or light-emission of an oscillating dipole in a molecule. The excitable energetic levels correspond to rotation-, vibration-, phonon-, or spinflip-processes. The molecules' electrons can be excited into a higher energetic, virtual state by a photon with an energy $h\nu_0$. After that, the system can relax and hence emit a photon with an energy $h\nu_1$. In the case of elastic scattering, the emitted photon has the same amount of energy as the incident photon: $h\nu_1 = h\nu_0$. This case is called Rayleigh scattering. If the molecule relaxes to a state of lower energy than the initial state, the emitted photon has a higher energy: $h\nu_1 > h\nu_0$. This is referred to as Anti-Stokes scattering. The molecule is also able to relax to a state of higher energy than the initial state. This is referred to as Stokes scattering and results in the emission of a lower energy photon: $h\nu_1 < h\nu_0$.[67,68] These effects can be used to draw conclusions about the material's properties like doping, presence of functional groups or composition. A schematic energy level diagram illustrating Rayleigh, Stokes and Anti-Stokes scattering can be seen in fig. 2.8. The emitting photons are refracted by prisms or grids onto a charge-coupled device (CCD), where the intensity/counts per wavelength/wavenumber is measured. The Raman measurements were carried out using a Olympus BX41 Raman microscope with a Symphony CCD detection system and a He-Ne laser ($\lambda = 633\,\mathrm{nm}$).

2.6.2 Dynamic Light Scattering

The dynamic light scattering (DLS) technique is a common way for the estimation of particle sizes. A sample containing suspended particles is illuminated by a monochromatic laser ($\lambda = 633\,\mathrm{nm}$). The laser light gets scattered (Rayleigh-scattering) on the particles and is detected in close to backscattering geometry. A coherent and monochromatic laser beam loses its coherence when being scattered by the particles. This causes the formation of a speckle pattern. The Brownian molecular fluctuations and the size of the particles influence the scattering of the laser beam such that the speckle pattern can be used to analyze the particles. The dynamic information is derived from the autocorrelation of the intensity I during the experiment, with $g_2(q,\tau)$ as the second order autocorrelation function, q as the wave vector and the delay time τ:[69,70]

$$g_2(q,\tau) = \frac{\langle I(t)\, I(t+\tau)\rangle}{\langle I(t)\rangle^2} \tag{2.16}$$

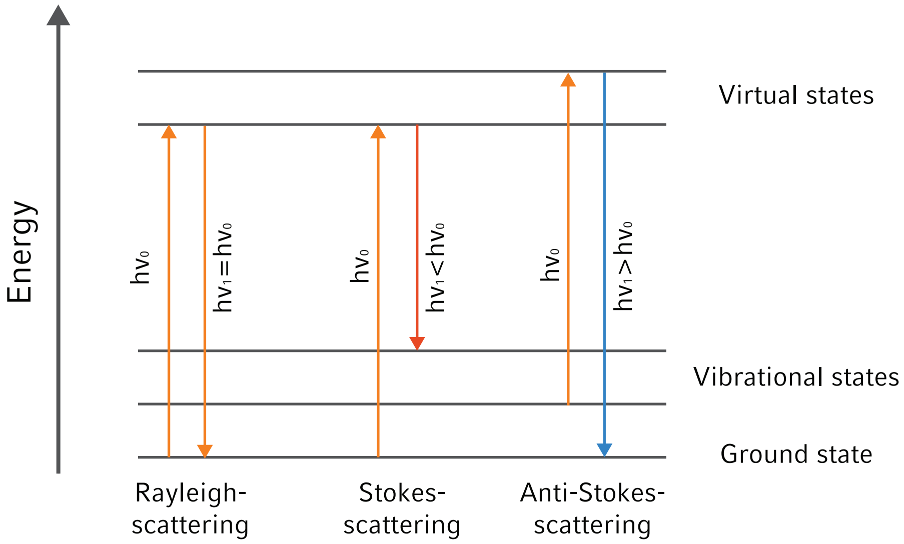

Figure 2.8: Energy scheme for RAYLEIGH scattering ($h\nu_1 = h\nu_0$), STOKES scattering ($h\nu_1 < h\nu_0$) and anti-STOKES scattering ($h\nu_1 > h\nu_0$).

The correlation data need to be evaluated further to get useful information. The decay rate Γ can be determined by treating the first order autocorrelation function g_1 as exponential decay:[71]

$$g_1(q,\tau) = e^{-\Gamma\tau} \tag{2.17}$$

The diffusion coefficient D_t can be directly calculated from the following equation:

$$\Gamma = q^2 D_t \tag{2.18}$$

With knowing D_t, the diffusion of particles in a viscous medium can be described by the STOKES-EINSTEIN equation and the hydrodynamic radius R can be directly estimated, with kT as the thermal kinetic energy and η as the dynamic viscosity:[72,73]

$$D_t = \frac{kT}{6\pi\eta R} \tag{2.19}$$

Bibliography

[1] P. T. Kissinger & W. R. Heineman. *Journal of chemical education*, **1983**. *60*(9), 702.

[2] B.-Y. Chang & S.-M. Park. *Annual Review of Analytical Chemistry*, **2010**. *3*(1), 207.

[3] D. D. Macdonald. *Electrochimica Acta*, **2006**. *51*(8-9), 1376–1388.

[4] G. Instruments. *G. Instruments, Complex impedance in Corrosion*, **2007**. 1–30.

[5] S. Wang, J. Zhang, O. Gharbi, V. Vivier, M. Gao & M. E. Orazem. *Nature Reviews Methods Primers*, **2021**. *1*(1), 1–21.

[6] J. Huang, Z. Li, B. Y. Liaw & J. Zhang. *Journal of Power Sources*, **2016**. *309*, 82–98.

[7] B. E. Warren. *X-ray Diffraction* (Courier Corporation), **1990**.

[8] H. Stanjek & W. Häusler. *Hyperfine interactions*, **2004**. *154*(1), 107–119.

[9] W. L. Bragg. *Scientia*, **1929**. *23*(45).

[10] P. Scherrer. In *Kolloidchemie Ein Lehrbuch*, 387–409 (Springer), **1912**.

[11] E. Abbe. *Archiv für mikroskopische Anatomie*, **1873**. *9*(1), 413–468.

[12] W. Zhou, R. Apkarian, Z. L. Wang & D. Joy. In *Scanning microscopy for nanotechnology*, 1–40 (Springer), **2006**.

[13] M. Knoll & E. Ruska. *Zeitschrift für Physik*, **1932**. *78*(5-6), 318–339.

[14] T. E. Everhart & R. Thornley. *Journal of scientific instruments*, **1960**. *37*(7), 246.

[15] R. Wirth. *European Journal of Mineralogy*, **2004**. *16*(6), 863–876.

[16] A. A. Tseng. *Small*, **2005**. *1*(10), 924–939.

[17] C. A. Volkert & A. M. Minor. *MRS bulletin*, **2007**. *32*(5), 389–399.

[18] J. H. Orloff & L. W. Swanson. *Journal of vacuum science and technology*, **1975**. *12*(6), 1209–1213.

[19] N. Ashcroft & N. Mermin. *Solid state physics*. Science: Physics (Saunders College), **1976**.

[20] M. Zhong, W. Liu, G. Ning, L. Yang & Y. Chen. *Journal of Materials Processing Technology*, **2004**. *147*(2), 167 – 173.

[21] H. Yamauchi, K. Takagi, I. Yuito & U. Kawabe. *Applied Physics Letters*, **1976**. *29*(10), 638–640.

[22] R. Fowler & L. Nordheim. In *Proceedings of the Royal Society of London A: Mathematical, Physical and Engineering Sciences*, volume 119 (The Royal Society), **1928** 173–181.

[23] J. Orloff. *Handbook of charged particle optics* (CRC press), **2017**.

[24] H. Nishiyama, T. Ohshima & H. Shinada. *Applied Surface Science*, **1999**. *146*(1), 382–386.

[25] D. Williams & C. Carter. *Transmission Electron Microscopy: A Textbook for Materials Science*. Number 1 in Transmission Electron Microscopy: A Textbook for Materials Science (Springer), **1996**.

[26] V. Harsch. *Aviation, space, and environmental medicine*, **2007**. *78*(11), 1075–1077.

[27] A. Martin. *Advances in electronics and electron physics*, **1986**. *67*, 183–328.

[28] M. Von Ardenne. *Zeitschrift für Physik*, **1938**. *109*(9), 553–572.

[29] A. Muller & J. Grazul. *Journal of electron microscopy*, **2001**. *50*(3), 219–226.

[30] F. Eggert. *Standardfreie Elektronenstrahl-Mikroanalyse: mit dem EDX im Rasterelektronenmikroskop; ein Handbuch für die Praxis* (BoD–Books on Demand), **2005**.

[31] R. F. Egerton. *Reports on Progress in Physics*, **2008**. *72*(1), 016502.

[32] P. Maynard. *Drawing Distinctions: The Varieties of Graphic Expression* (Cornell University Press), **2005**.

[33] K. S. G. der Wissenschaften zu Leipzig. Mathematisch-Physische Klasse. *Berichte über die Verhandlungen der Königlich Sächsischen Gesellschaft der Wissenschaften zu Leipzig*, volume 69 (Weidmannsche Buchhandlung), **1917**.

[34] T. Lehmann, E. Pelikan, W. Oberschelp & R. Repges. *Die Radon-Transformation* (Springer), **1997**.

[35] V. Vladimirov. *Equations of Mathematical Physics* (Nauka), **1971**.

[36] I. Gelfand. *Generalized functions* (Academic Press), **1968**.

[37] T. Buzug. *Computed tomography: from photon statistics to modern cone-beam CT* (Springer Science & Business Media), **2008**.

[38] P. Toft & J. Sørensen. *The Radon transform-theory and implementation*. Ph.D. thesis, Technical University of Denmark Tekniske Universitet, Institut for Informatik og Matematisk Modellering, **1996**.

[39] M. Holschneider. *Inverse problems*, **1991**. *7*(6), 853.

[40] M. Radermacher. In *Electron tomography*, 245–273 (Springer), **2006**.

[41] D. Schäfer, M. Grass & P. van de Haar. *Medical Physics*, **2011**. *38*(S1), 85–94.

[42] R. Gordon, R. Bender & G. Herman. *Journal of theoretical Biology*, **1970**. *29*(3), 471–481.

[43] S. Kaczmarz. *Bulletin International de l'Academie Polonaise des Sciences et des Lettres*, **1937**. *35*, 355–357.

[44] A. Ramm & A. Katsevich. *The Radon transform and local tomography* (CRC press), **1996**.

[45] F. Tabak. *Robust Algorithms for Discrete Tomography*. Ph.D. thesis, Delft University of Technology, **2012**.

[46] A. Lent. *Image Analysis and Evaluation*, **1977**. 249–257.

[47] G. Herman & H. Liu. *Computer Graphics and Image Processing*, **1979**. *9*(1), 1–21.

[48] A. Kak & M. Slaney. *Principles of computerized tomographic imaging* (Society for Industrial and Applied Mathematics), **2001**.

[49] J. Harris. *Seismic Tomography Project*, **1991**. *2*(1).

[50] A. Andersen & A. Kak. *Ultrasonic Imaging*, **1984**. *6*(1), 81–94.

[51] J. Trampert & J. Leveque. *Journal of Geophysical Research: Solid Earth*, **1990**. *95*(B8), 12553–12559.

[52] T. Yoshinaga. *International Journal of Imaging Systems and Technology*, **1999**. *10*(6), 432–436.

[53] K. Batenburg & J. Sijbers. *Image Processing*, **2011**. *20*(9), 2542–2553.

[54] K. S. W. Sing, D. H. Everett, R. A. W. Haul, L. Moscou, R. A. Pierotti, J. Rouquerol & T. Siemieniewska. *Pure and Applied Chemistry*, **1985**. *57*(4), 603–619.

[55] J. Rouquerol, D. Avnir, D. Everett, C. Fairbridge, M. Haynes, N. Pernicone, J. Ramsay, K. Sing & K. Unger. In K. S. J. Rouquerol, F. Rodríguez-Reinoso & K. Unger, editors, *Characterization of Porous Solids III*, volume 87 of *Studies in Surface Science and Catalysis*, 1 – 9 (Elsevier), **1994**.

[56] S. Brunauer, P. Emmett & E. Teller. *Journal of the American Chemical Society*, **1938**. *60*(2), 309–319.

[57] R. Berera, R. van Grondelle & J. T. Kennis. *Photosynthesis research*, **2009**. *101*, 105–118.

[58] M. Achermann. *Optical Techniques for Solid-State Materials Characterization*, **2012**. 443–465.

[59] A. Nevin, A. Cesaratto, S. Bellei, C. D'Andrea, L. Toniolo, G. Valentini & D. Comelli. *Sensors*, **2014**. *14*(4), 6338–6355.

[60] J. R. Macdonald. *Annals of biomedical engineering*, **1992**. *20*, 289–305.

[61] J. R. Macdonald & W. B. Johnson. *Impedance spectroscopy: theory, experiment, and applications*, **2018**. 1–20.

[62] K. Gelderman, L. Lee & S. Donne. *Journal of chemical education*, **2007**. *84*(4), 685.

[63] R. Van de Krol, A. Goossens & J. Schoonman. *Journal of the Electrochemical Society*, **1997**. *144*(5), 1723.

[64] W. J. Albery, G. J. O'Shea & A. L. Smith. *Journal of the Chemical Society, Faraday Transactions*, **1996**. *92*(20), 4083–4085.

[65] M. E. Orazem & B. Tribollet. *New Jersey*, **2008**. *1*, 383–389.

[66] A. Lasia. *Electrochemical impedance spectroscopy and its applications* (Springer), **2002**.

[67] C. Raman. In *Proceedings of the Indian Academy of Sciences, Section A*, volume 37 (Indian Academy of Sciences), **1953** 342–349.

[68] D. Jeanmaire & R. Van Duyne. *Journal of Electroanalytical Chemistry and Interfacial Electrochemistry*, **1977**. *84*(1), 1 – 20.

[69] W. Goldburg. *American Journal of Physics*, **1999**. *67*(12), 1152–1160.

[70] B. Berne & R. Pecora. *Dynamic light scattering: with applications to chemistry, biology, and physics* (Courier Corporation), **2000**.

[71] S. Provencher & P. Stepánek. *Particle and Particle Systems Characterization*, **1996**. *13*(5), 291–294.

[72] F. Durst. *Grundlagen der Strömungsmechanik: eine Einführung in die Theorie der Strömung von Fluiden* (Springer-Verlag), **2007**.

[73] A. Einstein. *Annalen der Physik*, **1905**. *4*.

3 Ultra-thin Protective Coatings for Sustained Photoelectrochemical Water Oxidation with Mo:BiVO$_4$

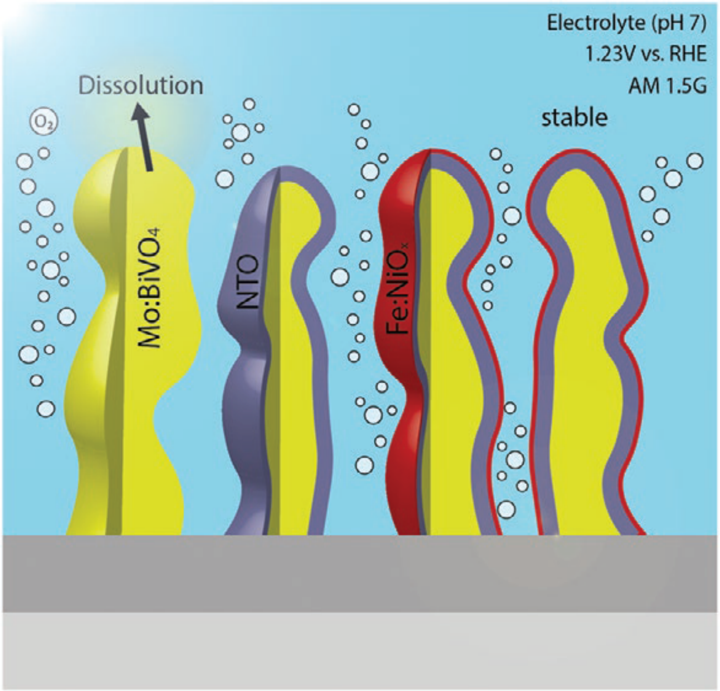

This chapter is based on the following publication:
Ultra-Thin Protective Coatings for Sustained Photoelectrochemical Water Oxidation with Mo:BiVO$_4$, M. Beetz, S. Häringer, P. Elsässer, J. Kampmann, L. Sauerland, F. Wolf, M. Günther, A. Fischer* and T. Bein* *Advanced Functional Materials*, **2021**, 31(45), 2011210.

Abstract

As global warming caused by the greenhouse effect is becoming one of the major issues of the 21st century, hydrogen as an alternative to fossil-based fuels and other energy carriers has gained importance in current research. One promising approach to produce hydrogen is photoelectrochemical water splitting, which uses solar energy combined with suitable semiconducting photoabsorber electrodes to generate hydrogen and oxygen from water. However, most water splitting applications reported to date suffer from degradation of the photoabsorber, resulting in a loss of activity after just a few seconds or minutes. Here, a new approach using conformal ultra-thin and oxidation-stable protective layers is presented on Mo:$BiVO_4$ thin films combined with a thin $Fe_{0.1}Ni_{0.9}O$ water oxidation co-catalyst, applied by electrochemical deposition, to achieve unprecedented photocurrent densities of up to 5.6 mA cm^{-2} under simulated AM1.5G illumination and a neutral pH while providing more stable electrodes for water oxidation.

3.1 Introduction

With increasing demands for renewable energy sources and substitution of fossil fuels in the next few years, the development of new energy storage solutions is of great importance. Hydrogen generated with energy from intermittent sustainable sources such as solar or wind is an attractive way to store energy.[1–5] Photoelectrochemical water splitting uses sunlight to dissociate water into hydrogen and oxygen by means of semiconductor absorber electrodes. Especially bismuth vanadate ($BiVO_4$) exhibits potential as a suitable ternary oxide for photoelectrochemical water oxidation due to its great light absorption abilities of a substantial part of the visible spectrum, which allows for theoretical photocurrents of up to 7.5 mA cm^{-2} under AM1.5G illumination (100 mW cm^{-2}).[6] However, recent studies featured a maximum photocurrent of 0.7 mA cm^{-2} or 1.9 mA cm^{-2} at 1.23 V versus RHE under simulated AM1.5G illumination (400 - 700 nm LED at 100 mW cm^{-2}) using 1 at% tungsten-doped bismuth vanadate (W:$BiVO_4$)[7] or 10 at% molybdenum-doped bismuth vanadate (Mo:$BiVO_4$)[8] without any additional water-oxidation co-catalysts, respectively, featuring some of the highest photocurrents ever achieved using this material. The comparability of bare photocurrents is quite difficult, if other factors like long-term stability, experimental conditions (pH of the electrolyte, illumination spectra, applied voltage, usage of sacrificial agents) or the effect of doping are not taken into account. Doping of $BiVO_4$ enhances charge separation and increases the charge carrier densities while lowering the surface charge transfer resistance. Theoretical calculations also indicate the importance of doping sites for adsorption of OH, O, and OOH species on the interface of the semiconductor.[9] The far from theoretical photoelectrochemical activity primarily suffers from the materials' slow water-oxidation kinetics at the semiconductor/electrolyte interface since charge recombination and charge transfer resistance are rather unfavorable for bare $BiVO_4$.[10] The water-oxidation kinetics can be significantly enhanced using a suitable water-oxidation catalyst like cobalt phosphate (CoPi) or iron-doped nickel oxides on the interface to the electrolyte.[8,11–13] Using this approach, the Mo:$BiVO_4$/CoPi electrode can offer one of the highest photocurrent densities of all known materials in this field.[10,14] Rohloff et al.[8] achieved 4.6 mA cm^{-2} at 1.23 V versus RHE under simulated AM1.5G illumination (400 - 700 nm LED at 100 mW cm^{-2}) using the most active 10 at% Mo:$BiVO_4$ combined with CoPi as water-oxidation co-catalyst to overcome the slow water-oxidation kinetics. However, its long-term stability is rather poor compared to other long-known materials like hematite.[15–17] In this context, corrosion, especially dissolution or degradation of the pristine material to inactive species, was shown to be a limiting factor for the stability of various kinds of electrodes used in photoelectrochemical devices.[18–21] In the past, there have been several attempts to increase the stability of $BiVO_4$ using protective layers.[19] However, most approaches, like atomic layer deposition (ALD), usually require rather thick layers, such as 40 nm of TiO_2, to achieve a homogenous and pin-hole free protective layer. Additionally, this leads to a strong reduction of the achieved photocurrent density compared to unprotected materials.[5,22–24] Further, TiO_2 is prone to crystallization as rutile and anatase under operating conditions of an electrode, thus forming a discontinuous layer of TiO_2 nanoparticles on top of the electrode rather than a conformal protective layer, causing short lifetimes of minutes to hours of previously reported protective coatings.

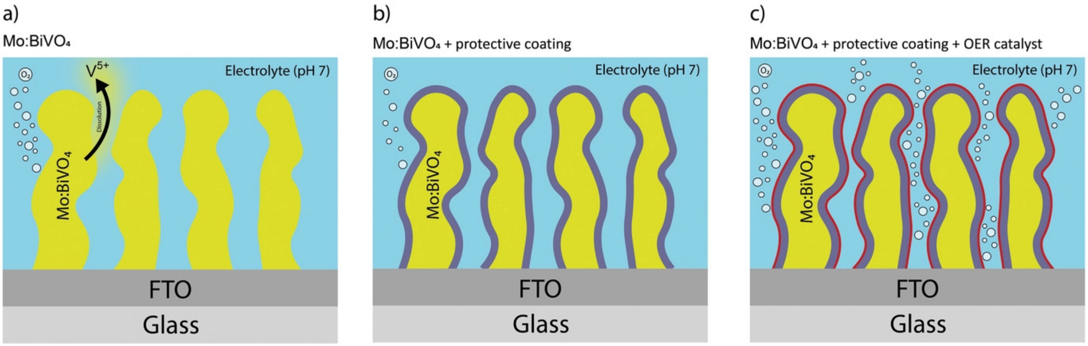

Figure 3.1: Schemes of Mo:$BiVO_4$-based photoanodes under operating conditions showing the protection strategy for enhanced durability and performance. a) Pure Mo:$BiVO_4$ suffers from corrosion during oxygen evolution by leaching vanadium(V) ions into the electrolyte. b) A thin protective coating prevents the dissolution of vanadium(V) ions in the electrolyte at reduced photoelectrochemical activity. c) An additional OER catalyst on-top of the protection layer enables effective water oxidation at reduced corrosion.

Here, we present a protection strategy based on ALD using ultra-thin (2.5 nm), conformal and oxidation-stable protection layers of niobium-doped titanium oxide (NTO, Nb:TiO_2), while maintaining photocurrents comparable to those of the unprotected Mo:$BiVO_4$ thin films for long time periods (Figure 3.1). NTO has been shown to be suitable as an oxidation-stable amorphous protection layer which showed impressive long-term stability in various water oxidation applications.[5,25–27] The electrochemical performance of the system could further be increased using an iron-doped nickel oxide co-catalyst, applied via electrochemical deposition (ECD) on top of the protection layer, featuring record activities of up to 5.6 mA cm^{-2}. After 16 h under operating conditions, those photocurrents stabilized at a constant photocurrent of 4.7 mA cm^{-2}. In contrast, the unprotected Mo:BiVO$_4$ reaches its highest photoelectrochemical activity with 1.9 mA cm^{-2} after 2 h, subsequently suffering from a constant loss in photoelectrochemical performance down to 1.2 mA cm^{-2} after more than 16 h due to constant degradation of the photoabsorber. To enable comparable photocurrents, all measurements were performed under simulated AM1.5G backside illumination with a 455 nm LED, calibrated to 100 mW cm^{-2} under consideration of the spectral mismatch of the LED to the sun's spectrum. To this end, the spectral mismatch from the LED to the AM1.5G spectrum was determined using the spectrum of the LED and the spectral photocurrent response of a Hamamatsu Si-diode to calibrate the LED's intensity accordingly. To ensure comparability and reliability of this calibration a linear sweep voltammogram using a Xe lamp AM 1.5 solar simulator (Solar Light Co. Model 16S, class ABA), calibrated using a Si-photodiode, and our calibrated 455 nm LED was recorded. The photocurrent response using this calibration is comparable in a range from 0.5 - 1.5 V versus RHE for both illumination types and exhibits similar photocurrents under our operating conditions of 1.23 V.

3.2 Results and Discussion

3.2.1 Electrode Preparation

The Mo:BiVO$_4$ thin films (with molybdenum content of 10 at%) were prepared using a dip-coating procedure under controlled atmospheric conditions, similar to the procedure previously described by Rohloff et al.[8] The molybdenum content of 10 at% was chosen due to its superior photoelectrochemical activity compared to higher or lower doping levels, featuring an optimum domain size and film thickness for efficient water-oxidation. The as-prepared thin films were annealed and calcined at 450 °C under air for 2 h resulting in bright-yellow and opaque films as shown in Figure 3.2a.

Thin protection layers (1, 2.5, 5, and 10 nm) of NTO, AlO$_x$ and SnO$_x$, respectively, were grown on top of the as-prepared Mo:BiVO$_4$ thin films using ALD, which already showed improved stability of photoanodes in previously reported publications.[5,27–31] The thickness of the applied ALD protective layers was monitored using ellipsometry on Si wavers and verified by SEM and FIB/TEM characterization (see Figure 3.3b–d).

Photoelectrochemical activities resulting from applying the various protection layers and thicknesses revealed that protection layers thicker than 5 nm led to a significant reduction of the photoelectrochemical performance of the material. Further, the SnO$_x$ and AlO$_x$ protected electrodes suffered from severe degradation after a few minutes under operating conditions (AM1.5G

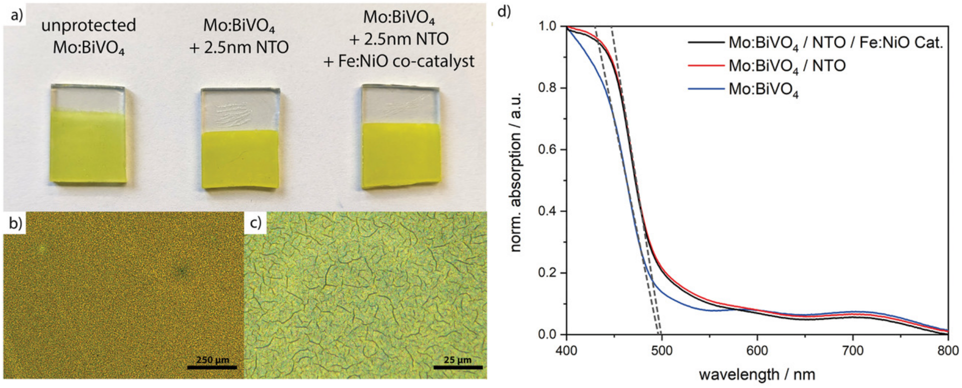

Figure 3.2: a) left-to-right: Photographs of an as-prepared Mo:BiVO$_4$ thin-film (left) with an additional 2.5 nm NTO protection layer (middle), and additional Fe:NiO-co-catalyst layer grown by electrochemical deposition (right). b,c) Light microscope images at different magnifications showing the homogeneity of the MBV+NTO+Cat films. d) UV/Vis spectra of the different Mo:BiVO$_4$ films on FTO coated glass substrates.

and 1.23 V vs RHE at pH 7). Chronoamperometric measurements of protected Mo:BiVO$_4$ electrodes using various thicknesses of SnO$_x$, AlO$_x$ and NTO are shown in the supporting information. While SnO$_x$ protected Mo:BiVO$_4$ films exhibited photocurrent densities of up to 1.23 mA cm^{-2} in the case of the 2 nm protective layer, comparable to the 2.5 nm NTO protected electrodes, the activity halved after 5 min and further decreased to even lower photocurrents of 0.20 mA cm^{-2} after 180 min. AlO$_x$ protected Mo:BiVO$_4$ films achieved photocurrents of up to 1.7 mA cm^{-2}, also suffering from heavy degradation with photocurrents down to 0.17 mA cm^{-2} after 180 min, in the case of the thinnest 1.5 nm protective layer, while thicker protective layers were completely photoelectrochemically inactive. This behavior can be attributed to the lack of conductivity of the AlO$_x$ and SnO$_x$ coatings, which becomes dominant at increasing thicknesses. Since NTO-protected Mo:BiVO$_4$ with a thickness of 2.5 nm of the protective layer emerged as the only photoelectrochemically stable electrode in this study while maintaining adequate photocurrents under the above conditions, the following studies were only performed using the 2.5 nm NTO Mo:BiVO$_4$ electrodes. Chronoamperometric electrochemical measurements of all protection layers and thicknesses can be found in the Supporting Information.

To further enhance efficiency, we applied an Fe$_{0.1}$Ni$_{0.9}$O oxygen evolution co-catalyst on top of the protected Mo:BiVO$_4$ thin films, using electrochemical deposition under galvanostatic conditions following a synthesis route described by Abdi et al.[7]

Pure Mo:BiVO$_4$ thin films, those with 2.5 nm NTO protective layer and those with additional Fe$_{0.1}$Ni$_{0.9}$O co-catalyst are referred to as “MBV”, “MBV+ NTO” and “MBV+ NTO+ Cat”, respectively, in the following.

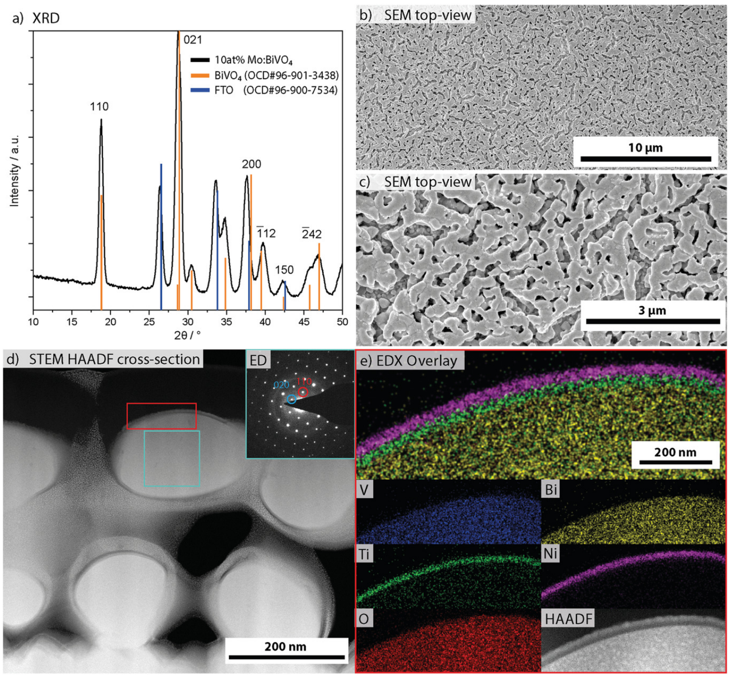

Figure 3.3: a) XRD diffraction pattern of the MBV+NTO+Cat shows distinct reflections which can be assigned to BiVO$_4$ (Crystallography Open Database (COD# 96-901-3438) and the subjacent FTO layer (COD# 96-900-7534). b,c) SEM images of the Mo:BiVO$_4$ thin films with NTO protection layer and FeNiO$_x$ co-catalyst at different magnifications. d) STEM-HAADF image from a FIB-prepared cross-section. The blue rectangle marks the area where the corresponding electron diffraction (ED) pattern was obtained. The red rectangle marks the area of the acquired EDX maps, seen in e). e) STEM-HAADF EDX maps of a prepared FIB lamella showing Bi and V co-localized in the Mo:BiVO$_4$ phase, with the Ti containing NTO protection-layer and the Ni containing co-catalyst layer (image selection in red box). The overlay EDX map shows the position of Bi, Ti and Ni in their respective color. The single crystal electron diffraction pattern of a single Mo:BiVO$_4$ crystal (blue square in TEM image) is shown in the inset.

3.2.2 Optical Characterization

Photographs of the freshly prepared MBV, MBV+NTO and MBV+NTO+Cat thin-film electrodes are shown in Figure 3.2a. All films are opaque and reveal the typical bright green-yellowish color of BiVO$_4$. The protected films appear visually brighter, which can be attributed to the enhanced scattering of the NTO protection layer on top of the Mo:BiVO$_4$ and its high refractive index caused by TiO$_2$. Light microscopy images demonstrate the homogeneity of the deposited thin films (Figure 3.2b, c). Larger magnifications already reveal the porous and worm-like structure, which is typical for Mo:BiVO$_4$ synthesized by this route.[8,32–35] UV-VIS optical absorption spectroscopy shows the typical absorption of BiVO$_4$ on FTO-coated glass. Evaluation of the optical absorption using the Tauc-method reveals an indirect optical bandgap of ≈2.4 eV for the unprotected as well as for the protected Mo:BiVO$_4$ films, which agrees with previously reported bandgaps.[31,36] However, these measurements show a slight shift to longer wavelengths in the absorption spectra for NTO coated films while the bandgap remains unchanged (see Figure 3.2d). We attribute this behavior to the additional contribution of the NTO protection layer.

3.2.3 Structural Characterization

The XRD pattern of an as-deposited Mo:$BiVO_4$ thin-film on FTO (Figure 3.3a) shows distinct reflections of the phase-pure scheelite $BiVO_4$ phase and the subjacent FTO layer. The monoclinic scheelite has proven to be the most photoelectrochemically active phase of $BiVO_4$, exhibiting also the highest stability under ambient conditions.[37] A shift to lower scattering angles in the diffraction pattern indicates a slightly larger unit cell corresponding to an enlargement of the d-spacing and hence the successful incorporation of molybdenum inside the crystal lattice (Figure 3.3a). The amorphous NTO protection layer and the co-catalyst layers are not visible in the XRD due to their very small layer thicknesses of equal or less than 2.5 nm. Scanning electron microscopy (SEM) reveals the previously described formation of the worm-like porous structure with an average diameter of ≈300 nm and pores of ≈50 nm in-between (Figure 3.3b,c).
Single crystal electron diffraction on a prepared FIB lamella further proves the presence of the desired scheelite-type structure of Mo:$BiVO_4$ (see Figure 3.3d-inset). The atomic ratios determined from the EDX elemental maps of Bi, V, Mo, and Ti were found to be 45.5%, 46.3%, 4.57%, and 3.65%, respectively, which corresponds to the expected ratios of the stoichiometric composition of 10 at% Mo:$BiVO_4$ and the titanium containing NTO protective layer.

3.2.4 Electrochemical Characterization

The photoelectrochemical performance regarding water-oxidation was investigated using cyclic-voltammetry, linear sweep voltammetry and chronoamperometry under atmospheric conditions (under air, room temperature and 967 hPa air pressure) using a H_3PO_4/NaOH buffer at pH 7 as electrolyte with a platinum-coil as counter electrode and a reversible hydrogen electrode (RHE) as reference. Linear sweep voltammetry (see Figure 3.4) of the unmodified Mo:$BiVO_4$ thin films exhibits a photocurrent response of 1.4 mA cm^{-2} at 1.23 V versus RHE, which is comparable to previously reported experiments.[8,38,39] Modification of the Mo:$BiVO_4$ with a 2.5 nm NTO protective layer results in a slight decrease in electrochemical activity to 1.3 mA cm^{-2} at 1.23 V versus RHE, which can be explained by the non-conductive properties of the amorphous NTO, entailing an increased resistance for charge carriers traveling to the electrolyte interface. The deposition of an $Fe_{0.1}Ni_{0.9}O$ co-catalyst on top of the NTO layer results in a strong increase of electrochemical performance with photocurrents of 5.6 mA cm^{-2} at 1.23 V versus RHE. This demonstrates an increase in activity by a factor of four to the pristine MBV electrode and thus, to the best of our knowledge, establishes previously unattained activities for this type of material in terms of morphology, utilized pH value and illumination. However, at 1.5 V versus

RHE the photocurrent density exceeds the theoretical maximum of 7.5 mA cm^{-2}. We attribute these corrosion currents to the dissolution of our catalyst, the protective layer or the FTO, which is used as a substrate under these harsh conditions.

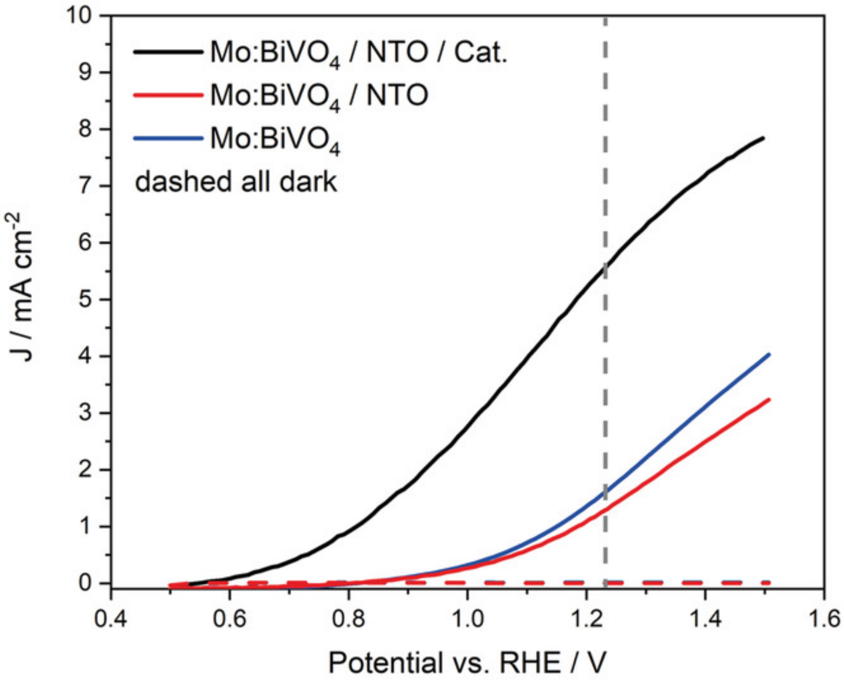

Figure 3.4: Linear sweep voltammetry of untreated Mo:BiVO$_4$ thin films (blue), with protective NTO coating (red), and protective NTO coating as well as deposited FeNiO$_x$ oxygen evolution catalyst (black). While the unprotected Mo:BiVO$_4$ reaches 1.5 mA cm^{-2}, the protected one with additional catalyst reaches up to 5.6 mA cm^{-2}. Without illumination the measured currents of all samples are shown as dashed line. The measurements were performed in pH 7 H_3PO_4/NaOH buffer solution, under simulated AM1.5G (455 nm LED calibrated to AM1.5G illumination) back side illumination and at a scan rate of 20 mV s^{-1}.

The long-term stability was further investigated using chronoamperometric measurements for 16 h at 1.23 V versus RHE under chopped illumination using on-off cycles of 10 min duration (see Figure 3.5). The unprotected Mo:BiVO$_4$ electrode (blue) achieved 2.5 mA cm^{-2} spontaneous current density at t = 0 s, which stabilized at a steady-state current density of 1.5 mA cm^{-2} after 2 min. The photocurrent response increased to a maximum of about 1.9 mA cm^{-2} (at 1.23 V versus RHE) steady-state current over the following 2 h.

The increase of photocurrent density can most likely be attributed to progressing corrosion of the electrode, probably of the photoabsorber itself. The dissolution of Mo:BiVO$_4$ into the electrolyte leads to a loss of active material and therefore to reduced activity in the following hours of the long-time stability test. According to previous studies, BiVO$_4$ undergoes leaching of V^{5+}-ions into the electrolyte during photo-induced corrosion, forming Bi_2O_3 or Bi metal.[18,40,41] We confirmed the leaching of vanadium ions with ICP-OES measurements of the electrolyte after photoelectrochemistry for 2 h. Thereby, the vanadium(V) concentrations, which are detected in

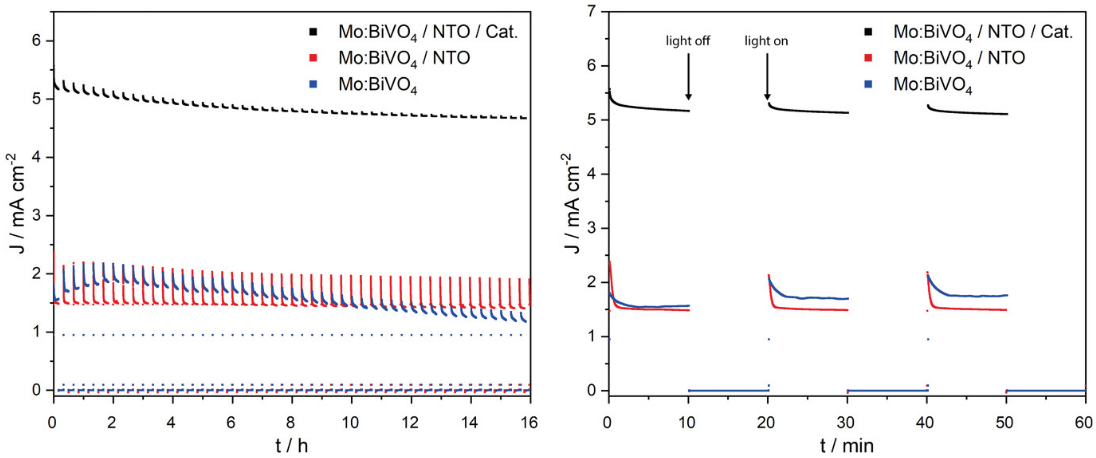

Figure 3.5: Chronoamperometric measurements for 16 h under chopped illumination (left) and a zoom-in of the first 60 min (right). Unmodified Mo:BiVO$_4$ (blue) shows a constant degradation of the photocurrent after 2 h. NTO-protected Mo:BiVO$_4$ shows a constant current without any signs of degradation for more than 16 h. An applied water oxidation catalyst (Fe$_x$Ni$_{1-x}$O) increases the photoelectrochemical performance by a factor of 4.

the electrolyte after 2 h of the stability test, are strongly dependent on the type and the thickness of the protective layer. Not surprisingly, bare MBV shows the strongest dissolution effect, whereas thicker protective layers of more than 5 nm NTO inhibit the dissolution almost completely, but also strongly reduce the photoelectrochemical activity. Hereby, a 2.5 nm NTO layer exhibits the best compromise between good photoelectrochemical performance and corrosion stability of the material.

These findings are in agreement with previously reported studies of this material. Our NTO-protected electrodes exhibit slightly lower photocurrents of ≈2.0 mA cm^{-2} in the beginning, but remain at a stable photocurrent density over the entire 16 h measurement, outperforming the unprotected electrodes after 10 h. Application of an Fe$_{0.1}$Ni$_{0.9}$O co-catalyst on-top of the NTO-protected Mo:BiVO$_4$ increases the photoelectrochemical activity by a factor of 4 compared to MBV, to about 5.6 mA cm^{-2} at the start of the measurement, stabilizing at 4.9 mA cm^{-2} after more than 16 h while maintaining its photoactive capabilities. Remarkably, the shape of the transient current responses (Figure 3.5) changes between the NTO-protected Mo:BiVO$_4$ electrodes without co-catalyst and the NTO-protected Mo:BiVO$_4$ electrodes with additional co-catalyst. These transients derive from the filling/emptying of surface states at the electrolyte/semiconductor interfaces, where photo-generated holes oxidize the water molecules.[42] However, these holes can also undergo recombination with electrons, reducing the number of available holes for the watersplitting process. This process can be described by the charge transfer efficiency η_{transfer}, which is defined as the ratio between the current used for water oxidation and the total current of holes generated. Compared to the pure Mo:BiVO$_4$, NTO-protected electrodes exhibit a much higher ratio of instantaneous current j_{ini} to steady-state current j_{ss} during the whole measurement. The ratio of j_{ss} to j_{ini} can be described as the hole transfer efficiency η_{transfer} and is commonly discussed in literature to compare minority carrier transfer efficiencies.[43–45] η_{transfer} for unprotected Mo:$BiVO_4$ was calculated to be 84%, which is comparable to the previously reported transfer efficiency.[8] However, the NTO-protected electrodes only show a hole transfer efficiency of 60%, which indicates a lowered PEC (photoelectrochemical) performance due to the accumulation of charges that cannot be transported to the catalytically active sites and therefore undergo recombination, reducing the charge transfer efficiency. Remarkably, the hole transfer efficiency with the additional $Fe_{0.1}Ni_{0.9}O$ co-catalyst layer increases to 93%, which explains the outstanding performance of our MBV+NTO+Cat electrodes.

This behavior can be attributed to the fact that the conductivity and charge transport in Nb-doped titania is generally quite poor compared to other metal oxides or to $BiVO_4$ itself, which leads to hole accumulation on its interface to the electrolyte.[46] However, the application of an $Fe_{0.1}Ni_{0.9}O$ co-catalyst leads to faster transient current responses, indicating the fast and effective hole transfer capabilities of the catalyst.

3.3 Conclusion

In conclusion, we were able to demonstrate a strategy for producing highly active and long-term stable photoanodes for water splitting oxidation applications. 10 at%-Mo:$BiVO_4$ was used as photo-absorbing semiconductor, protected against dissolution with a conformal, amorphous and oxidation-stable niobium-doped titanium oxide ALD coating and combined with $Fe_{0.1}Ni_{0.9}O$ as highly active water oxidation co-catalyst. The doping of niobium in titania suppresses the undesired crystallization of titanium dioxide and enables the formation of ultra-thin, contiguous layers on the corrugated photoabsorber surfaces. This strategy enables photoelectrochemical current densities of up to 5.6 mA cm^{-2} at pH 7 under AM1.5G illumination at 1.23 V versus RHE with unprecedented stability for more than 16 h. Thereby, these modified photoanodes outperform unmodified Mo:$BiVO_4$ by a factor of 4 and undoped $BiVO_4$ by a factor of 5. Such layers protect the actual photoactive semiconducting material while being thin enough for rapid charge transfer at the electrode-electrolyte interface. The added $Fe_{0.1}Ni_{0.9}O$ co-catalyst exhibits excellent catalytic abilities for water oxidation, which increases the hole transfer efficiencies toward the electrolyte and allows for the significant photocurrent increase compared to bare 10 at%-Mo:$BiVO_4$ electrodes. This study shows the importance of designing an oxidation-stable and ultra-thin protective layer like NTO combined with a highly active water oxidation co-catalyst such as $Fe_{0.1}Ni_{0.9}O$ to achieve both high performance and long-term stability with Mo:$BiVO_4$ photoanodes.

3.4 Experimental Section

Chemicals Origin: Chemicals stated in the experimental part were exclusively supplied by the following suppliers: Vanadium(V) oxytriethoxide: Aldrich, Bi(2-ethylhexanoate): Alfa Aesar, $MoO_2(acac)_2$: Aldrich, Chloroform: VWR, Iron(II) chloride: Aldrich, Nickel(II) chloride: Aldrich.

Synthesis of Mo:BiVO$_4$ Thin Films: The synthesis of the Mo:$BiVO_4$ thin films was performed similar to a procedure of Rohloff et al.[8] with a molybdenum content of 10 at%. 0.7 mmol (123 μL) of $VO(OEt)_3$ were dissolved in 1.5 mL chloroform. After stirring for 10 min, 0.7 mmol (445 mg) Bi(2-ethylhexanoate) and 0.072 mmol (22.6 mg) $MoO_2(acac)_2$ were added to the solution. After stirring overnight, the precursor was dip-coated on FTO-coated substrates at 300 mm min^{-1} withdrawal speed. The as-prepared films were dried at 60 °C for 15 min. After an aging step at 100 °C for 12 h, the films were calcined at 450 °C for 2 h (heating ramp of 0.5 °C min^{-1}) under atmospheric conditions.

Deposition of the Protection Layers by ALD: The NTO protection layer was grown using a sandwich methodology with alternating TiO_2 and NbO_x layers, according to Hufnagel et al.,[27] employing a Picosun R-200 Advanced ALD reactor at a temperature of 200 °C and a base pressure of 2 hPa. Nitrogen gas (Air Liquide, 99.999%) was used as purging and carrier gas. Titanium tetraisopropoxide (TTIP, Aldrich, 99.999%) was evaporated from a stainless steel vessel at 85 °C, niobium ethoxide (NEO, Strem, 99.9+%) was supplied from a glass vessel at 160 °C. Ultrapure water (MilliQ, 18.2 MΩ cm) was held in a stainless steel cylinder at 19 °C. Each TiO_2 ALD cycle comprised two TTIP pulses (1.6 s pulse, 4.5 s static exposure, 6 s purge) and one water pulse (2 s pulse, 4.5 s static exposure, 7.5 s purge). The resulting growth per cycle (GPC) was 0.038 nm $cycle^{-1}$. NbO_x was deposited using cycles of four NEO pulses (1.6 s pulse, 6.5 s static exposure, 6 s purge) and one water pulse as in the TiO_2 process. The growth per cycle was 0.068 nm $cycle^{-1}$. Mixed oxide layers were grown by interspersing one NbO_x cycle in the TiO_2 process every 10 intervals. Amorphous tin oxide and aluminum oxide layers were deposited in the same ALD machine at 200 °CC. Trimethylaluminum (TMA, Strem, min. 98%) was kept at 19 °CC as well as the ultrapure water. One AlO_x ALD cycle comprised one TMA pulse (0.1 s pulse, 4 s static exposure, 6 s purge) and one water pulse (0.1 s pulse, 4 s static exposure, 6 s purge). The resulting growth per cycle (GPC) was 0.1 nm $cycle^{-1}$. Tetrakis(dimethylamino)tin(IV) (TDMASn, Strem, 99%) was evaporated from a stainless steel cylinder at 75 °C. Ozone was produced by an ozone generator (INUSA AC2025). SnO_x was deposited using cycles of two TDMASn pulses (1.6 s pulse, 7.5 s static exposure, 7.5 s purge) and one ozone pulse (2 s pulse, 6 s static exposure, 4 s purge). The growth per cycle was 0.14 nm $cycle^{-1}$. The thickness of the ALD deposited ultra-thin protective layers was determined using ellipsometry (J. A. Woollam M-2000D) with films grown under identical conditions on Si(110) substrates. NTO, SnO_x and AlO_x layers were modelled using a Cauchy function.

Electrode Characterization: X-ray diffraction (XRD) patterns were recorded on a Bruker D8 Discover diffractometer using Cu-Kα radiation with $\lambda = 1.54178$ Å. The Open Crystallography Database (OCD) was used as XRD reference dataset. Crystallite sizes were estimated using the Scherrer equation. SEM images and FIB lamella preparation was done using an FEI Helios Nanolab G3 UC, equipped with a Schottky-type Field-Emitter and Ga^+-focused ion beam, operated between 1 and 30 kV. (S)TEM images and EDX maps were acquired on an FEI Titan Themis 80–300 microscope operated at 300 kV acceleration voltage, equipped with an X-FEG electron source, a monochromator, a Cs-corrector and a HAADF detector.

Electrochemical Deposition of $Fe_{0.1}Ni_{0.9}O$ Co-Catalyst: The iron-doped nickel oxide co-catalyst was deposited on the previously prepared and ALD-protected Mo:$BiVO_4$ thin films using consecutive cathodic electrodeposition, similar to reported procedures.[47–50] A 0.1×10^{-3} M precursor solution containing Fe(II)Cl_2 and Ni(II)Cl_2 was used to deposit the co-catalyst by applying -0.1 mA at galvanostatic conditions for 20 s. The voltage for the deposition varied between -0.5 and -0.8 V versus RHE. The as-deposited films were rinsed with water and dried at 60 °C for 2 h.

Photoelectrochemical Characterization: All samples were prepared for photoelectrochemical characterization by contacting the FTO substrate using Ag-based conductive lacquer. The sample area was determined by applying PTFE adhesive tape with a reflective coating as mask. The mask contained a circular hole with a diameter of 0.5 cm which corresponds to an exposed area of 0.1963 cm^2. The photoelectrochemical experiments were performed using a three-electrode setup with coiled Pt wire as counter electrode and a reversible hydrogen electrode (Gaskatel HydroFlex) as reference electrode. A H_3PO_4/NaOH buffer solution at pH 7 was used as electrolyte. The electrolyte was stirred during all measurements using a rod stirrer to prevent local concentration gradients. The samples were illuminated by a 455 nm LED, calibrated to AM1.5G conditions using a calibrated Si diode under consideration of the spectral missmatch. All experiments were performed at room temperature and under air. Cyclic voltammetry, linear sweep voltammetry, galvanostatic experiments as well as electrochemical deposition of the $Fe_{0.1}Ni_{0.9}O$ co-catalyst were performed using a Metrohm Autolab PGSTAT302N potentiostat/galvanostat.

Bibliography

[1] L. L. Mastropasqua, I. Pecenati, A. Giostri & S. Campanari. *Appl. Energy*, **2020**. *261*, 114392.

[2] R. P. Micena, O. R. Llerena-Pizarro, T. M. de Souza & J. L. Silveira. *Int. J. Hydrogen Energy*, **2020**. *45*, 2308.

[3] D. P. Pham, S. Lee, A. H. T. Le, E.-C. Cho, Y. H. Cho & J. Yi. *Chem. Commun.*, **2020**. *116*, 107926.

[4] L. Pan, Y. Liu, L. Yao, R. Dan, K. Sivula, M. Grätzel & A. Hagfeldt. *Nat. Commun.*, **2020**. *11*, 318.

[5] J. J. Kampmann, S. Betzler, H. Hajiyani, S. Häringer, M. Beetz, T. Harzer, J. Kraus, B. V. Lotsch, C. Scheu, R. Pentcheva, D. Fattakhova-Rohlfing & T. Bein. *Nanoscale*, **2020**. *12*, 7766.

[6] B. S. Kalanoor, H. Seo & S. S. Kalanur. *Mater. Sci. Technol.*, **2018**. *1*, 49.

[7] F. F. Abdi, N. Firet & R. van de Krol. *ChemCatChem*, **2013**. *5*, 490.

[8] M. Rohloff, B. Anke, S. Zhang, U. Gernert, C. Scheu, M. Lerch & A. Fischer. *Sustainable Energy Fuels*, **2017**. *1*, 1830.

[9] X. Zhao, J. Hu, S. Chen & Z. Chen. *Phys. Chem. Chem. Phys.*, **2018**. *20*, 13637.

[10] M. Barzgar Vishlaghi, A. Kahraman & S. Kaya. *J. Phys. Chem. C*, **2020**. *124*, 1337.

[11] D. K. Zhong & D. R. Gamelin. *J. Am. Chem. Soc.*, **2010**. *132*, 4202.

[12] Y. Kai-Hang, L. Haibo, H. Duan, X. Shuang, Q. Weitao, L. Mingyang, H. Yuwen, M. Wenjie, J. Hongbing & Y. Shihe. *Nat. Commun. 10*, 3687.

[13] Y. Y. Pihosh, I. Turkevych, K. Mawatari, J. Uemura, Y. Kazoe, S. Kosar, K. Makita, T. Sugaya, T. Matsui, D. Fujita, M. Tosa, M. Kondo & T. Kitamori. *Sci. Rep.*, **2015**. *5*, 11141.

[14] S. Kosar, Y. Pihosh, R. Bekarevich, K. Mitsuishi, K. Mawatari, Y. Kazoe, T. Kitamori, M. Tosa, A. B. Tarasov, E. A. Goodilin, Y. M. Struk, M. Kondo & I. Turkevych. *Appl. Nanosci.*, **2019**. *9*, 1017.

[15] P. Dias, A. Vilanova, T. Lopes, L. Andrade & A. Mendes. *Nano Energy*, **2016**. *23*, 70.

[16] O. Zandi & T. W. Hamann. *Phys. Chem. Chem. Phys.*, **2015**. *17*, 22485.

[17] Z. Z. Zhang, I. Karimata, H. Nagashima, S. Muto, K. Ohara, K. Sugimoto & T. Tachikawa. *Nat. Commun.*, **2019**. *10*, 4832.

[18] S. Zhang, M. Rohloff, O. Kasian, A. M. Mingers, K. J. J. Mayrhofer, A. Fischer, C. Scheu & S. Cherevko. *J. Mater. Chem. C*, **2019**. *123*, 23410.

[19] D. Lee, A. Kvit & K.-S. Choi. *Chem. Mater*, **2018**. *30*, 4704.

[20] S. S. Zhang, I. Ahmet, S.-H. Kim, O. Kasian, A. M. Mingers, P. Schnell, M. Kölbach, J. Lim, A. Fischer, K. J. J. Mayrhofer, S. Cherevko, B. Gault, R. van de Krol & C. Scheu. *ACS Appl. Energy Mater.*, **2020**. *3*, 9523.

[21] A. Qayum, M. Guo, J. Wei, S. Dong, X. Jiao, D. Chen & T. Wang. *J. Mater. Chem. A*, **2020**. *8*, 10989.

[22] T. Moehl, J. Suh, L. Sévery, R. Wick-Joliat & S. D. Tilley. *ACS Appl. Mater. Interfaces*, **2017**. *9*, 43614.

[23] M. F. M. F. Lichterman, K. Sun, S. Hu, X. Zhou, M. T. McDowell, M. R. Shaner, M. R. Richter, E. J. Crumlin, A. I. Carim, F. H. Saadi, B. S. Brunschwig & N. S. Lewis. *Catal. Today*, **2016**. *262*, 11.

[24] C. Ros, T. Andreu & J. R. Morante. *J. Mater. Chem. A*, **2020**. *8*, 10625.

[25] C. Das, P. Roy, M. Yang, H. Jha & P. Schmuki. *Nanoscale*, **2011**. *3*, 3094.

[26] M. Hannula, H. Ali-Löytty, K. Lahtonen, E. Sarlin, J. Saari & M. Valden. *Chem. Mater.*, **2018**. *30*, 1199.

[27] A. G. Hufnagel, S. Häringer, M. Beetz, B. Böller, D. Fattakhova-Rohlfing & T. Bein. *Nanoscale*, **2019**. *11*, 14285.

[28] B. J. O'Neill, D. H. K. Jackson, J. Lee, C. Canlas, P. C. Stair, C. L. Marshall, J. W. Elam, T. F. Kuech, J. A. Dumesic & G. W. Huber. *ACS Catal.*, **2015**. *5*, 1804.

[29] Q. Peng, J. S. Lewis, P. G. Hoertz, J. T. Glass & G. N. Parsons. *J. Vac. Sci. Technol.*, **2012**. *30*, 010803.

[30] S. Seo, S. Jeong, H. Park, H. Shin & N.-G. Park. *Chem. Commun.*, **2019**. *55*, 2403.

[31] J. Y. Kim. *Key Eng. Mater.*, **2017**. *753*, 156.

[32] D. T. T. Trinh, W. Khanitchaidecha, D. Channei & A. Nakaruk. *Res. Chem. Intermed.*, **2019**. *45*, 5217.

[33] Y. Liu, Y. Jiang, F. Li, F. Yu, W. Jiang & L. Xia. *J. Mater. Chem. A*, **2018**. *6*, 10761.

[34] L. Meng, W. Tian, F. Wu, F. Cao & L. Li. *J. Mater. Sci. Technol.*, **2019**. *35*, 1740.

[35] M. Huang, J. Bian, W. Xiong, C. Huang & R. Zhang. *J. Mater. Chem. A*, **2018**. *6*, 3602.

[36] F. Opoku, K. K. Govender, C. G. C. E. van Sittert & P. P. Govender. *New J. Chem.*, **2017**. *41*, 11701.

[37] S. Tokunaga, H. Kato & A. Kudo. *Chem. Mater*, **2001**. *13*, 4624.

[38] S. K. Pilli, T. E. Furtak, L. D. Brown, T. G. Deutsch, J. A. Turner & A. M. Herring. *Energy Environ. Sci.*, **2011**. *4*, 4025.

[39] J. A. Seabold, K. Zhu & N. R. Neale. *Phys. Chem. Chem. Phys.*, **2014**. *16*, 1121.

[40] X. X. Yao, X. Zhao, J. Hu, H. Xie, D. Wang, X. Cao, Z. Zhang, Y. Huang, Z. Chen & T. Sritharan. *iScience*, **2019**. *19*, 976.

[41] F. M. Toma, J. K. Cooper, V. Kunzelmann, M. T. McDowell, J. Yu, D. M. Larson, N. J. Borys, C. Abelyan, J. W. Beeman, K. M. Yu, J. Yang, L. Chen, M. R. Shaner, J. Spurgeon, F. A. Houle, K. A. Persson & I. D. Sharp. *Nat. Commun.*, **2016**. *7*, 12012.

[42] F. A. L. Laskowski, J. Qiu, M. R. Nellist, S. Z. Oener, A. M. Gordon & S. W. Boettcher. *Sustainable Energy Fuels*, **2018**. *2*, 1995.

[43] L. M. Peter. *J. Solid State Electrochem.*, **2013**. *17*, 315.

[44] L. M. Peter. *Chem. Rev.*, **1990**. *90*, 753.

[45] L. M. Abrantes & L. M. Peter. *J. Electroanal. Chem.*, **1983**. *150*, 593.

[46] D. Tafalla & P. Salvador. *J. Electroanal. Chem.*, **1989**. *270*, 285.

[47] Q. J. Wang & Y.-W. Chung. *Encyclopedia of Tribology* (Springer US, Boston, MA), p. s.l edition, **2013**.

[48] S. Mandati, B. V. Sarada, S. R. Dey & S. V. Joshi. *Semiconductors – Growth and Characterization* (InTech, London), **2018**.

[49] S. Jiao, L. Xu, K. Hu, J. Li, S. Gao & D. Xu. *J. Mater. Chem. C*, **2010**. *114*, 269.

[50] S. P. Mahesh, S. Seung Wook, G. V. Uma, K. Jihun, J. Hye Won, K. Soon Hyung & J. H. Kim. *J. Mater. Chem. A*, **2018**. *6*, 20678.

4 How photocorrosion can trick you

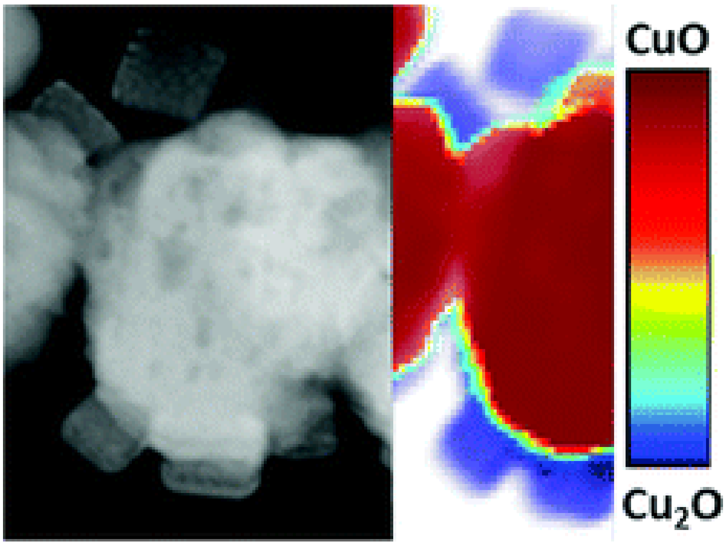

This chapter is based on the following publication:

How photocorrosion can trick you: a detailed study on low-bandgap Li doped CuO photocathodes for solar hydrogen production, J. Kampmann, S. Betzler, H. Hajiyani, S. Häringer, M. Beetz, T. Harzer, J. Kraus, B. V. Lotsch, C. Scheu, R. Pentcheva, D. Fattakhova-Rohlfing, T. Bein, *Nanoscale*, **2020**, 12(14), 7766 – 7775.

4.1 Abstract

The efficiency of photoelectrochemical tandem cells is still limited by the availability of stable low bandgap electrodes. In this work, we report a photocathode based on lithium doped copper(II) oxide, a black p-type semiconductor. Density functional theory calculations with a Hubbard U term show that low concentrations of Li ($Li_{0.03}Cu_{0.97}O$) lead to an upward shift of the valence band maximum that crosses the Fermi level and results in a p-type semiconductor. Therefore, Li doping emerged as a suitable approach to manipulate the electronic structure of copper oxide based photocathodes. As this material class suffers from instability in water under operating conditions, the recorded photocurrents are repeatedly misinterpreted as hydrogen evolution evidence. We investigated the photocorrosion behavior of $Li_xCu_{1-x}O$ cathodes in detail and give the first mechanistic study of the fundamental physical process. The reduced copper oxide species were localized by electron energy loss spectroscopy mapping. Cu_2O grows as distinct crystallites on the surface of $Li_xCu_{1-x}O$ instead of forming a dense layer. Additionally, there is no obvious Cu_2O gradient inside the films, as Cu_2O seems to form on all $Li_xCu_{1-x}O$ nanocrystals exposed to water. The application of a thin $Ti_{0.8}Nb_{0.2}O_x$ coating by atomic layer deposition and the deposition of a platinum co-catalyst increased the stability of $Li_xCu_{1-x}O$ against decomposition. These devices showed a stable hydrogen evolution for 15 minutes.

4.2 Introduction

Events like the Paris agreement in the year 2015 again demonstrate the desire of our modern society to reduce emissions caused by fossil fuels. Consequently, the focus on research for sustainable energy sources has been increasing in recent years. Compared to wind power, hydroelectric power and tidal power plants, sunlight is by far the most prominent energy source we can exploit to meet mankind's rising demands.[1] An additional challenge beside harvesting sunlight and converting it into electricity is large scale energy storage, which is essential for the replacement of fossil fuels. One approach to address this demanding task is the use of hydrogen gas for powering both fuel cells and fertilizer production, envisioning the establishment of a so called 'hydrogen economy'. Inspired by photosynthesis, photoelectrochemical (PEC) water splitting is a promising process to generate hydrogen and oxygen gas.[2–5] While there is lively discussion on the subject, potential advantages of a photoelectrochemical cell compared to the combination of an electrolyzer with a conventional solar cell can be the reduction of overpotentials as well as reduced fabrication cost and complexity of the final devices.[5,6] In contrast to photocatalysis, oxygen and hydrogen are produced in spatially separated compartments, hence avoiding subsequent separation, facilitating their storage and preventing the accumulation of an explosive gas mixture. Suitable semiconducting materials for PEC cathodes are based on silicon,[6–9] metal oxides[3,5] or organic semiconductors.[10–12] Many earth abundant metal oxides are known to exhibit reasonable stability as well as photoactivity in water splitting applications.[13–15] This led to the development of synthesis methods for novel binary[16–19] and ternary[20,21] metal oxides as well as doping of well-known metal oxides.[22–24] Besides the extensive work on materials with optical bandgaps in the range of 2.0 – 3.0 eV,[14,15,24–26] there is also need for low band gap photoabsorbers in order to build efficient PEC tandem cells. Such devices consist of an n-type photoanode connected to a p-type photocathode to harvest a substantial portion of the solar spectrum, reaching theoretical solar-to-hydrogen conversion efficiencies of up to 21.6%.[5,25,27] Copper oxide based photocathodes have aroused broad interest due to their low toxicity and the good availability of copper based compounds.[22,28–34] The reported band gaps of 1.35 eV – 1.7 eV and 2.0 – 2.2 eV for CuO and Cu_2O respectively, allow for significant light absorption in the visible range and provide enough energy for photoelectrochemical reactions.[35–39] The conduction band edges of the intrinsic p-type semiconductors CuO and Cu_2O[36,37] fit both the reduction potentials of water[14,38] and CO_2,[40] which enables the reduction of these reagents by photo-generated electrons. The incorporation of Al or Pd into the structure of cupric oxide was shown to increase both the photocorrosion stability and the performance of those devices significantly.[41,42] Besides this, doping CuO with Li has already been proven to be a suitable way to lower the optical band gap and increase the electrical conductivity,[22,23,35,43] which is key to enhance its performance for photoelectrochemical water splitting applications. Therefore, the photoelectrochemical study solely covers results on Li doped CuO and does not compare it with undoped CuO. Several groups have reported the discovery of highly efficient photocathodes based on CuO.[22,33,44–47] However, it has been observed that photocurrents may be easily misinterpreted as evidence for hydrogen evolution which should be critically scrutinized.[44–46] On the other hand, also justified doubts exist already about the stability of this metal oxide under reductive potentials.[48,49] High cathodic dark currents and a significant decay in performance within the first minutes under operating conditions could point towards cathodic corrosion of this photoabsorber.[35,50,51] The reduction potential of CuO in aqueous electrolyte lies above the reduction potential of water.[29] This implies the possibility of a competitive reduction of water and the photoabsorber itself, leading to the formation of reduced copper species such as Cu_2O and metallic copper under operating conditions, and consequently to a significant change of the photocathode morphology due to photocorrosion.[49,52,53] Other copper containing photocathode materials like Cu_2O,[14,54] $CuFeO_2$[17] and $CuBi_2O_4$[19] are also affected by photocorrosion, which further motivated us to investigate this phenomenon in detail. Recently, more detailed corrosion studies on CuO[55] and $BiVO_4$[56–58] concentrated on the mechanisms behind the loss in activity and addressed this by the use of protective layers and suitable cocatalysts. Here, we report on the first extensive photocorrosion study revealing detailed insights into the transformations taking place in copper(II) oxide thin film electrodes under operating conditions with special attention to the role of photo-induced electrons, which we propose to be applicable to various copper containing cathode materials used in photoelectrochemical measurements. We further describe a suitable approach to increase the stability of this p-type low bandgap semiconductor against decomposition and to decorate it with a Pt cocatalyst. With these results, we wish to contribute to the ongoing discussion about the stability of metal oxide photocathodes and point to ways towards the development of stable photoabsorbers for the generation of environmentally friendly hydrogen gas. Furthermore, we present a convenient method to manipulate the electronic structure of copper oxide which can be used to improve CO_2 reduction efficiencies.

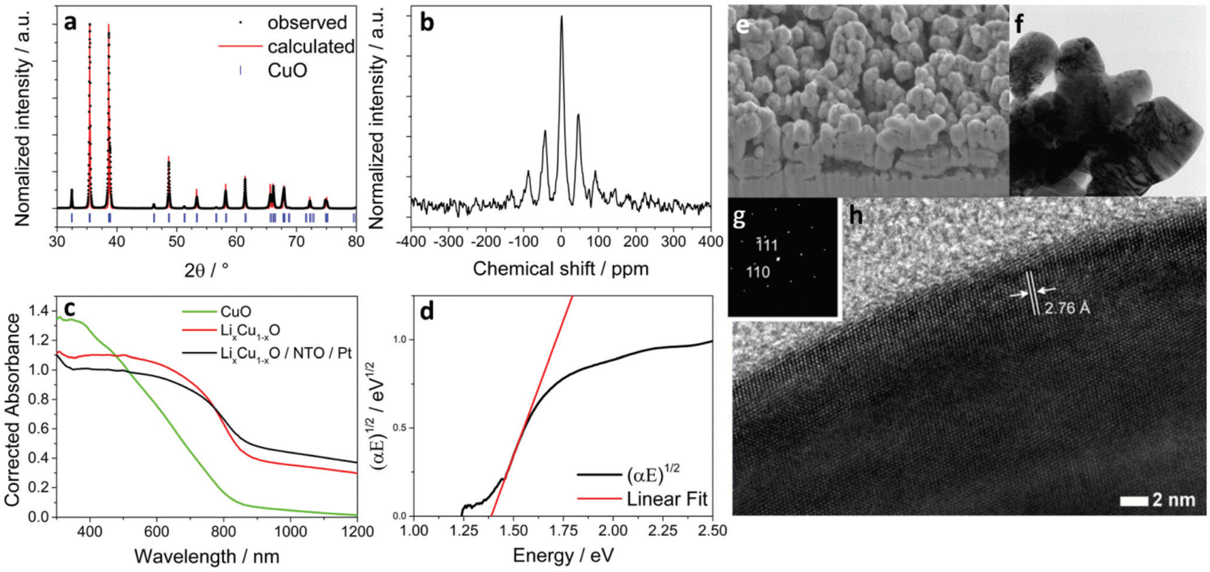

Figure 4.1: (a) Rietveld refinement of LixCu1–xO with observed data (·) and calculated pattern (red line), blue vertical bars mark the positions of the diffraction lines of CuO (tenorite). (b) 7Li-NMR spectra of LixCu1–xO showing a multiplet centered at 1.3 ppm. (c) UV-Vis absorption spectra of undoped CuO (green), LixCu1–xO (red) and protected LixCu1–xO/NTO/Pt films on FTO. (d) Tauc plot of a LixCu1–xO film on FTO showing an indirect bandgap of 1.39 eV. (e) SEM cross section image of LixCu1–xO. (f) TEM image of LixCu1–xO particles. (g and h) High-resolution TEM image of a highly crystalline LixCu1–xO nanoparticle and its corresponding electron diffraction pattern.

4.3 Results and Discussion

$Li_xCu_{1-x}O$ photocathode layers were prepared by spin coating an ethanolic solution of $Cu(NO_3)_2 \cdot 3\,H_2O$ and $LiNO_3$ onto an FTO substrate. Calcination of these coatings at 400 °C resulted in homogeneous black films with a thickness of about 1 µm. The calcined films obtained from the precursor solution contain large amounts of non-reacted $LiNO_3$ and Li_2CO_3 (ESI Fig. 1†) which can be removed by rinsing with water. X-ray diffraction (XRD) analysis (Fig. 4.1a) reveals that the films are structurally closely related to the CuO tenorite phase (space group: C2/c, a = 4.6803(8) Å; b = 3.4176(2) Å; c = 5.1278(8) Å; β = 99.442 (1)° (ESI Fig. 2†))[59,60] but exhibit slightly larger unit cell parameters (a = 4.6975(8) Å, b = 3.4346(6) Å, c = 5.1400(3) Å and β = 99.499(6)°). The small increase of the unit cell volume from 82.02(1) Å^3 for the pure CuO to 82.93(1) Å^3 for the CuO synthesized in the presence of Li salts indicates the incorporation of a small amount of Li^+ ions, with a somewhat bigger ionic radius of 0.90 Å (in CN = 6) compared to the ionic radius of Cu^{2+} ions of 0.87 Å (in CN = 6), into the crystal lattice.[23] Inductively coupled plasma atomic absorption spectroscopy (ICP-AAS) analysis confirms the presence of 4 at% lithium in the sample, which is the maximum amount that can be incorporated in the tenorite crystal structure.[61]

Another evidence for the incorporation of Li in the structure is provided by solid state ^{7}Li nuclear magnetic resonance (NMR) analysis, which shows a multiplet (from spinning sidebands) centered at 1.3 ppm in the spectrum of a carefully washed $Li_xCu_{1-x}O$ powder (Fig. 4.1b). This signal is indicative for a non-metallic single phase, free of contaminations with diamagnetic compounds (i.e. Li_2O, $LiCO_3$, $LiNO_3$). The electrical conductivity of Li-doped CuO was determined by Hall measurements (van der Pauw method) to be 6.0 × 10–3 S cm^{-1}, which is an increase by a factor of 2.5 compared to undoped CuO (2.4 × 10–3 S cm^{-1}). While films of undoped CuO are of dark brown color, films of $Li_xCu_{1-x}O$ are black. We attribute this observation to the formation of in-gap states, which can be caused by the introduction of point defects like cation doping or oxygen vacancies.[62] These optical properties were investigated by UV-Vis spectroscopy. $Li_xCu_{1-x}O$ films demonstrate favorable light harvesting efficiencies across a broad wavelength range between 350 – 800 nm, covering part of the near infra-red (IR) range, which exceeds that of our undoped CuO films (Fig. 4.1c). Absorbance data of $Li_xCu_{1-x}O$ films were used to calculate an indirect optical bandgap of 1.39 eV via Tauc plot analysis[63] (Fig. 4.1d), which is nearly the theoretical optimum for bottom materials used for high-efficiency PEC tandem cells.[27] The morphology of our $Li_xCu_{1-x}O$ films was investigated by scanning electron microscopy (SEM, Fig. 4.1e). The films are nanostructured and composed of interconnected nanoparticles forming disordered porous layers covering the whole FTO substrate. Transmission electron microscopy (TEM) images of $Li_xCu_{1-x}O$ films reveal that they are composed of intergrown particles with a size of around 150 – 300 nm (Fig. 4.1f). High-resolution TEM (HR-TEM) images (Fig. 4.1h) and electron diffraction analysis (Fig. 4.1g) reveal that these particles are single crystalline. The d(110)-spacing of monoclinic $Li_xCu_{1-x}O$ was determined to be 2.76 Å, being in good agreement with the XRD patterns.

To understand how the introduction of Li influences the electronic properties of CuO, we have performed density functional theory (DFT) calculations for Li-containing CuO including static electronic correlations within the GGA+U approach where the rotationally invariant formulation of Dudarev et al.[64] was employed (see ESI† for further details). We have investigated the band gap as a function of the Hubbard U parameter and find that up to U = 8 eV the indirect band

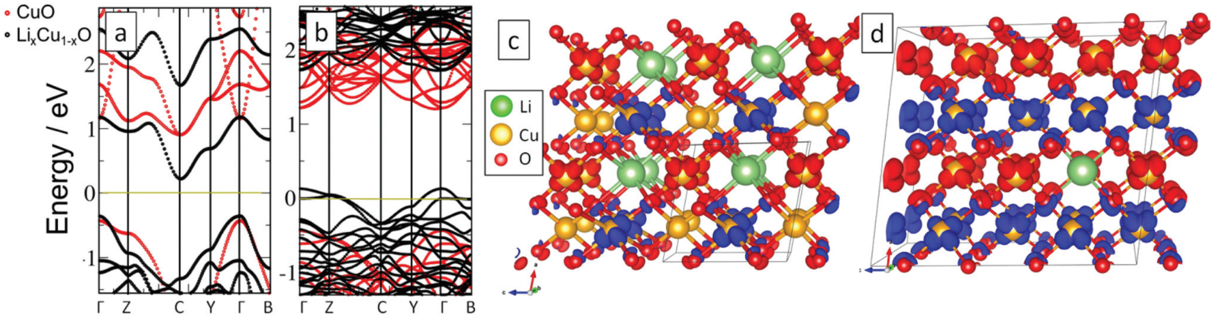

Figure 4.2: Electronic band structure of lithium doped CuO for two different Li concentrations of (a) $Li_{0.25}Cu_{0.75}O$ and (b) $Li_{0.032}Cu_{0.968}O$. The different numbers of bands are related to different cell sizes. The yellow line marks the Fermi level. In contrast to the insulating behaviour for $x_{Li} = 25\%$ (note the reduced band gap w.r.t. bulk CuO), the valence bands crossing the Fermi level for $x_{Li} = 3.2\%$ indicate p-type conductivity. Spin density of lithium doped CuO in two different Li concentrations of (c) $Li_{0.25}Cu_{0.75}O$ and (d) $Li_{0.032}Cu_{0.968}O$ (isosurface of 0.01 e $Å^{-3}$). Majority and minority spin densities are shown by blue and red, respectively. Note the significant contribution of oxygen for the low Li doping concentration of 3.2%.

gap of CuO increases monotonically with the band gap reaching 1.46 eV. Beyond U of 8 eV it changes to a direct band gap of 2.1 eV (ESI Fig. 3a†). The band gap of 1.46 eV obtained for U = 8 eV is in good agreement with the band gap of 1.39 eV determined from the Tauc plot above and consistent with previous LDA+U studies with a somewhat lower value of U = 6.5 eV by Heinemann et al.[37] The variation of lattice constants as a function of U is presented in ESI Fig. 3b.† The DFT predictions are in overall agreement with experimental lattice constants. The jump occurring between U = 8 eV and U = 8.5 eV is associated with the above-mentioned transition from indirect to direct band gap. To determine the preferential position of Li atoms in the CuO structure we have calculated the solution energy of Li at different lattice positions. For substitutional doping of Cu and O sites the calculated values are –4.20 eV and 1.04 eV, respectively, while for the interstitial doping the solution energy was determined to be –0.025 eV. Therefore, we can conclude that thermodynamically the preferred configuration corresponds to the substitutional doping of Cu sites with Li atoms. We have considered a high lithium content of $x_Li = 25$ at% and a low content of $x_Li = 3.2$ at%, which is close to the experimentally determined Li level of ca. 4 at%. The solution energies of $Li_{0.032}Cu_{0.968}O$ and $Li_{0.25}Cu_{0.75}O$ are –4.2 eV and –3.1 eV respectively, indicating a reduction of tendency to incorporate with increasing Li concentration due to Li–Li repulsion. The band structure of $Li_xCu_{1-x}O$ (Fig. 4.2a and b) shows a very strong dependence on the amount of introduced Li. While for high concentration the band gap is strongly decreased to 0.64 eV, for low concentration the main effect is an upward shift of the valence band maximum that crosses the Fermi level and makes the system a p-type semiconductor. As shown in the spin density plots in Fig. 4.2c and d, the underlying mechanisms are distinct: for $x_{Li} = 25$ at% substitution of Li^+ leads to a change in charge state of one copper to Cu^{3+}, while for $x_{Li} = 3.2$ at% the holes are delocalized at the oxygen sites leading to a p-type semiconductor.

To sum up, lithium doping causes an increased optical absorption of CuO in the infrared range and significantly increases the p-type conductivity, therefore we expect facilitated charge separation. As our morphology is beneficial for the strongly surface-dependent water splitting reaction,[5] we determined the photoelectrochemical performance of $Li_xCu_{1-x}O$ photocathodes by linear sweep voltammetry (LSV) in 0.1 M Na_2SO_4 aqueous solution (pH 7) starting at 0.7 V vs. RHE and scanning down towards –0.1 V vs. RHE under chopped AM 1.5 illumination. In the present case, the result of this procedure (Fig. 4.3a) is very misleading, as the $Li_xCu_{1-x}O$ film shows the typical behavior of a photocathode with instant photocurrent response upon illumination. This observation can easily be misinterpreted as a measure of hydrogen evolution efficiency, but indeed originates from both the reduction of water and the reduction of the transition metal oxide itself, which we elucidate in the present work. In addition, we performed cyclic voltammetry (CV) measurements in a potential range between 0.0 and 0.9 V vs. RHE (Fig. 4.3b). The material shows a negligible dark current, indicating electrochemical stability in the scanned potential range. Under AM1.5G illumination (100 mW cm^{--2}), a reductive current density can be observed below 0.5 V vs. RHE. However, significant oxidizing currents appear above 0.4 V vs. RHE in the back scan. To examine the electrochemical stability of our $Li_xCu_{1-x}O$ photocathodes, we applied different constant potentials from 0.0 to 0.6 V vs. RHE for 15 minutes each, in the dark as well as under illumination (ESI Fig. 7†). X-ray photoelectron spectroscopy (XPS) measurements of these films after electrochemical reaction were used to get further insights into the stability of the electrode material. From the binding energy of the Cu 2p3/2-peak (Fig. 4.3c and d), the oxidation state of the copper at the electrode surface could be assigned to Cu(II) (933.6 eV) or Cu(I) (932.4 eV).[65] As shown in Fig. 4.3c, copper(II) oxide remains stable without illumination down to 0.2 V vs. RHE. Below this potential a shift of the Cu 2p3/2-peak to lower binding energies is observed, indicative for the reduction of copper(II) oxide to copper(I) oxide. Under AM1.5G illumination, we observed copper(I) oxide formation already at 0.2 V vs. RHE, indicating photocorrosion by light induced electrons at this potential. Deconvolution of the Cu 2p3/2-peak as well as the corresponding Cu L3VV Auger signals support this conclusion (ESI Fig. 13†).

In agreement with the XPS data[65,66] and the Pourbaix diagram of copper,[67] we attribute the reductive currents to a competitive reduction of both 2 H^+ to H_2 and Cu^{2+} to Cu^{1+}, while the oxidizing currents result from the oxidation of Cu_1≡ to Cu^{2+}.[35] Furthermore, we extended the potential range of several CV measurements stepwise on a new sample (ESI Fig. 5†). With scanning to lower potentials, more Cu^{2+} is photoreduced to Cu^{1+}, which gets reoxidized to Cu^{2+} at 0.75 V vs. RHE. This extremely sensitive method indicates a photocorrosion onset at approximately 0.45 V vs. RHE. Notably, photocorrosion starts right with the photoelectrochemical measurement (ESI Fig. 19†) and is fully noticeable after 15 min. Impedance plots illustrate the impairing effect of photocorrosion on the charge transport properties on the photocathode–electrolyte interface (ESI Fig. 20†). With proceeding Cu_2O formation on the surface, we observed an increase in charge transfer resistance on $Li_xCu_{1-x}O$ electrodes.[68] We attribute this phenomenon to the high conduction band energy level of Cu_2O compared to CuO, which hinders electron transfer from $Li_xCu_{1-x}O$ towards the electrolyte. Electron energy loss spectroscopy (EELS) allows one to directly monitor the oxidation states of elements on the nanometer scale using the near edge fine structure. The Cu-L2,3 edges of CuO and Cu_2O are characterized by a pair of white lines which result from the excitation of 2p3/2 (L3) and 2p1/2 (L2) electrons to unoccupied 3d states (Fig. 4.3e). The white lines of CuO are shifted to lower energy losses compared to Cu_2O.[69,70]

Thus, the energetic position of the two white lines was used in this study to identify the local distribution of the oxidation states in the thin films (ESI Fig. 6†). EELS requires electron transparent samples (thickness below 100 nm),[70] which in this study was achieved by preparing thin lamellae with a focused ion beam microscope. The resulting lamella represents a cross-section through the thin film (Fig. 4.3f and g). A platinum protection layer was used to protect the sample from the gallium ions used for sample cutting and thinning. Oxidation state maps illustrate the local distribution of Cu_2O and CuO inside the thin film with the spatial resolution given by the pixel size of the map, which was commonly chosen between 2.5 and 5 nm using subpixel scanning to reduce beam damage. Both oxidation states are detected in the interfacial regions between the two phases. In the TEM images two different crystal morphologies are visible, large round crystals and smaller square crystals. The latter form preferably at the surface of the large crystals. EELS maps demonstrate that the two crystal morphologies correspond to the two oxidation states: the large crystals are pure CuO, while the smaller ones are Cu_2O (Fig. 4.3h). This is confirmed by high resolution TEM imaging of the two crystal morphologies (Fig. 4.3i and j) with their corresponding fast Fourier transforms (FFTs) indexed for CuO and Cu_2O (Fig. 4.3k and l). Interestingly, Cu_2O grows as distinct crystallites on the surface of CuO instead of forming a dense layer on its surface. Additionally, there is no obvious Cu_2O gradient inside the films, as Cu_2O seems to form on all CuO nanocrystals exposed to water. We see a similar photocorrosion behavior on undoped CuO. After a potentiostatic measurement for 15 minutes at 0.2 V vs. RHE, also the surface of CuO is covered with cubic crystallites. Both the post-photoelectrochemical XRD pattern of CuO as well as FFTs and electron diffraction pattern of the regions covered with cubic crystals indicate the formation of the cuprite phase (Cu_2O) (ESI Fig. 11†). Therefore, we expect the same corrosion mechanism like on $Li_xCu_{1-x}O$ photocathodes. To rule out artefacts introduced by the FIB sample preparation, FIB lamellae of reference samples that had not been used in photoelectrochemical experiments were investigated. The maps show a thin layer of reduced copper oxide at the surface of the CuO crystals (see ESI Fig. 8†), but no Cu_2O crystals. The reduction of the surface layer of CuO is most likely caused by a reaction of CuO with the Ga-ions used for the sample preparation. To stabilize our photoabsorber material, we coated our $Li_xCu_{1-x}O$ films with a protective layer by atomic layer deposition (ALD), as this is a proven approach to protect copper oxides against photocorrosion.[14,32,71] Among several tested coatings like TiO_2, $Ti_{0.8}Nb_{0.2}O_x$ (NTO), SnO_x, Al:ZnO and Al_2O_3, NTO exhibited the best results on our $Li_xCu_{1-x}O$ morphology. After deposition, the applied $Ti_{0.8}Nb_{0.2}O_x$ layers are amorphous (ESI Fig. 12†),[72,73] covering the complete surface of the nanostructured morphology of the $Li_xCu_{1-x}O$ films without the formation of pinholes (ESI Fig. 15†), which has already been demonstrated to successfully protect Cu_2O.[54] CV measurements of $Li_xCu_{1-x}O$/NTO films in aqueous 0.1 M Na_2SO_4 are free of oxidative current signals, indicating that the photoabsorber remains stable under illumination. In contrast to bare $Li_xCu_{1-x}O$, NTO covered films showed no activity in terms of water reduction (Fig. 4.4a and b, blue) due to the lack of a suitable cocatalyst.[3] For this reason, we electrodeposited Pt nanoparticles on our $Li_xCu_{1-x}O$/NTO from a 1 mM methanolic H_2PtCl_6 solution (see Experimental details for further information), as this is a proven way to improve HER kinetics on ALD protected copper oxide based photocathodes.[14] 20 nm sized Pt particles are formed on the surface of the nanostructured $Li_xCu_{1-x}O$/NTO films (Fig. 4.4e). A protection layer of 2.5 nm NTO showed the highest activity compared slightly thinner or thicker NTO layers, still allowing sufficient charge transport to the Pt cocatalyst (ESI Fig. 14†). We assume electron transport by tunneling through the protective layer due to its extremely small layer thickness. The described protection strategy causes no significant change in the light absorption properties of those devices compared to the pristine $Li_xCu_{1-x}O$ films (Fig. 4.1c). We see no signs of photocorrosion of $Li_xCu_{1-x}O$/NTO/Pt devices held for 15 min at 0.2 V vs. RHE under AM1.5G illumination. This is verified by EELS oxidation state mapping (Fig. 4.4f and k and ESI Fig. 16†). Based on LSV measurements under chopped illumination, these devices show a distinct activity towards hydrogen evolution reaching up to 350 $\mu A\,cm^{-2}$ at 0.0 V vs. RHE with a photocurrent onset at around 0.50 V vs. RHE (Fig. 4.4c). Furthermore, we quantified the incident-photon-to-currentefficiency (IPCE) at different potentials from 0.6 to 0.0 V vs. RHE (Fig. 4d). The photocathode is active over the whole visible spectrum, reaching parts of the IR range, with an IPCE maximum at an excitation wavelength of 380 nm. The IPCE increases with lower potentials, reaching up to 6.25% at 0.0 V vs. RHE.

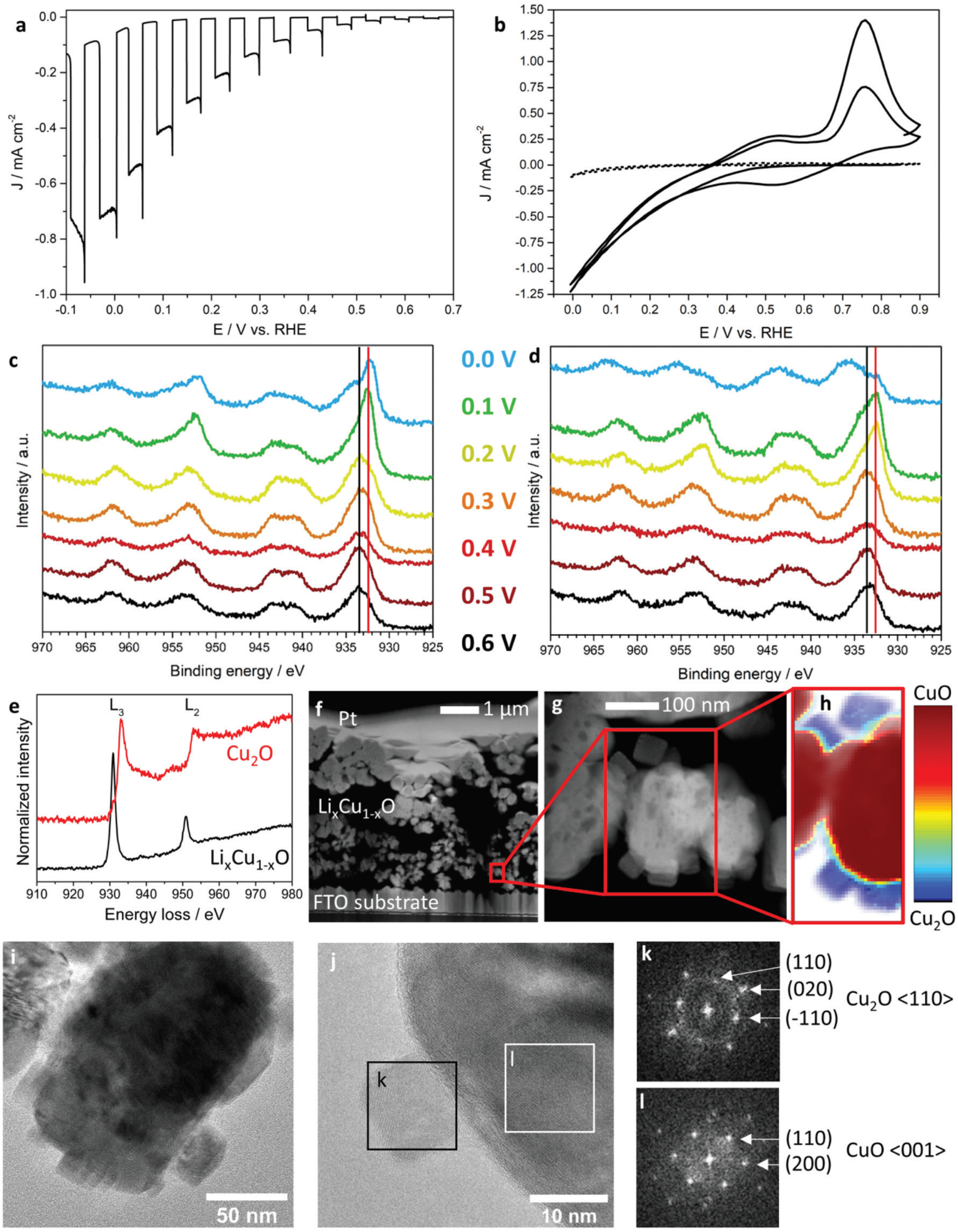

Figure 4.3: (a) Linear sweep voltammogram of a bare $Li_xCu_{1-x}O$ film under chopped AM 1.5 illumination, showing no signs of photocorrosion. The assumption of a working photocathode based on this experiment is very misleading, as the reductive currents originate from both water reduction and photocorrosion. (b) Cyclic voltammetry characterization of an unprotected $Li_xCu_{1-x}O$ photocathode in 0.1 M Na_2SO_4 at pH 7 in the dark (dashed line) and under AM 1.5 illumination through the substrate (solid line). (c and d) Cu 2p XPS spectra measured of bare $Li_xCu_{1-x}O$ films held at the respective potentials vs. RHE for 15 minutes each in the dark (c) and under AM1.5G illumination (d) (bars: black: Cu^{2+}, red: Cu^0 and Cu^{1+}). At a potential of 0.2 V vs. RHE, $Li_xCu_{1-x}O$ is stable in the dark but corrodes to Cu_2O under illumination. (e) Cu-$L_{2,3}$ edges of CuO and Cu_2O distinguish between both copper oxidation states. The photocorrosion could be localized in a TEM cross section image (f and g) with corresponding EELS map (h), showing cubic Cu_2O crystals on the $Li_xCu_{1-x}O$ surface. (i) Overview image of one crystal scratched from a $Li_xCu_{1-x}O$ film after an electrochemistry experiment performed for 15 min at 0.2 V under illumination, showing a roundish crystal overgrown by square crystals. (j) Average background subtraction filtered (ABSF) high resolution TEM image showing one square crystal at the surface of a spherical one. The FFTs of the marked regions were indexed for Cu_2O (k) and CuO (l), respectively.

In addition, we performed stability tests of bare $\mathrm{Li_xCu_{1-x}O}$ and $\mathrm{Li_xCu_{1-x}O}$/NTO/Pt films under illumination and quantified the evolved hydrogen. At a constant potential of 0.3 V vs. RHE, both photoelectrodes show a current response under illumination which is directly correlated to hydrogen evolution. The photocurrent of bare $\mathrm{Li_xCu_{1-x}O}$ decreases constantly and the hydrogen evolution stops after around 10 min of illumination due to photocorrosion of the material (ESI Fig. 18†), which results in a faradaic efficiency of 61% after 10 minutes (Fig. 4.5a). In contrast, the $\mathrm{Li_xCu_{1-x}O}$/NTO/Pt device produces a stable photocurrent and evolves hydrogen with a faradaic efficiency of 96% during the first 15 minutes after illumination (Fig. 4.5b). Afterwards, both the hydrogen evolution and the current drop. We attribute the activity loss to the detachment of the Pt nanoparticles due to hydrogen bubble formation (see ESI Fig. 17†), whereas the decrease of hydrogen concentration can be attributed to leakage from the photoelectrochemical cuvette-type cell used for hydrogen evolution experiments. We are currently working on the optimization of the cocatalyst deposition to increase both stability and activity of Li doped CuO photocathodes. Without direct contact to water, bare $\mathrm{Li_xCu_{1-x}O}$ is stable in a comparable potential range, as shown in a photoelectrochemical measurement in 1 mM iodide/triioide ($\mathrm{I^-/I_3^-}$) propylene carbonate electrolyte (Fig. 4.5c). No oxidative currents are detectable, which would indicate a $\mathrm{Cu^{1+}/Cu^{2+}}$ reaction similar to the one shown in Fig. 4.3b. Moreover, the $\mathrm{Li_xCu_{1-x}O}$ film was held under illumination at 0.1 V vs. RHE for 15 minutes. The corresponding EELS map of this sample shows no sign of photocorrosion. From this observation, we conclude that $\mathrm{Li_xCu_{1-x}O}$ could be used as stable photoabsorber as well as catalyst in a water-free electrolyte.

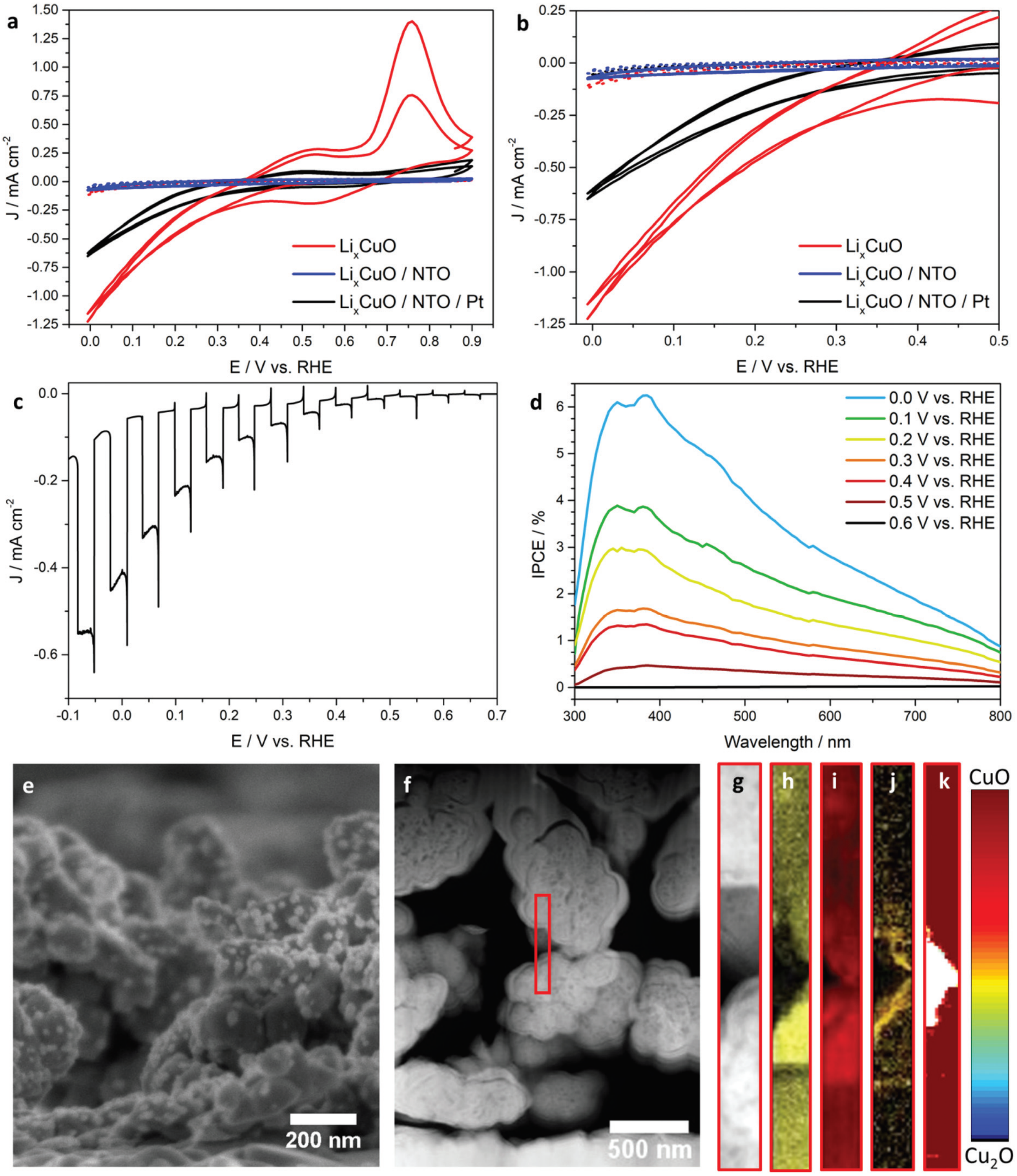

Figure 4.4: (a) Cyclic voltammetry measurements of $Li_xCu_{1-x}O$ films protected with 2.5 nm thin $Ti_{0.8}Nb_{0.2}O_x$ (NTO) layer (blue) and additionally functionalized with Pt nanoparticles (black) compared to a bare $Li_xCu_{1-x}O$ photocathode (red) in the dark (dashed) and under AM1.5 illumination (solid). (b) Magnification of (a) in the lower potential range. (c) Linear sweep voltammogram of a $Li_xCu_{1-x}O$/NTO/Pt film under chopped AM 1.5 illumination. (d) Incident-photon-to-current-efficiency (IPCE) measurements at different potentials. (e) SEM image of a $Li_xCu_{1-x}O$/NTO photocathode decorated with 20 nm sized Pt particles. (f) STEM image of a cross section of a $Li_xCu_{1-x}O$/NTO/Pt device held for 15 min at 0.2 V vs. RHE under AM1.5 illumination. The marked area (red, g) was used for EDX mapping of Cu (h), O (i) and Ti (j). The corresponding EELS map (k) shows no sign of photocorrosion.

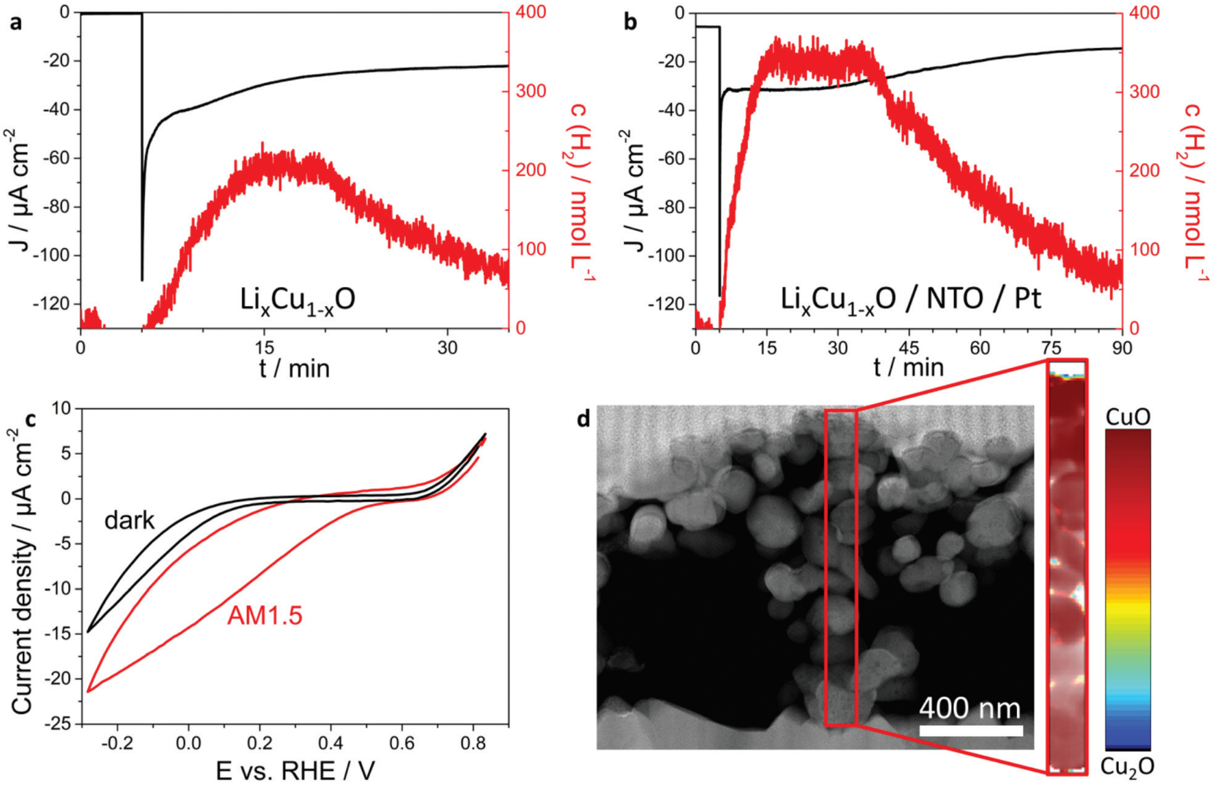

Figure 4.5: (a and b) Chronoamperometric data (black) at 0.3 V vs. RHE with corresponding H_2 evolution (red), which is directly correlated to illumination starting after 5 minutes. While unprotected $Li_xCu_{1-x}O$ films (a) start to degrade right after illumination, $Li_xCu_{1-x}O$/NTO/Pt photocathodes (b) show stable hydrogen evolution during the first 30 minutes. (c and d) To probe the role of the water during the electrochemical reaction, a propylene carbonate electrolyte with an iodide triiodide redox couple was used as replacement. The CV measurement (c) as well as the TEM cross section with corresponding EELS map (d) of the film after a 15 minutes' stability test at 0.1 V vs. RHE show no sign of photocorrosion.

4.4 Conclusions

In this study, we have presented black Li-doped CuO thin films as cathodic light absorber for photoelectrochemical hydrogen evolution. The substitution of 4 at% of Cu^{2+} with Li^{+} ions has a substantial influence on the optical and electronic properties. The optical bandgap is reduced while both electrical conductivity and p-type character increase upon Li doping, which is beneficial for the application as photocathode material in a PEC tandem cell. DFT+U calculations confirm that the system becomes a p-type semiconductor for low Li concentrations due to the pronounced delocalization of holes. While $Li_xCu_{1-x}O$ is stable in a non-aqueous electrolyte, it suffers from photocorrosion in contact with water. For the first time, the corrosion was studied in detail by cyclic voltammetry, X-ray photoelectron and electron energy loss spectroscopy. As a result, we present a detailed study on photocorrosion to provide a profound understanding of the underlying physical process which will be applicable to any copper based photocatalyst. Indeed, the performance of other reported photoelectrode systems should be critically revised.

Under illumination and in direct contact with water, the reduced Cu_2O forms as distinct cubic crystals on the $Li_xCu_{1-x}O$ surface. We demonstrate that $Li_xCu_{1-x}O$ films can be stabilized to some degree against photocorrosion by using approaches common in photoelectrochemical research namely the application of a thin Nb:TiO_2 protection layer in combination with a Pt cocatalyst. Still, our described approach cannot solve the fundamental problem of intrinsic instability of metal oxide-based photocathodes in aqueous electrolytes. We suggest that similar fundamental problems of photocorrosion stability will be witnessed also in other copper containing photoabsorbers, therefore the photoelectrochemical performance and possible light-triggered material transformation should be revisited with special care. We doubt that the intrinsic photocorrosion of copper oxide based photoelectrodes can be solved in any feasible way in aqueous electrolytes. However, the in situ growth of Cu_2O due to photoreduction could be used for other types of electrochemical processes. As an example, the use as specific catalyst for CO_2 reduction in a water-free, methanolic electrolyte can be envisioned as both copper oxides were already described to be very active for this application.[74] By manipulating their electronic structure using various dopants like Li^{+}, we expect to enhance both the efficiency of copper oxides and also fine tune the formation efficiencies for hydrocarbons like methane and ethylene.

Bibliography

[1] N. S. Lewis, G. Crabtree, A. J. Nozik, M. R. Wasielewski, P. Alivisatos, H. Kung, J. Tsao, E. Chandler, W. Walukiewicz, M. Spitler, R. Ellingson, R. Overend, J. Mazer, M. Gress, J. Horwitz, C. Ashton, B. Herndon, L. Shapard & R. M. Nault. Basic Research Needs for Solar Energy Utilization. Report of the Basic Energy Sciences Workshop on Solar Energy Utilization, April 18-21, 2005.

[2] L. Fornarini, A. J. Nozik & B. A. Parkinson. *The Journal of Physical Chemistry*, **1984**. *88*(15), 3238–3243.

[3] A. Heller. *Science (New York, N.Y.)*, **1984**. *223*(4641), 1141–1148.

[4] M. G. Walter, E. L. Warren, J. R. McKone, S. W. Boettcher, Q. Mi, E. A. Santori & N. S. Lewis. *Chemical reviews*, **2010**. *110*(11), 6446–6473.

[5] R. van de Krol, Y. Liang & J. Schoonman. *Journal of Materials Chemistry*, **2008**. *18*(20), 2311.

[6] O. Khaselev. *International Journal of Hydrogen Energy*, **2001**. *26*(2), 127–132.

[7] R. N. Dominey, N. S. Lewis, J. A. Bruce, D. C. Bookbinder & M. S. Wrighton. *Journal of the American Chemical Society*, **1982**. *104*(2), 467–482.

[8] U. Sim, T.-Y. Yang, J. Moon, J. An, J. Hwang, J.-H. Seo, J. Lee, K. Y. Kim, J. Lee, S. Han, B. H. Hong & K. T. Nam. *Energy & Environmental Science*, **2013**. *6*(12), 3658.

[9] Y. Hou, B. L. Abrams, P. C. K. Vesborg, M. E. Björketun, K. Herbst, L. Bech, A. M. Setti, C. D. Damsgaard, T. Pedersen, O. Hansen, J. Rossmeisl, S. Dahl, J. K. Nørskov & I. Chorkendorff. *Nature materials*, **2011**. *10*(6), 434–438.

[10] T. Sick, A. G. Hufnagel, J. Kampmann, I. Kondofersky, M. Calik, J. M. Rotter, A. Evans, M. Döblinger, S. Herbert, K. Peters, D. Böhm, P. Knochel, D. D. Medina, D. Fattakhova-Rohlfing & T. Bein. *Journal of the American Chemical Society*, **2018**. *140*(6), 2085–2092.

[11] M. Haro, C. Solis, G. Molina, L. Otero, J. Bisquert, S. Gimenez & A. Guerrero. *The Journal of Physical Chemistry C*, **2015**. *119*(12), 6488–6494.

[12] T. Bourgeteau, D. Tondelier, B. Geffroy, R. Brisse, S. Campidelli, R. Cornut & B. Jousselme. *Journal of Materials Chemistry A*, **2016**. *4*(13), 4831–4839.

[13] R. Sathre, C. D. Scown, W. R. Morrow, J. C. Stevens, I. D. Sharp, J. W. Ager, K. Walczak, F. A. Houle & J. B. Greenblatt. *Energy Environ. Sci.*, **2014**. *7*(10), 3264–3278.

[14] A. Paracchino, N. Mathews, T. Hisatomi, M. Stefik, S. D. Tilley & M. Grätzel. *Energy & Environmental Science*, **2012**. *5*(9), 8673.

[15] K. Sivula, F. Le Formal & M. Grätzel. *ChemSusChem*, **2011**. *4*(4), 432–449.

[16] R. Patil, S. Kelkar, R. Naphade & S. Ogale. *J. Mater. Chem. A*, **2014**. *2*(10), 3661–3668.

[17] M. S. Prévot & K. Sivula. *The Journal of Physical Chemistry C*, **2013**. *117*(35), 17879–17893.

[18] U. A. Joshi, A. M. Palasyuk & P. A. Maggard. *The Journal of Physical Chemistry C*, **2011**. *115*(27), 13534–13539.

[19] S. P. Berglund, F. F. Abdi, P. Bogdanoff, A. Chemseddine, D. Friedrich & R. van de Krol. *Chemistry of Materials*, **2016**. *28*(12), 4231–4242.

[20] I. Kondofersky, A. Müller, H. K. Dunn, A. Ivanova, G. Štefanić, M. Ehrensperger, C. Scheu, B. A. Parkinson, D. Fattakhova-Rohlfing & T. Bein. *Journal of the American Chemical Society*, **2016**. *138*(6), 1860–1867.

[21] K. Sliozberg, H. S. Stein, C. Khare, B. A. Parkinson, A. Ludwig & W. Schuhmann. *ACS applied materials & interfaces*, **2015**. *7*(8), 4883–4889.

[22] C.-Y. Chiang, Y. Shin, K. Aroh & S. Ehrman. *International Journal of Hydrogen Energy*, **2012**. *37*(10), 8232–8239.

[23] C.-Y. Chiang, Y. Shin & S. Ehrman. *Energy Procedia*, **2014**. *61*, 1799–1802.

[24] H. K. Dunn, J. M. Feckl, A. Müller, D. Fattakhova-Rohlfing, S. G. Morehead, J. Roos, L. M. Peter, C. Scheu & T. Bein. *Physical chemistry chemical physics : PCCP*, **2014**. *16*(44), 24610–24620.

[25] L. M. Peter. *Journal of Solid State Electrochemistry*, **2013**. *17*(2), 315–326.

[26] A. L. Linsebigler, G. Lu & J. T. Yates. *Chemical Reviews*, **1995**. *95*(3), 735–758.

[27] M. S. Prévot, N. Guijarro & K. Sivula. *ChemSusChem*, **2015**. *8*(8), 1359–1367.

[28] Y. Yang, Di Xu, Q. Wu & P. Diao. *Scientific reports*, **2016**. *6*, 35158.

[29] U. Shaislamov & H.-J. Lee. *Journal of the Korean Physical Society*, **2016**. *69*(7), 1242–1246.

[30] U. Shaislamov, K. Krishnamoorthy, S. J. Kim, A. Abidov, B. Allabergenov, S. Kim, S. Choi, R. Suresh, W. M. Ahmed & H.-J. Lee. *International Journal of Hydrogen Energy*, **2016**. *41*(4), 2253–2262.

[31] P. Basnet & Y. Zhao. *Catalysis Science & Technology*, **2016**. *6*(7), 2228–2238.

[32] Y.-F. Lim, C. S. Chua, C. J. J. Lee & D. Chi. *Physical chemistry chemical physics : PCCP*, **2014**. *16*(47), 25928–25934.

[33] C.-Y. Chiang, M.-H. Chang, H.-S. Liu, C. Y. Tai & S. Ehrman. *Industrial & Engineering Chemistry Research*, **2012**. *51*(14), 5207–5215.

[34] D. Barreca, P. Fornasiero, A. Gasparotto, V. Gombac, C. Maccato, T. Montini & E. Tondello. *ChemSusChem*, **2009**. *2*(3), 230–233.

[35] F. P. Koffyberg & F. A. Benko. *Journal of Applied Physics*, **1982**. *53*(2), 1173–1177.

[36] B. K. Meyer, A. Polity, D. Reppin, M. Becker, P. Hering, P. J. Klar, T. Sander, C. Reindl, J. Benz, M. Eickhoff, C. Heiliger, M. Heinemann, J. Bläsing, A. Krost, S. Shokovets, C. Müller & C. Ronning. *physica status solidi (b)*, **2012**. *249*(8), 1487–1509.

[37] M. Heinemann, B. Eifert & C. Heiliger. *Physical Review B*, **2013**. *87*(11).

[38] D. Chauhan, B. Bohara & M. W. Urie. volume 29. **2006**.

[39] L. C. Olsen, R. C. Bohara & M. W. Urie. *Applied Physics Letters*, **1979**. *34*(1), 47–49.

[40] X. Ba, L.-L. Yan, S. Huang, J. Yu, X.-J. Xia & Y. Yu. *The Journal of Physical Chemistry C*, **2014**. *118*(42), 24467–24478.

[41] S. Masudy-Panah, Y.-J. K. Eugene, N. D. Khiavi, R. Katal & X. Gong. *Journal of Materials Chemistry A*, **2018**. *6*(25), 11951–11965.

[42] S. Masudy-Panah, R. Katal, N. D. Khiavi, E. Shekarian, J. Hu & X. Gong. *Journal of Materials Chemistry A*, **2019**. *7*(39), 22332–22345.

[43] P. Chand, A. Gaur, A. Kumar & U. Kumar Gaur. *Applied Surface Science*, **2014**. *307*, 280–286.

[44] S. Masudy-Panah, R. S. Moakhar, C. S. Chua, A. Kushwaha, T. I. Wong & G. K. Dalapati. *RSC Advances*, **2016**. *6*(35), 29383–29390.

[45] Y. J. Jang, J.-W. Jang, S. H. Choi, J. Y. Kim, J. H. Kim, D. H. Youn, W. Y. Kim, S. Han & J. Sung Lee. *Nanoscale*, **2015**. *7*(17), 7624–7631.

[46] Z. Zhang & P. Wang. *J. Mater. Chem.*, **2012**. *22*(6), 2456–2464.

[47] C.-Y. Chiang, Y. Shin & S. Ehrman. *Journal of The Electrochemical Society*, **2011**. *159*(2), B227–B231.

[48] C.-M. Wang & C.-Y. Wang. *Journal of Nanophotonics*, **2014**. *8*(1), 084095.

[49] X. Guo, P. Diao, Di Xu, S. Huang, Y. Yang, T. Jin, Q. Wu, M. Xiang & M. Zhang. *International Journal of Hydrogen Energy*, **2014**. *39*(15), 7686–7696.

[50] Le Chen, S. Shet, H. Tang, H. Wang, T. Deutsch, Y. Yan, J. Turner & M. Al-Jassim. *Journal of Materials Chemistry*, **2010**. *20*(33), 6962.

[51] C.-Y. Chiang, K. Aroh, N. Franson, V. R. Satsangi, S. Dass & S. Ehrman. *International Journal of Hydrogen Energy*, **2011**. *36*(24), 15519–15526.

[52] S. Emin, F. F. Abdi, M. Fanetti, W. Peng, W. Smith, K. Sivula, B. Dam & M. Valant. *Journal of Electroanalytical Chemistry*, **2014**. *717-718*, 243–249.

[53] H. CHOI & M. KANG. *International Journal of Hydrogen Energy*, **2007**. *32*(16), 3841–3848.

[54] A. Paracchino, V. Laporte, K. Sivula, M. Grätzel & E. Thimsen. *Nature materials*, **2011**. *10*(6), 456–461.

[55] H. Xing, L. E, Z. Guo, D. Zhao, X. Li & Z. Liu. *Inorganic Chemistry Frontiers*, **2019**. *6*(9), 2488–2499.

[56] S. Zhang, M. Rohloff, O. Kasian, A. M. Mingers, K. J. J. Mayrhofer, A. Fischer, C. Scheu & S. Cherevko. *The Journal of Physical Chemistry C*, **2019**. *123*(38), 23410–23418.

[57] F. M. Toma, J. K. Cooper, V. Kunzelmann, M. T. McDowell, J. Yu, D. M. Larson, N. J. Borys, C. Abelyan, J. W. Beeman, K. M. Yu, J. Yang, Le Chen, M. R. Shaner, J. Spurgeon, F. A. Houle, K. A. Persson & I. D. Sharp. *Nature communications*, **2016**. *7*, 12012.

[58] D. K. Lee & K.-S. Choi. *Nature Energy*, **2018**. *3*(1), 53–60.

[59] G. Tunell, E. Posnjak & C. Ksanda. *Cryst. Mater.*, **1935**. *90*, 120–142.

[60] P. Niggli. *Cryst. Mater.*, **1922**. *57*, 253–299.

[61] Carretta, Corti & Rigamonti. *Physical review. B, Condensed matter*, **1993**. *48*(5), 3433–3444.

[62] C. Baeumer, C. Funck, A. Locatelli, T. O. Menteş, F. Genuzio, T. Heisig, F. Hensling, N. Raab, C. M. Schneider, S. Menzel, R. Waser & R. Dittmann. *Nano letters*, **2019**. *19*(1), 54–60.

[63] D. Roy, G. F. Samu, M. K. Hossain, C. Janáky & K. Rajeshwar. *Catalysis Today*, **2018**. *300*, 136–144.

[64] S. L. Dudarev, G. A. Botton, S. Y. Savrasov, C. J. Humphreys & A. P. Sutton. *Physical Review B*, **1998**. *57*(3), 1505–1509.

[65] M. C. Biesinger, L. W. Lau, A. R. Gerson & R. S. Smart. *Applied Surface Science*, **2010**. *257*(3), 887–898.

[66] S. Poulston, P. M. Parlett, P. Stone & M. Bowker. *Surface and Interface Analysis*, **1996**. *24*(12), 811–820.

[67] B. Beverskog & I. Puigdomenech. *Journal of The Electrochemical Society*, **1997**. *144*(10), 3476–3483.

[68] S. Masudy-Panah, R. Siavash Moakhar, C. S. Chua, H. R. Tan, T. I. Wong, D. Chi & G. K. Dalapati. *ACS applied materials & interfaces*, **2016**. *8*(2), 1206–1213.

[69] L. Laffont, M. Y. Wu, F. Chevallier, P. Poizot, M. Morcrette & J. M. Tarascon. *Micron (Oxford, England : 1993)*, **2006**. *37*(5), 459–464.

[70] R. D. Leapman, L. A. Grunes & P. L. Fejes. *Physical Review B*, **1982**. *26*(2), 614–635.

[71] J. Azevedo, S. D. Tilley, M. Schreier, M. Stefik, C. Sousa, J. P. Araújo, A. Mendes, M. Grätzel & M. T. Mayer. *Nano Energy*, **2016**. *24*, 10–16.

[72] V. Pore, M. Ritala, M. Leskelä, T. Saukkonen & M. Järn. *Crystal Growth & Design*, **2009**. *9*(7), 2974–2978.

[73] A. G. Hufnagel, S. Häringer, M. Beetz, B. Böller, D. Fattakhova-Rohlfing & T. Bein. *Nanoscale*, **2019**. *11*(30), 14285–14293.

[74] S. Ohya, S. Kaneco, H. Katsumata, T. Suzuki & K. Ohta. *Catalysis Today*, **2009**. *148*(3-4), 329–334.

5 Iridium Oxide Nanoparticles on Macroporous Antimony-Doped Tin Oxide Supports

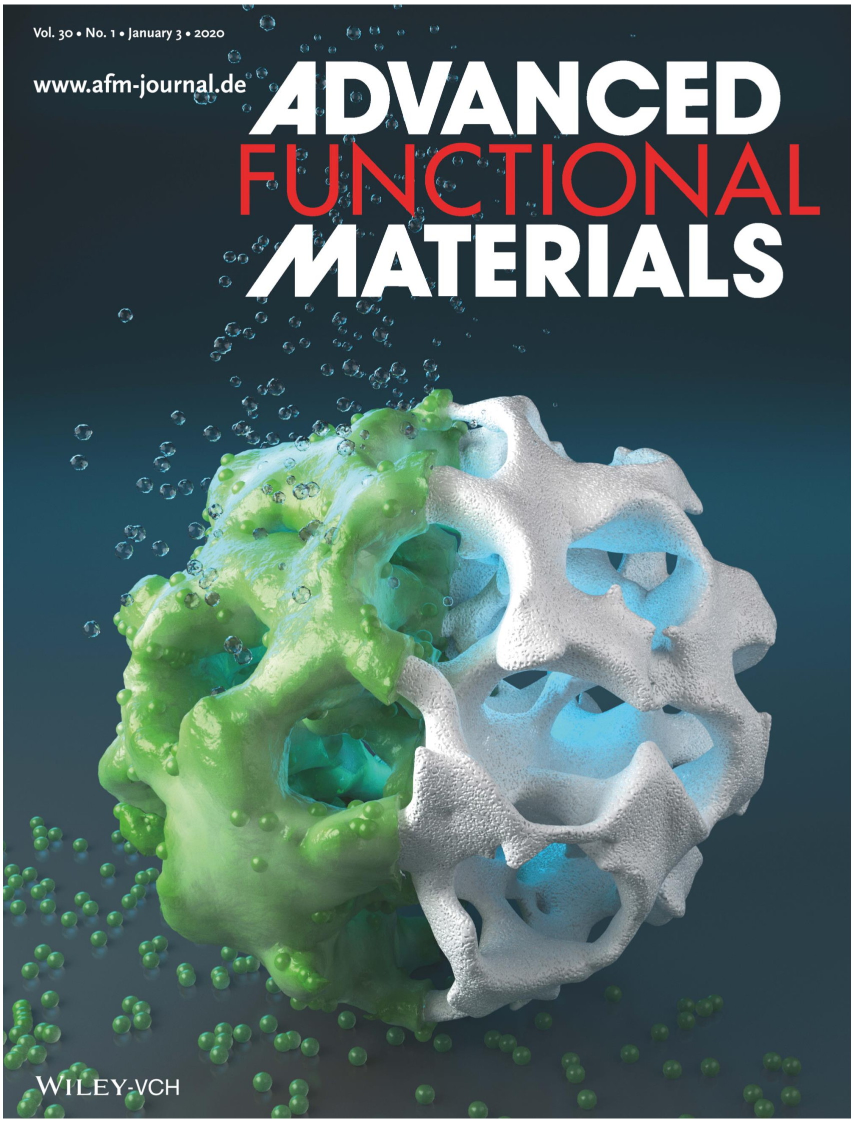

This chapter is based on the following publication:

Efficient OER Catalyst with Low Ir Volume Density Obtained by Homogeneous Deposition of Iridium Oxide Nanoparticles on Macroporous Antimony-Doped Tin Oxide Support, D. Böhm, M. Beetz, M. Schuster, K. Peters, A. G. Hufnagel, M. Döblinger, B. Böller, T. Bein, D. Fattakhova-Rohlfing, *Advanced Functional Materials*, **2019**, 30(1), 1906670.

5.1 Abstract

A multistep synthesis procedure for the homogeneous coating of a complex porous conductive oxide with small Ir nanoparticles is introduced to obtain a highly active electrocatalyst for water oxidation. At first, inverse opal macroporous Sb doped SnO_2 (ATO) microparticles with defined pore size, composition, and open-porous morphology are synthesized that reach a onductivity of $\approx 3.6\,\mathrm{S\,cm^{-1}}$ and are further used as catalyst support. ATO-supported iridium catalysts with a controlled amount of active material are prepared by solvothermal reduction of an IrO_x colloid in the presence of the porous ATO particles, whereby homogeneous coating of the complete outer and inner surface of the particles with nanodispersed metallic Ir is achieved. Thermal oxidation leads to the formation of ATO-supported IrO_2 nanoparticles with a void volume fraction of $\approx 89\%$ calculated for catalyst thin films based on scanning transmission electron microscope tomography data and microparticle size distribution. A remarkably low Ir bulk density of $\approx 0.08\,\mathrm{g\,cm^{-3}}$ for this supported oxide catalyst architecture with 25 wt% Ir is determined. This highly efficient oxygen evolution reaction catalyst reaches a current density of $63\,\mathrm{A\,g_{Ir^{-1}}}$ at an overpotential of 300 mV versus reversible hydrogen electrode, significantly exceeding a commercial TiO_2-supported IrO_2 reference catalyst under the same measurement conditions.

5.2 Introduction

Generation of hydrogen via the electrolysis of water is considered one of important pillars of a future sustainable economy. In this way, the renewably generated electricity is converted into hydrogen that can be stored and used when required, either in a fuel cell or to replace petrochemically produced hydrogen as a process feedstock.[1,2] Relatively recent but already advanced proton exchange membrane (PEM) electrolysis technology enjoys an upswing in the industrial and research interest due to its compact design enabling high efficiency, high applicable current density and intermittent operation capability, which makes it an excellent match for decentralized renewable generators with high output fluctuations.[3] However, the large scale application of PEM electrolysis is currently limited by the high cost of its components and in particular iridium used to catalyze the oxygen evolution reaction (OER) process.[4,5] In spite of intensive research on different classes of OER catalysts, iridium oxide remains the only material demonstrating sufficient long-term catalytic activity without stability fading.[6] This is however achieved by a high Ir loading in the electrode assemblies of about $1.5–3\,\mathrm{mg\,Ir\,cm^{-2}}$ in the state of the art PEM cells.[7–9] Taking into account the cost, scarcity and total availability of Ir, at least a 10-fold decrease in the Ir loading is required.[10] At the same time, a certain thickness of the catalyst layer of several µm is needed to enable its integration in the cells without the shortcuts in their functionality.[7] In fact, it is not only the decreased loading but the drastic decrease in the Ir volumetric packing density in the electrode assembly with the simultaneous increase in the OER activity that should be targeted to make PEM technology economically feasible for the large scale hydrogen generation. Due to a high economic impact of PEM electrolysis, considerable efforts have been made to improve the performance of Ir-based catalysts. Nanostructuring, and in particular inverse opal morphology with its high void volume were demonstrated to be beneficial for decreasing the catalyst loading in membrane based electrolyzers as has been recently reported by Park et al.[11] and by Faustini et al.[12] for IrO_2 or $RuIrO_2$ catalysts, respectively. The critical point in the fabrication of nanostructured Ir-based catalysts is however the simultaneous optimization of the nanomorphology and the catalytic activity, which is strongly influenced even by the subtle changes in phase composition and is sensitive to the fabrication method.

Another established approach is a dispersion of the Ir-based OER catalyst on a nanostructured support, which potentially results in a much larger active surface area for a given amount of catalyst than could be achieved by a solid compact structure.[13–18] TiO_2-supported IrO_2 has been used for years as dimensionally stable electrodes (DSA) in chlorine-alkali electrolysis[19] and in the state of the art PEM electrolysis.[7,9,20] The major advantages brought by the commercially available supported catalysts are however more an improved mechanical stability and simple processability of the catalyst layers rather than the decrease in Ir loading. Significant efforts have been made therefore to optimize the morphology of supports by using materials with high surface area, high electric conductivity and high oxidation stability such as mesoporous transparent conductive oxides (TCO). Mesoporous antimony doped tin oxide (ATO),[13,21] indium tin oxide (ITO),[21] fluorine-doped tin oxide (FTO), and niobiumdoped titania (NTO)[18,22] coated with a thin iridium active phase have been reported to show the high electrocatalytic activity with a substantially decreased iridium loading. Still, in spite of the progress achieved, the rather small pore size and compact structure of the mesoporous materials put constraints on the homogeneous dispersion of iridium layers and the volumetric density as well as on the gas transport at high current densities. Therefore, a combination of conductivity provided by TCOs with a low volumetric density of macroporous supports can be expected to enable a further decrease in the Ir loading per membrane area on a scale required for large scale application of the PEM technology.[7]

The challenges in the development of supported catalysts are the synthesis of an ideally conductive, corrosion-stable support with the optimized morphology, as well as its conformal coating with a very thin layer of catalyst in a simple and scalable way. We present a scalable approach to prepare a dimensionally stable OER catalyst with a very low Ir volumetric loading density but very high OER activity. In contrast to previous work on supported catalysts and Ir-based OER catalysts, our multistep synthesis approach allows for an independent optimization of all single components to result in a highly active and stable catalyst. With the introduced synthesis concept the composition (by choice of the transition metal precursor), morphology (by the size of porogen), and conductivity (by the doping level) of the oxidic support, as well as the iridium loading (by the ratio of Ir-precursor to oxidic support) and the active phase (by the oxidation procedure applied on the Ir@oxidic-support) can be tuned individually to enable the evelopment of highly active OER catalysts with high Ir-volume dispersion for future PEM-electrolysis.

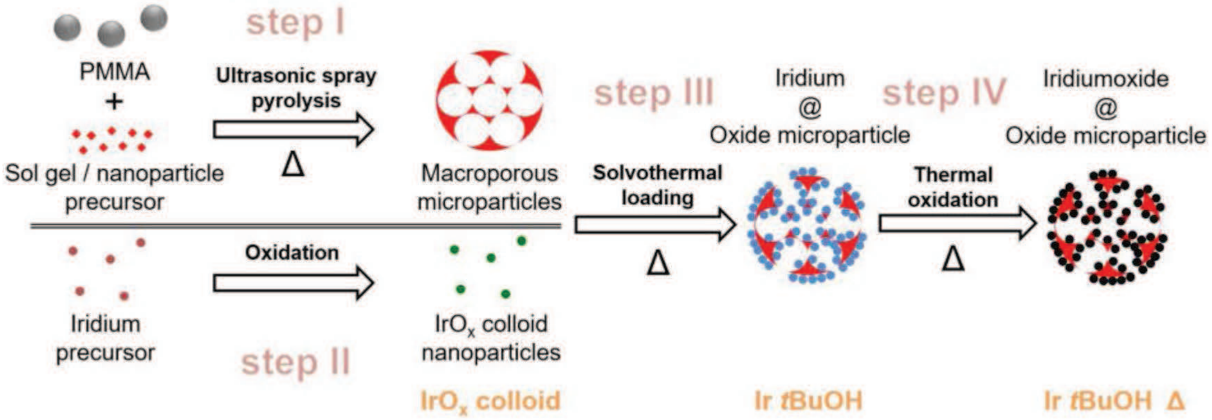

Figure 5.1: Synthesis of ATO microparticle-supported IrO_2 oxygen evolution reaction catalyst. Step I: Synthesis of macroporous oxide microparticles (red) by ultrasonic spray pyrolysis. Step II: Synthesis of IrO_x colloid nanoparticles (green) used for catalyst loading. Step III: Solvothermal loading of oxidic support by reduction of IrO_x to metallic Ir (blue) on the microparticle surface (assigned as "Ir tBuOH"). Step IV: Thermal oxidation of Ir-loaded ATO microparticles leads to the formation of IrO_2 nanoparticles (black, assigned as Ir tBuOHΔ) resulting in the final ATO-supported IrO_2-based OER catalyst.

5.3 Results and Discussion

Scheme 1 depicts the synthesis workflow starting from the ultrasonic spray pyrolysis of electrically conducting macroporous antimony-doped tin oxide ($Sb:SnO_2$ or ATO) microparticles templated by poly(methyl methacrylate) (PMMA) (Step I), and an iridium chloride precursor that is oxidized in an aqueous environment to form hydrous IrO_x colloid nanoparticles (Step II). A solvothermal reaction in tert-butanol/methanol/ H_2O as a key step leads to a reduction of the IrO_x colloid nanoparticles at the oxide microparticle surface (Step III) to form a homogeneous layer of metallic nanoparticles (referred to as Ir tBuOH) of comparable size ($\approx 2\,nm$). The resulting ATO microparticle-supported Ir nanoparticle product is referred to as SG280Δ-Ir-YX, with "SG" abbreviated for sol–gel derived product, subscript ("280" or "120") representing the PMMA bead diameter (in nm) used for the synthesis of inverse opal microparticles, "Δ" indicating thermally cured ATO scaffold particles, "Ir" indicating an Ir nanoparticle loaded product obtained by a solvothermal synthesis and "Y" = 1/2, 1, 2, 3, 4 being a multiplier of the iridium amount "X" on the ATO scaffold theoretically yielding a $\approx 15\,wt\%$ Ir content in the composite catalyst (see the Experimental Section and Table S1, Supporting Information, for further details). Thermal oxidation in air (Step IV) leads to the formation of ATO microparticle-supported IrO_2 nanoparticles referred to as SG280Δ-IrO_2-YX which represents IrO_2 nanoparticles supported on ATO scaffold particles originating from the thermal oxidation in air. In addition to the catalyst described above, particles with a smaller macropore size were prepared using 120 nm PMMA beads for the ATO microparticle synthesis. The samples are assigned as SG120Δ-Ir-YX and SG120Δ-IrO_2-YX for supported catalysts before and after thermal oxidation, respectively. As two series of the catalysts show very similar materials properties, mainly the characterization of particles with a larger pore size is shown in the paper, with characterization results of the smaller pore size catalyst series being shown in the supporting information. Macroporous ATO microparticles depicted in Figure 1 were synthesized using an ultrasonic spray pyrolysis (USP) approach (Scheme 1, Step I, also see Scheme S1 in the supporting Information and the Experimental Section for further details).[23] PMMA with bead sizes of ≈ 120 and ≈ 280 nm were used as templates to form ordered macroporous[24] ATO particles either from sol gel derived precursor (in the following referred to as SG120Δ and SG280Δ for 120 and 280 nm PMMA templated particles, respectively) or from presynthesized ATO nanoparticles[25] (referred to as NP120Δ). Resulting powders before (SG120, SG280, and NP120) and after thermal curing (SG120Δ, SG280Δ, and NP120Δ with "Δ" representing an additional heating step in air after the spray pyrolysis reaction) for the removal of residual carbon as well as undoped reference (SG280Δ w/o Sb) were analyzed by X-ray diffraction and Raman spectroscopy (see Figure S1a,c in the Supporting Information) confirming the exclusive formation of the SnO_2 cassiterite phase for undoped and ≈ 4 at% (sol–gel based) and ≈ 5 at% (nanoparticles based) Sb-doped samples. X-ray photoelectron spectroscopy (XPS) (see Figure S3 in the Supporting Information) and energy dispersive X-ray (EDX) analysis (value noted in Figure 1a) point to a Sb doping concentration of 4.3 at% for the SG280Δ samples, which is in a good agreement with the Sb content of 4.8 at% in the precursor solution. n-Type doping by antimony is known to increase the conductivity of stoichiometric SnO_2 significantly, with the highest values reported for an Sb-doping level of about 5 at%.[25] Dc measurements for densely compressed pellets return a high specific conductivity of $3.6\,\mathrm{S\,cm^{-1}}$ for the Sb-doped (SG280Δ) SnO_2 microparticle samples, which is an increase by a factor of ≈ 104 compared to a respective undoped sample SG280Δ ($3.8 \times 10^{-4}\,\mathrm{S\,cm^{-1}}$).

Scanning electron microscopy (SEM) and transmission electron microscopy (TEM) images reveal the formation of ATO microparticles with a mean diameter of 850 nm and inverse opal morphology with an outer pore opening diameter of 150 – 190 nm (mean Ø172 nm, N = 191) (Figure 1a,b) and a mean inner pore diameter determined from high resolution (HR)-TEM images of ≈ 232 nm indicating a shrinkage of the initial pores obtained by the 280 nm PMMA beads by ≈17% during the spray pyrolysis reaction. The pore size of the inverse opal ATO microparticles can be easily tuned by the size of the PMMA beads, as shown in Figures S4 and S5 (Supporting Information) for sol–gel and nanoparticle based ATO microparticles templated with 120 nm PMMA beads.

120 nm PMMA porogen templating thereby results in the formation of pore opening diameters of 55 – 75 nm (mean Ø65 nm, N = 137) on the outer microparticle surface and mean inner pore diameter of $\approx$ 83 nm as shown by electron microscopy translating to a pore shrinkage of $\approx$ 30% during the pyrolysis reaction.

According to X-ray diffraction (XRD) and high resolution TEM images, the scaffold is composed of $\approx$ 5 nm nanocrystals (Figure 1d and Figure S1, Supporting Information). Nitrogen sorption measurements (Figure S6, Supporting Information) correspond to mainly macroporous adsorbent with minor contribution of microporosity originating from textural porosity of interconnected small crystalline domains. A Brunauer–Emmett–Teller surface area of 54 and 52 $m^2\,g^{-1}$ was determined for 120 and 280 nm PMMA templated ATO microparticles, respectively. Direct evidence of macropores of about 70 nm for sample SG120Δ is given by the pore size distribution shown in inset of Figure S6a (Supporting Information), which is in a good agreement with the pore size quantification by SEM and TEM (see Figure S4 in the Supporting Information). The pore size distribution of SG280Δ does not show any porosity beyond a minor amount of micropores which can be explained by a detection limitation of the nitrogen sorption technique with regard to larger macropores (80 nm) as present in 280 nm PMMA templated microparticles. However, the visibly open porosity observed by SEM and TEM (Figure 1) in combination with the BET surface area strongly suggest interconnected macropores also for the 280 nm PMMA templated ATO microparticles. For the synthesis of a highly OER active iridium phase we have introduced a facile synthesis method for ultrasmall colloidal IrO_x particles (Scheme 1, Step II), which was used as an Ir precursor phase for the solvothermal loading of the oxidic scaffold. The procedure employs the rapid oxidation of an $Ir(III)Cl_3$ precursor in aqueous solution with KO_2, which was inspired by a synthesis introduced by Sutto for the fabrication of ultrasmall metal oxide nanoparticles.[26] The as-prepared IrO_x colloid (Figure 2e,f and Figure S7a, Supporting Information) consists of approximately spherical particles with a mean diameter of $\approx$ 2.4 nm as shown by scanning transmission electron microscope (STEM). The electron diffraction pattern (Figure 2f) of the particles only shows a diffuse ring that does not correspond to a distinct crystallographic plane but represents a mean Ir–O atomic distance in this poorly crystalline hydrated material.[27] The hydrous IrO_x particles are also easily reduced and crystallize in the electron beam evidenced by a visible growth and aggregation of nanoparticles with extended illumination periods (see Figure S8 in the Supporting Information).

Hydrous IrO_x colloids display a remarkable electrocatalytic performance but a rather limited long-term stability which requires an additional thermal treatment for the transformation to a stable active IrO_2 phase.[28,29] To obtain a more stable unsupported nanosized IrO_2 reference catalyst the precursor colloid was therefore oxidized in air at a moderate temperature of 375 °C to avoid significant particle growth and sintering. Powder X-ray diffraction patterns of the IrOx colloid

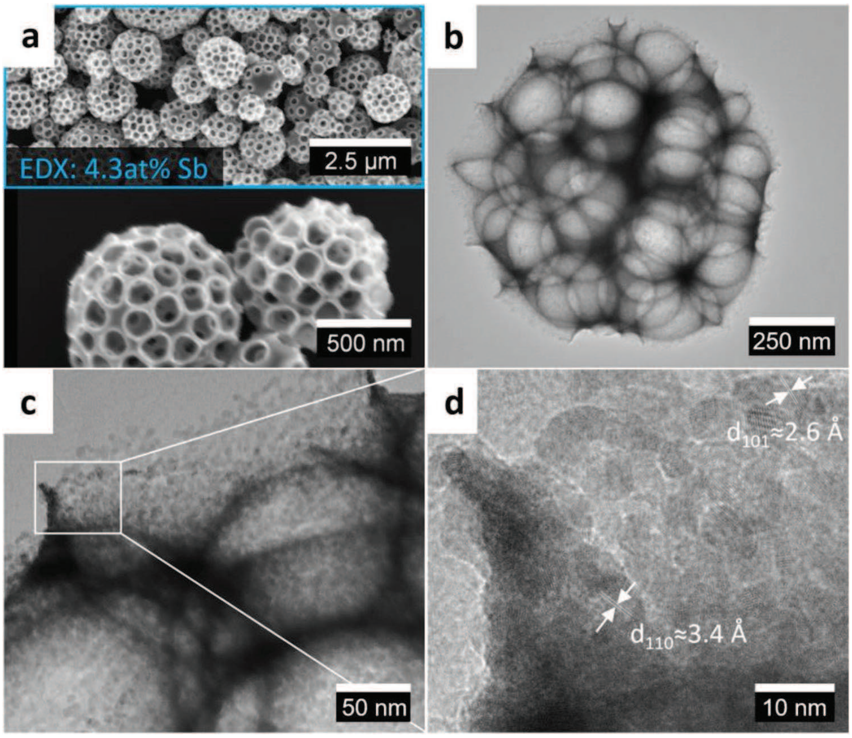

Figure 5.2: a–c) Electron microscopy images of macroporous antimony-doped tin oxide microparticles templated with 280 nm PMMA beads (SG280Δ). d) Lattice spacings indexed for individual ATO crystallites determined by intensity profiles of crystallites and correlated to d-spacings and orientation according to ICDD card number 00-041-1445 (SnO_2, tetragonal symmetry, $a = b = 4.7382(4)\text{Å}, c = 3.1871(1)\text{Å}, a = b = g = 90°$).

sample (Figure 2a) show a broad peak centered around 33° 2θ that is shifted to 35°2θ upon heating. According to the XRD line broadening and peak positions, the as-prepared as well as the heated IrO_x colloid is composed of a nanosized iridium oxide phase presumably differing in the degree of crystallinity and present crystal water causing a slight peak shift.[27] After calcination, aggregated nanoparticles (Figure 2g and Figure S7b, Supporting Information) with a mean particle size of ≈ 3.0 nm are observed with an electron diffraction pattern (Figure 2h) displaying diffraction rings mainly associated with the tetragonal IrO_2 phase. The increase in crystallinity accompanied by only negligible particle growth can directly be observed by STEM and is furthermore indicated by XRD (Figure 2a). The tetragonal iridium oxide phase of the IrO_x colloid before and after calcination is further confirmed by Raman spectroscopy (Figure 2b) displaying the characteristic Eg band around 560 cm^{-1} and a broad peak around 740 cm^{-1}, which is presumably formed by an overlapping B2g and A1g band at 728 and 752 cm^{-1}, respectively.[30,31] For the preparation of the IrO_2/ATO composite catalyst a solvothermal reaction of the precursor IrO_x colloid in presence of the porous ATO microparticles scaffold is introduced as integral part of this work to homogeneously coat the accessible surface of a porous support with iridium nanoparticles (Scheme 1, Step III). To obtain an unsupported reference catalyst the solvothermal reaction is

simply performed without the presence of the oxidic support. The solvothermal treatment of the IrO_x colloid in tertbutanol/MeOH/H_2O (with or without the presence of oxidic support material in the reaction) leads to a reduction and formation of metallic iridium nanoparticles, whereby unsupported Ir nanoparticles are referred to as "Ir tBuOH" in the following. The reduction process is indicated by the broad diffraction peak centered at around $41°2\theta$ corresponding to the cubic Ir phase and the absence of any peaks related to the tetragonal IrO_2 phase or hydrous IrO_x (Figure 2a and Figure S9a, Supporting Information). HR-TEM and STEM images reveal the formation of crystalline uniform nanoparticles (Ir tBuOH; Figure 2i,j and Figure S7c, Supporting Information) with an average diameter of The electron diffraction pattern (Figure 2j) indicates the presence of metallic iridium (cubic phase), which is in agreement with the X-ray diffraction (Figure 2a). The XRD pattern of particles after calcination at $375°C$ in air (Ir tBuOHΔ) shows a broad peak around $33°2\theta$, indicating the presence of a nanosized iridium oxide phase (Figure 2a and Figure S9b, Supporting Information). During thermal treatment the metallic nanoparticles undergo a transformation to the tetragonal IrO_2 phase (Ir tBuOHΔ; Figure 2k,l) as confirmed by electron microscopy with broad diffraction rings visible in Figure 2l, which matches well with the X-ray diffraction data.
This process is accompanied only by a minor particle growth to a mean diameter of $\approx 3.2\,\mathrm{nm}$ (Figure 2k). The presence of an iridium oxide phase is further confirmed by Raman spectroscopy (Figure 2b) for the calcined metallic Ir nanoparticles (Ir tBuOHΔ) sample. However, the Raman spectrum of metallic Ir nanoparticles after solvothermal reduction (Ir tBuOH) also displays the characteristic bands of the oxide phase at 560 and around 740 cm^{-1}, which can be explained by an oxide- or hydroxide-terminated nanoparticle surface, which is detected by Raman spectroscopy but not by XRD. To further investigate and distinguish the electronic properties of the synthesized iridium and iridium oxide phases and to derive the oxidation states of the iridium present, XPS (Figure 2c,d) was conducted. Fitting of the Ir 4f7/2 peak in the XPS spectrum of hydrous iridium oxide colloid (IrO_x colloid) returned a binding energy of 61.9 eV versus 62.1 eV for the calcined sample (IrO_x colloidΔ). Although an oxidation state of +IV can be assigned to iridium in both nanoparticle samples in accordance to literature values,[32] subtle differences in the XPS spectra of both oxide species can be observed.

By comparison, the ratio between the Ir 4f5/2 and Ir 4f7/2 peak is higher in the calcined sample, and we observe a visibly increased peak area and a shifted position of the Ir 4f7/2 and Ir 4f5/2 satellite peaks. The subtle changes in the XPS spectra in combination with the observed small shift in the XRD pattern (Figure 2a) are attributed to an increase in crystallinity with an accompanying loss of crystal-bound water which slightly alters the chemical surrounding of the Ir atoms in the hydrous oxide nanoparticles. Solvothermal reduction of the IrO_x colloid nanoparticles in tert-butanol/MeOH/H_2O causes a shift of the Ir 4f7/2 binding energy to 60.6 eV (Ir tBuOH in Figure 2d) which is assigned to Ir(0)[32] and is in agreement with the corresponding X-ray

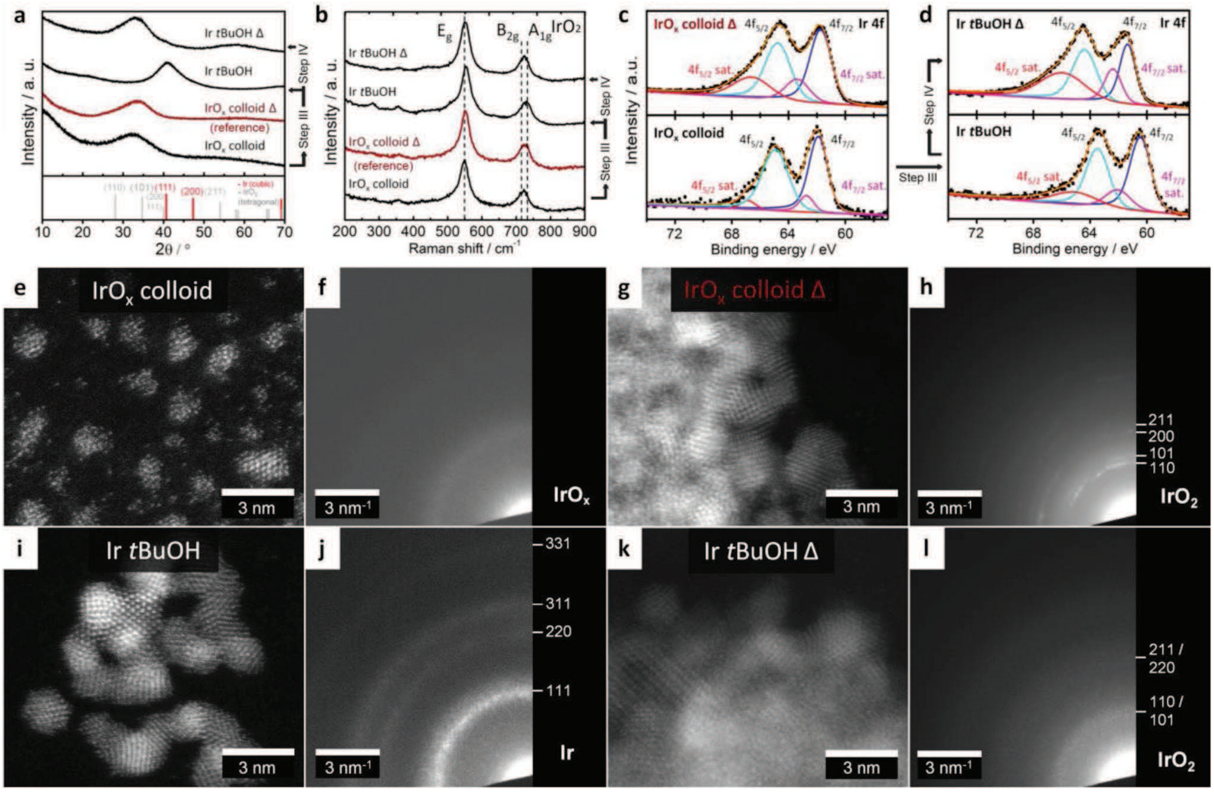

Figure 5.3: Structural and spectroscopic characterization of iridium and iridium oxide nanoparticles. a) X-ray diffraction pattern of IrO_x colloid before (IrO_x colloid) and after thermal oxidation (IrO_x colloidΔ, red curve) and metallic iridium nanoparticles (Ir tBuOH) and IrO_2 nanoparticles (Ir tBuOHΔ). Ir pattern: ICDD card number 00-006-0598 (red) (cubic symmetry, $a = b = c = 3.8394Å, a = b = g = 90°$). IrO_2 pattern: ICDD card number 00-015-0870 (gray) (tetragonal symmetry, $a = b = 4.4983Å, c = 3.1544Å, a = b = g = 90°$). b) Raman spectra of Ir/IrO_2 nanoparticles with reference band at 561 cm^{-1} (Eg) and close bands at 728 cm^{-1} (B2g) and at 752 cm^{-1} (A1g) correspond to the tetragonal iridium oxide phase.[30,31] XPS spectra of c) IrO_x colloid before and after thermal oxidation and d) iridium nanoparticles (Ir tBuOH) and IrO_2 nanoparticles (Ir tBuOHΔ). An Ir 4f7/2 core electron binding energy of 60.8 eV was assigned to metallic Ir(0) and an Ir 4f7/2 binding energy of 61.9 eV was assigned to Ir(IV)O_2.[32] e,g,i,k) Scanning transmission electron microscopy data and f,h,j,l) electron diffraction (ED) patterns of respective Ir/IrO_2 samples. Phase identification and assignment of lattice planes in ED pattern according to literature values.

diffraction (Figure 2a). Upon thermal oxidation the Ir 4f7/2 peak shifts again to higher binding energies (61.3 eV) and is therefore assigned to the oxide phase (Ir (+IV)).[32] However, the Ir 4f spectrum of the final IrO_2 nanoparticles differs from the spectra of the IrO_x colloid samples shown in Figure 2c. A significantly increased signal intensity, a further shift of the Ir 4f7/2 and Ir 4f5/2 satellite peaks and a slightly increased Ir 4f5/2 to Ir 4f7/2 ratio are observed. This indicates the formation of a nanoparticle oxide phase, as shown by the diffraction data, with a slightly altered chemical surrounding of the Ir atoms in contrast to the initial hydrous oxide phase. The results can be interpreted as a slightly altered local structure of the oxide phase differing in the degree of crystallinity and the number of defects caused by altered change in the Ir/O ratio over the course of the multistep synthesis. These structural differences not distinguishable in the powder X-ray diffraction data can have a significant impact on the OER activity and stability of the Ir-active phase (see section on electrochemical characterization). The crucial step in the synthesis of highly active oxide supported catalysts is the homogeneous coating of a complex support morphology with a thin compact layer of iridium nanoparticles. Simple infiltration of the oxidic support with IrO_x colloid results in a very poor support coverage, with the majority of colloidal nanoparticles remaining in the dispersion. We found, however, that the solvothermal treatment of this mixture in tert-butanol/methanol/H_2O (step III) leads to a reduction of IrO_x colloid to metallic Ir nanoparticles of similar size, conformally precipitating on the surface of porous ATO particles. The resulting composite catalyst is termed as SG280Δ-Ir-YX, with Y = 1/2, 1, 2, 3, 4 as a multiplier of the iridium amount declared as “X” which corresponds to an amount of precursor for a theoretical loading of 15 wt% Ir in the supported catalyst. The subscript represents the diameter of the templating porogen PMMA with 280 nm. Analogous results presented in the Supporting Information on ATO microparticles templated by 120 nm PMMA beads demonstrate a successful homogeneous coating of complex porous substrates also with decreased pore size (Figures S10a,c, S11, S12a,b,e,f, and S13 and Table S1, Supporting Information). The diffractograms of Ir-loaded ATO microparticles templated by 280 nm PMMA beads (Figure S10b, Supporting Information) exhibit peaks associated with the cassiterite (ATO) phase and an additional peak corresponding to the Ir 111 reflection that increases in intensity with the amount of IrO_x colloid added to the solvothermal synthesis, although its maximum intensity is lower than for the SG120Δ based samples (Figure S10a, Supporting Information). As was shown above for the unsupported Ir nanoparticles, thermal oxidation of Ir-loaded ATO microparticles at $375°C$ in air (Scheme 1, Step IV) leads to a transformation of metallic Ir particles to a nanosized tetragonal IrO_2 phase. Raman spectra of IrO_2-loaded as well as Ir-loaded ATO microparticles (Figure S11, Supporting Information) show two broad peaks around 550 and 740 cm^{-1} corresponding to the Eg band and the overlapping B2g/A1g band of IrO_2.[30,31] The absence of any signal from the underlying ATO indicates a complete coverage of the surface with Ir/IrO_2 particles. As indicated by scanning electron microscopy and EDX, Ir- (Figure S12a–d, Supporting Information) and IrO_2 (Figure S12e–h, Supporting Information) nanoparticle-coated ATO microparticles after solvothermal loading do not show a visible difference in shape or morphology as compared to the parent microparticle support (Figure 1 and Figure S4, Supporting Information). Also, the presence of chloride ions in the solvothermal reaction introduced by the $IrCl_3$ precursor has no significant impact on the microparticle phase (Figure S1b, Supporting Information), composition (Figure S2e, Supporting Information) or conductivity (Figure S2e,f, Supporting Information). EDX (Figure S12a,c,e,g, Supporting Information) confirms the presence of iridium, which is homogeneously distributed on the microparticle scale. The loading of ATO microparticles with iridium nanoparticles and the oxidation state of the active Ir phase were also investigated by XPS (Figure S14, Supporting Information), which confirms the formation of a metallic Ir phase

(Figure S14a, Supporting Information) upon solvothermal treatment in the presence of ATO microparticles as shown for unsupported nanoparticles (Figure 2d) which underwent the same synthesis procedure. Calcination also leads to the formation of the respective oxide phase (Figure S14a, Supporting Information and Figure 2d). Table S1 (Supporting Information) summarizes the theoretical and experimentally determined Ir fractions in the ATO microparticle-supported Ir and IrO_2 nanoparticle materials. The measured values deviate only slightly from the theoretical ones with the exception of the highly Ir-loaded sample ATO-SG280/ IrO_2-4X. The reason for the smaller loading capacity of the large-pore ATO microparticles at high iridium amounts (“4X” sample with theoretical loading of 43 wt% Ir) compared to the ATO-SG120/IrO_2 series is expected to be caused by the slightly smaller surface area available for particle adhesion. In summary, a near quantitative adsorption of the supplied iridium on the ATO scaffold could be realized for a broad range (7 to ≈ 40 wt% Ir) of ATO/Ir ratios by our solvothermal loading method. For a more detailed analysis of the spatial IrO_2 distribution on the macroporous ATO microparticles, high resolution transmission electron microscopy with energy-dispersive X-ray spectroscopy analysis and elemental distribution mapping was performed as shown in Figure 3. The overview images (Figure 3a,b) of the microparticles show that the morphology and pore structure of the unloaded particles has been maintained. The lattice spacings derived from electron diffraction patterns of individual ATO/IrO_2 particles (Figure 3d) indicate the exclusive presence of the cassiterite (ATO) and tetragonal IrO_2 phase. The deposition of a thin layer of IrO_2 nanoparticles on the inner ATO surface is shown by the lattice fringes visible in the high resolution TEM images, which can be assigned to the cassiterite and IrO_2 phase for individual nanocrystals (Figure 3c). Furthermore, the inner pore diameter of IrO_2- loaded 280 nm PMMA-templated particles could be quantified to ≈ 216 nm (Ø inner pore diameter, N = 14) according to HR-TEM images as shown in Figure 3 versus ≈ 71 nm (Ø inner pore diameter, N = 6) for 120 nm PMMA templated microparticles (Figure S13b, Supporting Information). As the inner pore diameter of unloaded ATO microparticles is ≈ 232 nm (Ø inner pore diameter, N = 27) and ≈ 83 nm (Ø inner pore diameter, N = 13, Supporting Information) for SG280Δ and SG120Δ, respectively, a mean thickness of the IrO_2 nanoparticle catalyst coating of ≈ 16 nm (ATO-SG120Δ-IrO2-2X) and ≈ 12 nm (ATOSG120Δ- IrO_2-2X) can be calculated. The reduction of the mean pore diameter is caused by a layer of nanocrystals of about 3 nm diameter (see Figure 2) that can be identified in the HR-TEM images of both samples (Figure 3c and Figure S13c, Supporting Information), which is in good agreement with the crystallite domain size derived from X-ray diffraction data (Figure 2a).

The active material layer on the ATO microparticle surface is therefore built up from an average of two to three IrO_2 nanoparticles for ≈ 25 wt % Ir loaded microparticles. EDX elemental mappings of outer ATO pores was performed (Figure 3e and Figure S13e, Supporting Information) for Ir coated ATO with both pore sizes. For both samples a colocalization of the Sn-L, Sb-L, and

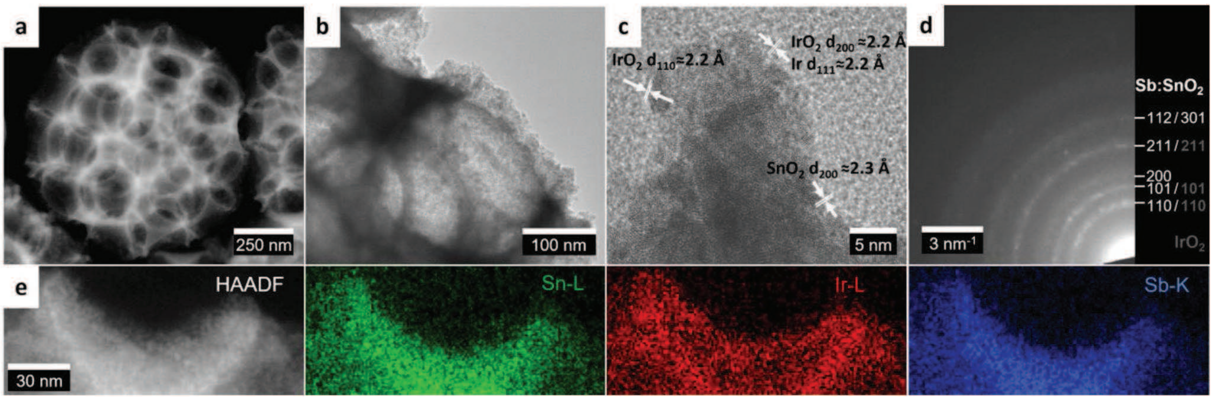

Figure 5.4: Transmission electron micrographs and EDX mapping of IrO_2 nanoparticles supported on macroporous ATO microparticles templated with 280 nm PMMA beads. a–c) Electron micrographs, d) electron diffraction pattern, and e) STEM/EDX elemental mapping of an outer pore. ATO microparticles with IrO_2 loadings of 25 wt % Ir (ATO-SG280Δ-IrO_2-2X). Phase identification and assignment of lattice spacings in d) electron diffraction pattern and c) high resolution TEM image according to literature values. SnO_2 (cassiterite) pattern: ICDD card number 00-041-1445 IrO_2 pattern: ICDD card number 00-015-0870.

Ir-L signal was observed. As the Ir-L signal extends beyond the areas of high tin and antimony concentration, we infer a homogeneous coating of the ATO surface with IrO_2. The distribution and interconnection of ATO, IrO_2 and void volume within this composite catalyst is of critical importance for the OER activity and its possible application in membrane based electrolyzers and was therefore studied by the 3D reconstruction of a representative, fully processed particle by means of STEM tomography (see the Experimental Section and Figure S15–S18, Supporting Information). The reconstruction for a 280 nm PMMA templated ATO-based particle is shown in Figure 4. Due to the higher electron scattering efficiency of high-atomic-number atoms (Z-contrast), a strong contrast between Sn and Ir is observed in high-angle annular dark-field (HAADF) imaging. The employed tomography algorithms were used to render a discrete 3D reconstruction, in which the volume occupied by ATO and IrO_2 is represented by orange and violet colors, respectively. Figure 4a shows the combined 3D intensity volume of ATO and IrO_2 reconstructed from a series of HAADF-STEM images recorded at different tilt angles. Figure 4b,c shows the extracted 3D intensity volume of the ATO scaffold and the loaded IrO_2 nanoparticle layer, respectively. The 3D intensity volume of IrO_2 (Figure 4c) closely follows the geometry of the ATO scaffold (Figure 4b). A calculated particle cross-section, shown in Figure 4d, confirms the homogeneous coverage of the total internal pore surface with IrO_2. The porosity and the volume dispersion of iridium could also be extracted from the 3D particle reconstruction. For the specific SG280Δ-IrO_2-2X particle with ≈ 25 wt % iridium, a void volume of 84.4 % including ATO as void and 59.7 % excluding ATO as void was determined (Figure S18, Supporting Information). To calculate the volume dispersion of iridium in a catalyst film composed of ATO microparticle-supported IrO_2 nanoparticles expected in a membrane-electrode assembly of a PEM electrolyzer, the porosity of individual microparticles as well as the packing density of the microparticles have to be taken into account. The void volume present in a catalyst film of spherical microparticles can be approximated by a random closed packing model[33] to reach 34 vol % for the experimentally determined particle size distribution (for further details and calculation, see Figure S19 in the Supporting Information). This results in an iridium volume fraction of 10.3 vol % in a catalyst film composed of SG280Δ-IrO_2-2X particles with ≈ 25 wt % iridium loading. The resulting Ir density of ≈ $0.08\,g_{Ir}\,cm^{-3}$ of bulk catalyst powder is much lower than the ≈ $1.5\,g_{Ir}\,cm^{-3}$ determined for a commercial IrO_2/TiO_2 reference catalyst. Thus, when employed in a PEM electrolyzer cell, a supported catalyst synthesized by the introduced procedure enables the preparation of a continuous, porous anode catalyst layer with a significantly lowered Ir loading than possible with commercial catalysts. Electrochemical characterization was performed to assess the performance of macroporous ATO microparticle-supported iridium oxide nanoparticles as an oxygen evolution reaction catalyst in acidic media. For the experiments shown in Figure 5a,b (120 and 280 nm PMMA-templated ATO microparticles, respectively), thin films of the catalyst particles dropcast onto Au-coated quartz crystal microbalance (QCM) sensors were used as working electrodes. The amount of iridium on the QCM chips was obtained from the absolute mass deposited onto the sensors and the iridium fraction determined by EDX measurements of the catalyst film (for Ir fractions of ATO supported catalysts see Table S1 in the Supporting Information). The morphology of thin films of unsupported IrO_2 nanoparticle reference catalysts “IrO_x colloidΔ” and “Ir tBuOHΔ” were investigated by SEM together with their unheated precursor phases “IrO_x colloid” and “Ir tBuOH” as shown in Figure S20 (Supporting Information).

Ir-mass based OER currents for an overpotential of 300 mV for 120 and 280 nm PMMA-templated ATO based catalysts in Figure 5a,b, respectively, show a similar maximum in activity for the 2X samples (55 $A\,g^{-1}$ for ATO-SG120Δ-IrO_2-2X and 63.5 $A\,g^{-1}$ for ATO-SG280Δ-IrO_2-2X after 10 CV cycles, respectively) that correspond to a Ir loading of ≈ 25 wt % . The slightly higher performance of the 280 nm PMMA templated supported catalyst is thereby attributed to a better dispersion of the IrO_2 nanoparticles on the internal surface of the porous microparticle. Higher Ir loadings of up to 40 wt % do not further increase the noble metal mass-based OER activity but rather resulted in a decrease. On the other hand, low Ir loadings of up to 15 wt % Ir for ATO-SG120Δ-IrO_2-1X and ATO-SG280Δ-1X exhibit activities of only 8.4 and 24.3 $A\,g^{-1}$, respectively. Compared to the unsupported IrO_2 nanoparticle (Ir tBuOHΔ) reference catalyst from the same synthesis, a 4- and 4.6-fold increase versus the most active ATO-SG120 Δ-IrO_2-2X and ATO-SG280Δ-2X sample could be observed. A comparable difference is observed for unsupported calcined IrO_2 from the colloid synthesis (IrO_2 colloidΔ). The bestperforming ATO-supported samples with ≈ 25 wt % Ir have a 7.3-fold (ATO-SG120Δ-IrO_2-2X) and 8.4-fold (ATO-SG280Δ-2X) higher Ir mass-based activity at ηOER = 300 mV than an industrial TiO_2-supported IrO_2 catalyst composed of IrO_2 nanocrystals with domain sizes of ≈ 4 nm (according to XRD analysis) on a nanocrystalline TiO_2 scaffold (Figure S21, Supporting Information) with a stated Ir loading of 75 wt % (Elyst Ir75,

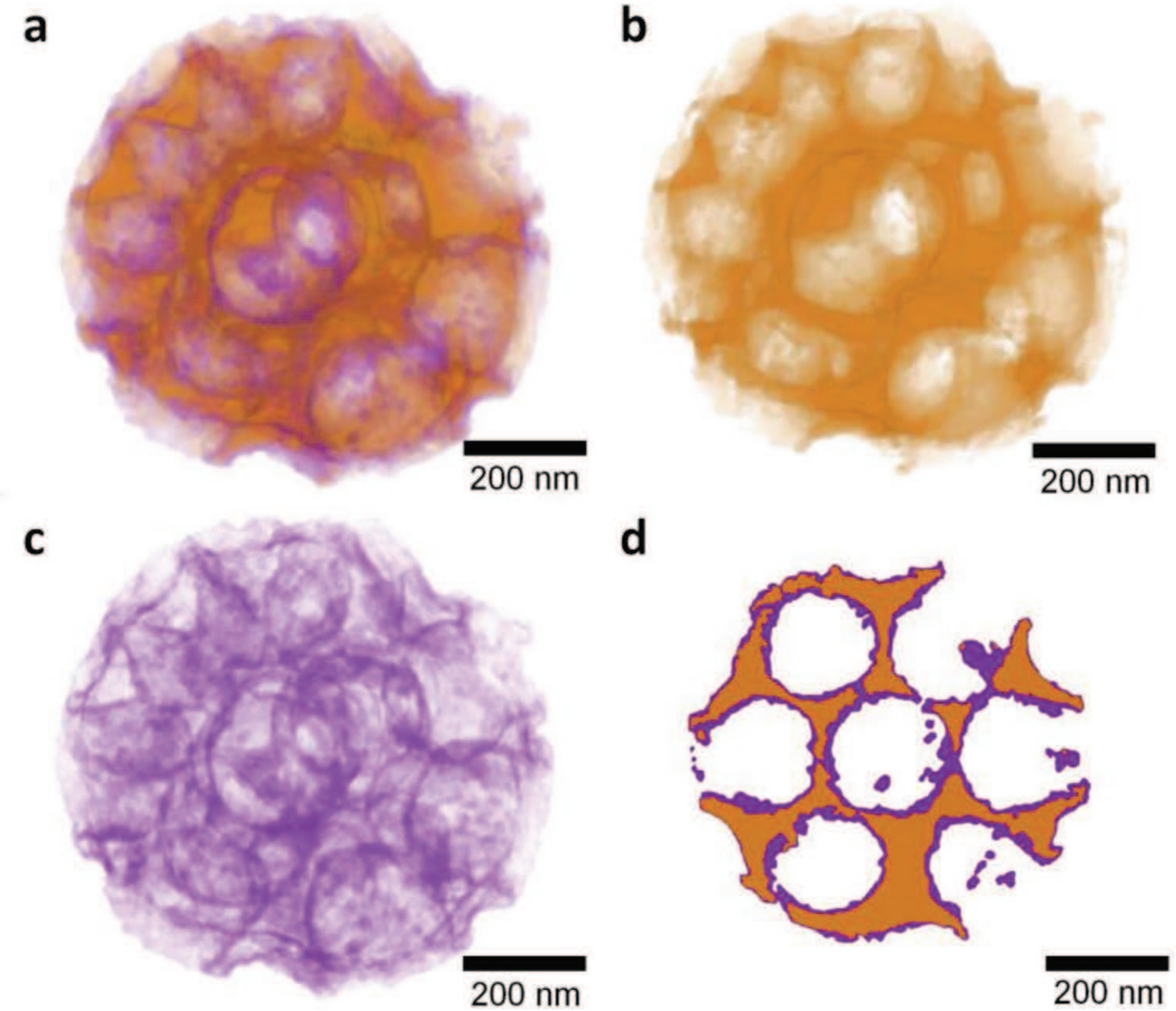

Figure 5.5: STEM-based tomography with 3D intensity volume reconstruction of IrO_2 nanoparticles supported on macroporous ATO microparticles templated by 280 nm PMMA (≈25 wt % Ir). a) Total (ATO and IrO_2) 3D intensity volume derived from particle reprojection. b) Extracted ATO 3D intensity volume from a complete particle. c) Extracted IrO_2 3D intensity volume from a complete particle. d) Extracted cross section of an IrO_2-coated ATO microparticle from the 3D intensity volume.

Umicore, Germany).[34] The significantly higher mass-based activity of the IrO_2/ATO versus the IrO_2/TiO_2 supported reference catalyst may at first be explained by an optimized dispersion of IrO_2 nanoparticles on the surface of the macroporous ATO resulting in a high catalytically accessible surface area. A further beneficial effect of the open macroporous morphology is an optimized mass transport through the catalyst layer enabling high current densities (Figure S22e,f, Supporting Information) without a limitation through pore clogging by evolving oxygen, which is a possible scenario for a micro- or mesoporous structure composed of aggregated nanoparticles. IrO_2 nanoparticles oxidized at a temperature of 375°C show a similar size of crystalline domains of tetragonal IrO_2 phase (≈ 2–3 nm) as the reference catalyst (≈ 4 nm), but a lower crystallinity

(Figure 2a and Figure S21, Supporting Information). According to Geiger et al., Ir(O_x) heated at ≈375°C is not fully crystalline but at the upper temperature range of an intermediate phase between the amorphous IrO_x and thermal IrO_2 with an increased intrinsic activity compared to the thermal oxide phase at the expense of a lower conductivity.[35] For comparison with the literature, the best performing ATO supported Ir-based catalyst reported to our knowledge are high surface area (≈260 $m^2\,g^{-1}$) mesoporous-ATO supported core–shell $IrNi_x$@IrO_x nanoparticles prepared by Nong et al., which were obtained by electrochemical leaching of respective supported $IrNi_x$ nanoparticles. The composite catalyst with a loading of ≈19 wt % Ir exhibits an OER activity of ≈90 A g_{Ir}^{-1} at an overpotential of 280 mV.[14]

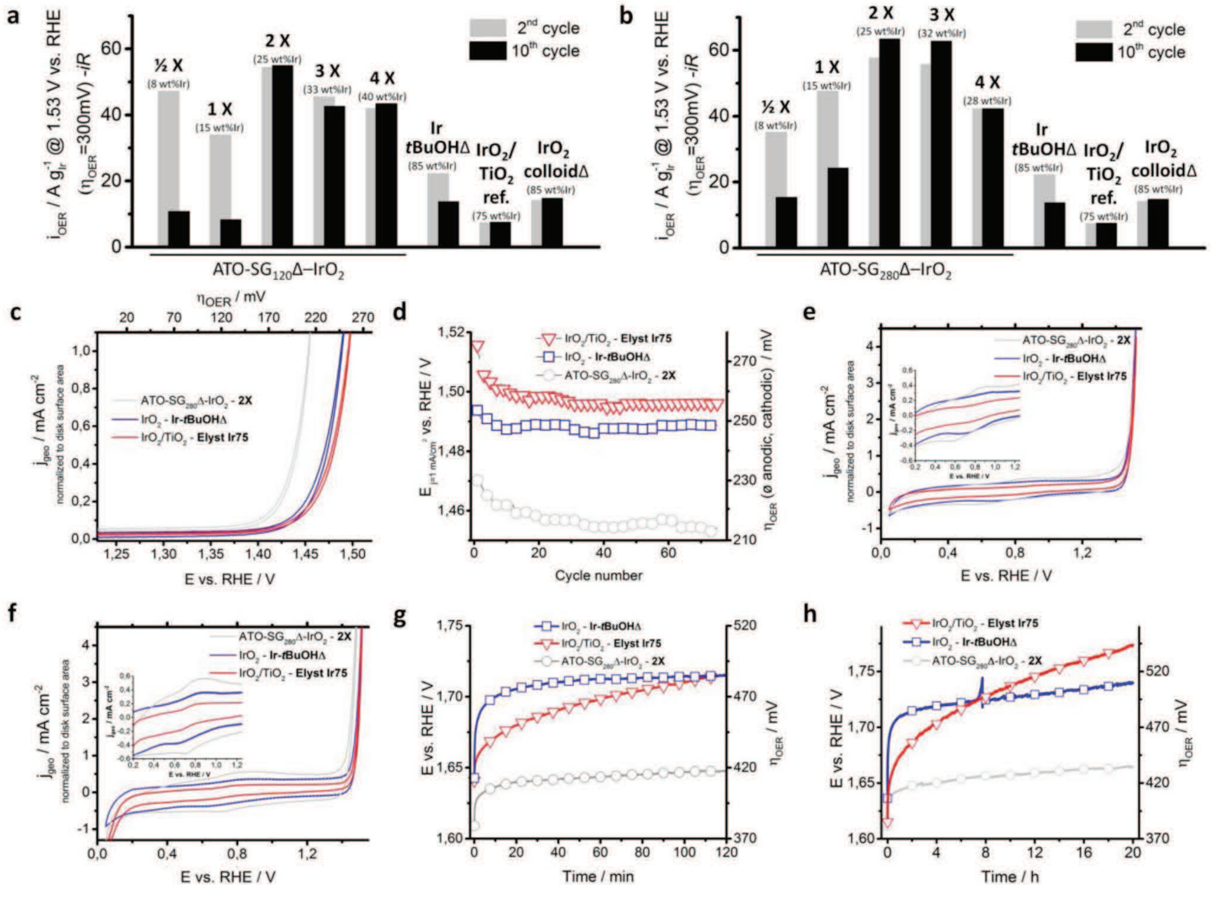

Figure 5.6: Electrochemical characterization of IrO_2 nanoparticles supported on macroporous ATO microparticles. Iridium mass-based catalytic activity of IrO_2 nanoparticle-loaded microparticles templated by a) 120 nm (ATO-SG120Δ-IrO_2) and b) 280 nm (ATO-SG280Δ-IrO_2) PMMA for ηOER = 300 mV. c–f) Rotating disc electrode (RDE) measurements of IrO_2 nanoparticles (Ir-tBuOHΔ, blue), 25 wt % Ir loaded ATO (ATO-SG280Δ-IrO_2-2X, gray) and commercial TiO_2-supported IrO_2 with 75 wt % Ir loading (IrO_2/TiO_2-Elyst Ir75, red). c) 75th scan cycle of RDE measurement with scan rate of 5 mV s^{-1}. d) Extracted overpotentials (ηOER) for each cycle required for 1 mA cm^{-2}. Cyclic voltammograms e) before and f) after 75 RDE cycles at a scan rate of 50 mV s^{-1}. Chronopotentiometry measurements at g) j = 10 mA cm^{-2} over 120 min and h) 20 h on FTO substrates with catalyst loading of 15 μg_{Ir}.

The reported 30 % higher initial activity of this catalyst as compared to our best performing sample is however obtained for a more compact structure, with a high volumetric Ir performance density disadvantageous for the application in PEM electrolyzers. Besides ATO supported catalysts, recently a nanostructured porous NTO with remarkably high conductivity of $\approx 440\,\mathrm{S}^{-1}$ was introduced by Hufnagel et al. to support a $\approx 1\,\mathrm{nm}$ thin IrO_2 coating based on atomic layer deposition. The thin film catalyst with a low Ir-loading of $\approx 8\,\mathrm{wt\,\%}$ thereby showed an onset potential of $\approx 250\,\mathrm{mV}$ and an OER activity of $\approx 654\,\mathrm{A\,g_{Ir}}^{-1}$ at an overpotential of 460 mV, as compared to an onset potential of $\approx 215\,\mathrm{mV}$ and an activity of over $3200\,\mathrm{A\,g_{Ir}}^{-1}$ for our catalyst at a slightly lower overpotential of 420 mV.[36] The best performing IrO_2 catalyst supported by mesoporous NTO with a surface area of $\approx 83\,\mathrm{m^2\,g^{-1}}$ was reported by Hu et al., with an onset potential as low as 200 mV for a 33 wt % Ir loaded catalyst. The maximum OER activity of $\approx 548\,\mathrm{A\,g_{Ir}}^{-1}$ at an overpotential of 362 mV was thereby measured for a 26 wt % Ir containing catalyst with an increased overpotential of 270 mV.[18] In comparison, our catalyst shows a significantly higher mass based activity of $\approx 1100\,\mathrm{A\,g_{Ir}}^{-1}$ at a slightly higher overpotential of 380 mV. The decreased activity of our introduced ATO-supported samples with low loading (8 and 15 wt % Ir) is attributed to an incomplete layer of IrO_2 nanoparticles on the porous ATO microparticle, whereas a complete layer is formed at 25 wt % Ir. As the conductivity of the ATO scaffold ($\approx 3.6\,\mathrm{S}^{-1}$, Figure S2, Supporting Information) is lower than that of a layer of IrO_2 nanoparticles of similar particle size ($\approx 26\,\mathrm{S}^{-1}$),[37] the absence of a continuous conducting pathway through the IrO_2 layer limits the performance. For the case of a the poor conductive TiO_2 support, Bernsmeier et al. have correlated catalyst conductivity for different Ir contents with the OER activity. They have demonstrated that the high performance values can be reached only for Ir loadings exceeding $\approx 25\,\mathrm{wt\,\%}$ Ir, while below this threshold value practically no activity was observed. Furthermore, a minimum in the electrical conductivity of $\approx 1.0 \times 10^{-3}\,\mathrm{S}^{-1}$ in the catalyst films is suggested to eliminate negative effects of slow electron transport on the catalytic performance.[38] The conductivity of the ATO scaffold used in our work exceeds this conductivity limit (as opposed to TiO_2), which explains the considerably high OER performance of our composite catalysts even at low Ir contents of 8 wt % and 15 wt % . To further investigate the slightly reduced performance of low Ir loaded (<25 wt % Ir) catalyst, the trend in the conductivity of loosely compressed powders of IrO_2/ATO catalyst with varying Ir content as well as the IrO_2/TiO_2 reference catalyst were measured (Figure S22 and Table S2, Supporting Information). The conductivity of the ATO/IrO_2 composite catalyst is rather low for low Ir loadings of 8 and 15 wt % Ir (1.00×10^{-6} and $1.79 \times 10^{-5}\,\mathrm{S}^{-1}$, respectively). The electrocatalytic activity of the samples is however very high, with the values equaling or even exceeding those of the commercial IrO_2/TiO_2 reference catalyst with much higher Ir loading (75 wt %) and much higher conductivity. The conductivity of the ATO/IrO_2 composite powders rises to $1.16 \times 10^{-2}\,\mathrm{S}^{-1}$ for the 25 wt % Ir sample (SG120Δ-IrO_2-2X). Higher iridium contents of 33 and 40 wt % further increase the conductivity up to a value of $0.88\,\mathrm{S}^{-1}$. In comparison, a value of 4.42 S^{-1} was determined for the commercial IrO_2/TiO_2 reference catalyst with 75 wt % Ir under same measurement conditions. Due to the low compressive force applied by the in house constructed dc-conductivity measurement setup (Figure S23, Supporting Information) and thus limited contact between particles across the powder-pellet thickness, the absolute values are expected to be significantly underestimated. However, the measurements performed in similar conditions enable to estimate a trend among the equally prepared samples series (Table S2, Supporting Information). As can be seen from the measured values, for the samples with Ir loading beyond 25 wt % (percolation threshold) the conductivity mainly depends on the Ir content, showing nearly linear dependence on the Ir loading. However, for the samples with very low Ir loadings below 25 wt % the conductivity of the support becomes a decisive factor, providing for a high electrocatalytic activity even without a direct contact between the IrO_2 nanoparticles. In total, there is no a linear correlation between the electrical conductivity and the electrocatalytic activity, as the commercial IrO_2/TiO_2 reference catalyst featuring the highest conductivity shows the lowest electrocatalytic activity among the investigated series. The effect of limited conductivity in the low-iridium-loading samples (1/2X and 1X with 8 and 15 wt % Ir, respectively) becomes pronounced at higher current densities as shown in Figure S22 (Supporting Information). However, at low overpotentials of ηOER $<$ 380 mV, eVen samples with low Ir loading possess an Ir mass-based activity comparable to the industrial TiO_2-supported reference despite a significantly reduced Ir content. To investigate OER kinetics, rotating disc electrode (RDE) measurements of selected catalyst samples were performed under controlled reaction conditions (1600 rpm, 60°C , O_2- purged electrolyte). The TiO_2-supported IrO_2 reference (Elyst Ir75) exhibits an overpotential of 258 mV, Ir tBuOHΔ requires a slightly lower overpotential of 250 mV and the ATO microparticle- supported IrO_2 nanoparticles require only an overpotential of 215 mV to reach an OER current of 1 mA cm^{-2} in the 75th scan cycle (Figure 5c,d and for more details, see Figure S24 in the Supporting Information). The RDE performance data thus confirm the synthesis of highly OER-active IrO_2 nanoparticles by the multistep synthesis introduced in this work and furthermore emphasize the importance of a nanostructured conductive support that can enhance the catalytic activity due to a high volume dispersion of the active iridium oxide nanoparticle phase. To investigate possible electrochemical side reactions, cyclic voltammograms of ATO-supported IrO_2 were recorded over a broad potential range between the hydrogen evolution reaction (HER) and OER onset potentials (0.05–1.52 V vs. RHE) before and after each RDE activity measurement (Figure 5e,f, respectively). For all samples a very broad redox peak centered around 0.8 V versus RHE attributed to the Ir(III)/Ir(IV) redox reactionßcitepap39,pap40 can be observed with increasing intensities in the order TiO_2/IrO_2 reference < Ir tBuOHΔ < ATO-SG280Δ-IrO_2-2X. After the RDE activity measurements, the intensity of the aforementioned feature has notably increased for all samples (for more details, see Figures S24 and S25 in the Supporting Information). We assign this increase to a redox surface activation of the crystalline (thermal) iridium oxide in the first few cycles [39] with the formation of a highly catalytically active surface hydroxide layer. [40] This results in an increase in OER activity as seen by a decline of the required overpotentials during the early CV cycles in Figure 5d or by a shift of the CV curves shown in Figure S24 (Supporting Information). Finally, the short (Figure 5g: 120 min) and intermediate term (Figure 5h: 20 h) corrosion behavior of the IrO_2 nanoparticle- based supported catalyst was investigated by chronopotentiometry measurements at a current density of $10\,mA\,cm^{-2}$. Unsupported IrO_2 nanoparticles (Ir tBuOH Δ) display a required potential of 1.72 V versus RHE remaining constant over the measurement period. For ATO-supported particles (ATO-SG280Δ-IrO_2-2X) the potential is lower by ≈ 70 mV at 1.65 V versus RHE. The TiO_2-supported reference catalyst (Elyst Ir75) shows a slight increase in the potential over the measurement period up to 1.72 V versus RHE after 120 min, matching that of unsupported IrO_2 nanoparticles. However, intermediate term measurements show the same trend for unsupported as well as ATO-supported IrO_2 nanoparticles, with only a slight increase in potential to 1.74 and 1.66 V versus RHE after 20 h, respectively. In contrast to the catalyst particles with the conducting ATO support, the potential of TiO_2-supported IrO_2 reference catalyst constantly rises with time and reaches the highest measured end potential with 1.77 V versus RHE after 20 h in the chronopotentiometric measurement, which indicates a lower activity and stability as compared to the IrO_2 nanoparticle catalysts introduced in this work. Small differences in the absolute potential obtained by the 120 min versus 20 h measurement period indicated by an offset of the V–t curves are thereby attributed to slightly varying amounts of catalyst coated onto the FTO substrate. Deviations of the slope of the curves as visible for the TiO/IrO_2 reference however may originate from a slightly altered catalyst dissolution during the two different experiments, as manifested by a detachment of active material from the electrode. Electron microscopy of catalyst samples after OER measurements (Figure S26, Supporting Information) further confirms a rather stable iridium content in the electrodes for a chronopotentiometric current density of $10\,mA\,cm^{-2}$ (20 h) and $100\,mA\,cm^{-2}$ (1.5 h), amounting to 24 and 23 wt % Ir, respectively, for the ATO-SG280Δ-IrO_2-2X sample with an initial Ir-loading of 25 wt % . Contrarily, analysis of the antimony content indicates a leaching process during the OER at the applied potentials shown by a reduction from initially ≈ 4.3 at % Sb (Figure 1a) to below 3 at % Sb after the OER experiments (Figure S26, Supporting Information). The stability of ATO as a catalyst support for proton exchange membrane fuel cells has been discussed in the literature. [41–43] Surface segregation of antimony caused by the preparation method [41] or by potential cycling [43] were discussed to lead to Sb-dissolution in an acidic environment. This results in a reduced conductivity of the surface of the obtained core–shell structure that can directly affect the electrocatalytic performance of attached catalyst nanoparticles. [43] Geiger et al. [44] recently investigated the corrosion stability of tin-oxide based catalysts (ATO, ITO, FTO) in acidic media and under applied potentials. They could show that these materials (dopants and SnO_2 host structure) possess a critical dissolution rate under cathodic potential. But also the anodic potential range for the thermodynamic stability of ATO is reported to be limited to theoretically 1.1 V versus RHE with measured critical Sb- and related Sn-dissolution upon anodic polarization,[44] rendering the material inappropriate for an industrial long-term application at high potentials and current densities. For an adoption of this model system for industrial use a more oxidation stable conductive oxide support such as fluorine- doped tin oxide (corrosion stable up to 2.7 V vs RHE)[44] or niobium-doped TiO_2 may therefore be employed. The overall high Ir mass-based activity of the synthesized iridium oxide catalyst is attributed to the small size of the spherical IrO_2 nanoparticles obtained by the synthesis approach and the low-temperature calcination that is known to result in an increased fraction of high-surface-energy crystal facets and defects which are associated with high OER activity.[45] However, the key factor for increased OER activity is the high Ir volume dispersion resulting from the homogeneous coating of nanoparticles onto the surface of the ordered porous conducting support. Catalysts prepared by the introduced multistep synthesis procedure provide two complementary current transmission pathways from the electrode contact to the reaction interface and thereby limit the series resistance and ensure electrical contact to nanoparticles of the catalytically active phase. The comparably small mass-specific charge for the corresponding redox feature of the IrO_2/TiO_2 reference is attributed to a higher degree of crystallinity and slightly larger crystalline domain sizes of the thermal oxide resulting in a comparably low redox-active surface area with iridium being stable in the +IV oxidation state. The unsupported IrO_2 nanoparticles (Ir tBuOHΔ) as well as the ATO-supported nanoparticles (ATOSG280Δ-IrO_2-2X) oxidized at a low temperature possess small crystalline domains (Figures 2 and 3) and a moderate degree of crystallinity (as shown in Figure 2a and Figure S10, Supporting Information), therefore exhibiting an increased redoxactive surface. For the well-dispersed IrO_2 nanoparticles on the porous ATO scaffold the accessible redox-active surface area is further increased as indicated by the increased mass-specific charge (Figure 5e,f).

5.4 Conclusion

This work introduces a multistep synthesis procedure for the homogeneous decoration of complex porous Sb-doped SnO_2 structures as an example for a conductive oxidic OER catalyst support for iridium nanoparticles in the range of 2–3 nm. Detailed structural characterization of the synthesized inverse opal macroporous ATO-microparticle/Ir(O_2) model catalyst system thereby shows how to independently tune the morphology, porosity, and conductivity of an oxide support material through the ultrasonic spray pyrolysis of a sol–gel or nanoparticle precursor. Furthermore, the ATO/IrO_2 catalyst was thoroughly investigated by high-resolution (S)TEM imaging, which allowed for a detailed analysis of the catalyst particle distribution within the porous 3D structure by means of STEM tomography. An approximation of the iridium volume dispersion in a thin film of porous microparticles returns a roughly 18 times lower iridium volume density than for a TiO_2-supported reference catalyst; this would allow for the fabrication of PEM electrolyzer anodes with strongly reduced Ir loading and retention of the film thickness required for electrolyzer operation. The ATO-microparticle/IrO_2 catalyst with 25 wt % Ir furthermore shows improved OER activity and stability compared to similarly prepared pure IrO_2 nanoparticles, presumably due to the homogeneous dispersion and stabilization of the small IrO_2 particles on the ATO surface. The model catalyst system shown here significantly outperformed an industrial TiO_2-supported IrO_2 catalyst in Ir mass-based OER activity, underlining the advantage of a suitable oxide support morphology and a homogeneous distribution of the active material on a conductive support. On the other hand, even lower iridium loadings ($\leq$15 wt % Ir) on the macroporous microparticle scaffold result in considerably lower catalytic performance, suggesting a major current transport pathway through the iridium oxide nanoparticle layer which is lacking in samples with a very low Ir-loading in which the nanoparticles do not form a continuous layer. This emphasizes the need for a highly conductive support to effectively contact isolated catalyst nanoparticles. Overall, this study shows that combining iridium oxide nanoparticles with a suitable conductive and rationally designed porous oxide promises to be a suitable approach toward highly active anodes for PEM electrolyzers with drastically reduced iridium loading and increased long term stability.

5.5 Experimental Section

Synthesis of Macroporous ATO Microparticles (Oxidic Catalyst Support) by Spray Drying: The synthesis of macroporous ATO microparticles by USP is based on the USP synthesis of macroporous silica particles with polymer bead templating initially proposed by Iskandar et al.[46] and later modified by Hieda et al.[23] to obtain macroporous (Sb-doped) SnO_2 microparticles. For the synthesis of sol–gel based macroporous antimony doped tin-oxide microparticles, first antimony (III) acetate (224 µmol/67 mg, SIGMA-ALDRICH, 99.99 % trace metals basis) was dissolved in ethanol (4 mL) by stirring for 1 h. The antimony solution was slowly added to 1.14 g (4.376 mmol) tin (IV) chloride (SIGMA-ALDRICH, 98 % purity) under constant stirring. Possibly precipitated solids were dissolved by further stirring and by using an ultrasonic bath for 5 min. Finally, an aqueous PMMA bead colloid (120 or 280 nm, respectively) was added to the precursor solution to obtain a final polymer bead content of 5.85 wt % and a total metal–salt concentration of 180×10^{-3} m. The synthesis of PMMA beads with mean diameters of 280 and 120 nm was conducted according to the emulsion polymerization route described elsewhere resulting in an aqueous colloidal solution[47,48] (see the Supporting Information for further details). The in-house constructed spray pyrolysis setup consists of a T-shaped high-temperature polypropylene discharge pipe system (OSTENDORF KUNSTOFFE) that connects the carrier gas flow (laboratory pressured air) at a flow rate of $\approx 60\,\mathrm{L\,h^{-1}}$ to a 45 cm long quartz tube (25 mm diameter) placed in a single zone tube furnace (EUROTHERM 2404 temperature controller) with a temperature set point of 615°C (609°C oven temperature). The lower part of the pipe system including the precursor solution was sealed with a thin three-layer polyethylene cling film (TOPPITS) versus a water filled beaker with a 1.7 MHz FULOON 24V DC (700 mA, max. 400 mL aerosol $\mathrm{h^{-1}}$) household ultrasonic nebulizer (SHENZEN KULETONG TECHNOLOGY CO LTD) placed inside. Aerosol collection was achieved with an in-house constructed filter system with polytetrafluoroethylene (PTFE) inset (50 mm diameter RCT-BIOFIL-PX-SU, 0.65 µm pore size, 60 µm thickness, REICHELT CHEMIETECHNIK GMBH + CO). The obtained ATO powder was calcined at 450°C in air for 5 h with a heating rate of 1.4°C $\mathrm{min^{-1}}$ to finish thermal curing and remove residual carbon traces. The spray pyrolysis of porous ATO based on a presynthesized ATO nanoparticle precursor followed the synthesis of nanoparticle-based titanium oxide microparticles proposed by Iskander et al.[49] Highly conducting, 4.5 at % Sb-doped tin oxide nanoparticles with a size of about 3 nm were solvothermally synthesized in tert-butanol according to literature.[25] ATO nanoparticle (3–4 nm) powder (200 mg) was dispersed in a mixture of ethanol (2.8 mL) and hydrochloric acid (37 wt % , 0.16 mL) by stirring for 2 h. The dispersion was mixed with an aqueous PMMA bead colloid (120 nm mean diameter) to obtain a 2 wt % dispersion of ATO/PMMA. After 15 min sonication and further stirring for 2 h, the spray drying was performed according to the synthesis of sol–gel based ATO particles with a furnace temperature of 500°C . The obtained product was further processed according to the method used for the sol–gel based microparticles. Synthesis of Colloidal $\mathrm{IrO_x}$ Catalyst Nanoparticles (Ir Active Phase Precursor): The synthesis of an iridium oxide nanoparticle colloid is based on an aqueous oxidation method introduced by Sutto[26] with a further solvothermal treatment in tert-butanol introduced by Szeifert et al.[50] For the synthesis of an iridium oxide nanoparticle colloid per reaction 0.075 mmol (30.09 mg) iridium (III) chloride hydrate (SIGMA-ALDRICH, 99 % reaction grade) were dissolved in 4 mL bidistilled water (Millipore Q grade) and stirred for 1 h in air at room temperature. Subsequently the precursor solution was cooled with an ice bath and 0.5 mmol (35.5 mg) potassium superoxide powder ($\mathrm{KO_2}$, ABCR, 96.5 % purity) was slowly added to the cooled solution within 1 min under continuous stirring and quenched after 1 min by addition of 2.5 mL of precooled methanol (analytical grade). For the synthesis of ATO supported $\mathrm{IrO_x}$ catalyst or the synthesis of unsupported Ir catalyst the obtained yellow-green $\mathrm{IrO_x}$ nanoparticle colloid was either used after 30 min stirring time or further stirred overnight which resulted in the formation of a blue $\mathrm{IrO_x}$ colloid. Conformal Coating of Oxidic Support (ATO Microparticles) with Ir Nanoparticles by Solvothermal Reduction in tBuOH: The solvothermal treatment of synthesized $\mathrm{IrO_x}$ colloid was performed in glass-lined stainless steel autoclaves (Parr Series 4760 FH, PARR INSTRUMENT COMPANY). For the synthesis of unsupported Ir catalyst nanoparticles, per autoclave reaction 37.5–300 µmol previously prepared $\mathrm{IrO_x}$ colloid were added to 90 mL of prewarmed (60°C) tert-butanol (GRÜSSING GMBH, 99 % purity). An additional amount of water and methanol at a volume ratio of 2:1 were added to obtain a final volume of 180 mL. The solvothermal loading of macroporous ATO scaffold (0.49 mmol, 75 mg) microparticles with iridium nanoparticles was achieved by the reduction of iridium oxide colloid nanoparticles in the presence of dispersed scaffold microparticles during the solvothermal reaction in tert-butanol. Sealed autoclaves with internal temperature and pressure sensor were heated to 175°C for 12 h with a temperature controlled (HEJU LTR2500, JUCHHEIM GMBH & CO. KG) ceramic heating mantle (KJT 950W) and kept under constant stirring. The reaction product was washed by centrifugation (7197 rcf, 15 min) with bidistilled water (Millipore Q grade, 18 MΩ). The product was redispersed in a few mL bidistilled H_2O and freeze-dried using an ALPHA 1-4 machine (MARTIN CHRIST GEFRIERTROCKNUNGSANLAGEN GMBH). Obtained powders of Ir nanoparticle loaded ATO scaffolds were characterized, used for the preparation of electrodes and further electrochemical measurements or calcined to obtain IrO_x nanoparticle coated porous ATO scaffold. Calcination of Ir nanoparticles and Ir-NP@porous-ATO-microparticles (solvothermally treated IrO_x colloid) was performed in a NABERTHERM laboratory oven (model N15/65SHA) at 375°C in air with a heating rate of 1.94°C min^{-1} and a dwell time of 1 h. Physicochemical Characterization: Wide-angle X-ray diffraction analysis was carried out in transmission mode using a STOE STADI P diffractometer with Cu $K_{\alpha 1}$ radiation ($\lambda = 1.54060$ Å) and a Ge(111) single crystal monochromator equipped with a DECTRIS solid state strip detector Mythen 1K. Powder XRD patterns of the samples were collected with an omega-2theta scan in the 2ϑ range from 5° to 90° with a step size of 1° and fixed integration time of 25–35 s per step and a resolution of 0.05°. The size of the crystalline domains was calculated from the XRD patterns for the Ir 111 (ICDD#00-006-0598), IrO_2 112 (ICDD#00- 015-0870), and SnO_2 110 (ICDD#00-041-1445) reflection, respectively, using the Scherrer equation. Raman spectroscopy was carried out using a LabRAM HR UV–Vis (HORIBA JOBIN YVON) Raman Microscope (OLYMPUS BX41) with a SYMPHONY CCD detection system and a He–Ne laser ($\lambda = 633$ nm). Spectra were recorded using a lens with a 10-fold magnification in the range from 100 to 1000 $^{-1}$ with filters of OD 0.3–0.6. Spectrum accumulation mode was used with integration times of 30 s per spectrum and 600 cycles. The data acquisition was carried out with LabSpec software. HR-TEM and HAADF-STEM images as well as electron diffraction patterns were recorded using a FEI Titan Themis 80–300 transmission electron microscope with aberration correction of the probe-forming lenses operated at 120 kV or 300 kV, respectively. EDX was performed using a SuperX windowless, four quadrant Silicon drift detector with a solid angle of 0.7 sr. TEM specimens were prepared by dispersing IrO_x colloids, catalyst nanoparticles, or Ir loaded ATO microparticles respectively in a 1:1 (v:v) ratio of water to ethanol and depositing them on a carbon-film coated copper grid, followed by drying in air. HAADF-STEM tilt series of 29 images for TEM tomography were recorded in 5° steps from –70° to +70°. For a reconstruction of the 3D intensity volume and a presentation of different phases of Ir and ATO, respectively, a masked simultaneous iterative reconstruction technique (SIRT) with further refinement by a discrete algebraic reconstruction technique (DART) were employed (see the Supporting Information for further details). SEM images were obtained with a FEI Helios Nanolab G3 UC scanning electron microscope equipped with a field emission gun operated at 3–5 kV. SEM specimens were prepared by dispersing dried catalyst nanoparticles, microparticles, and composites in a (1:1 v/v) water to ethanol ratio on FTO or Si substrates that were glued onto a stainless-steel sample holder with silver lacquer. EDX measurements were performed at an operating voltage of 20 kV with a X-MaxN Silicon Drift Detector with 80 mm^2 detector area (OXFORD INSTRUMENTS) and AZTec acquisition software (OXFORD INSTRUMENTS). For the analysis of the porosity of the samples, the calcined samples were degassed for 12 h at 120°C under vacuum. Nitrogen sorption measurements were performed on a QUANTACHROME Autosorb-1 instrument at the boiling point of liquid nitrogen (77 K). The specific surface area was determined with the Brunauer–Emmett–Teller (BET) method at p/p0 = 0.05–0.2. The pore size distribution was calculated using a nonlocal DFT equilibrium model for silica with cylindrical pores. XPS analysis was conducted with the non-monochromated Mg Kα radiation of a VSW TA10 X-ray source and a VSW HA100 hemispherical analyzer. For the XPS measurements the nanoparticles were drop-casted on silicon substrates in air bevor the transfer to the UHV chamber. Peaks were fitted using a convolution of a Doniach–Šunjic ́-function[53] and a Gaussian function with linear background subtraction. If possible, the carbon 1s peak was calibrated to 284.8 eV to compensate for charging effects. An Ir 4f7/2 core electron binding energy of 60.8 eV was assigned to metallic Ir(0) and an Ir 4f7/2 binding energy of 61.9 eV was assigned to Ir(iv)O_2.[32] Conductivity measurements of macroporous ATO microparticles were carried out on an HMS 3000 apparatus (ECOPIA) in the Van der Pauw geometry (5 mm separation of electrodes). Powder samples were measured in form of pellets that were compressed for 10 min at 150 kg cm^{-2}. Conductivity measurements of ATO/IrO_2 and commercial TiO_2 supported reference catalyst were conducted due to restrictions on sample volume on an in-house constructed dc-conductivity measurements cell on loosely compressed powders by recording I–V curves between –5 to +5 V by an AUTOLAB 302N. Electrochemical Characterization: Unsupported IrO_x, IrO_2 nanoparticles and ATO supported IrO_2 nanoparticles were dispersed in 1:1 (v/v) H_2O to isopropanol and drop-casted onto conducting FTO glass or Au-coated QCM sensors (14 mm, 5 and 10 MHz AT-cut Cr/ Au crystals from KVG QUARTZ CRYSTAL TECHNOLOGY GMBH and QUARTZ PRO AB). Electrodes were masked with PTFE tape to leave a circular electrode area of 0.196 and 0.126 cm^2, respectively. Prior to each measurement, the samples were either dried at 60°C or calcined at 375°C in air. The frequency of uncoated and coated QCM sensor crystals was determined with a QCM200 5 MHz measurement system (STANFORD RESEARCH SYSTEMS INC.) and an openQCM 5/10 MHz measurement system (NOVAETECH SRL). Deposited mass loadings on QCM chips were calculated according to the Sauerbrey equation [51] from determined frequency differences Δf, an overlapping electrode area A of 0.196 cm^2 and a sensitivity factor Cf of 56.6 and 4.4 Hz μg^{-1} cm^2 for 5 and 10 MHz AT-cut crystals, respectively. All electrochemical measurements at room temperature were carried out in a three-electrode setup with a quartz cell filled with 20 mL 0.5 m H_2SO_4 (SIGMA-ALDRICH, Titripur volumetric standard) as electrolyte using an PGSTAT302N potentiostat/galvanostat (METROHM AUTOLAB B.V.) equipped with a FRA32 M impedance analyzer connected to a Hydroflex reversible hydrogen electrode (GASKATEL Gesellschaft für Gassysteme durch Katalyse und Elektrochemie mbH) or Hg/$HgSO_4$/K_2SO_4 (sat.) (REF601, RADIOMETER ANALYTICALHACH COMPANY) for cyclic voltammetry and chronopotentiometry measurements, respectively. The electrochemical activity of catalysts on FTO and QCM substrates was measured by iR-drop corrected linear sweep voltammetry (LSV) in a potential window of 1.0–1.8 V versus RHE and 1.0–1.65 V versus RHE, respectively, in 10 scan cycles with a scan rate of 10 mV s^{-1}. Impedance spectroscopy data at 0.5 V versus RHE was recorded prior to each measurement to determine the corresponding electrolyte resistance (95 %) from the high frequency region. Iridium mass-based catalyst activity was either directly calculated with measured QCM determined mass loadings or calculated from the coating volume (3–15 µL) of a dispersion of known concentration (2 mg mL^{-1}) in combination with the Ir ratio in ATO/Ir(O_2) catalysts determined by SEM/EDX (mean value of at least three independent measurements). Current densities were determined from the mean value of capacity current-corrected (mean current in the potential region 1.0–1.23 V vs. RHE) anodic and cathodic scans of the respective LSV cycle. Stability measurements of electrodes (active material corresponding to 15 μg_{Ir} (76 μg_{Ir} cm^{-2}) deposited on FTO glass substrates) were performed with an Hg/$HgSO_4$/K_2SO_4(sat.) reference electrode at room temperature under constant stirring of the electrolyte. Potentials versus the reversible hydrogen electrode ERHE were calculated by measuring the open circuit potential of the Hg/$HgSO_4$/K_2SO_4(sat.) reference electrode against a Hydroflex RHE (GASKATEL Gesellschaft für Gassysteme durch Katalyse und Elektrochemie mbH) before and after each chronopotentiometry measurement and by shifting the measured potential accordingly. RDE measurements were conducted with an MSR Electrode rotator with mirror finished polished 5 mm diameter glassy carbon disc insets (PINE RESEARCH INSTRUMENTATION) connected to an Autolab PGSTAT302N potentiostat/galvanostat equipped with a FRA32 M impedance analyzer (METROHM AUTOLAB B.V.) and an in-house constructed glass/silicone cell with Luggin-capillary for the reference electrode compartment. Electrolyte temperature of 60°C was maintained by an oil bath with external stirrer and monitored with an immersed silicone coated K-element temperature sensor. The Nernst potential for water oxidation was kept constant by continuous O_2 (AIR LIQUIDE, AlphaGaz 2 N5 purity) purging of the electrolyte (0.5 m H_2SO_4, SIGMAALDRICH, Titripur volumetric standard). Catalyst loadings of 50 μg_{Ir} cm^{-2} (10 μg_{Ir} per disc) were drop-casted on cleaned glassy carbon discs and dried at 60°C before applying 10 µL of a 1:100 dilution of a Nafion perfluorinated resin solution (SIGMA-ALDRICH, 5 wt % in lower aliphatic alcohols and water (15–20 % water)) in a H_2O/iPrOH mixture (1:1 v/v). The electrolyte resistance was determined before and after each RDE measurement in the high frequency region of recorded impedance spectra at 0.5 V versus RHE. Due to low current densities reached in the measurement protocol and repeatedly low electrolyte resistance values around 5 Ω, an iR drop correction of the recorded data was not performed. The applied measurement protocol consisted of 75 LSV cycles starting from 1.0 V versus RHE. The upper vertex potential was defined to be at a current density of $j = 1\,\mathrm{mA\,cm^{-2}}$ (iabs = 0.2 mA, A = 0.196 $\mathrm{cm^2}$). Reported current densities were determined from the mean value of capacity current (mean value in potential region 1.0–1.23 V vs. RHE) corrected anodic and cathode scans for a given overpotential ηOER of the respective scan cycle. Extracted overpotentials ηOER for each cycle required to reach an OER current of 1 $\mathrm{mA\,cm^{-2}}$ were corrected for the capacitive current and calculated as a mean of anodic and cathodic scan. Additional cyclic voltammetry measurements over the potential range of 0.05–1.52 V versus RHE were performed during RDE measurements to identify redox active features and to compare the electrocatalytically active surface area of catalyst samples. 3 cyclic voltammograms at a scan rate of 50 $\mathrm{mV\,s^{-1}}$ were therefore recorded prior to each RDE measurement (as described above), after 50 and after 75 RDE LSV cycles.

Bibliography

[1] S.-i. Inage. *Wiley Interdisciplinary Reviews: Energy and Environment*, **2015**. *4*(1), 115–132.

[2] N. Armaroli & V. Balzani. *ChemSusChem*, **2011**. *4*(1), 21–36.

[3] F. Barbir. *Solar Energy*, **2005**. *78*(5), 661–669.

[4] C. Hagelüken. *Competition and Conflicts on Resource Use, Natural Resource Management and Policy*, volume 46. **2015**.

[5] K. E. Ayers, C. Capuano & E. B. Anderson. *ECS Transactions*, **2012**. *41*(10), 15–22.

[6] N. Danilovic, R. Subbaraman, K.-C. Chang, S. H. Chang, Y. J. Kang, J. Snyder, A. P. Paulikas, D. Strmcnik, Y.-T. Kim, D. Myers, V. R. Stamenkovic & N. M. Markovic. *The Journal of Physical Chemistry Letters*, **2014**. *5*(14), 2474–2478.

[7] M. Bernt & H. A. Gasteiger. *Journal of The Electrochemical Society*, **2016**. *163*(11), F3179–F3189.

[8] M. Carmo, D. L. Fritz, J. Mergel & D. Stolten. *International Journal of Hydrogen Energy*, **2013**. *38*(12), 4901–4934.

[9] E. Oakton, D. Lebedev, M. Povia, D. F. Abbott, E. Fabbri, A. Fedorov, M. Nachtegaal, C. Copéret & T. J. Schmidt. *ACS Catalysis*, **2017**. *7*(4), 2346–2352.

[10] U. Babic, M. Suermann, F. Büchi, L. Gubler & T. Schmidt. *Journal of The Electrochemical Society*, **2017**. *164*, F387–F399.

[11] J. E. Park, S. Kim, O.-H. Kim, C.-Y. Ahn, M.-J. Kim, S. Y. Kang, T. I. Jeon, J.-G. Shim, D. W. Lee, J. H. Lee, Y.-H. Cho & Y.-E. Sung. *Nano Energy*, **2019**. *58*, 158–166.

[12] M. Faustini, M. Giraud, D. Jones, J. Rozière, M. Dupont, T. R. Porter, S. Nowak, M. Bahri, O. Ersen, C. Sanchez, C. Boissière, C. Tard & J. Peron. *Advanced Energy Materials*, **2019**. *9*(4), 1802136.

[13] H.-S. Oh, H. N. Nong & P. Strasser. *Advanced Functional Materials*, **2015**. *25*(7), 1074–1081.

[14] H. N. Nong, H.-S. Oh, T. Reier, E. Willinger, M.-G. Willinger, V. Petkov, D. Teschner & P. Strasser. *Angewandte Chemie*, **2015**. *127*(10), 3018–3022.

[15] H. Yoo, K. Oh, Y. R. Lee, K. H. Row, G. Lee & J. Choi. *International Journal of Hydrogen Energy*, **2017**. *42*(10), 6657–6664.

[16] C. Hao, H. Lv, Q. Zhao, B. Li, C. Zhang, C. Mi, Y. Song & J. Ma. *International Journal of Hydrogen Energy*, **2017**. *42*(15), 9384–9395.

[17] V. K. Puthiyapura, S. Pasupathi, H. Su, X. Liu, B. Pollet & K. Scott. *International Journal of Hydrogen Energy*, **2014**. *39*(5), 1905–1913.

[18] W. Hu, S. Chen & Q. Xia. *International Journal of Hydrogen Energy*, **2014**. *39*(13), 6967–6976.

[19] S. Trasatti. *Electrochimica Acta*, **2000**. *45*(15-16), 2377–2385.

[20] S. M. Alia, B. Rasimick, C. Ngo, K. C. Neyerlin, S. S. Kocha, S. Pylypenko, H. Xu & B. S. Pivovar. *Journal of The Electrochemical Society*, **2016**. *163*(11), F3105–F3112.

[21] H.-S. Oh, H. N. Nong & P. Strasser. *Advanced Functional Materials*, **2015**. *25*(7), 1074–1081.

[22] C. Hao, H. Lv, C. Mi, Y. Song & J. Ma. *ACS Sustainable Chemistry & Engineering*, **2016**. *4*(3), 746–756.

[23] K. Hieda, T. Hyodo, Y. Shimizu & M. Egashira. *Sensors and Actuators B: Chemical*, **2008**. *133*(1), 144–150.

[24] S. Y. Lee, L. Gradon, S. Janeczko, F. Iskandar & K. Okuyama. *ACS nano*, **2010**. *4*(8), 4717–4724.

[25] K. Peters, P. Zeller, G. Stefanic, V. Skoromets, H. Němec, P. Kužel & D. Fattakhova-Rohlfing. *Chemistry of Materials*, **2015**. *27*(3), 1090–1099.

[26] T. E. Sutto. *Inorganic chemistry*, **2014**. *53*(9), 4570–4578.

[27] A. Minguzzi, C. Locatelli, O. Lugaresi, E. Achilli, G. Cappelletti, M. Scavini, M. Coduri, P. Masala, B. Sacchi, A. Vertova, P. Ghigna & S. Rondinini. *ACS Catalysis*, **2015**. *5*(9), 5104–5115.

[28] S. Cherevko, S. Geiger, O. Kasian, A. Mingers & K. J. Mayrhofer. *Journal of Electroanalytical Chemistry*, **2016**. *774*, 102–110.

[29] S. Cherevko, T. Reier, A. R. Zeradjanin, Z. Pawolek, P. Strasser & K. J. Mayrhofer. *Electrochemistry Communications*, **2014**. *48*, 81–85.

[30] A. V. Korotcov, Y.-S. Huang, K.-K. Tiong & D.-S. Tsai. *Journal of Raman Spectroscopy*, **2007**. *38*(6), 737–749.

[31] Y. S. Huang, S. S. Lin, C. R. Huang, M. C. Lee, T. E. Dann & F. Z. Chien. *Solid State Communications*, **1989**. *70*(5), 517–522.

[32] S. J. Freakley, J. Ruiz-Esquius & D. J. Morgan. *Surface and Interface Analysis*, **2017**. *49*(8), 794–799.

[33] K. W. Desmond & E. R. Weeks. *Physical review. E, Statistical, nonlinear, and soft matter physics*, **2014**. *90*(2), 022204.

[34] S. A. Lopez M & B. P. *Patent*, **2004**.

[35] S. Geiger, O. Kasian, A. M. Mingers, K. J. J. Mayrhofer & S. Cherevko. *Scientific Reports*, **2017**. *7*(1), 4595.

[36] A. G. Hufnagel, S. Häringer, M. Beetz, B. Böller, D. Fattakhova-Rohlfing & T. Bein. *Nanoscale*, **2019**. *11*, 14285–14293.

[37] J. Lim, D. Park, S. S. Jeon, C.-W. Roh, J. Choi, D. Yoon, M. Park, H. Jung & H. Lee. *Advanced Functional Materials*, **2018**. *28*(4), 1704796.

[38] D. Bernsmeier, M. Bernicke, R. Schmack, R. Sachse, B. Paul, A. Bergmann, P. Strasser, E. Ortel & R. Kraehnert. *ChemSusChem*, **2018**. *11*(14), 2367–2374.

[39] S. Fierro, L. Ouattara, E. H. Calderon & C. Comninellis. *Electrochemistry Communications*, **2008**. *10*(6), 955–959.

[40] D. F. Abbott, D. Lebedev, K. Waltar, M. Povia, M. Nachtegaal, E. Fabbri, C. Copéret & T. J. Schmidt. *Chemistry of Materials*, **2016**. *28*(18), 6591–6604.

[41] E. Fabbri, A. Rabis, R. Kötz & T. J. Schmidt. *Physical Chemistry Chemical Physics*, **2014**. *16*(27), 13672–13681.

[42] G. Cognard, G. Ozouf, C. Beauger, G. Berthomé, D. Riassetto, L. Dubau, R. Chattot, M. Chatenet & F. Maillard. *Applied Catalysis B: Environmental*, **2017**. *201*, 381–390.

[43] G. Cognard, G. Ozouf, C. Beauger, L. Dubau, M. López-Haro, M. Chatenet & F. Maillard. *Electrochimica Acta*, **2017**. *245*, 993–1004.

[44] S. Geiger, O. Kasian, A. Mingers, K. Mayrhofer & S. Cherevko. *Scientific Reports*, **2017**. *7*, 4595.

[45] W. Xu, G. M. Haarberg, S. Sunde, F. Seland, A. P. Ratvik, E. Zimmerman, T. Shimamune, J. Gustavsson & T. Åkre. *Journal of The Electrochemical Society*, **2017**. *164*(9), F895–F900.

[46] F. Iskandar, A. B. D. Nandiyanto, K. M. Yun, C. J. Hogan, K. Okuyama & P. Biswas. *Advanced Materials*, **2007**. *19*(10), 1408–1412.

[47] B. Mandlmeier, J. M. Szeifert, D. Fattakhova-Rohlfing, H. Amenitsch & T. Bein. *Journal of the American Chemical Society*, **2011**. *133*(43), 17274–17282.

[48] B. Mandlmeier, N. K. Minar, J. M. Feckl, D. Fattakhova-Rohlfing & T. Bein. *Journal of Materials Chemistry A*, **2014**. *2*(18), 6504.

[49] F. Iskandar, Mikrajuddin & K. Okuyama. *Nano Letters*, **2001**. *1*(5), 231–234.

[50] J. M. Szeifert, J. M. Feckl, D. Fattakhova-Rohlfing, Y. Liu, V. Kalousek, J. Rathousky & T. Bein. *Journal of the American Chemical Society*, **2010**. *132*(36), 12605–12611.

[51] G. Sauerbrey. *Zeitschrift für Physik*, **1959**. *155*(2), 206–222.

6 Carbon-templated conductive oxide supports for oxygen evolution catalysis

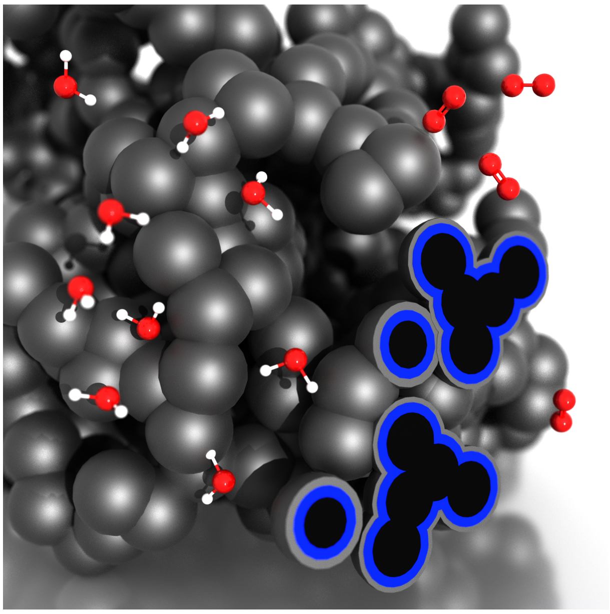

This chapter is based on the following publication:

Carbon-templated conductive oxide supports for oxygen evolution catalysis, A. G. Hufnagel, S. Häringer, M. Beetz, B. Böller, D. Fattakhova-Rohlfing, T. Bein, **2019**, 11(30), 15428 – 14293.

6.1 Abstract

We present a novel route for the preparation of supported $IrO2$ catalysts for the oxygen evolution reaction in proton exchange membrane electrolyzers. It uses carbon soot as a nanostructure template, which is sequentially coated with a conductive niobium-doped titanium oxide (NTO) layer and an ultrathin, highly pure IrO_2 catalyst layer by atomic layer deposition (ALD). The NTO acts as an oxidation-stable conductor between the metal current distributor and the catalyst. The highly controlled film growth by ALD enables the fabrication of electrodes with a very low noble metal loading. Nonetheless, these electrodes exhibit very high catalytic activity and good stability under cyclic and constant load conditions. At an IrO_2 content of less than 10 percent by mass of the oxide material and an area-based Ir content of $153\,\mu g\,cm^{-2}$, the nanostructured NTO/IrO_2 electrode achieves an oxygen evolution current density of $1\,mA\,cm^{-2}$ at an overpotential of $\approx 250\,mV$, which is significantly lower than the reported values for particulate NTO/IrO_2 catalysts.

6.2 Introduction

If an energy economy independent from fossil fuels is to be established, large-scale hydrogen production from renewable energy sources should replace the current practice of steam reforming natural gas. As renewable energy is mostly harvested in the form of electricity (photovoltaics, wind turbines etc.), hydrogen evolution by electrolysis of water is an obvious, attractive choice. The more recent proton exchange membrane (PEM) electrolysis technology has experienced an upsurge in research interest in recent years due to its advantages over the well-established alkaline water electrolysis, including faster response to load changes (important when the power supply is fluctuating, as is the case with most renewables) as well as higher current densities and consequently more compact system design.[1,2] However, the acidic environment, coupled with the high anodic potential at the oxygen-evolving electrode, necessitates a stable oxygen evolution catalyst, which is also efficient and connected via a low-resistance pathway to the current collector. Because of its excellent catalytic activity and long-term stability, state-of-the-art oxygen evolution catalysts for the acidic environment of the PEM anode are based on IrO_2, which at 0.001 ppm abundance (by mass) in the earth's crust is one of the rarest elements.[2] Due to this scarcity, many attempts have been made to reduce the loading of the anode with IrO_2. An established method is the dispersion of the IrO_2 on a high-surface-area support material, which is also stable against corrosion and oxidation. The state-of-the-art support material is $TiO2$.[3–7] However, due to the low intrinsic conductivity of TiO_2, a high IrO_2 loading is typically needed to establish a continuous conductive pathway to the current collector.[2]

Transparent conductive oxide materials (TCOs) provide a solution to this quandary. A porous

TCO support can be coated with an IrO_2-based catalyst and provide the conductive pathway to the current collector.[8–14] In such a configuration, the expensive IrO_2 is only used in the function where it is difficult to replace (i.e. as an OER catalyst), whereas the current conduction can be handled by the much cheaper TCO. To ensure maximum utilization of the IrO_2 and thus enable catalysts with a very low IrO_2 loading, the electrochemically active surface area (ECSA) must be maximized. This can be achieved by either applying the IrO_2 in the shape of extremely small nanoparticles or as an ultrathin ($\leq$1 nm) film. A high IrO_2 loading to achieve conductivity is thus not necessary. Niobium-doped titanium oxide (NTO, Nb:TiO_2) can be assembled into a variety of porous structures and has shown promise as such an oxidation-stable yet conductive catalyst support material for the oxygen electrode in both electrolyzers and fuel cells.[9,10,15,16] While existing studies have used NTO powders loaded with IrO_2, we propose that nanostructured films with easily accessible meso- and macropores can be of great advantage as they are based on a continuous conductive matrix, ensuring good current conduction, while the large pores facilitate electrolyte access and gas removal. In PEM fuel cells, such films are formed by commercially available carbon black agglomerate particles.[17,18] However, the considerably higher anode potential in PEM electrolyzers precludes the use of carbon, which undergoes anodic oxidation at $\geq$1 V vs. RHE.[19] Lately, nanomaterials have been developed that replicate the morphology of carbon in stable oxide materials for a number of applications, including photodetectors and Li-ion battery electrodes.[20–26] The conversion of the carbon black nanostructure into a porous TCO material is expected to result in a conductive and oxidation-stable OER catalyst support that is well suited for PEM electrolyzer applications. This replication can be achieved by atomic layer deposition (ALD), which excels at controlled thin film growth. ALD combines unrivaled conformality in porous structures with subnanometer thickness control and the ability to prepare doped and mixed materials by alternating deposition of multiple components. It is thus ideally suited to prepare ternary oxide films with a complex morphology, using a hard template, such as carbon black, to direct the resulting film morphology.

Here, we demonstrate the preparation and performance characterization of a new type of OER catalyst structure for PEM electrolysis. We used atomic layer deposition to grow macroporous support structures of NTO on carbon-based hard templates derived from flame soot. We then applied a conformal, ultrathin film ($\approx$1 nm) of pure, crystalline IrO_2 to the surface of the NTO support and examined its performance as an OER electrode in an acidic electrolyte. This new approach to the production of a nanostructure-supported OER catalyst results in electrodes with impressive performance and stability in spite of their very low IrO_2 loading. The combination of the nanostructure provided by the easily scalable soot template with the precisely controlled NTO deposition and tunable ultra-low IrO_2 loading by ALD make this a very attractive electrode concept for overcoming the challenges involved in PEM electrolyzer anode design.

6.3 Results and Discussion

6.3.1 Preparation and characterization of carbon soot templates

The multi-step preparation of the nanostructured OER electrodes requires a solid template to direct the final morphology. For this purpose, we prepared carbon soot substrates with accurate control over thickness and morphology by manually drawing smooth, heat-resistant substrates such as soda-lime glass (SLG), fused silica and Ti foil through the flame of a wick burner fueled with 2-propanol (Fig. 1a). We found this to be the preferred fuel as it ensures a good rate of soot deposition and leaves no low-volatility residue in the deposited film. The burner was constructed so as to produce a wide sheet of flame that covers the entire substrate, which allows for homogeneous growth on large areas. The thickness can be easily tuned in the micrometer range by repeatedly drawing the substrate through the flame.

Fig. 1b and c shows cross-section SEM micrographs of a soot layer deposited on SLG. The structure is highly porous yet continuous. It consists of primary carbon particles that are spherical and ≈30 to 50 nm in diameter. These form extended interwoven chains similar to the aggregated secondary particles found in commercial carbon blacks.[27] The pore system is highly interconnected with a wide distribution of pore sizes, ranging from tens to hundreds of nanometers. We expect this structure to be well suited for an OER catalyst support as it allows easy electrolyte access and gas egress, and the interconnected web ensures electrical contact and mechanical stability.

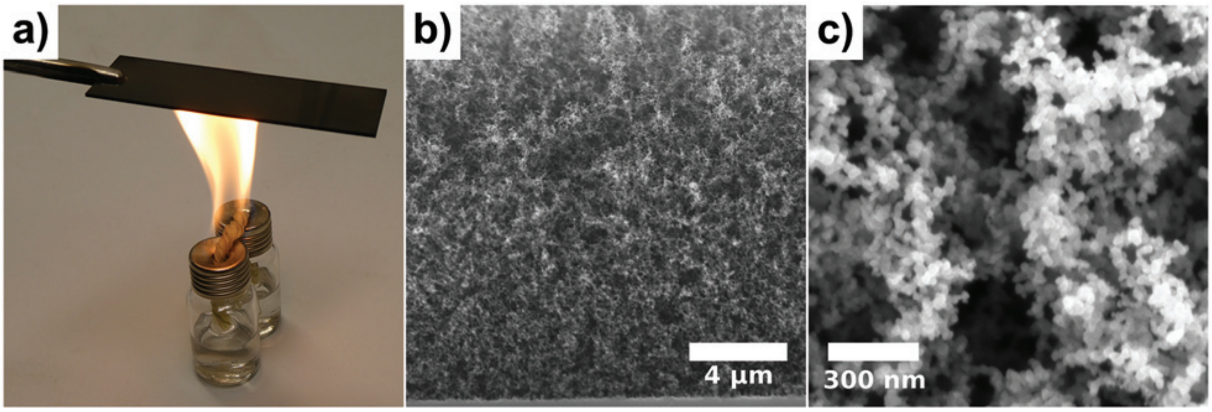

Figure 6.1: Photo image of carbon film preparation (a). Cross-sectional SEM micrographs of a 2-propanol soot layer on SLG (c, d).

6.3.2 ALD of NTO coatings

The next step of the electrode preparation procedure is the application of the NTO layer, which serves as a corrosionstable current conductor. We used alternating ALD of TiO_2 and NbO_x

from titanium(IV) isopropoxide (TTIP), niobium(V) ethoxide (NEO) and water to prepare these layers on carbon-soot templates grown on Ti foil as well as on flat fused silica and Si(100) substrates. The mixing ratio of Nb/(Ti + Nb) in the resulting layers was varied from 3 to 29 % by varying the cycle ratio of the two ALD processes (Table S1†). The elemental ratio, determined by EDX from as-deposited films grown on carbon soot on fused silica, very accurately tracks the cycle ratio of the two ALD processes, allowing for accurate adjustment of the Nb content in the films. To crystallize the oxide layers and activate the niobium dopant, the films were then heat-treated in 5 % H_2/N_2. Sample XRD patterns of NTO-coated carbon soot films (soot layer ≈10 µm, oxide layer ≈80 nm) after treatment at different temperatures are shown in Fig. S2.† A striking difference is observed between the as-deposited samples containing 3 and 20 % Nb, respectively. While a low Nb content results in a highly crystalline anatase phase already during deposition, the high Nb content effectively prevents crystallization of the film material under the conditions of the deposition.[28] After heating to 600°C , the NTO film with 20 % Nb has crystallized in the anatase lattice as well. After treatment at 700°C , the film with a low Nb content has undergone quantitative phase transformation into the rutile modification, while a high Nb content prevents this transition and the film is still composed exclusively of the anatase phase.[29] Despite the relatively high niobium content, no segregation of a separate NbO_x phase is visible in the XRD data. Rather, a shift of the reflections of the TiO_2 phases to lower angles is observed, most obviously in the anatase (101) reflection at 25.3°C 2θ. This shift indicates that the Nb is incorporated into the anatase lattice, expanding it without changing the crystal structure.[30] The approximate crystallite size was calculated from the broadening of the anatase (101) and rutile (110) reflections using the Scherrer equation (eqn (1), Table S2,† $K = 0.9$). Fig. S3† shows SEM images of a flat 20 % Nb NTO layer on fused silica after deposition and after annealing at 700°C . The as-deposited amorphous layer shows no obvious visible features. By contrast, the annealed layer consists of a mosaic of large crystals sized on the order of 10 µm. This is evidence of explosive crystallization, which has been previously observed in ALD NTO.[28,31] Niemelä et al. showed that the conductivity-limiting mechanism in ALD NTO films changes from grain-boundary scattering at low Nb contents to intra-grain phonon scattering in the larger grains found at high Nb levels.[32] They concluded that for applications where high conductivity is required, the high-Nb regime is advantageous. We assume that a similar explosive crystallization process also takes place on the carbon supports, resulting in the fairly large crystallite sizes on the order of the carbon soot primary particles (cf. Table S2†) and ensuring good grainboundary contact of the nanostructured NTO, which is a key requirement for good conductivity throughout the nanostructured layer. The conductivity of NTO thin films with different Nb contents and heat treatments was measured using the van der Pauw method on fused silica substrates. As-deposited, the conductivity was below the detection limit in all cases. Fig. 2 shows the conductivities obtained by annealing at 600 or 700°C . At both temperatures a similar trend is observed with a clear conductivity maximum at 20 % Nb. Between 10 and 30 % Nb, conductivity of films annealed at 700°C is markedly higher than that achievable by annealing at 600°C . The conditions at which the highest conductivity ($440\,\mathrm{S\,cm^{-1}}$) was observed were chosen for the electrocatalyst supports for use in OER electrode preparation. These supports consist of a ≈20 µm soot layer deposited on titanium foil, coated with a 20 % Nb NTO layer of 40 or 80 nm by ALD and annealed at 700°C in 5 % H_2/N_2.

6.3.3 ALD of IrO_2

To complete the OER electrodes, the iridium oxide catalyst phase has to be applied with a low mass loading and high dispersion onto the carbon/NTO structure. One way to achieve this is a conformal ultrathin film, prepared by ALD. The atomic layer deposition of iridium metal and iridium oxide has been extensively studied.[33–39] It was reported by Hämäläinen et al. that both iridium metal and iridium(IV) oxide can be grown using $Ir(acac)_3$ and ozone as precursors.[35,37] At temperatures up to 195°C , crystallographically pure IrO_2 is obtained. At higher temperatures, the resulting films exhibited increasing amounts of metallic Ir according to XRD. Because of this, a deposition temperature of 188°C was chosen for this study. This resulted in the growth of rutile IrO_2 with no crystalline impurities or Ir metal detectable by XRD (Fig. S5†). The thickness of the IrO_2 films was determined by spectroscopic ellipsometry on oxide-terminated Si(100) substrates. Good fits were obtained by modeling the IrO_2 layer using a dual Lorentz oscillator model as proposed by Kohli et al.[40] The nucleation and growth behavior of the $Ir(acac)_3/O_3$ ALD process has recently been studied by Mattinen et al., who report a very long nucleation delay of 120 cycles and a growth rate of $0.033\,\mathrm{nm\,cycle^{-1}}$. As the present study investigates extremely low IrO_2 loading for oxygen evolution catalysis, the films studied here were deposited within this nucleation regime, where complete substrate coverage and uniformity cannot be presupposed. The use of an Al_2O_3 underlayer to aid nucleation, as demonstrated by Hämäläinen et al., was avoided as it might inhibit electrical contact between the conductive support and the IrO_2 film.[37] The composition of ALD IrO_2 films on single crystal Si substrates was investigated by XPS (Fig. S6 and S7†). The detailed XP spectrum of the Ir 4f region (Fig. S7†) shows that the Ir 4f7/2 and Ir 4f5/2 signals are centered on binding energies of 61.9 and 64.9 eV, respectively, which is in good agreement with reported values for anhydrous IrO_2.[41] No evidence of metallic iridium was found, leading us to conclude that the ALD process yields films in which the iridium is exclusively present as iridium(IV) oxide.

6.3.4 Electrode preparation and characterization

To prepare OER catalyst electrodes, the catalyst support structure described above was subjected to 50 ALD cycles of the IrO_2 process, which resulted in a layer thickness of between 0.64 and

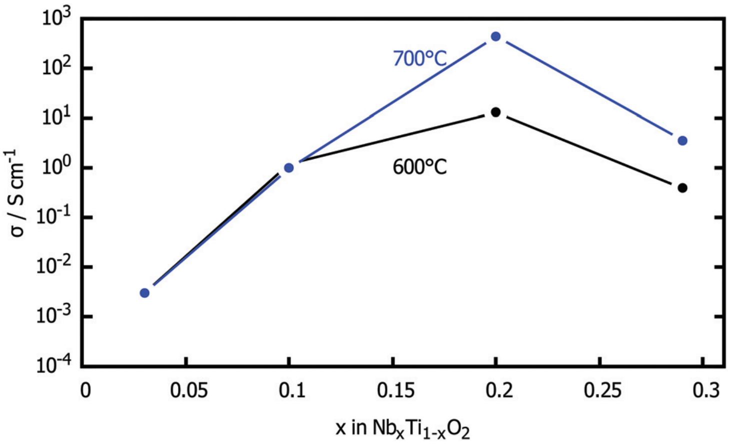

Figure 6.2: Conductivity of annealed NTO films on fused silica.

0.87 nm on Si witness substrates, determined by ellipsometry. Fluoride-doped tin oxide (FTO) substrates were processed in the same IrO_2 ALD process to obtain a flat catalyst electrode. Due to the small amount of IrO_2 present in the nanostructured electrodes as well as the small particle size, crystalline IrO_2 could not be detected by XRD. Fig. 3 shows Raman spectra of a Ti/C/NTO film and a Ti/C/NTO/IrO_2 film. The anatase crystal are strongly scattering and their signals dominate the spectra. The Eg, B1g and A1g modes can be clearly assigned, according to Stagi, who also observed the small shoulder at 200 cm^{-1}.[42] IrO_2 has distinct Raman signals at 560 (Eg) and 720 cm^{-1} (A1g, B2g).[43] Despite the small amount of IrO_2 deposited onto the electrode support, these signals can be clearly observed in the magnification of their Raman spectra (inset in Fig. 3). The Eg signal appears as a peak between the neighboring anatase signals and the A1g/B2g signal is visible as a shoulder on the TiO_2 peak centered on 628 cm^{-1}. Scanning (SEM) and transmission (TEM) electron microscopy was used to investigate the structure and composition of the electrodes (Ti/C/NTO/IrO_2). Fig. 4a shows an SEM image of the fractured cross-section of a Ti/C/NTO/IrO_2 electrode. The porous nanostructure of the carbon soot has been preserved through the NTO deposition, annealing and IrO_2 deposition. There is no evidence of pore clogging at the surface of the carbon layer and the deeper pores are still accessible. Fig. S8† shows EDX element distribution maps for Ti, Nb and Ir of a similar cross-section. All three are evenly distributed throughout the entire thickness of the nanostructured film. We therefore expect a similar composition in terms of the Nb content of the NTO, and thus uniform conductivity, as well as the IrO_2 catalyst loading of the entire electrode. The atomic ratio Ir/(Ti + Nb + Ir), determined by area-averaged EDX excluding the substrate, was found to be 3–4 % at different spots of the cross-section, which corresponds to an IrO_2 mass fraction of 7–9.5 % of the oxide material. Fig. 4b shows a detail back-scattered electron image of the fracture face of a carbon/oxide particle. Due to the atomic number contrast inherent to this type of image, the components of the structure can be clearly distinguished. The carbon support (darkest) is still present, encased by the NTO layer. Everything is covered by the IrO_2 layer, which appears brightest due to its high atomic weight. No major holes in the iridium oxide layers are visible. An HAADF-STEM image of a particle from the electrode structure is shown in Fig. 4c. This imaging mode also shows the thin IrO_2 layer, bright due to its high scattering cross-section, evenly coating the outside of the particle. The continuous inner pore structure containing the carbon template is also visible. A detail TEM image of a single particle is shown in Fig. 4d. It reveals that the IrO_2 layer consists of closely packed crystalline particles. This implies that the electrode presents a large surface area of IrO_2 to the electrolyte, which is in good electrical contact with the underlying NTO. Fig. 4e shows a HAADF-STEM image of an electrode particle together with EDX element distribution maps of the marked area. Ti and Nb are co-located in the center of the particle with the exception of the template hollow. Iridium is found at the surface, as demonstrated by the strong signal observed at the particle circumference, where the electron beam passes tangentially through the particle surface rather than axially, thus exciting a larger volume of IrO_2.

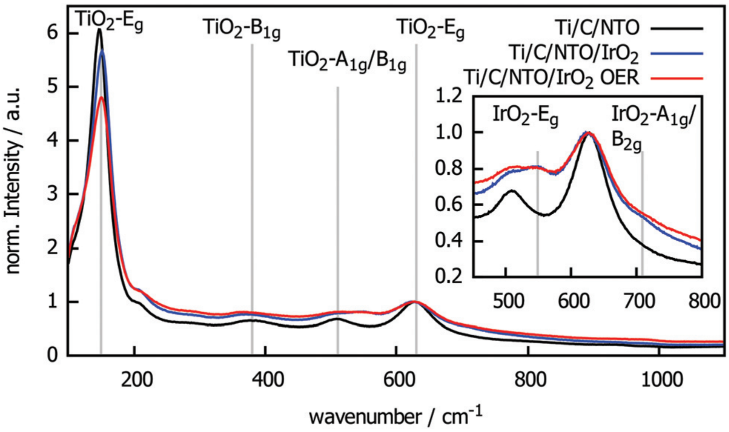

Figure 6.3: Raman spectra of a carbon/NTO support (black), support with IrO_2 layer (blue) and electrode after electrochemical testing (red). The inset shows a magnification of the IrO_2 signals. Assignment of signals according to ref. [43] and [42].

6.3.5 Electrochemical characterization

With the successful application of the iridium oxide, this Ti/C/NTO/IrO_2 structure represents the completed OER electrode. Its oxygen evolution activity was investigated in a three-electrode electrochemical cell using gently stirred 0.5 M H_2SO_4 as the electrolyte. All electrochemical measurements were performed at room temperature. First, in order to investigate whether the IrO_2 layer in the electrode nanostructure is indeed fully contacted and accessible to the electrolyte, we performed cyclic voltammetry at varying scan speeds in the range between 0.55 and 0.85 V vs. RHE, where no faradaic process is observed (Fig. S9a†). As expected for a capacitive region, the

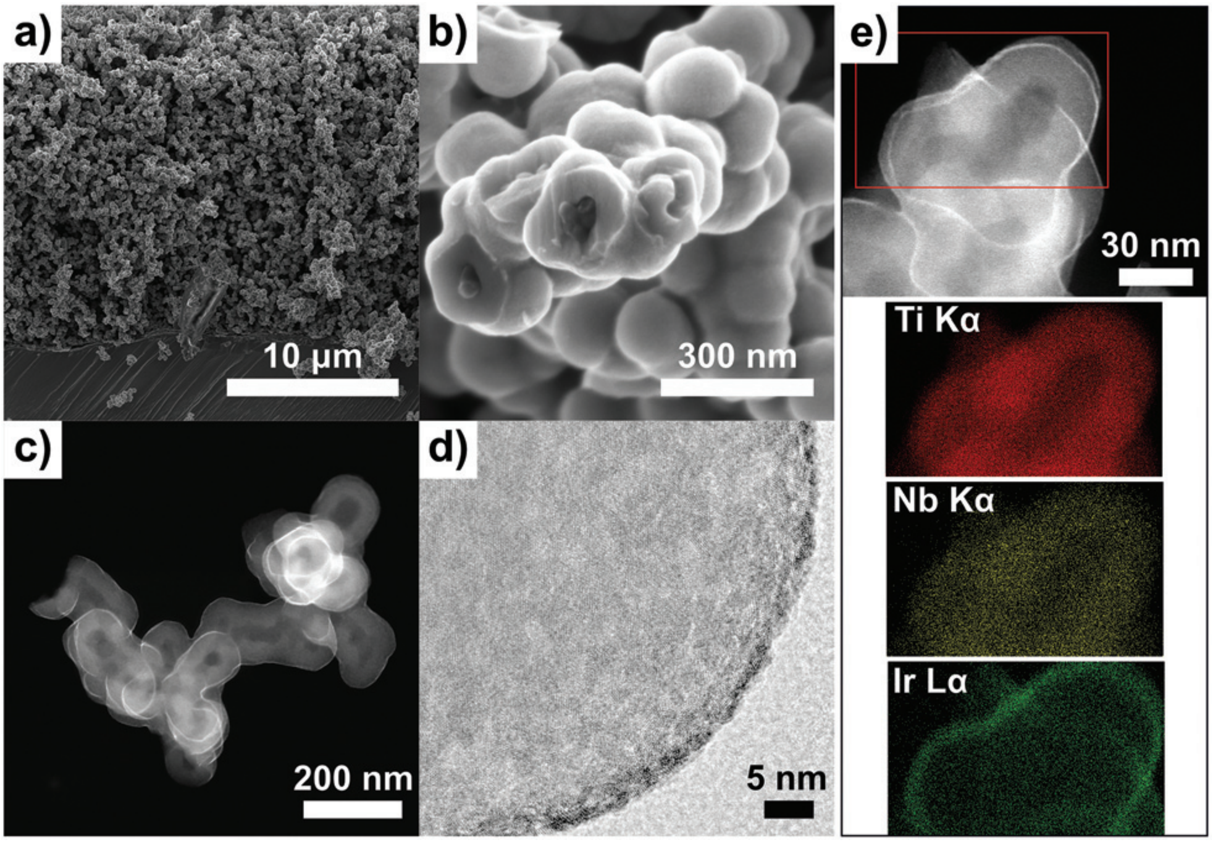

Figure 6.4: Cross-sectional SEM secondary electron image of a complete electrode (Ti/C/NTO/IrO_2) (a). SEM back-scattered electron image of a fracture site in the oxide nanostructure (b). HAADF-STEM image of one isolated particle of the electrode structure (c). Bright-field TEM image of part of an electrode particle (d). EDX element distribution maps of the area highlighted by the red frame in the STEM image (e).

currents are fairly constant in the scanned potential range. The currents at 0.70 V were extracted from the cathodic and anodic scans and plotted against the scan rate in Fig. S9b.† As a reference, the same experiment was performed with an FTO electrode coated with the same IrO_2 layer. The capacitive currents follow a linear trend in both cases, though some deviation is observed for the nanostructured electrode at the highest currents. The slopes give the capacitance of the flat and nanostructured electrodes as $28\,\mu F\,cm^{-2}$ and $3570\,\mu F\,cm^{-2}$, respectively. The direct calculation of the electrochemically active surface area would require an accurate value for the reference capacitance, which is difficult to obtain, as it depends on the material preparation as well as pseudocapacitance effects of IrO_2.[44,45] We therefore restrict our analysis to comparing the two electrodes investigated here. Assuming that the capacitive behavior of the IrO_2 film is the same on both the FTO and Ti/C/NTO substrates, the relative specific ECSA is given by the ratio of the two capacitances. For FTO a roughness factor of ≈1.2 was determined by atomic force microscopy. The ECSA of the Ti/C/NTO/IrO_2 electrode is therefore 1.2 times the capacitance ratio, i.e. $153\,cm_{ECSA}{}^2/cm_{geo}{}^2$. Fig. 5a shows cyclovoltammograms of a Ti/C/NTO/IrO_2

electrode, a reference sample with no IrO_2 layer and another reference with the same ALD IrO_2 applied to an FTO substrate. The nanostructured electrode with no IrO_2 coating shows no significant water oxidation current below 1.7 V vs. RHE. By comparison, the Ti/C/NTO/IrO_2 electrode exhibits significant water oxidation activity with an onset at about 1.45 V vs. RHE at 0.5 mA cm^{-2} and reaches a current density of 100 mA cm^{-2} at 1.64 V vs. RHE. The FTO/IrO_2 sample also catalyzes the OER. Its current is much lower as a result of the smaller surface area. The Ti/C/NTO/IrO_2 electrode was subjected to 50 consecutive CV cycles and the overpotentials at 1, 10 and 100 mA cm^{-2} (anodic scans) are plotted in Fig. 5c (see Fig. S11† for full CV cycles). The three data sets show the same trend with a rise of about 35 mV over the first three cycles, followed by a much slower rise by about 20 mV over the course of the remaining cycles. Small jumps in the overpotential are a result of bubble formation and detachment. The overpotential at 1 mA cm^{-2} is between 240 and 260 mV for all but the first cycle. This is a much smaller overpotential than that reported for oxide-supported catalysts with comparable IrO_2 content. For comparison, Hu et al. reported an overpotential of 300 mV for an NTO catalyst with 17 wt % IrO_2, while Tong et al. measured 397 mV with 13 wt % IrO_2 on Sb:SnO_2 (ATO) at the same current density.[9,14] The long-term stability of the Ti/C/NTO/IrO_2 under constant load was investigated by chronopotentiometry over 12 h at a constant current density of 100 mA cm^{-2}. After an initial increase, the overpotential steadies out at ≈0.6 V with a slight positive drift over the duration of the measurement (Fig. 5b). No sudden potential jumps, which might indicate a failure of the catalyst structure or conductivity, can be observed. The ramifications for the stability of the Ti/C/NTO/IrO_2 electrode structure are discussed below. A Tafel plot, constructed from data recorded after 50 CV cycles of a Ti/C/NTO/IrO_2 electrode, is shown in Fig. 5d. The overpotential follows a linear trend between ≈1 and 30mA cm^{-2} with a slope of 69 mV per decade. This is comparable to, though slightly higher than values reported for ATO-supported IrO_2 catalysts.[11,14] Tong et al. reported 62 mV dec^{-1} at 13 wt % IrO_2 loading.[14] Assuming a 1 nm thick crystalline compact layer of IrO_2 evenly coating the support with the surface area calculated above, this corresponds to an iridium loading of 153 µg cm^{-2} (178 µg cm^{-2} of IrO_2). This value should be viewed as an upper limit, as the IrO_2 layer thickness determined by ellipsometry was consistently smaller than 1 nm. At this loading, a current density of 100 mA cm_{geom}^{-2} corresponds to a mass-based current of 654 A g_{Ir}^{-1} (561 A g_{IrO2}^{-1}). During potential cycling, this is attained at ηOER $\leq$ 460 mV in all 50 cycles (Fig. 5c). During chronopotentiometric testing, the required overpotential rises to 620 mV over the course of 12 h (Fig. 5b). For comparison, Hu et al. report an initial mass activity of $approx$400 A g_{IrO2}^{-1} at ηOER = 470 mV for NTO loaded with 17 wt % IrO_2 and 1500 A $g_{IrO_2}^{-1}$ for a 26 wt % loading.[9] Oh etál. observed initially 100 A g_{Ir}^{-1} at ηOER = 310 mV for an ATO-supported 20 wt % IrO_x catalyst, which reduced to ≈60 A g_{Ir}^{-1} after a 15 h chronopotentiometric experiment at 1 mA cm_{geom}^{-2}.

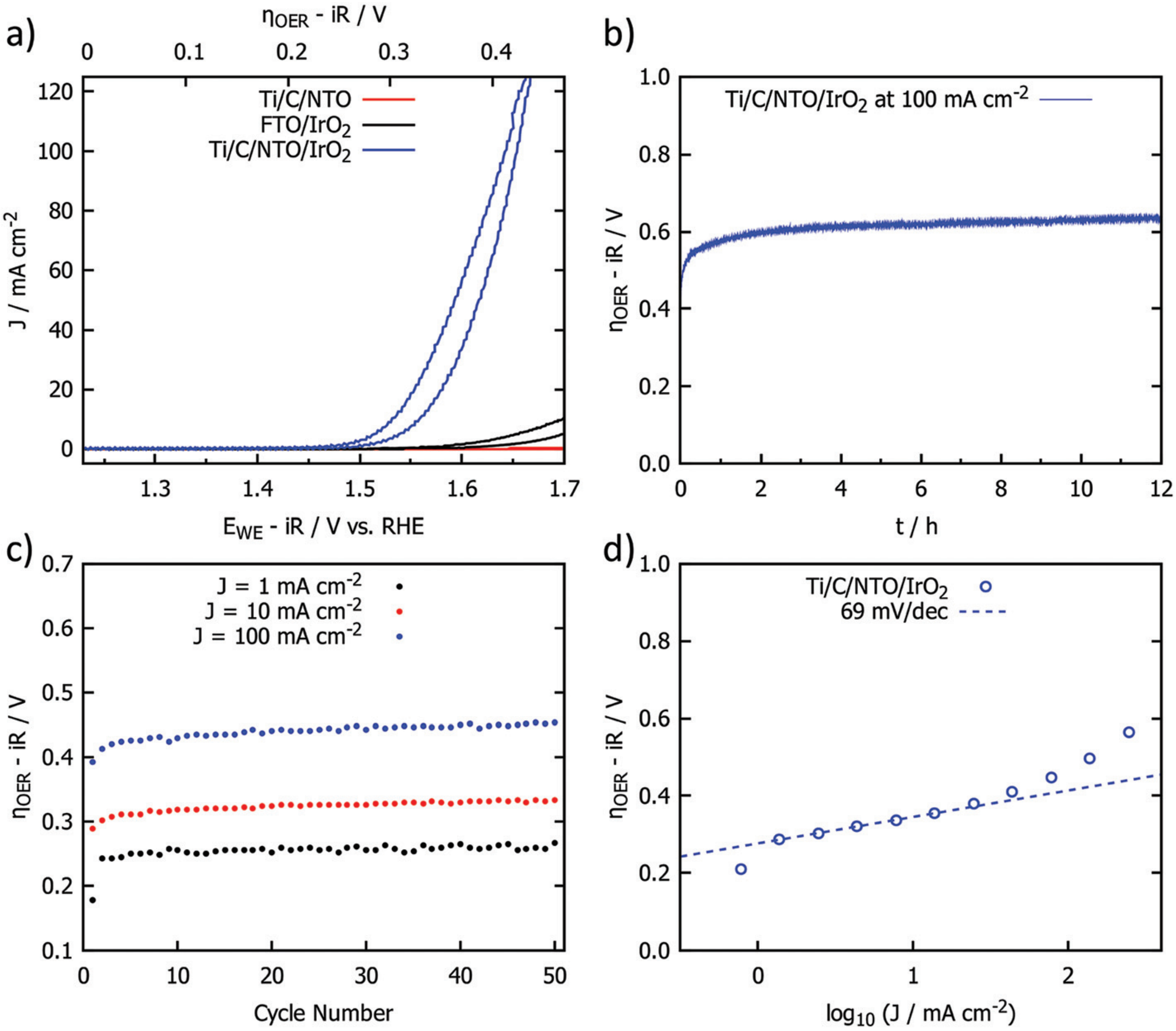

Figure 6.5: Cyclovoltammograms (2nd cycles) of Ti/C/NTO/IrO_2, Ti/C/NTO and FTO/IrO_2 electrodes recorded in 0.5 M H_2SO_4 at 20 mV s^{-1} (a). Chronopotentiometric stability data of a Ti/C/NTO/IrO_2 electrode at 100 mA cm^{-2} (b). OER overpotentials at 1, 10 and 100 mA cm^{-2} extracted from the anodic scans of prolonged cycling of a Ti/C/NTO/IrO_2 electrode (c). Tafel plot of a Ti/C/NTO/IrO_2 electrode (d).

6.3.6 Post-mortem analysis of a Ti/C/NTO/IrO_2 electrode

As our electrodes exhibited some change in their performance characteristics during cycling and constant load operation, we investigated the aging of the Ti/C/NTO/IrO_2 nanostructure under OER conditions by ex situ analysis of the electrode used in the chronopotentiometric stability test (Fig. 5b). As shown in Fig. S12,† the Ti substrate is visible in several places on the electrode, where the catalyst nanostructure delaminated as a result of prolonged intense bubble formation. We note, however, that in an actual PEM electrolyzer the catalyst structure is firmly sandwiched between the current collector and the PEM and that the removal of larger parts of the catalyst structure is thereby prohibited. The cell impedance was ≈3 Ω before and after the stability test. Together with the high catalytic activity observed throughout the experiment, this leads us to conclude that the conductivity of the NTO phase did not suffer at the high applied potential and that electronic contact with the IrO_2 layer was retained. The Raman spectrum after electrochemical testing, repeated rinsing with ultrapure water and drying at 60°C is shown as the red curve in Fig. 3. The signals from both the anatase NTO and the IrO_2 phase are still observed after >12 h exposure to the acidic electrolyte and highly anodic potential. Both phases, therefore, show remarkable stability. However, the electrode after OER stability testing shows slightly diminished IrO_2 signal intensities compared to the pristine electrode, which indicates that some of the catalyst material was lost during the measurement. The HAADF-STEM image in Fig. S13a† reveals that the structure is still conformally coated with the strongly scattering IrO_2 overlayer, though it no longer appears as well-formed and continuous as before the OER experiments (cf. Fig. 4c). From these results as well as the slight rise in overpotential during the stability measurement we conclude that the IrO_2 layer was partially removed during the experiment. Dissolution of the IrO_2 is unlikely to be the cause of this as the reported rate of dissolution of crystalline IrO_2 during OER in acidic media is on the order of $0.1\,\mathrm{ng\,cm^{-2}\,min^{-1}}$, compared to the IrO_2 loading of $178\,\mathrm{\mu g\,cm^{-2}}$ calculated for the Ti/C/NTO/IrO_2 electrode.[46] More likely is a loss of adhesion at the NTO/IrO_2 interface, which would cause the IrO_2 film to flake off. We expect that close scrutiny of this interface will pinpoint ways to improve its durability by optimizing the deposition and annealing steps.

6.4 Conclusions and Outlook

We have demonstrated a new type of oxide-based anode structure for PEM water electrolysis. It uses NTO as an oxidationstable conductive link between the metal current distributor and the catalyst, which takes the shape of an ultrathin IrO_2 film with optimum utilization of the noble metal for OER catalysis. The material shows competitive activity and promising stability at a low Ir loading of $\leq 153\,\mathrm{\mu g\,cm^{-2}}$. The activity of Ir-based ternary oxides such as $Ru_xIr_yO_2$ has been demonstrated to be superior to that of IrO_2.[2] As the ALD method lends itself well to the controlled preparation of mixed oxides, we expect that IrO_2 in our system could be easily replaced with an even more active catalyst. We envision that the anode system reported here can be applied in practical PEM electrolyzers in a number of ways. Using existing ALD particle coating technology and commercial carbon black as the substrate, supported catalyst powders could be made and used for ink-based MEA preparation. Alternatively, our method could be used to deposit a soot layer onto typical current distributor materials (e.g. Ti foam) and add the ALD NTO and IrO_2 layers. The result would be an integrated current collector/porous catalyst with optimal conductive contact at the interfaces and excellent Ir utilization at low loading. This could be used directly as the anode in a MEA assembly. ALD has a reputation as an expensive technique that is difficult to scale to large areas. However, the high power density of PEM electrolyzers implies that the geometric electrode areas to be coated are quite moderate even for larger systems. State-of-the-art PEM stacks have a cell area of several hundred square centimeters.[2] Existing ALD tools for industrial production can process substrate surface areas of several square meters per batch and larger reactors are in development.[47] If efficient reclamation of the excess Ir used in the ALD process is taken into account, it is conceivable that the cost savings due to the reduced IrO_2-loading and elimination of ink-based electrode deposition can easily balance the cost of ALD for this application.

6.5 Experimental Details

The substrates, SLG microscope slides, Ti foil (Alfa Aesar, 99.5 % , 0.25 mm) and polished Si (100) single crystal wafers were used as received. Fused silica (GVB GmbH, FN08) and FTO-coated (Pilkington, 7 Ω square^{-1}) glass slides were cleaned prior to use by sequential sonication in Extran® solution, ultrapure water and 2-propanol for 15 min each and dried using nitrogen.

6.5.1 Deposition of carbon soot nanostructures

Carbon soot nanostructured films were grown by repeatedly drawing the substrates through the top third of the flame of a custom-built wick burner fueled by technical grade 2-propanol. The flame sheet was approximately 4 cm wide at the base and 8 cm high. Typically, a microscope slide (25 × 75 mm) was drawn back and forth all the way through the flame within 1 s and this was repeated 10 times, resulting in a homogeneous soot film of ≈20 µm. Fused silica and Ti foil samples were prepared in the same way.

6.5.2 ALD of NTO layers

TiO_2 and NbO_x layers were grown using a Picosun R-200 Advanced ALD reactor at a temperature of 200°C and a base pressure of 2 hPa. Nitrogen (Air Liquide, 99.999 %) was used as the purge and carrier gas. The carrier gas line flow during pulses was 40 sccm. Titanium tetraisopropoxide (TTIP, Aldrich, 99.999 %) was evaporated from a stainless steel vessel at 85°C , niobium ethoxide (NEO, Strem, 99.9+ %) was supplied from a glass vessel at 160°C . Ultrapure water (MilliQ, 18.2 MΩ cm) was held in a stainless steel cylinder at 19°C . Each TiO_2 ALD cycle comprised two TTIP pulses (1.6 s pulse, 4.5 s static exposure, 6 s purge) and one water pulse (2 s pulse, 4.5 s static exposure, 7.5 s purge). The resulting GPC was 0.038 nm cycle^{-1} with a non-uniformity of 4 % across a 20 cm wafer.

NbO_x was deposited using cycles of four NEO pulses (1.6 s pulse, 6.5 s static exposure, 6 s purge) and one water pulse as in the TiO_2 process. The GPC was 0.068 nm cycle^{-1} and the non-uniformity was 4 % . Mixed oxide layers were grown by interspersing one NbO_x cycle in the TiO_2 process at regular intervals as shown in Table S1.† Before being used as electrodes, the films were annealed in forming gas (5 % vol. H_2, 95 % vol. N_2, Air Liquide ARCAL F5) at 700°C with a heating rate of 6°C min^{-1} and a dwell time of 120 min.

6.5.3 ALD of IrO_2 layers

$Ir(acac)_3$ (technical grade) was kindly donated by Heraeus Holding GmbH (Germany) and used as received. IrO_2 ALD was carried out in the same reactor at 188°C . The carrier gas line flow during pulses was 40 sccm. $Ir(acac)_3$ was sublimated from a borosilicate glass container at 185°C . Ozone was supplied by an ozone generator (INUSA AC2025) from a feed of 500 sccm 1 % N_2/O_2 (Air Liquide, 99.9995 %). Each cycle consisted of three $Ir(acac)_3$ pulses and one ozone pulse, separated by purge intervals. An $Ir(acac)_3$ pulse comprised a 1.6 s pulse, 5 s static exposure and 10 s purge time. For the ozone pulse the times were 4 s, 2 s and 10 s, respectively. 50 cycles were used for the OER catalyst coatings, which resulted in a layer thickness of 0.64 to 0.87 nm, determined by spectroscopic ellipsometry on Si(100) substrates.

6.5.4 Electrode characterization

ALD film thicknesses were determined by spectroscopic ellipsometry (J. A. Woollam M-2000D) on Si(100) substrates. TiO_2, NbO_x and NTO layers were modeled using a Cauchy function. IrO_2 layers were modeled using a dual Lorentz oscillator model as reported by Kohli et al.[40] X-ray diffraction patterns were recorded on a Bruker D8 Discover diffractometer using Ni-filtered Cu Kα radiation ($\lambda = 0.154178$ nm). The source was operated operated at 30 mA and 40 kV. Reference XRD reflection data were obtained from the ICSD database. The crystallite size p was calculated using the Scherrer equation (eqn (1)), where K is the Scherrer constant, FWHM is the line broadening at halfmaximum and ϑ is the Bragg angle.

$$p = \frac{K\lambda}{\text{FWHM}\cos(\theta)} \tag{6.1}$$

The conductivity of NTO films on fused silica was measured using the van der Pauw method (ECOPIA, Model HMS 3000, 0.55 T). The samples were contacted using spring-loaded goldplated pins. SEM images were acquired on an FEI Helios NanoLab G3 UC FEG-SEM equipped with an Oxford Instruments EDX detector, operating at acceleration voltages between 2 and 20 kV. Cross-section samples were prepared by fracturing the film samples on Ti foil using a pair of pliers. TEM and HAADF-STEM images were acquired on an FEI Titan Themis 80–300 kV instrument operated at an acceleration voltage of 300 kV. For TEM imaging, particles were scraped off the electrode films, suspended in absolute ethanol and deposited on a holey carbon-coated copper grid. Raman spectra were recorded using an Olympus BX41 optical microscope (10×, N.A. 0.25

objective lens) coupled to a Horiba monochromator and Symphony CCD detector. A 20 mW HeNe laser, attenuated by an OD 0.3 filter was used for excitation. The resulting spectra were normalized by the height of the anatase Eg line at 628 cm^{-1}. For X-ray photoelectron spectroscopy (XPS) a VSW TA10 X-ray source and a VSW HA100 hemispherical analyzer were used. All spectra were measured with non-monochromatic Mg Kα radiation. Fits of the photoelectron peaks are based on a convolution of a Doniach-Šunjić-function and a Gaussian function and the subtraction of a linear background.

6.5.5 Electrochemical characterization

FTO/IrO_2 working electrodes were prepared by contacting the FTO with Ag-based conductive lacquer; the active area was limited by masking with PTFE adhesive tape with a 0.238 cm^2 circular hole. Ti/C/NTO/IrO_2 and Ti/C/NTO electrodes were contacted via the Ti foil and masked with epoxy to obtain a comparable active area. Experiments were performed in a three-electrode electrochemical cell, using a coiled Pt wire as the counter electrode and a hydrogen electrode (Gaskatel HydroFlex®) as the reference electrode. The latter was checked against a Hg/HgO reference electrode before and after the experiments and showed no drift in relative potential. The electrolyte was aqueous 0.5 M H_2SO_4, which was gently stirred during the measurements (in air). All experiments were performed at room temperature. A Metrohm Autolab PGSTAT302N potentiostat/galvanostat was used for cyclic voltammetry, chronopotentiometry and impedance spectroscopy. The CV and CP measurements were corrected for 95 % of the iR-drop. The cell resistance was determined as the high frequency real axis intercept of impedance spectra recorded at 1 V vs. RHE. It was typically 3 Ω for the electrodes on Ti and 12 Ω for electrodes on FTO. Tafel plots were constructed by galvanostatically holding an exponentially increasing range of current densities and reading out the stabilized overpotential after 30 s.

Bibliography

[1] *Journal of the American Chemical Society*, **1973**. *95*(24), 8212–8214.

[2] M. Carmo, D. L. Fritz, J. Mergel & D. Stolten. *International Journal of Hydrogen Energy*, **2013**. *38*(12), 4901–4934.

[3] *Williams, Pat Ward* (Oxford University Press), **2011**.

[4] S. T. and. *US Ophthalmic Review*, **2012**. *05*(02), 105.

[5] J.-P. Suchsland, B. Klose-Schubert, D. Herein, T. Martin, C. Eickes & M. Lennartz. *ECS Transactions*, **2013**. *50*(2), 1659–1667.

[6] M. Bernt & H. A. Gasteiger. *Journal of The Electrochemical Society*, **2016**. *163*(11), F3179–F3189.

[7] E. Oakton, D. Lebedev, M. Povia, D. F. Abbott, E. Fabbri, A. Fedorov, M. Nachtegaal, C. Copéret & T. J. Schmidt. *ACS Catalysis*, **2017**. *7*(4), 2346–2352.

[8] A. T. Marshall & R. G. Haverkamp. *Electrochimica Acta*, **2010**. *55*(6), 1978–1984.

[9] W. Hu, S. Chen & Q. Xia. *International Journal of Hydrogen Energy*, **2014**. *39*(13), 6967–6976.

[10] C. Hao, H. Lv, C. Mi, Y. Song & J. Ma. *ACS Sustainable Chemistry & Engineering*, **2015**. *4*(3), 746–756.

[11] H.-S. Oh, H. N. Nong, T. Reier, A. Bergmann, M. Gliech, J. F. de Araújo, E. Willinger, R. Schlögl, D. Teschner & P. Strasser. *Journal of the American Chemical Society*, **2016**. *138*(38), 12552–12563.

[12] C. Hao, H. Lv, Q. Zhao, B. Li, C. Zhang, C. Mi, Y. Song & J. Ma. *International Journal of Hydrogen Energy*, **2017**. *42*(15), 9384–9395.

[13] C. Massué, V. Pfeifer, X. Huang, J. Noack, A. Tarasov, S. Cap & R. Schlögl. *ChemSusChem*, **2017**. *10*(9), 1943–1957.

[14] J. Tong, Y. Liu, Q. Peng, W. Hu & Q. Wu. *Journal of Materials Science*, **2017**. *52*(23), 13427–13443.

[15] Y. Liu, J. M. Szeifert, J. M. Feckl, B. Mandlmeier, J. Rathousky, O. Hayden, D. Fattakhova-Rohlfing & T. Bein. *ACS Nano*, **2010**. *4*(9), 5373–5381.

[16] K.-W. Park & K.-S. Seol. *Electrochemistry Communications*, **2007**. *9*(9), 2256–2260.

[17] Y. Shao, J. Liu, Y. Wang & Y. Lin. *J. Mater. Chem.*, **2009**. *19*(1), 46–59.

[18] I. Khalakhan, R. Fiala, J. Lavková, P. Kúš, A. Ostroverkh, M. Václavů, M. Vorokhta, I. Matolínová & V. Matolín. *Fuel Cells*, **2016**. *16*(5), 652–655.

[19] S. Maass, F. Finsterwalder, G. Frank, R. Hartmann & C. Merten. *Journal of Power Sources*, **2008**. *176*(2), 444–451.

[20] X. Deng, L. Mammen, H.-J. Butt & D. Vollmer. *Science*, **2011**. *335*(6064), 67–70.

[21] S. Liu, M. Sakai, B. Liu, C. Terashima, K. Nakata & A. Fujishima. *RSC Advances*, **2013**. *3*(45), 22825.

[22] K. Senevirathne, V. Neburchilov, V. Alzate, R. Baker, R. Neagu, J. Zhang, S. Campbell, H. Chhina & S. Ye. *Journal of Power Sources*, **2013**. *232*, 401.

[23] Y. Cao, S. Deng, Q. Hu, Q. Zhong, Q.-P. Luo, L. Yuan & J. Zhou. *RSC Advances*, **2015**. *5*(104), 85969–85973.

[24] A. E. Kandjani, Y. M. Sabri, M. R. Field, V. E. Coyle, R. Smith & S. K. Bhargava. *Chemistry of Materials*, **2016**. *28*(21), 7919–7927.

[25] S. Lu, H. Wang, J. Zhou, X. Wu & W. Qin. *Nanoscale*, **2017**. *9*(3), 1184–1192.

[26] M. Putkonen, P. Heikkilä, A. T. Pasanen, H. Rautkoski, L. Svärd, P. Simell, M. Vähä-Nissi & T. Sajavaara. *Journal of Vacuum Science & Technology A: Vacuum, Surfaces, and Films*, **2018**. *36*(1), 01A102.

[27]

[28] V. Pore, M. Ritala, M. Leskelä, T. Saukkonen & M. Järn. *Crystal Growth & Design*, **2009**. *9*(7), 2974–2978.

[29] J. Arbiol, J. Cerdà, G. Dezanneau, A. Cirera, F. Peiró, A. Cornet & J. R. Morante. *Journal of Applied Physics*, **2002**. *92*(2), 853–861.

[30] Y. Furubayashi, T. Hitosugi, Y. Yamamoto, K. Inaba, G. Kinoda, Y. Hirose, T. Shimada & T. Hasegawa. *Applied Physics Letters*, **2005**. *86*(25), 252101.

[31] J.-P. Niemelä, H. Yamauchi & M. Karppinen. *Thin Solid Films*, **2014**. *551*, 19–22.

[32] J.-P. Niemelä, Y. Hirose, T. Hasegawa & M. Karppinen. *Applied Physics Letters*, **2015**. *106*(4), 042101.

[33] S. Choi, Y.-K. Cha, B.-S. Seo, S. Park, J.-H. Park, S. Shin, K. S. Seol, J.-B. Park, Y.-S. Jung, Y. Park, Y. Park, I.-K. Yoo & S.-H. Choi. *Journal of Physics D: Applied Physics*, **2007**. *40*(5), 1426–1429.

[34] S.-W. Kim, S.-H. Kwon, D.-K. Kwak & S.-W. Kang. *Journal of Applied Physics*, **2008**. *103*(2), 023517.

[35] J. Hämäläinen, M. Kemell, F. Munnik, U. Kreissig, M. Ritala & M. Leskelä. *Chemistry of Materials*, **2008**. *20*(9), 2903–2907.

[36] K. Knapas & M. Ritala. *Chemistry of Materials*, **2011**. *23*(11), 2766–2771.

[37] J. Hämäläinen, T. Hatanpää, E. Puukilainen, T. Sajavaara, M. Ritala & M. Leskelä. *Journal of Materials Chemistry*, **2011**. *21*(41), 16488.

[38] J. Hämäläinen, M. Ritala & M. Leskelä. *Chemistry of Materials*, **2013**. *26*(1), 786–801.

[39] M. Mattinen, J. Hämäläinen, F. Gao, P. Jalkanen, K. Mizohata, J. Räisänen, R. L. Puurunen, M. Ritala & M. Leskelä. *Langmuir*, **2016**. *32*(41), 10559–10569.

[40] S. Kohli, C. D. Rithner & P. K. Dorhout. *Journal of Applied Physics*, **2002**. *91*(3), 1149–1154.

[41] S. J. Freakley, J. Ruiz-Esquius & D. J. Morgan. *Surface and Interface Analysis*, **2017**. *49*(8), 794–799.

[42] L. Stagi, C. M. Carbonaro, R. Corpino, D. Chiriu & P. C. Ricci. *physica status solidi (b)*, **2014**. *252*(1), 124–129.

[43] A. V. Korotcov, Y.-S. Huang, K.-K. Tiong & D.-S. Tsai. *Journal of Raman Spectroscopy*, **2007**. *38*(6), 737–749.

[44] C. C. L. McCrory, S. Jung, J. C. Peters & T. F. Jaramillo. *Journal of the American Chemical Society*, **2013**. *135*(45), 16977–16987.

[45] S. Zhao, H. Yu, R. Maric, N. Danilovic, C. B. Capuano, K. E. Ayers & W. E. Mustain. *Journal of The Electrochemical Society*, **2015**. *162*(12), F1292–F1298.

[46] S. Cherevko, S. Geiger, O. Kasian, N. Kulyk, J.-P. Grote, A. Savan, B. R. Shrestha, S. Merzlikin, B. Breitbach, A. Ludwig & K. J. Mayrhofer. *Catalysis Today*, **2016**. *262*, 170–180.

[47] J. M. J. Maula. *Chinese Optics Letters*, **2010**. *8*(S1), 53–58.

7 V(III)-Doped Nickel Oxide-Based Nanocatalysts for Electrochemical Water Splitting: Influence of Phase, Composition, and Doping on the Electrocatalytic Activity

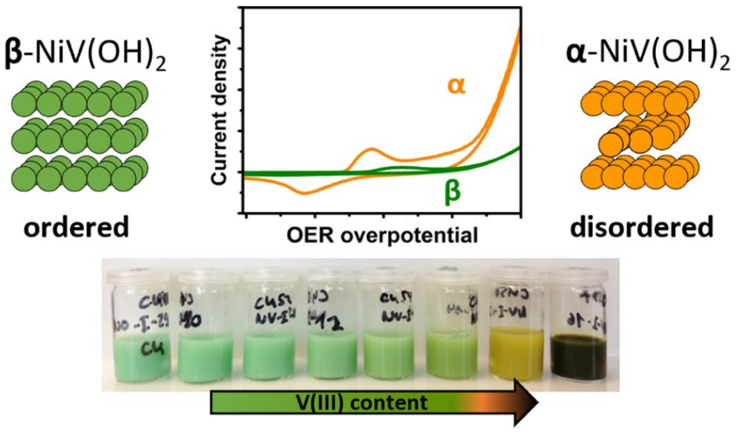

This chapter is based on the following publication:

V(III)-Doped Nickel Oxide-Based Nanocatalysts for Electrochemical Water Splitting: Influence of Phase, Composition, and Doping on the Electrocatalytic Activity, D. Böhm, M. Beetz, C. Kutz, S. Zhang, C. Scheu, T. Bein and D. Fattakhova-Rohlfing, *Chemistry of Materials*, **2020**, 32(24), 10394 – 10406.

7.1 Abstract

Doped nickel oxide-based compounds are attracting great interest as very efficient and abundant catalysts and were thoroughly investigated as battery materials in the past. However, there is still no clear understanding of the influence of dopants on the complex dynamic character of their chemically and potentially driven transformations. We have developed a synthesis procedure enabling the controlled formation of nanosized nickel hydroxide and nickel oxide polymorphs substituted with vanadium(III) [V(III)] ions and further investigated their structure–activity correlation for electrochemical water oxidation. This work therefore primarily focuses on an in-depth structural characterization of the homogeneously doped nanosized α- and β-$Ni(OH)_2$ polymorphs. It could be shown that concentrations of 10 at.% V(III) and higher can effectively inhibit a spontaneous phase transformation known as chemical aging of the turbostratic α-phase to the more crystalline β-$Ni(OH)_2$ phase in neutral aqueous media. The Fe-impurity biased electrocatalytic activity determined for α-/β-$Ni_{1-x}V_x(OH)_2$ showed only a minor increase of 10% oxygen evolution reaction (OER) activity for an 1 at.% doped nonaged sample resembling the α-phase, while a 5 at.% V(III)-doped sample chemically aged over 24 h led to a doubled OER activity versus the undoped reference which transformed into β-$Ni(OH)_2$ over that period of time.

7.2 Introduction

Hydrogen generated by energy from renewable sources is regarded as a potential clean energy carrier and storage medium for the future energy and mobility sector.[1,2] In addition, the generated "green" hydrogen can further be used as a process feedstock to lower the environmental impact in industry and generate valuable chemicals.[3] Alkaline electrolysis has been in commercial use for decades and employs nickel-based electrocatalysts that exhibit some of the highest activity within the 3d metal group, in addition to their relatively low cost and great abundance in contrast to noblemetal catalysts such as RuO_2 and IrO_2.[4,5]

Oxygen evolution reaction (OER) catalysts on the anode side are therefore required to promote the kinetically more demanding half-reaction of the overall water splitting reaction involving four proton-coupled electron-transfer reactions and an O–O bond-formation step.[6] In recent years, diverse nickelbased OER catalysts such as Ni-transition-metal (TM)-layered double hydroxides (LDH),[7–9] Ni-TM-phosphides (Ni-TMP),[10,11] and micro- and nanostructured nickel-TM-oxides and -hydroxides[12,13] have gained considerable attention because of their high catalytic activity and stability under alkaline OER conditions.[14] The outstanding performance of these catalysts is attributed to the synergistic effects of nickel and neighboring TMs as well as to nanosizing and nanostructuring, leading to a significantly increased catalytic surface area or an increased share of exposed highly active crystal facets or coordination unsaturated edge structures.[14] Among the TMs investigated for doping nickel-based materials to date, iron was first reported by Edison in 1908 to influence the electrochemical behavior of nickel hydroxide used for alkaline storage batteries and studied in detail in 1987 by Corrigan concerning its influence on the OER activity of nickel oxide anodes.[15] Since then, Ni–Fe based catalysts were intensively investigated because of their high performance, although the exact mechanism behind the extraordinary decrease in the OER overpotential (ηOER) as well as the structure and identity of the catalytically active site were still unclear. This has been attributed to the numerous difficulties arising from the complex structure–activity relationship in the nickel hydroxide structure.[7]

Recent studies revealed that even trace concentrations of TM ions, down to the parts per billion level in the electrolyte, have a tremendous effect on the OER activity of pure undoped $Ni(OH)_2$ anodes, which otherwise exhibit a low OER activity and rather high OER overpotential.[16,17] In situ X-ray absorption spectroscopy analysis of Ni–Fe oxides together with density-functional theory calculations by the group of Bell have indicated that iron and not nickel is the active site for the catalytic reaction in the mixed-metal oxide films.[17,18] However, the fact that pure iron (oxy)hydroxide films do not show a reasonable OER activity and that the performance of mixed Ni–Fe catalysts reaches a maximum activity for ≈25 at.% Fe level indicates that a surrounding NiOOH matrix is required for the dopant active sites.[18] It could be further shown by X-ray absorption spectroscopy and cyclic voltammetry (CV) that an initially present α-$Ni(OH)_2$ phase with nickel in oxidation state +II is transformed into a structurally similar Ni^{3+}-containing γ-NiOOH phase at elevated potential, representing an initial active phase for OER. This model is in accordance with the phase-transition model of $Ni(OH)_2$ first proposed by Bode et al. and extended by Mellsop et al.[18–20]

These findings highlight the importance of the initial $Ni(OH)_2$ phase as a second important factor determining the electrochemical properties of Ni-based catalysts, whose final structure can strongly vary depending on the synthesis conditions and chemical or electrochemical post-treatments. The α-$Ni(OH)_2$ phase is a layered brucite-type structure composed of Ni^{2+} ions bound to six octahedrally coordinated OH^- anions (each hydroxide being bonded to three nickel ions), with water molecules between the parallel layers.[17] It is further known that several forms of structural disorders exist, including stacking defects, different degrees of hydration, and incorporation of foreign anions resulting in a turbostratic structure.[21] An interesting and electrochemically relevant reaction for the nickel hydroxide is known as chemical aging, in which α-$Ni(OH)_2$ is converted to a well-ordered β-$Ni(OH)_2$ phase with parallel-stacked layers accompanied by a removal of interlayer H_2O. Depending on the pH value, this process can proceed via either a dissolution/precipitation mechanism comparable to Ostwald-ripening, or a “zipper” model displacing interlayer H_2O molecules with hydroxide as the “teeth” on a nickel backbone.[22] Among other TM ions, doping with trivalent Al^{3+} was shown to significantly affect the stacking of $Ni(OH)_2$ layers during the aging process and thereby to stabilize the α-phase.[23,24]

In a recent work by Fan et al., the synthesis of highly OER active monolayers of vanadium(III) [V(III)]-doped $Ni(OH)_2$ LDH of the α-$Ni(OH)_2$ phase was demonstrated, even outperforming the similarly synthesized Ni–$Fe(OH)_2$ LDH. The effect of V-doping on the catalytic activity and the complex nature of Ni–Fe active sites in $Ni(OH)_2$-based OER catalysts are still under investigation. The increased catalytic activity in the Ni(Fe)V–hydroxide system is therefore attributed to a modulation of the electronic structure of the Ni–Fe active sites to optimize the adsorption energies of OER reaction intermediates, an increased conductivity, and an optimized nanomorphology.[7,25] According to reports on the OER mechanism and the activity of $Ni(OH)_2$-based OER catalysts under a strict Fe-free environment, doping elements such as V(III) are not regarded as directly being part of the catalytically active sites but rather modulate the electronic structure of the existing Ni–Fe active sites.[7,25–27] Goncalves et al., therefore, recently presented a literature overview of Vcontaining OER catalysts, identifying the key aspects responsible for the enhanced catalytic activity of various mixed vanadium oxides.[28] besides being indirectly involved in the OER active sites, an optimized nanomorphology with an increased number of accessible active sites or the formation of defect-rich $Ni(OH)_2$ phases or both are expected to significantly influence the overall OER activity.[7] To investigate such a structure–activity relationship of V(III)-doped $Ni(OH)_2$, we have synthesized nanosized $Ni_{1-x}V_x(OH)_2$ with different degrees of V-doping to address the following questions: (i) whether the doping element vanadium is incorporated in the crystal structure and how it affects the morphology on the nanoscale, (ii) how V-doping influences the phase transformation of α- to β-$Ni(OH)_2$ phase during the chemical aging process, and (iii) how the altered phases and nanostructures of doped $Ni(OH)_2$ correlate with the catalyst performance toward the OER. V(III) was chosen as a doping element in this work as preliminary experiments with a series of TMs [Co(II), Mn(II), Cr(III), and V(III)] showed a comparably strong effect on the phase transition of α- to β-$Ni(OH)_2$. As small particle sizes below 10 nm[29–31] and a high degree of disorder[32,33] within the structure of nickel hydroxide are reported to positively influence the catalytic activity of the material, as shown for recent examples of highly OER-active nanostructured α-$Ni(OH)_2$,[34–36] we have modified a rapid aqueous oxidation method introduced by Sutto for the synthesis of various metal hydroxide nanoparticles39 to obtain nanosized undoped and V-doped α-$Ni(OH)_2$.

7.3 Result and Discussion

7.3.1 Structural Characterization of Time-Dependent Phase Transitions of Undoped and V(III)-Doped $Ni(OH)_2$.

Figure 1 depicts the synthesis approach used for the fabrication of pure and vanadium-doped α- and β-$Ni(OH)_2$ polymorphs. Rapid oxidation of the aqueous Ni(II)/V(III) solution and quenching with MeOH under optimized reaction conditions (see the Supporting Information Figures S1–S4)

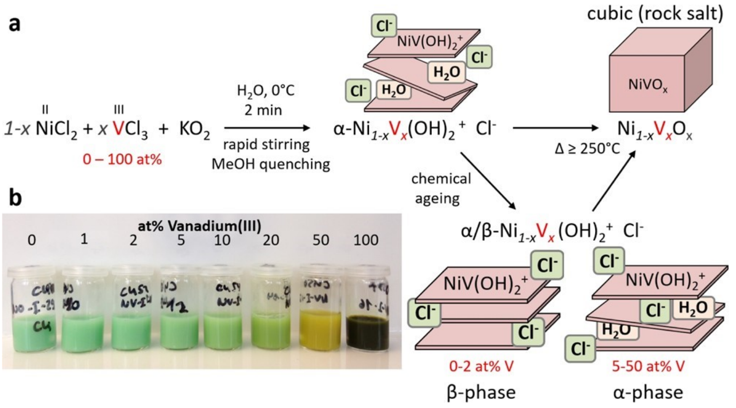

Figure 7.1: Schematic illustration of products prepared by the α/β-$Ni_{1-x}V_x(OH)^{2+}Cl^-$ synthesis route. (a) Schematic illustration of rapid co-precipitation by KO_2, phase transformation by chemical aging, and calcination of $Ni_xV_{1-x}(OH)_2$. (b) Image of $Ni_{1-x}V_x(OH)^{2+}Cl^-$ product series with $x \in [0; 1]$.

lead to the coprecipitation of an α-$Ni_{1-x}V_x(OH)^{2+}$Cl– product whose color gradually shifts from turquoise and green to yellow for increased V(III) concentrations (Figure 1b).

The transformation to the β-$Ni(OH)_2$ phase could be achieved by stirring the aqueous reaction product under ambient conditions, as revealed by X-ray diffractograms (Figure 2a). Reaction products stirred and aged for up to 1 h (Figure 2a black curve) display broad reflections correlated with the α-$Ni(OH)_2$ phase (see the zoomed insets in Figure 2a for details), which gradually transforms into the β-phase with broad reflections visible after 3 h of aging time (dark gray curve). The proposed models for this phase transition known as chemical aging are the ripening and zipper models, wherein the latter one is assumed to dominate under the given reaction conditions in deionized (DI) water.[22] Aging in DI water was chosen to avoid simultaneous vanadium leaching possibly under strong alkaline conditions which could alter the composition and thereby affect the process. The different broadening of the 100 and 101 reflections is therefore associated with a β-phase $Ni(OH)_2$ structure with defects in layer stacking,[33,37] which increases in order by visibly sharpened reflections upon extended aging periods of 24 h (brownish curve) and 2 weeks (orange curve). To effectively discriminate between α- and/or β-phase $Ni(OH)_2$, we have used Raman spectroscopy, which is very sensitive toward structural variation induced by the degree of hydration, crystallinity, or impurities in the form of doping elements. Differently aged products (Figure 2b) indicate the presence of a $Ni(OH)_2$ phase by the strongly visible lattice vibrational mode at 450 cm^{-1} associated with both the α-(lattice mode) and β-phase (A1g mode).[21] With increasing aging time, the α-phase-associated second-order lattice vibrational mode at 1075 cm^{-123} is reduced and not further visible in the spectra of the 24 h-aged sample. In parallel with ongoing aging periods, an increased intensity for the β-phase-associated Eg mode is shown at ≈315 cm^{-1} as well as for the vibrational mode at 3581 cm^{-1} associated with surface OH, lattice/bulk OH, and interlayer H_2O.[21] According to the Raman spectra and X-ray diffractograms, for up to 1 h of aging, pure α-$Ni(OH)_2$ is formed, which slowly undergoes a phase transition to β-$Ni(OH)_2$ by chemical aging in DI water within ≈24 h, with an intermediate product associated with an interstratified α/β-phase $Ni(OH)_2$ structure after 3 h of aging.[22] The emerging β-phase $Ni(OH)_2$ structure for the 3 h-aged samples thereby exhibits strong structural defects shown by respective XRD line broadening and the presence of α- and β-phase related Raman bands, which are associated with a disordered stacking sequence.[22] Dynamic light scattering (DLS) (Figure 2c) shows no measurable signal for fresh (aged below 1 h) $Ni(OH)_2$, as the product is strongly agglomerated and practically not dispersible. However, after 3 h of aging in solution, nanoparticles in the range of ≈10–20 nm are detected, and for 24 h-aged $Ni(OH)_2$, the particle sizes increase to ≈80 nm. The observed change in particle size indicates that XRD line broadening and sharpening upon aging are not solely based on the stacking disorder, as proposed by Delmas and Tessier, but may also originate from the nanosized morphology.[33] To the best of our knowledge, morphological changes on the nanoscale from interstratified α-$Ni(OH)_2$ to β-$Ni(OH)_2$ nanoparticles were not reported in the literature so far, although β-$Ni(OH)_2$ nanoparticles in the range of 10–25 nm were observed but not specifically characterized as an aging product of α-$Ni(OH)_2$.[12] Further transformation to larger β-$Ni(OH)_2$ sheet-like structures with a disordered stacking sequence upon chemical aging and transformation to an ordered β-$Ni(OH)_2$ phase are well described in the literature, including their properties as OER catalysts.[19,38–40] The focus in most of the recent literature is therefore on the activity of specifically synthesized α- or β-phases featuring various nanostructures,[12,34,35,41] however, lacking a detailed investigation of the nanomorphology change during the chemical aging process and the effect of doping elements on this process. In this work, we therefore wish to address the question of how the addition of V(III) ions in the synthesis influences the time-dependent phase transformation and morphological changes and to correlate these modifications with changes in OER activity. The addition of 2 at.% V(III) results in the formation of a product with visibly altered crystallinity, as indicated by the broadened reflections in the respective diffractogram in Figure 2d for the ≈3 h-aged doping series, as compared to the undoped material (black curve). With increasing V(III) concentration, the reflections broaden significantly, which indicates a delayed aging process with increased stacking defects and small crystallite domain sizes. A successful doping of V(III) in the $Ni(OH)_2$ structure by the proposed rapid coprecipitation synthesis is indicated by a gradual shift of the 100 reflection at ≈34° 2ϑ and the 110 reflection at ≈60° 2θ to higher angles in the concentration range of 0–50 at.% V(III) due to the slightly smaller ionic radius of V^{3+}(≈ 0.64Å)[42] versus Ni^{2+}(0.69 Å).[42] Inductively coupled plasma–optical emission spectrometry (ICP–OES) measurements (Figure S1) of washed coprecipitation products furthermore confirmed the quantitative incorporation of vanadium ions over a range of 1–15 at.%. Even for a 50 at.% V(III) concentration in the precursor solution, ≈39 at.% vanadium is incorporated in the reaction product without any visible side phase formation (as observed by

XRD) (Figure 2d). The presence of vanadium ions is visible in the Raman spectra of samples doped with as little as 1 at.% V(III), with an additional band present at around ≈775 cm^{-1} attributed to the V–O vibrational mode, which was not reported in the literature so far for doped $Ni(OH)_2$ but for nickel–vanadium mixed oxides.[43] With increasing vanadium content, a broad band at ≈845 cm^{-1} with a shoulder at ≈900 cm^{-1} arises. These may be attributed to vanadium oxide anions, which may form after the solubility limit of V^{3+} ions in $Ni(OH)_2$ is reached.[43,44] The insertion of vanadate anions into the interlayer space was described by Park et al.[45] This concentration-dependent increase of interlayer ion-associated bands is correlated with a decrease in the intensity of the β-phase-associated band at 3581 cm^{-1}, suggesting a lower content of stacked $Ni(OH)_2$ sheets or β-$Ni(OH)_2$ particle size with the surrounding α-phase.[22,29] Doping concentrations of 50 at.% V(III) in the precursor solution, corresponding to ≈39 at.% V(III) content in the product (Table S1), show one dominant band at 850 cm^{-1}, besides the broadened bands at ≈775 and ≈900 cm^{-1}. The difference in band intensities may therefore be explained by an altered amount of excitable inter- and intralayer V–O vibrations.

A chemical aging period of 24 h for the $Ni_{1-x}V_x(OH)_2$ series reveals a correlation between the V-doping concentration and the crystallization process over an intermediate nanocrystalline β-phase $Ni(OH)_2$ (3 h-aged sample) with high stacking disorder to form the β-phase product (24 h-aged sample) with increased stacking order. Doping concentrations as low as 2 at.% V(III) (Figure 2e) significantly delay the ordering of $Ni_{1-x}V_x(OH)_2$ sheets with concentrations from 10 at.% V and higher, fully preventing further crystallization, as shown by the matching diffractograms of 3 versus 24 h-aged samples with respective concentrations. An inhibiting effect of V(III) ions on the β-$Ni(OH)_2$ crystallization and ordering by chemical aging is also visible in the Raman spectra of the differently aged doping series. The intensity of the band corresponding to the A1g lattice mode at ≈450 cm^{-1}, corresponding to both α- and β-$Ni(OH)_2$,[21] is inversely correlated to the V(III) concentration as well as to the band at 3581 cm^{-1}, which is associated with an O–H stretch/lattice OH and layer H_2O mode[21] observed for undoped β-phase $Ni(OH)_2$ (Figure 2b).

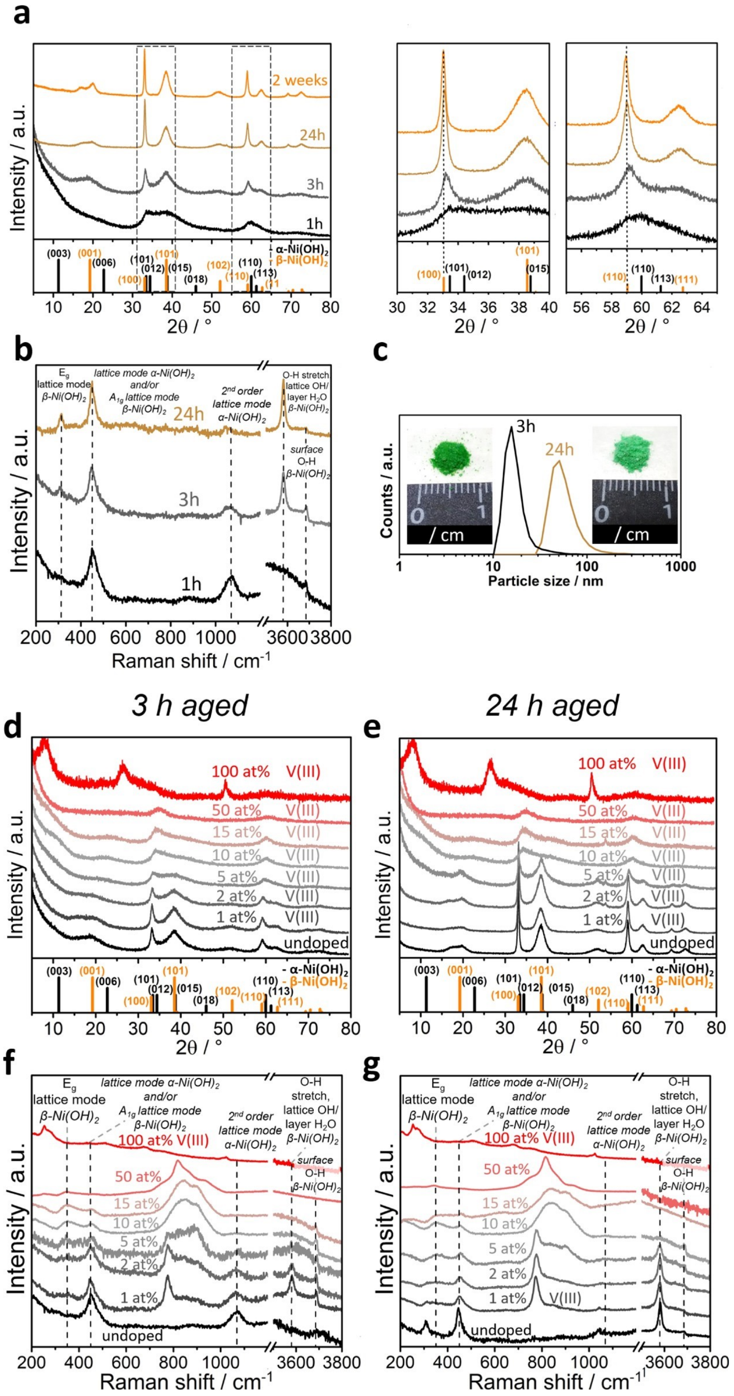

Figure 7.2: Structural characterization of time-dependent phase transitions of undoped and V(III)-doped $NiOH_2$ in aqueous solution. (a) X-ray diffractograms of undoped $Ni(OH)_2$ after 1, 3, and 24 h and 2 weeks of stirring of the aqueous reaction product mixture before drying. (b) Raman spectra of undoped $Ni(OH)_2$ after 1, 3, and 24 h of stirring of the aqueous reaction product mixture before drying. (c) DLS data of a diluted sample of undoped $Ni(OH)_2$ after 3 and 24 h of stirring of the aqueous reaction product mixture. X-ray diffractograms of a series of V(III)-doped $Ni(OH)_2$ [0–100 at.% V(III)] after (d) 1 and (e) 24 h of stirring of the aqueous reaction product mixture. α-$Ni(OH)_2$ $[Ni(OH)_2 \cdot {}_0 \cdot {}_{75}H_2O]$ pattern: ICDD card # 00-038-0715 (rhombohedral, a = b = 3.08 Å, c = 23.41 Å, $\alpha = \beta = 90°$, $\gamma = 120°$). β-$Ni(OH)_2$ ($Ni(OH)_2$) pattern: ICDD card # 00-014-0117 (hexagonal, a = b = 3.126 Å, c = 4.605 Å, $\alpha = \beta = 90°$, $\gamma = 120°$). (e) Raman spectra of a series of V(III)-doped $Ni(OH)_2$ [0–100 at.% V(III)] after (f) 1 and (g) 24 h of stirring of the aqueous reaction product mixture. The bands at 450 cm^{-1} (lattice mode) and 1070 cm^{-1} (2nd order lattice mode) are assigned to the α-$Ni(OH)_2$ phase.[21,22] Bands at 447 cm^{-1} (A1g lattice mode), 3581 cm^{-1} (O–H stretch/lattice OH/ layer H_2O mode), and 3690 cm^{-1} (surface O–H stretch) were assigned to the β-$Ni(OH)_2$ phase.[22]

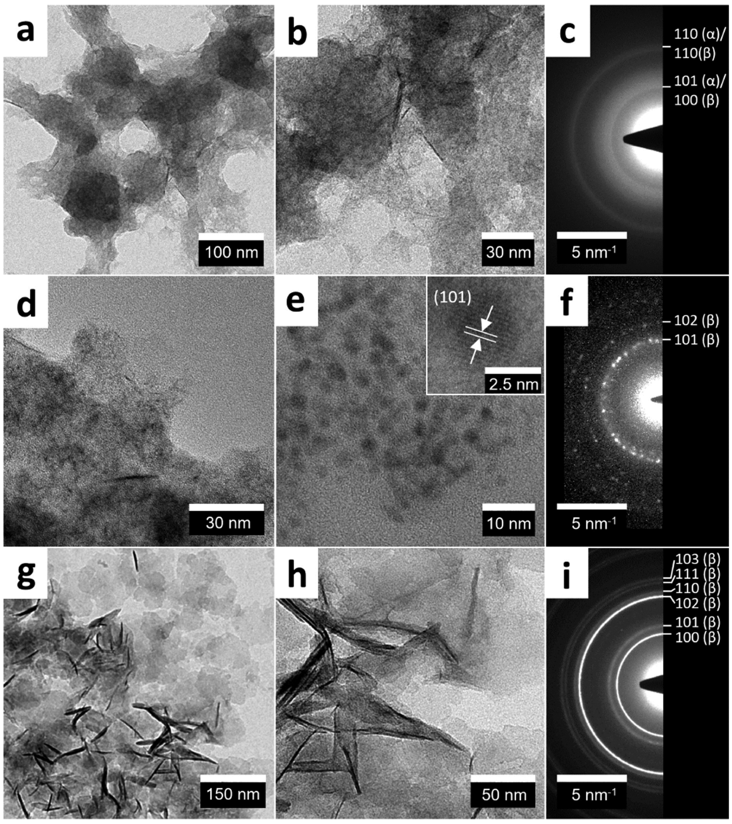

Figure 7.3: Structural characterization of time-dependent phase transformations by TEM of (a–c) 1, (d–f) 3, and (g–i) 24 h-aged $Ni(OH)_2$ samples. TEM images of 1 h-aged $Ni(OH)_2$ (a,b) and turbostratic phase with selected area electron diffraction pattern (c). TEM images of 3 haged sample (d,e) with nanoparticle [(e), and inset] morphology and ED pattern (f). TEM images of the 24 h-aged $Ni(OH)_2$ sample with a nanosheet morphology and ED pattern (i). α-$Ni(OH)_2$ ($Ni(OH)_2 \cdot 0.75\ H_2O$) pattern: ICDD card # 00-038-0715. β-$Ni(OH)_2$ ($Ni(OH)_2$) pattern: ICDD card # 00-014-0117.

7.3.2 Electron Microscopy and Electron Energy-Loss Spectroscopy for the Investigation of Time-Dependent Phase Transitions and Nanoscale Morphology of Undoped and V(III)-Doped Ni(OH)$_2$

Time-dependent phase transitions induced by chemical aging were investigated in more detail by electron microscopy to correlate the changes in the crystal structure analyzed by XRD and Raman spectroscopy of the nanoscale morphology and local structure of the material. Figure 3a–c confirms the amorphous and agglomerated structure of up to 1 h chemically aged Ni(OH)$_2$, as indicated above by XRD, Raman, and DLS data. The electron diffraction pattern shows broad diffuse rings that are attributed to the presence of α-phase Ni(OH)$_2$. The crystallization of small nanoparticles in the range of 2–4 nm from the surrounding turbostratic α-phase (Figure 3d) for 3 haged Ni(OH)$_2$ could be observed directly in high-resolution transmission electron microscopy (TEM) images (Figure 3e and inset) and was already proposed by DLS measurements (Figure 2c), with lattice spacings of single nanoparticles (Figure S5a) corresponding to the β-phase. In agreement with the XRD data, the electron diffraction results confirm the increase in crystallinity and transformation to well-stacked β- phase Ni(OH)$_2$ for 24 h-aged Ni(OH)$_2$ (Figure 3i). The visibly sharpened β-Ni(OH)$_2$ 101 reflection observed by XRD (Figure 2a) upon chemical aging suggests — besides a lower amount of defects in the layer stacking — a growth of the nanosized material along the crystallographic ac-plane that is directly observable in the form of a nanosheet-like morphology and evident in the respective electron diffraction pattern (Figure 3i). The microstructure of doped Ni(OH)$_2$ was investigated for 5 at.% (Figure 4) and 10/15 at.% (Figure S6) V-containing products chemically aged for ≈3 and 24 h, respectively. 5 at.% V-doped Ni(OH)$_2$ aged for 3 h depicted in Figure 4a,b resembles the nanoparticle-based morphology of undoped and equally long-aged hydroxide depicted in Figure 3d,e. Although the crystallinity shown by XRD (Figure 2d) is lower than that of the undoped counterpart (Figure 2a), the electron diffraction pattern (Figures 3f and 4c) indicates a similar β- phase Ni(OH)$_2$ structure with the disordered stacking sequence.

An influence on the phase transformation process becomes evident for 5 at.%-doped samples chemically aged for 24 h. As suggested by the X-ray diffractograms in Figure 2d,e, vanadium doping strongly inhibits the crystallization and proper Ni(OH)$_2$ sheet stacking, which is illustrated by a comparison of the respective electron diffraction patterns (Figures 3i and 4f). According to our TEM investigations, V-doping inhibits particle growth along the crystallographic ac-plane, as only short and stacked sheet-like structures are observable by TEM (Figure 4e) in contrast to tens of nanometer-long well-defined sheets (Figure 3g,h) for equally aged undoped material. Higher concentrations of 10 and 15 at.% V(III) in 3 and 24 h-aged samples (Figure S6a–f), respectively, show very similar nanostructures of particles (3 h-aged) and small sheet-like fragments (24 h-aged) in high resolution-TEM images. ICP–OES measurements (Table S1) confirm that the

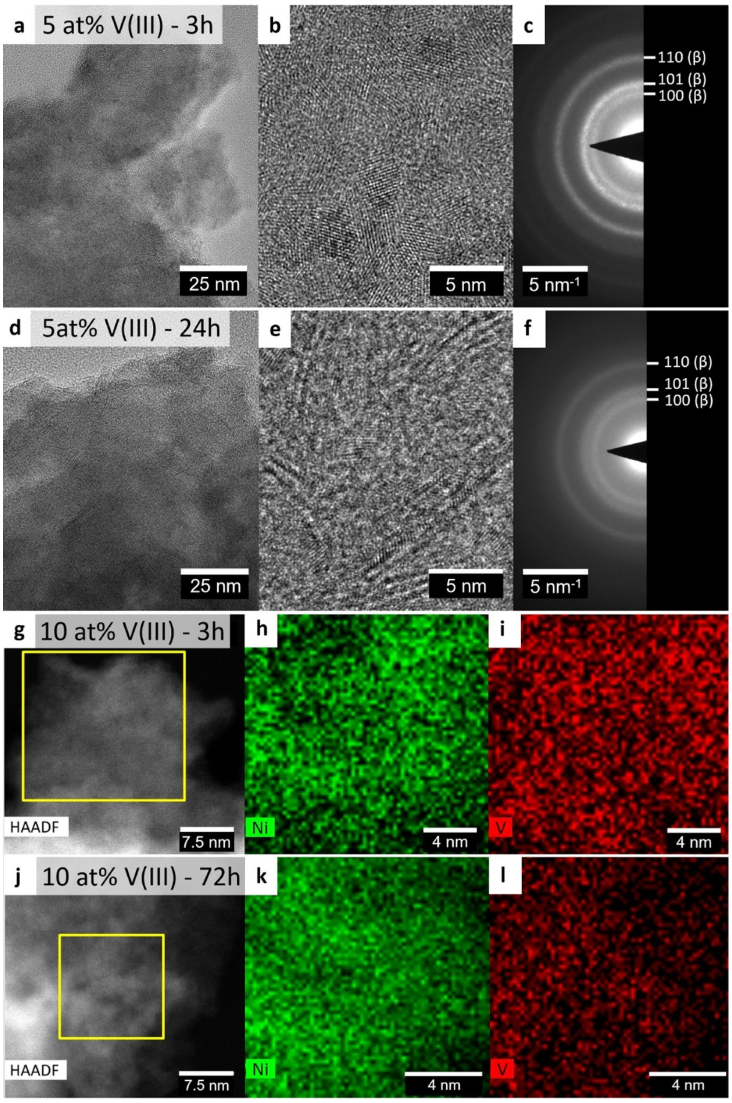

Figure 7.4: Structural characterization of time-dependent phase transformations of V(III)-doped $Ni(OH)_2$ by TEM. TEM images and electron diffraction patterns of 5 at.% V(III)-doped $Ni(OH)_2$ after 3 (a–c) and 24 h (d–f) of aging time. β-$Ni(OH)_2$ ($Ni(OH)_2$) pattern: ICDD card # 00-014-0117. (g–l) STEM atomic number-contrast micrographs and EDX elemental mappings of Ni and V.

V(III) contents in the $Ni_{1-x}V_x(OH)_2$ samples are very close to the nominal doping level of up to 15 at.% V. Scanning TEM (STEM)–energy-dispersive X-ray spectroscopy (EDX) mapping measurements of 10 at.% V-doped samples chemically aged for 3 h (Figure 4g–i) and 24 h (Figure 4j–l) further confirm the uniform distribution of V on the nanoscale (Figure S7a–f), as well as on the micrometer-scale (Figure S7g–i). It can be concluded that the rapid coprecipitation of the Ni(II) and V(III) precursors by KO_2 in an aqueous solution leads to homogeneously doped α-$Ni_{1-x}V_x(OH)_2$ that undergoes a transformation to β-phase nanoparticles after ≈1–3 h, and for low doping concentrations (up to ≈5 at.%), a further assembly/growth of nanoparticles to sheet-like β-$Ni(OH)_2$ particles within 24 h without a detectable segregation of the V(III) dopant. Higher V(III) concentrations ≥10 at.% thereby inhibit the proper stacking required for the β-phase formation also with a 24 h-aging duration. To further investigate the influence of V(III) doping on the phase transformation upon chemical aging, electron energyloss spectra (EELS) (Figures 5 and S8) were recorded. As shown in Figure 5b, Ni-L_3 and Ni-L_2 edges of α-$Ni(OH)_2$ (15 min) and α-$Ni_{0.9}V_{0.1}(OH)_2$ (72 h) are at very similar positions. In contrast, the edges of β-$Ni(OH)_2$ (72 h) shift toward higher energy loss. The so-called chemical shift is caused by a shift in the unoccupied states with respect to the core states (2p for L_2 and L_3 edges), which may indicate the changes in the valence state and the local coordination of the present phase.[46] For example, there is a clear peak shift of ≈0.3 eV between α- and β-$Ni(OH)_2$. On the other hand, the introduction of 10 at.% V(III) hardly changes the chemical shift of the α-like $Ni_{0.9}V_{0.1}(OH)_2$. The calculated electronegativity (dimensionless values according to the Pauling scale) values of Ni^{2+} and V^{3+} are $\mathcal{X}_i = 1.36750$ and $\mathcal{X}_i = 1.545{,}50$ respectively. A shift of the Ni-L_3 edge due to the partial oxidation of Ni^{2+} may not be ruled out, but it clearly plays a lesser role. The EELS measurements serve as further evidence for the V(III)-induced inhibition of phase transformation and stacking of turbostratic α-$Ni(OH)_2$ to the well-stacked β-$Ni(OH)_2$ under the given synthesis conditions.

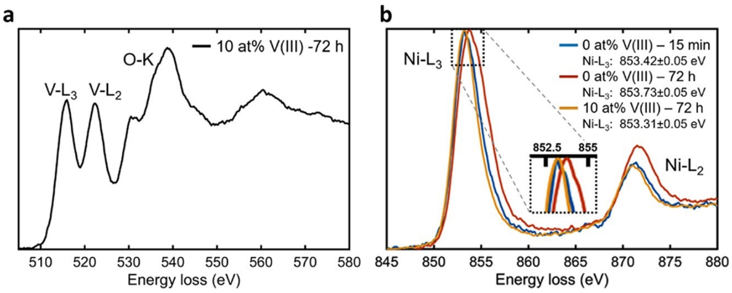

Figure 7.5: Structural characterization of time-dependent phase transformation of V(III)-doped $Ni(OH)_2$ by EELS. (a) EELS spectrum with V-L_3, VL_2, and O–K edges of the 10 at.% V(III)-doped $Ni(OH)_2$ sample after 72 h of aging. (b) Overlay of EELS spectra in the energy loss region of Ni-L_3 and Ni-L_2 edges of $Ni(OH)_2$ samples after 15 min (blue curve), 72 h (orange curve) of aging, and 10 at.% V(III)-doped $Ni(OH)_2$ samples after 72 h of aging (yellow curve).

7.3.3 OER Catalysis Performance of Chemically Aged $Ni_{1-x}V_x(OH)_2$.

The electrochemical performance of chemically aged $Ni_{1-x}V_x(OH)_2$ toward the OER was measured for thin film samples in a diluted KOH electrolyte (see the Experimental Section for sample preparation and exact measurement conditions) with potential trace impurities of Fe ions. SEM images of prepared electrodes of 1 and 24 h-aged product reveal an aggregated particle-like morphology and a smoother sheet-like morphology (indicated by red arrows in Figure S9d), respectively. In cyclic voltammograms, α-phase electrodes (Figures 6a and S10a) show a pronounced Ni^{2+}/Ni^{3+} redox feature centered around 160 mV with respect to the theoretical OER potential of 1.23 V versus reversible hydrogen electrode (RHE) and referenced to ηOER. The Ni^{3+} oxidation peak located at ηOER ≈250 mV in the first cycle with a marked shift to ηOER ≈175 mV for later cycles is attributed to the α–γ phase transformation, as proposed in the literature.[20,47,48] The shift of the oxidation peak to lower potentials within the first cycles is therefore assumed to result from the restructuring of the initial anodic $Ni(OH)_2$ layer.[20] Upon cycling (4th vs 20th cycle), the Ni^{2+}/Ni^{3+} redox feature slightly decreases accompanied by an increase in the OER activity, which is explained by the quasireversible formation of the catalytically active γ-NiOOH phase, as widely accepted in the literature.[19,20,36]

In comparison, the aged β-$Ni(OH)_2$ phase (Figures 6b and S10b) does not show a visible reduction to Ni^{2+} during CV cycling, but a Ni^{3+} oxidation feature that is ηOER ≈50 mV further positive-centered at ηOER ≈300 mV than for the α-phase product. During cycling, this Ni^{2+}/Ni^{3+} oxidation feature is analogously lowered to ηOER ≈225 mV, which is ≈50 mV higher than that of the α-phase. The oxidation peak is therefore associated with a less reversible β-$Ni(OH)_2$ to β-NiOOH transformation and in agreement with the structural characterization of the 24 h-aged $Ni(OH)_2$ product.[20,47,48]

In terms of OER activity, the turbostratic α-phase product (0 at.% V–1 h aged) (Figure 6e) shows, with ≈34.5 mA cm^{-2}, more than 4 times the activity as compared to that with ≈6.8 mA cm^{-2} for the 24 h-aged β-phase $Ni(OH)_2$ (0 at.% V–24 h-aged) (Figure 6f), with both values being determined for the 20th CV scan cycle at an OER overpotential of 400 mV. The overpotentials required to reach an OER current density of 10 mA cm^{-2} were calculated to be ≈340 and ≈432 mV for the 1 and 24 h-aged samples, respectively. In comparison, α-$Ni(OH)_2$ OER catalysts reported by Luan et al. exhibit an OER overpotential of 260–320 mV depending on the morphology with the highest performance obtained for a nanoparticle-based catalyst.[36] A further example of an optimized OER catalyst was reported by Zhang et al. who synthesized an α-$Ni(OH)_2$-nanosheet catalyst on a nickel foam substrate that showed an ηOER of 266 mV.[35] The limited OER activity of our prepared catalyst samples compared to literature reports is attributed to the nonoptimized electrode morphology in the form of densely coated, micrometer thick (see Figure S9), and relatively poorly conductive hydroxide layers deposited simply by drop-casting. Together with the nonoptimized nanomorphology, a comparably low electrochemically active surface area is expected, which further lowers the performance.

The effect of V(III) doping on the cyclic voltammograms of 1 h-aged $Ni(OH)_2$ (Figures 6c and S11a) is a significantly broadened Ni^{2+}/Ni^{3+} oxidation feature beginning around ηOER = 150 mV and ranging up to the OER potential depending on the doping concentration. The low potential part of the feature therefore indicates the presence of α-$Ni(OH)_2$, which undergoes the α–γ phase transformation.[20,47,48] The broadening of the oxidation peak enhanced for higher doping concentrations is further regarded to result from a restructuring of the initial anodic $Ni(OH)_2$ layer that is still observable after 20 scan cycles, as opposed to the undoped α-phase product, where this process is completed within the first 2–3 scan cycles (see Figure 6a). The OER activity of the 1 h-aged sample shows a maximum of ≈38.1 mA cm^{-2} for the 1 at.% V doped sample (Figure 6e and Table S2) and a decrease directly correlated with the doping ion concentration.

In comparison, 24 h chemically aged $Ni_{1-x}V_x(OH)_2$ shows a lower and anodically shifted Ni^{2+}/Ni^{3+} redox feature, as observed for equally aged undoped $Ni(OH)_2$, indicating a β-$Ni(OH)_2$ to β-NiOOH transformation for doping concentrations below 10 at.% V(III). Higher doping concentrations lead to a cathodic shift of the oxidation feature onset by ≈50 mV, which we attribute to a partial contribution by the α–γ phase transformation (Figures 6d and S11b). According to voltammograms, it can be concluded that 24 h-aged $Ni(OH)_2$ doped with ≥10 at.% V(III) shows characteristics of a α/β-$Ni(OH)_2$ mixed or interstratified phase.

The OER activity (Figure 6f and Table S3) exhibits a maximum at a V(III) concentration of 5 at.%, which results in an approximately doubled (≈14.6 vs ≈6.8 mA cm^{-2} at ηOER = 400 mV, 20th scan cycle) catalytic performance for the doped sample.

The discrepancy between the V(III) ion concentrations of catalytically most efficient 1 h- and 24 h-aged samples indicates that the structure/morphology of $Ni(OH)_2$ modified by doping is the reason for the altered OER activity, which is in agreement with literature reports on the electrocatalytic activity of different $Ni(OH)_2$ phases[20,35] and active center sites.[36] It has to be emphasized that not the doping element vanadium is regarded to be part of the active sites and directly involved in the OER, but it mainly accounts for structural/morphological changes that make the Ni–Fe active sites developed in the non-Fe-free environment more accessible. By this mechanism, the V(III) doping indirectly influences the initial OER activity, which was investigated in this work and correlated to the structure.

7.3.4 Structural Characterization and OER Catalysis Performance of Calcined $Ni_{1-x}V_xO$.

With a series of V(III) doping concentrations, the phase transformation from hydroxide to the rock-salt $Ni_{1-x}V_xO$ structure upon calcination was investigated. For the 1 h-aged $Ni(OH)_2$ sample with an α-phase structure, a transition temperature of ≈275 °C was measured by thermogravimetric analysis with differential scanning calorimetry (Figure S12a).

For undoped $Ni(OH)_2$, a calcination temperature of 250 °C was applied to obtain a nanosized product that can be assigned to the NiO rock salt phase with a further growth of crystalline domain sizes at higher calcination temperatures of up to 450 °C (Figure S12b). In comparison, for the 24 h-aged β-phase $Ni(OH)_2$ product, an increased phase transition temperature of close to 300 °C was measured (Figure S12c).

As the applied temperature range of 250–300 °C is below or very close to literature-reported nickel hydroxide–oxide phasetransition temperatures of ≈285 °C[49] for α-$Ni(OH)_2$ and ≈315–325 °C[49,50] for β-$Ni(OH)_2$, presumably a distorted nanosized NiO rock salt phase with residual water content is formed as reported in the literature for similarly low calcination temperatures and indicated by the broad NiO 111 and 200 reflections.[51]

XRD patterns of 300 and 250 °C-calcined samples of 1 haged $Ni_{1-x}V_xOH$ (Figures 7a and S13b, respectively) reveal an inhibited growth of crystalline domains with increasing V(III) content based on significantly broadened peaks and thermogravimetric analysis (Figure S13a). The phase-transition temperature of 1 h-aged $Ni_{0.9}V_{0.1}O$ is increased by ≈+50 °C versus the equally prepared undoped α-$Ni(OH)_2$. The hydroxide to rock salt $Ni_{1-x}V_xO$ transformation (Figure S13a) is regarded to originate from a different degree of stacking disorder and interlayer H_2O in the hydroxide phase caused by vanadium doping. Even at higher calcination temperatures of up to 450 °C, V(III) doping levels of 10 at.% significantly decrease the crystalline domain size, as indicated by the corresponding peak broadening (Figure S13c).

Possible ways to tune the crystallinity are therefore altering the calcination temperature (Figure 7b,c) or the doping level. The calculated crystalline domain sizes of the rock salt structure according to Scherrer's equation derived from XRD signal broadening reveal a continuous decrease from ≈4.5 nm for undoped down to ≈2 nm for 10 at.% V-doped samples calcined at 250 °C (Figure S13d, black data points). Analogously, samples calcined at 300 °C show domain sizes ranging from ≈8.5 nm for undoped NiO down to ≈2.5 nm for 15 at.% V(III)-doped $Ni_{1-x}V_xO$ (Figure S13d, red data points). Along with the decrease of crystallinity due to doping ions, an increase of the lattice parameter from ≈4.185 Å (undoped–300 °C-calcined) to ≈4.205 Å (≥10 at.%–300 °C-calcined) determined from fitted reflection centers of X-ray diffractograms can be observed (Figure S13e and Table S4). The calculated lattice parameters linearly rise between 0 and 2 at.% V, leveling off at 5 at.% and reaching a maximum for 10 at.% doping. The lattice parameters are larger than those for rock salt NiO (4.178 Å, ICDD #01-071-1179) and are associated with a NiOx phase containing hydroxyl group residues not fully transformed into the stoichiometric NiO rock salt phase within that temperature range.[52] Increased V(III)-ion doping that was shown to reduce the crystalline domain size is therefore regarded to lead to increased amounts of hydroxyl group residues enlarging the resulting crystallographic unit cell upon calcination at a moderate temperature of 300 °C. This hypothesis is supported by the formation of a hydrated NiOx phase with even larger lattice parameters ranging from 4.27 to 4.30 Å (depending on the doping level) for a decreased calcination temperature of 250 °C (Figure S13e and Table S5).

Strikingly, even for high V(III) precursor concentrations of 50 at.% resulting in a doping level of ≈39 at.% (Table S1), no additional phases originating from V_2O_3, VO_2, or V_2O_5 can be observed at calcination temperatures of up to 300 °C. At even higher calcination temperatures of 450 °C for a $Ni_{0.9}V_{0.1}OH_x$ sample, no phase separation could be detected (Figure S13c). The high solvation limit of V(III) in the NiOx phase, significantly exceeding the proposed limit of 5–10 at.% V(III) by Park et al., may be attributed to a stabilization effect for nanoscale phases, as described by Fominykh et al. for Feand Co-doped NiO.[13,53] Above the solubility limit, vanadium ions are not further incorporated into the $Ni(OH)_2$ lattice and result in a colored supernatant after washing the synthesis product that is discarded.

Electrodes calcined at 250 °C (Figure S14) and 300 °C were investigated regarding their electrocatalytic activity with focus on the influence of their doping level. Calcination of 1 h-aged α-$Ni(OH)_2$ $Ni_{0.9}V_{0.1}O_x$ product to 250 °C leads to a significant increase of the Ni^{2+}/Ni^{3+} redox feature with an accompanied shift of the oxidation feature from ηOER ≈200 mV to ηOER ≈175 mV.

The activity of the 250 °C-calcined sample determined after 15 scan cycles therefore remained comparable to that of the hydroxide-based sample (Figure 7b) with a Tafel slope even outperforming both the unheated α- and β-phase products (Figure S15).

The cyclic voltammogram of V(III)-doped $Ni_{1-x}V_xOH$ calcined at 300 °C shows a strong increase of the Ni^{2+}/Ni^{3+} redox feature for up to 10 at.%-doped samples, which is attributed to the decreased crystallite domain size and thus increased accessible active sites. An even higher V(III) content leads to a reduction of the redox feature, as the doping ion is shown to be redox inactive in the scanned potential range (see 100 at.% V in Figure 7c).

Concerning the electrocatalytic activity for the OER, samples with 10–50 at.% V(III) content show the best performance with up to ≈27.5 mA cm^{-2} among the 300 °C calcined samples (Figure 7d). The discussed effects of Vdoping on the $Ni(OH)_2$ to NiO phase transition and the resulting crystallite domain sizes upon calcination therefore explain the high catalytic activity of nanosized nickel– vanadium-oxide-based OER catalysts upon calcination at temperatures up to 300 °C. For even higher calcination temperatures of 350 and 450 °C, a decrease in intensity of the Ni^{2+}/Ni^{3+} redox feature is observed with a further shift of the oxidation feature to ηOER ≈150 mV, accompanied by a significant decline of catalytic activity (Figure 7b).

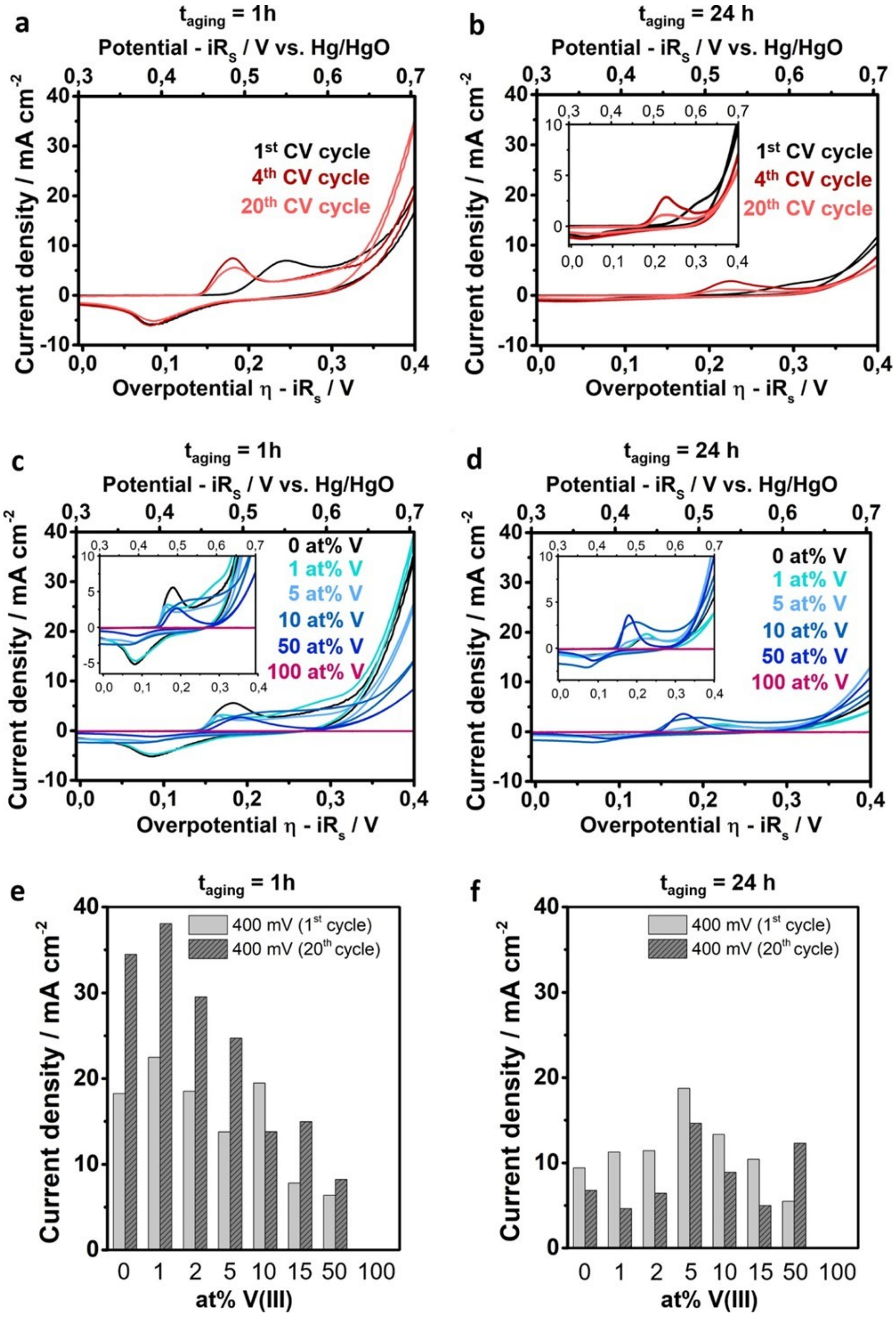

Figure 7.6: Electrochemical characterization of chemically aged and V(III)-doped $Ni(OH)_2$. Cyclic voltammograms (1st, 4th, and 20th scan cycles) of (a) 1 and (b) 24 h-aged undoped $Ni(OH)_2$. (c) Cyclic voltammograms (20th scan cycle each) of (c) 1 and (d) 24 h-aged 0, 1, 5, 10, and 50 at.% V(III) containing $Ni(OH)_2$ (nominal doping concentration) and 100 at.% V(III)-based sample. Plot of OER activities of V(III) containing $Ni(OH)_2$ at an overpotential of 400 mV for the 1st and 20th CV scan cycles for 1 (e) and 24 h (f) chemically aged samples. Mass loading on FTO substrate electrodes ≈50 µg cm^{-2}.

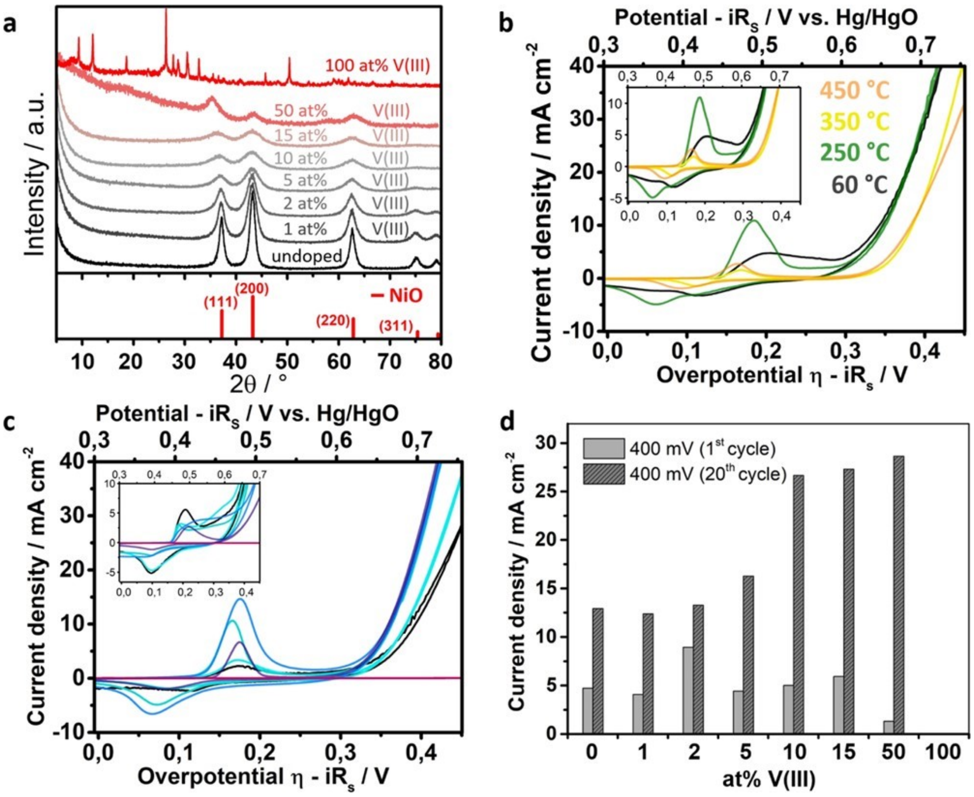

Figure 7.7: Characterization of structure and electrochemical activity of V(III)-doped $Ni(OH)_2$ after calcination. (a) X-ray diffractogram of 300 °C-calcined V(III)-doped $Ni(OH)_2$ [0–50 at.% V(III) black and gray scale]. (b) CV curves (20th scan cycle each) of 1 h-aged 60 °C dried (black) and heated at 250 °C (green), 350 °C (yellow), and 450 °C (orange) $Ni_{0.9}V_{0.1}O_x$. (c) CV curves (20th scan cycle each) of 300 °C-calcined Ni(OH)2 with doping concentrations ranging from 0 (black), 5 (light turquoise), 10 (turquoise), 15 (blue), 50 (darkviolet), and 100 at.% (violet) V(III). (d) Plot of OER activities of V(III) containing (0–100 at.% V), 300 °C-calcined $Ni(OH)_2$ at an overpotential of 400 mV for the 1st and 20th CV scan cycles. Mass loading on FTO substrate electrodes 50 µg cm^{-2}.

7.4 Conclusion

Employing in-depth structural characterization, we have demonstrated that the rapid coprecipitation of nickel(II) and vanadium(III) chloride by potassium superoxide under cooling is a suitable synthesis approach for obtaining homogeneously doped α-$Ni(OH)_2$. Chemical aging by stirring of the reaction product in DI water —a known route for the conversion of α- to β- phase[22,54] — is strongly inhibited by V(III) ions. Samples from 5 at.% V(III) and higher therefore show a delayed transformation to a $Ni(OH)_2$ β-phase product with stacking disorder within 24 h, with samples of 10 at.% V-content and higher structurally resembling the initial turbostratic α-phase. Foreign-ion incorporation in the α- or β-phase $Ni(OH)_2$ has been reported for a variety of TM ions and mostly results in a slightly distorted $Ni(OH)_2$ structure,[23,24,37] as also shown in this work. We attribute the inhibiting effect on the phase transition to the presence of vanadium ions in the structure that prevent the formation of larger $Ni(OH)_2$ nanosheets. These sheet-like structures can stack for low-doping concentrations (<5 at.%) according to the proposed models[19,22] and form β-$Ni(OH)_2$ with a higher (doped samples) or lower (undoped samples) content of stacking defects. Regarding the electrochemical activity toward the OER, it could be shown that a very low V-doping content of 1 at.% can enhance the activity of α-phase-related 1 h-aged $Ni(OH)_2$ by ≈10% to ≈37.5 mA cm^{-2} (ηOER = 400 mV). The catalytic performance of the chemically aged product resembling the β- phase $Ni(OH)_2$, on the other hand, is generally lower by a factor of ≈3 [≈7.5 mA cm^{-2} for undoped, 24 h-aged $Ni(OH)_2$], but it can be doubled to ≈15 mA cm^{-2} by 5 at.% V-doping. We attribute this minor enhancement observed for the 1 h short-aged product to the fact that already the undoped product resembles the highly disordered α-phase, which is reported to be electrocatalytically more active than the ordered β-phase.[35,36,41] The increase in activity is more pronounced for the V-doped and chemically aged samples because of the difference in crystallinity and phase. For these samples, a higher V(III) content effectively prevents the transformation to the ordered and stacked β-phase $Ni(OH)_2$. Vanadium doping in this synthesis procedure is therefore regarded to enhance the OER activity not as part of the active centers which are regarded to be Ni–Fe-based in the Fe trace ion-containing environment but indirectly by its influence on crystallization upon chemical aging. The resulting structure and nanomorphology greatly affect the number of accessible active sites and therefore alters the overall OER activity of the doped material.

Further evidence for this hypothesis is obtained by the analysis of calcined $Ni_{1-x}V_x(OH)_2$. Again, V-doping can be directly correlated to a decreased crystallization or crystalline domain growth of $Ni_{1-x}V_xO$ in the cubic rock-salt structure. Here, even higher doping concentrations of up to 50 at.% enhance the OER activity of the given samples from ≈12 to ≈27.5 mA cm^{-2} although pure vanadium oxide was shown to be redox inactive in the applied potential range.

7.5 Experimental Section

7.5.1 Synthesis of (V-Doped) Nickel Hydroxide Polymorphs

The synthesis of undoped and V-doped nickel hydroxide polymorphs is based on a rapid aqueous oxidation method introduced by Sutto.[55] For the synthesis of different nickel hydroxide polymorphs, 1.125 mmol nickel(II) chloride (Sigma-Aldrich, 98%) was dissolved in 7.5 mL of bidistilled water (Millipore Q grade) to obtain a 0.15 M solution, which was stirred for 1 h in air at room temperature. For V-doped $Ni(OH)_2$ samples, V(III)chloride (Sigma-Aldrich, 97%) was added to the solution to obtain final concentrations of 1, 2, 5, 10, 15, and 50 at.% vanadium and further stirred for 1 h for complete intermixing. Subsequently, the precursor solution was cooled in an ice bath and 2.25 mmol potassium superoxide powder (KO_2, ABCR, 96.5% purity) was slowly added to the solution within 15 s under continuous stirring and quenched after 2 min by addition of 3.75 mL of precooled methanol (analytical grade). Amorphous α-$Ni(OH)_2$ was obtained as a powder after washing and evaporation of the solvent on a hot plate at 60 °C for 30 min and further drying in a laboratory oven in air at 60 °C for 16 h. Ultrasmall β-$Ni(OH)_2$ nanoparticles were obtained as a powder in the same way, while the stirring time after the washing step was prolonged to 3 h. After a stirring time of 24 h, plate-like β-$Ni(OH)_2$ nanoparticles were obtained in the abovedescribed way. During that stirring period, a color change from dark to light turquoise could be observed. The product was not obtained as a powder after evaporation of the solvent but as a film on the glass slide. It had a brighter color compared to the α-$Ni(OH)_2$ powder after the film was scraped off and homogenized in a mortar.

7.5.2 Synthesis of (V-Doped) Nickel Oxide Powder

Dried samples obtained from the synthesis of undoped and V-doped nickel hydroxide were heated in a laboratory oven (NABERTHERM, model N15/65SHA) at 250 and 300 °C in air with a ramp time of 2 h and a dwell time of 2 h.

7.5.3 (V-Doped) Ni(OH)2 and NiO Electrode Preparation

Thin films of the catalytic layer were prepared by drop-casting a diluted dispersion of the wet pellet of nickel hydroxide onto FTO (fluorinedoped tin oxide, TEC15 substrates, DYESOL, Australia) or quartz crystal microbalance (QCM) substrates. FTO substrates were cleaned with an aqueous solution of an alkaline cleaner Extran (MERCK MILLIPORE), bidistilled H_2O, and acetone. To enhance the hydrophilic properties of the surface, substrates were oxygen plasma-cleaned (Femto oxygen plasma surface cleaner, DIENER ELECTRONIC) prior to the drop-casting procedure. A Tefloncoated glass fiber tape leaving an exposed area of 0.159 cm^2 was used for masking. To precisely determine the mass loadings of equally prepared FTO electrodes, 0.5 in. Au-coated QCM sensors (KVG 10 MHz QCM device with gold electrodes, Quartz Crystal Technology GmbH) were acetone-cleaned, equally prepared, and drop-casted with the catalysts according to the method employed for the FTO substrates. Dispersions with a concentration of ≈2 mg mL^{-1} were prepared by mixing 0.2 mL stock solution (wet pellet after the last washing step in 3.5 mL H_2O) with 2.8 mL of Milli-Q H_2O. To reach a mass loading of ≈50 µg cm^{-2}, 4 µL of the dispersion was deposited 1–4 times on a masked (0.159 cm^2) substrate, intermediately dried on a hot plate at 50 °C, and completely dried for 16 h at 60 °C in a laboratory oven. (V-doped) nickel oxide electrodes were fabricated by calcination of substrates at temperatures of 250 and 300 °C with a heating ramp of 2 h and a dwell time of 2 h.

7.5.4 Physico-Chemical Characterization

Wide-angle X-ray diffraction analysis was carried out in transmission mode using a STOE STADI P diffractometer with Cu $K_{\alpha 1}$ radiation ($\lambda = 1.54060$ Å) and a Ge(111) single-crystal monochromator equipped with a DECTRIS solid-state strip detector Mythen 1K. Powder XRD patterns of samples were collected with an ω–2θ scan in the 2θ range from 5 to 90° with a step size of 1°, a fixed integration time of 25–35 s per step, and a resolution of 0.05°. The size of crystalline domains of β-$Ni(OH)_2$ nanoparticles was calculated from line broadening of the 101 reflection with Scherrer's equation and the XRD reference pattern for the β-$Ni(OH)_2$ phase (ICDD card number 00-014-0117: hexagonal, a = b = 3.126 Å, c = 4.605 Å, $\alpha = \beta = 90°$, $\gamma = 120°$). Raman spectroscopy was carried out using a LabRAM HR UV–Vis (HORIBA JOBIN YVON) Raman microscope (OLYMPUS BX41) equipped with a SYMPHONY CCD detection system and a He–Ne laser ($\lambda = 633$ nm). The spectra were recorded using a lens with a 10–fold magnification in the range from 100 to 1000 cm^{-1} with filters of OD 0.3–0.6. Spectrum accumulation mode was used with integrating 600 times 30 s per spectrum. Data acquisition was carried out with LabSpec software.

TEM specimens were prepared from nanoparticles in a 1:1 (v/v) ratio of water to ethanol solution and deposited on a carbon-filmcoated copper grid and dried in air. High-resolution TEM and STEM images as well as electron diffraction patterns were recorded using two FEI Titan Themis microscopes with aberration correction of the probe-forming lenses operated at 120 or 300 kV. EDX analysis was performed using a SuperX windowless, four-quadrant silicon drift detector with a solid angle of 0.7 sr. Electron energy-loss spectra (EELS) were acquired on a Gatan Quantum ERS spectrometer, collecting electrons scattered up to 35 mrad. Dual EELS acquisition enabled the reliable determination of the edge onset of Ni-L3. Multivariate statistical analysis59 was performed on the spectrum imaging datasets to reduce the noise.

SEM images were obtained with an FEI Helios Nanolab G3 UC scanning electron microscope equipped with a field emission gun operated at 3–5 kV. Specimens were prepared from nanoparticles in a 1:1 (v/v) ratio of water to ethanol solution and deposited on FTO or Si substrates that were glued onto a stainless-steel sample holder with silver lacquer. EDX measurements were performed at an operating voltage of 20 kV with a X-MaxN silicon drift detector with an 80 mm2 detector area (Oxford Instruments) and AZTec acquisition software (Oxford Instruments).

7.5.5 Electrochemical Characterization

For electrode preparation, dispersions with a concentration of around 2 mg mL^{-1} were produced by mixing 0.2 mL of stock solution (wet pellet in 3.5 mL H_2O) with 2.8 mL of Milli-Q H_2O, stirred for 10 min at 500 rpm, and sonicated for ≈30 min. To reach a mass loading of ≈50 µg cm^{-2}, 4 µL dispersion was deposited on a plasma-cleaned FTO substrate or Aucoated QCM sensors (14 mm, 5 and 10 MHz AT-cut Cr/Au crystals from KVG Quartz Crystal Technology GmbH and Quartz Pro AB) before drying on a hot plate at 50 °C. Electrodes were masked with the PTFE tape to leave circular electrode areas of 0.196 cm^2 (FTO) and 0.126 cm^2 (Au-QCM sensors), respectively. The frequency of uncoated and coated QCM sensor crystals was determined with a QCM200 5 MHz measurement system (Stanford Research Systems Inc.) and an openQCM 5/10 MHz measurement system (Novaetech S.r.l.). Deposited mass loadings on QCM chips were calculated according to the Sauerbrey equation from the determined frequency differences Δf, an overlapping electrode area A of 0.196 cm^2, and sensitivity factors C_f of 56.6 and 4.4 Hz µg^{-1} cm^2 for a 1 in. 5 MHz and 1/2 in. 10 MHz AT-cut crystals, respectively.

All electrochemical measurements at room temperature were carried out in a three-electrode setup with the quartz cell filled with 15 mL of 0.5 M KOH (Sigma-Aldrich, volumetric solution) as the electrolyte using an PGSTAT302N potentiostat/galvanostat (Metrohm Autolab B.V.) equipped with an FRA32 M impedance analyzer connected to a Hg/HgO (0.5 M KOH) reference electrode. To convert all potentials measured against the Hg/HgO (0.5 M KOH) reference electrode and to ensure stability of the potential before and after every measurement session, the potential was measured against a RHE (HydroFlex, GASKATEL Gesellschaft für Gassysteme durch Katalyse und Elektrochemie mbH) stored in 0.5 M KOH and that was in turn verified by a self-constructed Pt-wire/H_2 (≈1 atm) electrode. The potential was determined to be 0.925 V, which is in accordance with literature-stated values.[16]

The electrochemical activity of the catalyst on FTO substrates was measured by iR-drop-corrected linear sweep voltammetry (LSV) in a potential window of 1.1–1.7 V versus RHE in 20 scan cycles with a scan rate of 10 mV s^{-1}. Impedance spectroscopy data at 1.0 V versus RHE were recorded prior to each measurement to determine the corresponding electrolyte resistance (95%) from the high-frequency region. The compensated resistance was typically in the range of 18–20 Ω. Nickel hydroxide mass-based catalyst activity was either directly calculated with the measured QCM determined mass loadings (of an equal drop-cast volume) or calculated from the coating volume (3–15 µL) of a dispersion of known concentration (2 mg mL^{-1}). Current densities were determined from the mean value of capacity currentcorrected (mean current in the potential region 1.0–1.23 V vs RHE) anodic and cathodic scans of the respective LSV cycle.

7.5.6 Supporting Information

The Supporting Information is available free of charge at `https://pubs.acs.org/doi/10.1021/acs.chemmater.0c02851`. Experimental details, XRD patterns, SEM images, TEM images, TGA/DSC curves, mass-based activities at different overpotentials, and CV measurements.

Bibliography

[1] D. Parra, L. Valverde, F. J. Pino & M. K. Patel. *Renewable and Sustainable Energy Reviews*, **2019**. *101*, 279–294.

[2] A. Boretti. *International Journal of Hydrogen Energy*, **2013**. *38*(4), 1806–1812.

[3] D. Kushnir, T. Hansen, V. Vogl & M. Åhman. *Journal of Cleaner Production*, **2020**. *242*, 118185.

[4] R. Subbaraman, D. Tripkovic, K.-C. Chang, D. Strmcnik, A. P. Paulikas, P. Hirunsit, M. Chan, J. Greeley, V. Stamenkovic & N. M. Markovic. *Nature materials*, **2012**. *11*(6), 550–557.

[5] B. Steen & G. Borg. *Ecological Economics*, **2002**. *42*(3), 401–413.

[6] C. Hu, L. Zhang & J. Gong. *Energy & Environmental Science*, **2019**. *12*(9), 2620–2645.

[7] K. Fan, H. Chen, Y. Ji, H. Huang, P. M. Claesson, Q. Daniel, B. Philippe, H. Rensmo, F. Li, Y. Luo & L. Sun. *Nature communications*, **2016**. *7*, 11981.

[8] W. Ma, R. Ma, C. Wang, J. Liang, X. Liu, K. Zhou & T. Sasaki. *ACS nano*, **2015**. *9*(2), 1977–1984.

[9] Z. Cai, X. Bu, P. Wang, J. C. Ho, J. Yang & X. Wang. *Journal of Materials Chemistry A*, **2019**. *7*(10), 5069–5089.

[10] B. You, N. Jiang, M. Sheng, M. W. Bhushan & Y. Sun. *ACS Catalysis*, **2016**. *6*(2), 714–721.

[11] M. Ledendecker, S. Krick Calderón, C. Papp, H.-P. Steinrück, M. Antonietti & M. Shalom. *Angewandte Chemie (International ed. in English)*, **2015**. *54*(42), 12361–12365.

[12] M. Gao, W. Sheng, Z. Zhuang, Q. Fang, S. Gu, J. Jiang & Y. Yan. *Journal of the American Chemical Society*, **2014**. *136*(19), 7077–7084.

[13] K. Fominykh, P. Chernev, I. Zaharieva, J. Sicklinger, G. Stefanic, M. Döblinger, A. Müller, A. Pokharel, S. Böcklein, C. Scheu, T. Bein & D. Fattakhova-Rohlfing. *ACS nano*, **2015**. *9*(5), 5180–5188.

[14] V. Vij, S. Sultan, A. M. Harzandi, A. Meena, J. N. Tiwari, W.-G. Lee, T. Yoon & K. S. Kim. *ACS Catalysis*, **2017**. *7*(10), 7196–7225.

[15] D. A. Corrigan. *Journal of The Electrochemical Society*, **1987**. *134*(2), 377–384.

[16] L. Trotochaud, S. L. Young, J. K. Ranney & S. W. Boettcher. *Journal of the American Chemical Society*, **2014**. *136*(18), 6744–6753.

[17] S. Klaus, Y. Cai, M. W. Louie, L. Trotochaud & A. T. Bell. *The Journal of Physical Chemistry C*, **2015**. *119*(13), 7243–7254.

[18] D. Friebel, M. W. Louie, M. Bajdich, K. E. Sanwald, Y. Cai, A. M. Wise, M.-J. Cheng, D. Sokaras, T.-C. Weng, R. Alonso-Mori, R. C. Davis, J. R. Bargar, J. K. Nørskov, A. Nilsson & A. T. Bell. *Journal of the American Chemical Society*, **2015**. *137*(3), 1305–1313.

[19] H. Bode, K. Dehmelt & J. Witte. *Electrochimica Acta*, **1966**. *11*(8), 1079–1087.

[20] S. R. Mellsop, A. Gardiner, B. Johannessen & A. T. Marshall. *Electrochimica Acta*, **2015**. *168*, 356–364.

[21] D. S. Hall, D. J. Lockwood, S. Poirier, C. Bock & B. R. MacDougall. *The journal of physical chemistry. A*, **2012**. *116*(25), 6771–6784.

[22] D. S. Hall, D. J. Lockwood, S. Poirier, C. Bock & B. R. MacDougall. *ACS applied materials & interfaces*, **2014**. *6*(5), 3141–3149.

[23] H. Chen, J. M. Wang, T. Pan, Y. L. Zhao, J. Q. Zhang & C. N. Cao. *Journal of Power Sources*, **2005**. *143*(1-2), 243–255.

[24] Y. Zhao. *International Journal of Hydrogen Energy*, **2004**. *29*(8), 889–896.

[25] P. Li, X. Duan, Y. Kuang, Y. Li, G. Zhang, W. Liu & X. Sun. *Advanced Energy Materials*, **2018**. *8*(15), 1703341.

[26] Z. Zand, P. Salimi, M. R. Mohammadi, R. Bagheri, P. Chernev, Z. Song, H. Dau, M. Görlin & M. M. Najafpour. *ACS Sustainable Chemistry & Engineering*, **2019**. *7*(20), 17252–17262.

[27] J. Jiang, F. Sun, S. Zhou, W. Hu, H. Zhang, J. Dong, Z. Jiang, J. Zhao, J. Li, W. Yan & M. Wang. *Nature communications*, **2018**. *9*(1), 2885.

[28] J. M. Gonçalves, M. Ireno da Silva, L. Angnes & K. Araki. *Journal of Materials Chemistry A*, **2020**. *8*(5), 2171–2206.

[29] R. Wang, J. Lang, Y. Liu, Z. Lin & X. Yan. *NPG Asia Materials*, **2015**. *7*(6), e183–e183.

[30] K. Fominykh, J. M. Feckl, J. Sicklinger, M. Döblinger, S. Böcklein, J. Ziegler, L. Peter, J. Rathousky, E.-W. Scheidt, T. Bein & D. Fattakhova-Rohlfing. *Advanced Functional Materials*, **2014**. *24*(21), 3123–3129.

[31] T. Reier, M. Oezaslan & P. Strasser. *ACS Catalysis*, **2012**. *2*(8), 1765–1772.

[32] C. Tessier, P. H. Haumesser, P. Bernard & C. Delmas. *Journal of The Electrochemical Society*, **1999**. *146*(6), 2059–2067.

[33] C. Delmas & C. Tessier. *Journal of Materials Chemistry*, **1997**. *7*(8), 1439–1443.

[34] L. Xu, Y.-S. Ding, C.-H. Chen, L. Zhao, C. Rimkus, R. Joesten & S. L. Suib. *Chemistry of Materials*, **2008**. *20*(1), 308–316.

[35] Q. Zhang, C. Zhang, J. Liang, P. Yin & Y. Tian. *ACS Sustainable Chemistry & Engineering*, **2017**. *5*(5), 3808–3818.

[36] C. Luan, G. Liu, Y. Liu, L. Yu, Y. Wang, Y. Xiao, H. Qiao, X. Dai & X. Zhang. *ACS nano*, **2018**. *12*(4), 3875–3885.

[37] C. Tessier. *Solid State Ionics*, **2000**. *133*(1-2), 11–23.

[38] M. C. Bernard, P. Bernard, M. Keddam, S. Senyarich & H. Takenouti. *Electrochimica Acta*, **1996**. *41*(1), 91–93.

[39] G. Briggs, G. W. Stott & W. Wynne-Jones. *Electrochimica Acta*, **1962**. *7*(3), 249–256.

[40] W. Visscher & E. Barendrecht. *Journal of Electroanalytical Chemistry and Interfacial Electrochemistry*, **1983**. *154*(1-2), 69–80.

[41] S. C. Jung, S. L. Sim, Y. W. Soon, C. M. Lim, P. Hing & J. R. Jennings. *Nanotechnology*, **2016**. *27*(27), 275401.

[42] R. D. Shannon. *Acta Crystallographica Section A*, **1976**. *32*(5), 751–767.

[43] M. S. Bhuvaneswari, S. Selvasekarapandian, O. Kamishima, J. Kawamura & T. Hattori. *Journal of Power Sources*, **2005**. *139*(1-2), 279–283.

[44] J. P. Schreckenbach, K. Witke, D. Butte & G. Marx. *Fresenius' Journal of Analytical Chemistry*, **1999**. *363*(2), 211–214.

[45] H. W. Park, J. S. Chae, S.-M. Park, K.-B. Kim & K. C. Roh. *Metals and Materials International*, **2013**. *19*(4), 887–894.

[46] S. Zhang, L. Diehl, S. Wrede, B. V. Lotsch & C. Scheu. *Catalysts*, **2020**. *10*(1), 13.

[47] M. E. G. Lyons, R. L. Doyle, I. Godwin, M. O'Brien & L. Russell. *Journal of The Electrochemical Society*, **2012**. *159*(12), H932–H944.

[48] B. S. Yeo & A. T. Bell. *The Journal of Physical Chemistry C*, **2012**. *116*(15), 8394–8400.

[49] X. Liang, J. Xiao, Y. Gou & B. Chen. *Journal of Materials Research*, **2011**. *26*(24), 3091–3097.

[50] T. Sato, T. Nakamura & F. Ozawa. *Journal of Applied Chemistry and Biotechnology*, **1975**. *25*(8), 583–590.

[51] W. Xing, F. Li, Z.-f. Yan & G. Q. Lu. *Journal of Power Sources*, **2004**. *134*(2), 324–330.

[52] H. W. Park, B.-K. Na, B. W. Cho, S.-M. Park & K. C. Roh. *Physical chemistry chemical physics : PCCP*, **2013**. *15*(40), 17626–17635.

[53] S. Le Bihan & M. Figlarz. *Journal of Crystal Growth*, **1972**. *13-14*, 458–461.

[54] S. Zhang & C. Scheu. *Microscopy (Oxford, England)*, **2018**. *67*(suppl_1), i133–i141.

[55] T. E. Sutto. *Inorganic chemistry*, **2014**. *53*(9), 4570–4578.

Interim Comment

Especially in the field of plasmonics, detailed knowledge about shape, size and dimensions of nanoparticles is crucial for understanding and predicition of electronic properties or light absoprtion behaviors. With such particles often referred to as nano antennas the light-matter interaction is essential for their application in energy conversion and plasmonic chemistry or for surface-enhanced sensing and spectroscopy.

Optical nano antennas, like their radio frequency counterparts, propagate, receive or transmit electromagnetic waves and convert the incident energy to plasmonic resonance or electromagnetic excitation. The resonance behavior strongly depends on the size, shape and material of the antenna. Therefore, plasmonic resonance can also be used to gain specific information about nanoparticles acting as an optical antenna at a resolution unable for microscopes to detect, such as adsorption of single atoms at a nanoparticle. However, simulation and resonance prediction of nano antennas requires very specific information about the shape and size of those particles.

While conventional transmission electron microscopy can provide two-dimensional spatial imaging of nanoparticles, electron tomography is able to completely resolve the shape, size and structure of a nanoparticle in three-dimensional space. These properties can be used as a template for plasmonic resonance simulation and allow in combination with a very precisely tunable synthesis the development of highly specific and tunable optical nano antennas.

The following two chapters demonstrate the practical application of electron tomography for a deeper understanding of a controlled growth-mechanism and plasmonic light absorption behavior on the example of gold nanostar antennas.

8 Understanding the role of $AgNO_3$ concentration and seed morphology in the achievement of tunable shape control in gold nanostars

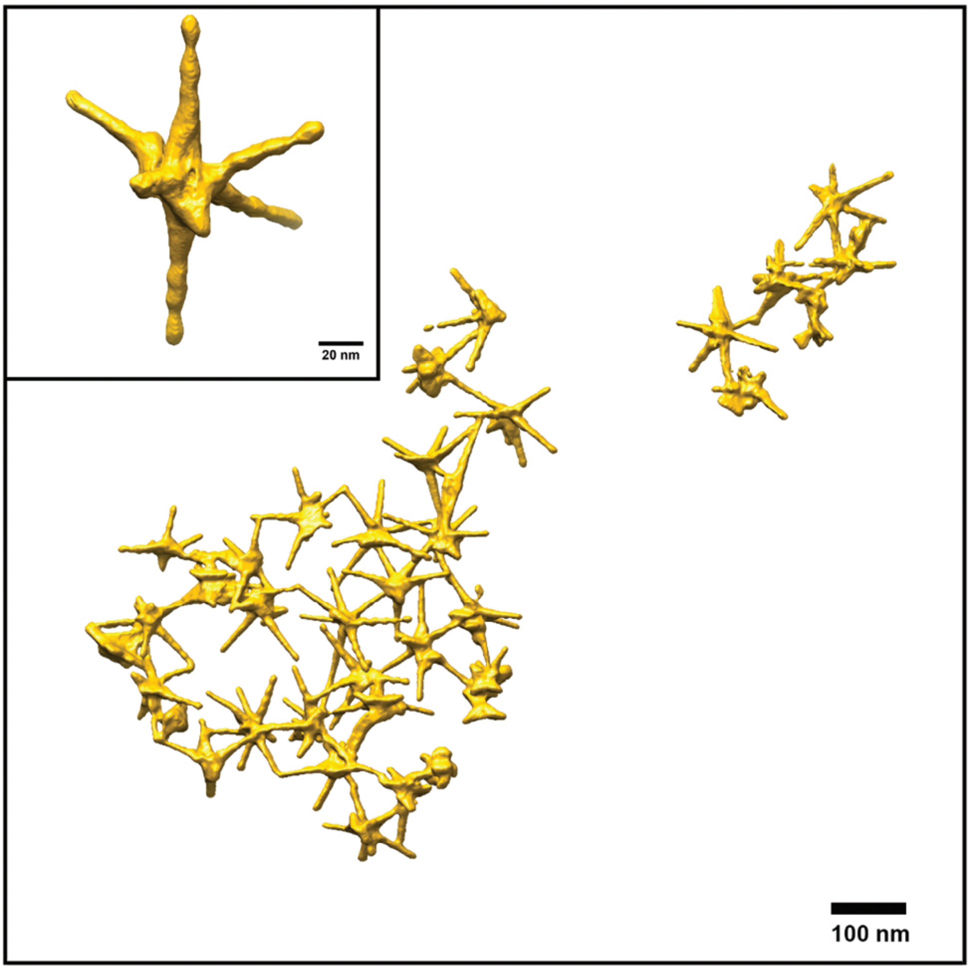

This chapter is based on the following publication:

Understanding the role of $AgNO_3$ concentration and seed morphology in the achievement of tunable shape control in gold nanostars, S. Atta, M. Beetz, L. Fabris, *Nanoscale*, **2019**, 11, 2946 – 2958.

8.1 Abstract

Gold nanostars are one of the most fascinating anisotropic nanoparticles. The morphology of a nanostar can be controlled by changing various synthetic parameters; however, the detailed growth mechanism is still not fully understood. Herein, we investigate this process in six-branched nanostars, focusing first on the properties of a single crystalline seed, which evolves to include penta-twinned defects as the gateway to anisotropic growth into the 6-branched morphology. In particular, we report on a high-yield seedmediated protocol for the synthesis of these particles with high dimensional monodispersity in the presence of Triton-X, ascorbic acid, and $AgNO_3$. Detailed spectroscopic and microscopic analyses have allowed the identification of several key intermediates in the growth process, revealing that it proceeds via penta-twinned intermediate seeds. Importantly, we report the first experimental evidence tracking the location of silver with sub-nanometer resolution and prove its role as a stabilizing agent in these highly branched nanostructures. Our results indicate that metallic silver on the spikes stabilizes the nanostar morphology and the remaining silver, present when $AgNO_3$ is added at a high concentration, deposits on the core and between the bases of neighboring spikes. Importantly, we also demonstrate the possibility of achieving dimensional monodispersity, reproducibility, and tunability in colloidal gold nanostars that are substantially higher than those previously reported, which could be leveraged to carry out holistic computational–experimental studies to understand, predict, and tailor their plasmonic response.

8.2 Introduction

Among the various types of gold nanoparticle systems providing features facilitating field localization, gold nanostars have been widely recognized owing to their tunable plasmon resonances, as they have the potential to be extended from the visible to the infrared.[1–4] Generally speaking, there is a strong correlation between the optical properties and morphology in plasmonic nanoparticles, with sharp edges and tips being further able to create a localized electric field enhancement in proximity to the nanoparticle surface. Due to the structureand size-dependence of the localized surface plasmon resonance (LSPR) bands, morphological control during the synthesis is very important.[5,6] For instance, we have observed how small differences in the shape and number of branches of a nanostar lead to drastic shifts in the LSPR band position and width, with highly branched nanostars being characterized by broad and blue shifted resonances.[7] For this reason, an increasing number of synthetic procedures have been developed to control the size and shape of plasmonic nanoparticles, among which both seed and non-seed mediated methods have shown to afford morphological tunability.[8–10] Importantly, it is crucial to obtain colloidal nanoparticles with high yield and reproducibility and large batch monodispersity. However, while good tunability in the synthesis of anisotropic nanoparticles has been achieved in the case of short, low aspect ratio branches,[11] morphological control in gold nanostars with high aspect ratio features is still not satisfactory.[3,12,13] To improve dimensional monodispersity and reproducibility in gold nanostars (i. e. the ability to consistently obtain nanostars with exactly the same length both within and among batches), it is necessary to develop a fundamental understanding of the role of the chemical variables and their impact on the growth mechanism, and to investigate the key factors affecting growth. One of the issues in achieving this goal (particularly in highly branched nanostructures) so far has been the difficulty in trapping the reaction intermediates due to the generally fast reaction kinetics of these particles, and to understand, as a consequence, how any ill-defined morphology can affect the final products.[14] One of the goals of this work was therefore to develop a fundamental understanding of the growth mechanism of gold nanostars characterized by a few spikes with high shape anisotropy and to identify a simple synthetic methodology that could yield highly monodisperse gold nanostars with consistent reproducibility. Importantly, while some progress has been made in the mechanistic understanding of the growth of branched nanostructures,[15,16] still much needs to (and should) be understood about branched nanostructures with high aspect ratio features, especially for their promising role in optics and plasmonics.

The use of Ag^+ is common in the seed-mediated synthesis of gold nanostars for tuning the spike morphology up to a certain length by gradually increasing the $AgNO_3$ concentration in the growth solution.[17] This phenomenon is similar to that observed in gold nanorods.[18–20] However, while several mechanisms have been proposed to explain in detail the role of $AgNO_3$, they are still highly debated despite the decade-long scientific efforts.[19] For example, a face-specific cetyltrimethylammonium-Br-Ag^+ capping complex was hypothesized to be formed to block specific gold facets thus leading to the formation of nanorods.[21] In another proposed mechanism, underpotential deposition (UPD) of monolayers or sub-monolayers of silver on the gold nanorod surface was invoked as a factor leading to anisotropic growth.[22] In this mechanism, silver deposits on the surface of the nanorods and selectively blocks the selected facets, such as 110, rather than the others, for instance 100 or 111.[23] Unfortunately, while the presence of trace amounts of silver has been reported on the surface of gold nanorods,[23–25] a mechanistic investigation of the role of $AgNO_3$ at different concentrations in the growth of gold nanorods or nanostars has not been carried out yet. In this respect, structural and elemental characterization could provide essential insight into the growth mechanism, ultimately allowing to improve the monodispersity and reproducibility of gold nanostars.

In this manuscript, we describe a novel type of gold nanostar, that we define as 6-branched based on the dominating number of spikes obtained from the statistical analysis of several particles imaged at various tilt angles with scanning transmission electron microscopy (STEM) and shown in Fig. S1† (panel m). For these particles, we elucidate the role of the synthetic parameters employed in the surfactant-based seed-mediated protocol followed to synthesize them. We also propose a growth mechanism that focuses on the properties of the seeds and how they affect the final nanoparticle morphology. These nanoparticles show exceptionally high dimensional monodispersity compared to nanostar systems reported before[26–29] and can be synthesized with high tunability and reproducibility. The reduced number of spikes, whose length and shape can be rationally controlled, limits the side-by-side spike cross-talk, thus reducing LSPR peak broadening, and enables the establishment of fundamental relationships between the morphology and plasmonic properties, which has not been possible so far due to the irreproducibility of the traditional synthetic protocols for gold nanostars.[30] For these reasons, these nanoparticles represent the first example of a branched nanostructure that can be synthesized by design to possess pre-determined physical and optical properties. Based on this potential, it is important to understand the role of the reagents and their interplay during nanostar growth. To address this need, we performed a systematic study to determine how the concentration of the surfactant (Triton X), the reducing agent (ascorbic acid), and $AgNO_3$, and their interaction with the evolving seeds affect the morphology, and thus the LSPR bands of the resulting gold nanostars. By investigating the mechanism of gold nanostar formation in this surfactant-mediated synthesis, we propose a kinetically controlled process as the basis of the growth.

8.3 Results and Discussion

We define this novel type of gold nanostar as 6-branched because the majority of the produced nanoparticles have six branches, even though a closer look reveals a non-zero number of particles with spike numbers between 3 and 7. To confirm that the statistical distribution obtained via traditional 2D TEM micrographs correctly portrays the tridimensionality of the nanostructure, we carried out the tomographic reconstruction of a ca. 70 nm-spike sample, and observed that indeed the number of discernible spikes varied with the tilt angle in the tomogram (Fig. 1). For instance, the number of spikes of a typical star at 0, 40, and 230 degrees is five, six, and four, respectively (Fig. S1a, S1b, and S1d†). To overcome this issue, we determined the maximum number of spikes for a nanostar to be the maximum number measured after exploring all possible orientations in the multiparticle tilt series shown in Fig. S1g–l.† The statistical analysis shows that the product is a mixture of branched nanoparticles with three to seven spikes with $\approx 1\,\%$ spherical impurities, even in the absence of purification. To determine the average spike length for these nanostars, we accounted for the maximum spike length of a spike taking into account the whole tilt series, and generated the statistical distribution as shown in Fig. S1n.† This specific sample, with an average spike length of 70 nm, was obtained when the concentrations of the reagents used were 0.15 M (Triton X), 1.6 mM (ascorbic acid), 30 µM ($AgNO_3$), and 0.14 nM (seeds). Compared to the statistical distribution of the spike lengths obtained with the traditional dimensional analysis carried out with 2D TEM (vide infra), the tomographic reconstruction led to a decrease in the standard deviation by a factor of 10.

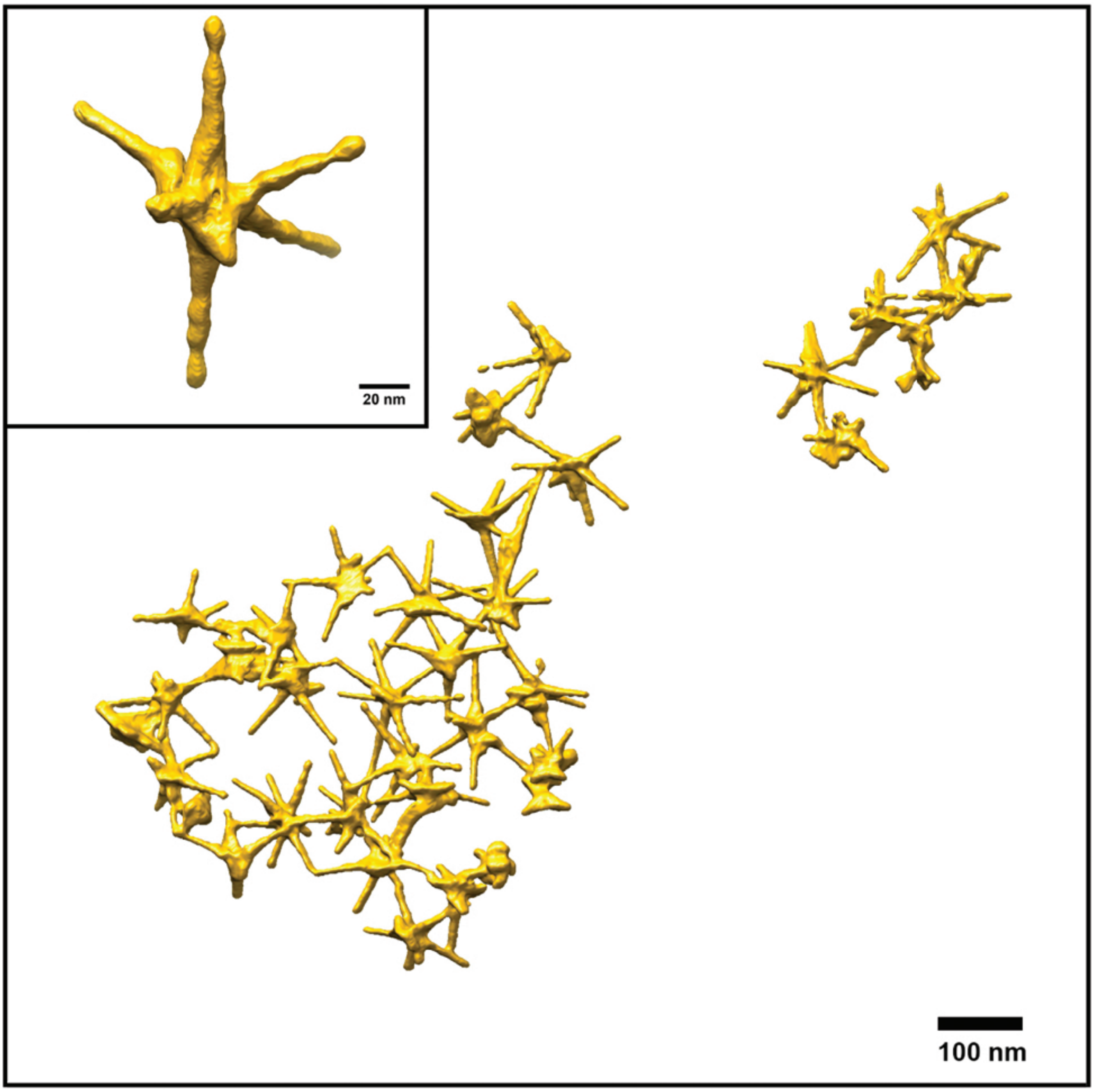

Figure 8.1: 3D reconstruction of a set of nanostars with 70 nm average spike length collected through STEM tomography from –60° to +60° with 10° steps. The inset shows the detailed reconstruction of an individual star collected at high magnification. From the analysis of the multi-particle sample at various tilt angles, we determined the average number of spikes, as shown in the histogram of Fig. S1.†

Among all the reagents needed in this synthesis, the two main recognized parameters influencing anisotropic growth are the properties of the seeds and the concentration of $AgNO_3$. However, in the specific synthesis explored in this work, investigating their interplay with the added surfactant

(Triton X) and the reducing agent (ascorbic acid) also provided useful insight. Nonetheless, our primary goal was to first understand how seed evolution and silver concentration and position affect the growth and yield high shape anisotropy in few-spiked gold nanostars. Therefore, we first carried out the synthesis by varying the concentrations of the four main reagents (i.e., Triton X, ascorbic acid, $AgNO_3$, and seeds) and characterized the obtained nanoparticles to extrapolate trends to identify the optimal synthetic conditions to achieve 6-branched nanostars, the ideal starting point for a more indepth analysis. In this seed-mediated synthesis, seed and growth solutions were prepared separately, but with an equal concentration of the surfactant, starting from concentration values similar to those reported in the initial manuscript of Pallavicini et al., but differing from them to achieve monodispersity and eliminate byproducts.[31] By varying the concentration of the four variables independently, we have investigated and determined how to obtain highly monodisperse 6-branched gold nanostars. While we are aware that multiple parameter spaces could likely provide the ideal conditions to achieve similar results, we deem it beyond the scope of this work to search for additional concentration values, considering it is more important instead to focus on understanding the growth mechanism under these specific sets of conditions. In Fig. 1, we have investigated the role of Triton X and ascorbic acid by modifying their concentrations while keeping the concentrations of $AgNO_3$ and seeds constant at 100 µM and 0.14 nM, respectively. We have examined four different concentrations of Triton X (0.01 M, 0.04 M, 0.15 M, and 0.3 M), and three different concentrations of ascorbic acid (0.8 mM, 1.6 mM, and 3.9 mM). In Fig. 2, the concentration of Triton X varies along a column while the concentration of ascorbic acid is kept constant. For example, in column 1 of Fig. 2, the concentration of Triton X increased from 0.01 M to 0.3 M (0.01 M (1a), 0.04 M (1d), 0.15 M (1g), and 0.3 M (1j)), while the concentration of ascorbic acid was kept constant (0.8 mM). On the other hand, the concentration of Triton X was kept constant throughout a row while the concentration of ascorbic acid was varied. For example, in row 1 of Fig. 2, the concentration of ascorbic acid was increased from 0.8 mM to 3.9 mM (0.8 mM (1a), 1.6 mM (1b), and 3.9 mM (1c)) while the concentration of Triton X was kept constant (0.01 M).

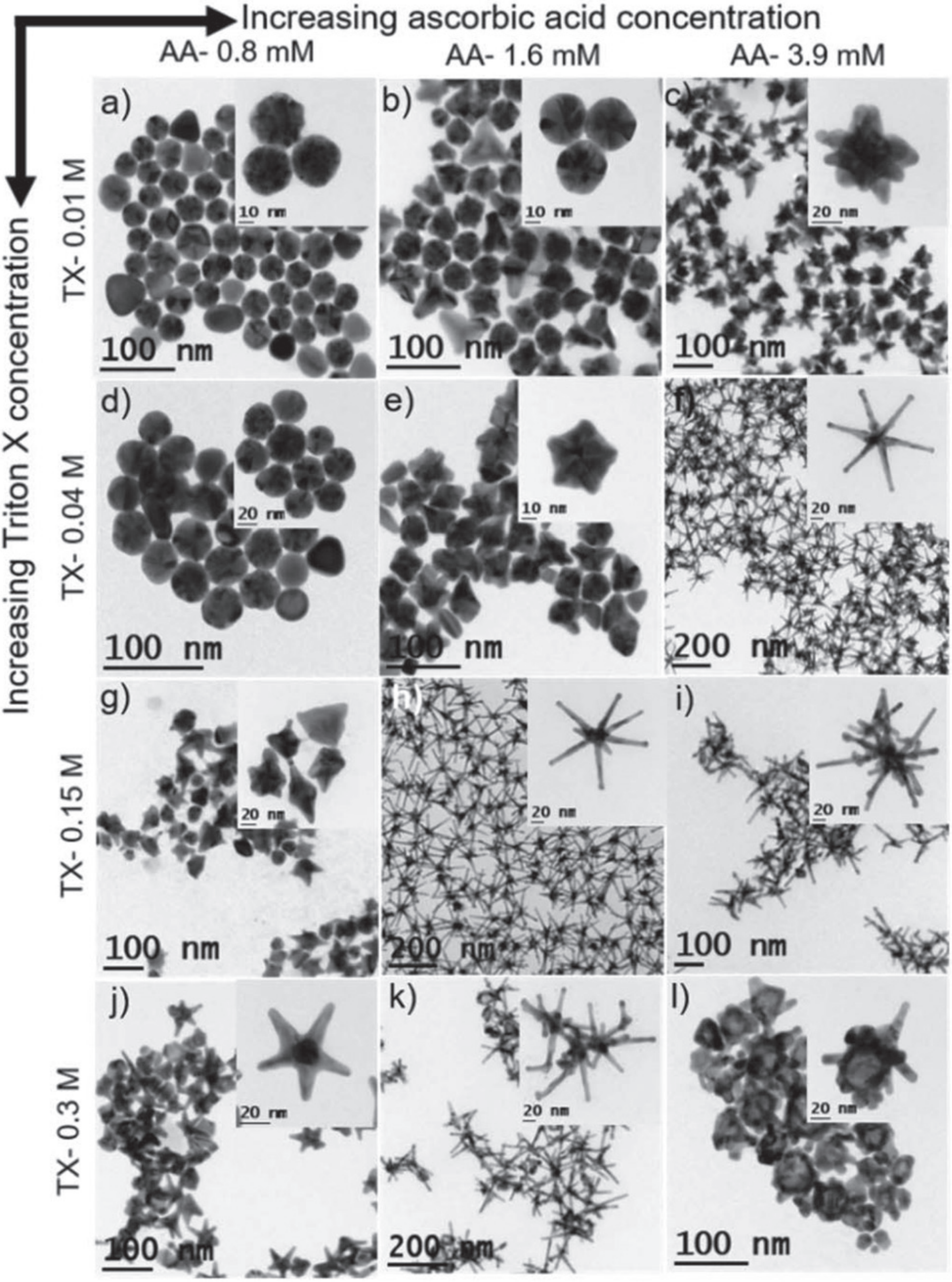

Figure 8.2: (a–l) TEM images of the gold nanoparticles where the concentrations of the two chemical variables (Triton X and ascorbic acid) were progressively changed. In a column, the concentration of Triton X (TX) was varied from 0.01 to 0.3 M while it was kept constant in a row. For example, the concentrations of Triton X in column 1 were 0.01 M (a), 0.04 M (d), 0.15 M (g), and 0.3 M (j). On the other hand, the concentration of ascorbic acid was kept constant in a column while it was increased from 0.8 mM to 3.9 mM in a row. For example, the concentrations of ascorbic acid in row 1 were 0.8 mM (a), 1.6 mM (b), and 3.9 mM (c). The concentrations of $AgNO_3$ (100 µM) and seeds (0.14 nM) were kept constant.

TEM micrographs in Fig. 2 reveal that the 6-branched morphology can be obtained only at ideal concentrations of both the surfactant (Triton X) and reducing agent (ascorbic acid). In a column of Fig. 2, when the concentration of Triton X was increased at a constant ascorbic acid concentration, the morphology changed from polyhedral nanoparticles to 6-branched stars. For example, in column 1 (Fig. 2a, d, g, and j), the morphology of the nanoparticles changed from polyhedral to 6-branched stars at very high Triton X (0.3 M) and very low ascorbic acid (0.8 mM) concentrations. However, the same change in the morphology was also observed at moderately high Triton X (0.15 M) and moderate ascorbic acid (1.6 mM) concentrations in column 2 (Fig. 2h), and at moderately low Triton X (0.04 M) and high ascorbic acid (3.9 mM) concentrations in column 3 (Fig. 2f). Interestingly, at a very low concentration of Triton X (0.01 M) and very high concentration of ascorbic acid (3.9 mM) (Fig. 2c), multibranched stars were formed, where multiple ($n >> 6$) branches were grown from the central core. Complex hyperbranched nanoparticles, with multiple side branches on each of the six main branches (Fig. 2k and i), were formed when both Triton X and ascorbic acid concentrations were higher than the ideal concentrations for 6-branched star formation. Multibranched hollow gold nanoparticles were formed at a very high concentration of Triton X and ascorbic acid (Fig. 2l); we are still investigating their mechanism of formation. We observed similar morphological changes from polyhedral to 6-branched stars to complex hyperbranched nanoparticles in a row when the ascorbic acid concentration was increased at constant Triton X concentration (Fig. 2g–i).

At ideal ascorbic acid (and $AgNO_3$) concentrations for 6-branched nanostar synthesis, the final nanoparticle morphology depends strongly on the concentration of Triton X. We observed that multibranched stars were formed in the absence of Triton X (Fig. S3†), while hyperbranched nanostars were formed at high Triton X concentration (Fig. 2k). In agreement with previous reports, it appears that at a very low concentration of Triton X, gold ions are not tightly bound to the surface by the surfactant Triton X and can be easily reduced by ascorbic acid.[31] By increasing the surfactant concentration above the critical micelle concentration (CMC) of Triton X (0.3 mM), the number of Au-encapsulating Triton X micelles increases,[32] thus decreasing the amount of free Au ions. A reduction in the available free Au ions leads to more controllable gold reduction and branch generation during the growth process. A similar effect has been observed in other surfactantmediated gold nanostar syntheses, in which morphological changes from polyhedral to branched stars were also observed on increasing the surfactant concentration.[29] For gold nanorods, it has been reported that a high concentration of the surfactant (cetyltrimethylammonium bromide, CTAB) is necessary to achieve high aspect ratios, as high amounts of CTAB limit the number of free Au ions and reduce the secondary nucleation events, thus leading to the formation of longer nanorods.[33] However, because it is still unclear how micelle encapsulation for 6-branched nanostars occurs, we can only hypothesize that at extremely high concentrations of Triton X (>0.15 M), unzipping of the surfactant at the surface of the spikes may be taking place (mediated by the excess surfactant in solution), leading to the generation of secondary nucleation events on the spikes,[34] and thus resulting in the formation of hyperbranched nanostars (Fig. 2k).

Ascorbic acid can tune the morphology of the resulting nanoparticles as well, with higher amounts leading to the desired 6-branched nanostars. We believe this to be due to the increase in the negative charge on the growing seeds due to the excess ascorbic acid in the growth solution, resulting in the migration of gold atoms toward low surface energy facets, such as 111, from high surface energy facets like 110, or to an increase in crystal growth kinetics at a higher ascorbic acid concentration.[35,36] Clearly, additional experiments will be necessary to provide further evidence on the nature of the observed nanostar reshaping.

Having established the ideal parameter space for Triton X and ascorbic acid, we then focused our investigation on the determination of seed quality (size and crystallinity) (Fig. 3a). To avoid Ostwald ripening of the seeds on the grid during TEM analysis, we employed n-pentane thiol as a capping agent to quench the reaction and stabilize the seeds, as previously performed to analyze the morphology of growth intermediates. HRTEM micrographs of the seeds disclose that most of the particles have a single crystalline morphology, with an interplanar spacing of 0.23 nm, typical of the (111) plane in FCC gold, and a diameter of around 3 nm (Fig. 3a). It has been proposed that twinned seeds may be fundamental to ensure spike growth on nanostars;[17,37] however, the direct correlation between the defect nature and nanostar morphology has never been shown. We have therefore carried out a detailed analysis of the crystallographic properties of the seeds to correlate them to the resulting nanostar product. The morphology was investigated by quenching the reaction with n-pentane thiol as a capping agent 10 s after the addition of Triton X, ascorbic acid, and $AgNO_3$ for 6-branched stars and multibranched stars. The morphology of the seed turned from single crystalline to twinned crystal, with all gold planes belonging to the 111 family. To be specific, penta-twinned intermediate seeds were formed when the concentrations of Triton X, ascorbic acid, and $AgNO_3$ were ideal for the formation of 6-branched stars (Fig. 3c), whereas multiply twinned intermediate seeds having multiple 111 facets were formed when the concentrations of Triton X, ascorbic acid, and $AgNO_3$ were kept at values observed to produce multibranched stars (Fig. 3g–i). Interestingly, the morphology of a typical penta-twinned intermediate seed (Fig. 3e), which has one nucleation center having five different 111 facets and two nucleation centers having four different 111 facets, gives an overview of the 3D construction of the intermediate seed, which is decahedral (Fig. 3f). The formation of multiple 111 facets in a multiply twinned intermediate supports our hypothesis that at high ascorbic acid concentrations multiple low energy facets 111 are formed, whereas the reduction rates of gold(III) at 0.15 M Triton-X, 1.6 mM ascorbic acid, and 100 µM $AgNO_3$ lead only to the formation of penta-twinned defects.

Interestingly, STEM micrographs of 6-branched nanostars (Fig. 4b–f) show an anisotropic growth over the 111 facets on either side of the twin boundaries for the penta-twinned intermediate seeds, which arises due to the low twinning energy and angle strain.[38] The corresponding fast Fourier transform image further confirms that the two 111 crystal facets are oriented with a common 111 twin plane (Fig. 4e). This is further confirmed by the STEM micrographs of the tips (Fig. 4g–l) which provide a clear view of the crystallographic structure of the penta-twinned seeds from which the spikes were grown, as illustrated in Fig. 3f. On comparing Fig. 4g–l and 3f, one can observe that while in principle these particles should possess either five or seven spikes, the distribution shown in Fig. 3f identifies quite comparable numbers of 5-, 6-, and 7-branched nanostars, with a higher frequency of 6-branched nanostars. We have observed that polyhedral nanoparticles were formed in the absence of $AgNO_3$, thus indicating that $AgNO_3$ is necessary for the formation of the desired 6-branched nanostars (Fig. S4†). The $AgNO_3$ concentration affects the stability of the particle as well, as we observed spherical impurities at or below 30 µM $AgNO_3$, likely due to nanostar reshaping. However, we have not seen the transformation from polyhedral nanoparticles to 6-branched stars by increasing the concentration of $AgNO_3$ at non-ideal concentrations of Triton-X and ascorbic acid (Fig. S5†). We have investigated the effect of $AgNO_3$ when the concentrations of the other reagents are optimized to obtain highly monodisperse and reproducible 6-branched stars (0.15 M Triton X, 1.6 mM ascorbic acid, and 0.14 nM seeds) (Fig. 2h). The concentration of $AgNO_3$ was increased in small increments of 10 µM to determine the possibility of fine-tuning the morphology through $AgNO_3$ (Fig. 5 and Fig. S6†). The spike length increased rapidly by roughly 8 nm by increasing $AgNO_3$ concentration in 10 µM increments from 30 to 60 µM $AgNO_3$. Then, it slowly increased by around 2–3 nm on increasing the amount of $AgNO_3$ from 60 to 100 µM in 10 µM steps (Fig. 5k, and Fig. S7† for dimensional analysis). This evolution was followed by monitoring the red-shift of the longitudinal LSPR band in the UV-Vis spectrum (Fig. 5j and Fig. S6†). The red-shift was also accompanied by a visible change in the solution color from blue to brown as the concentration of $AgNO_3$ increased. Importantly, the narrow standard deviations in LSPR positions measured across different syntheses (Fig. S6†) are a clear indication of the high reproducibility afforded by our synthetic protocol. At a $AgNO_3$ concentration higher than 100 µM, the spike length did not further increase (Fig. 5j and k), rather a blue shift in the LSPR band, reported to indicate a shortening or thickening of the spike, was instead observed.[6,17] The blue shift of the LSPR at 110 µM $AgNO_3$ concentration could also however be due to the deposition of atomic Ag on the core (vide infra), as the ascorbic acid in excess can reduce the remaining silver ions, resulting in an increase in the nanostar core diameter from 25 to 35 nm. Vo-Dinh and coworkers reported that silver overgrowth on gold nanostars is possible and can blue shift the plasmon resonance of the longitudinal mode.[39]

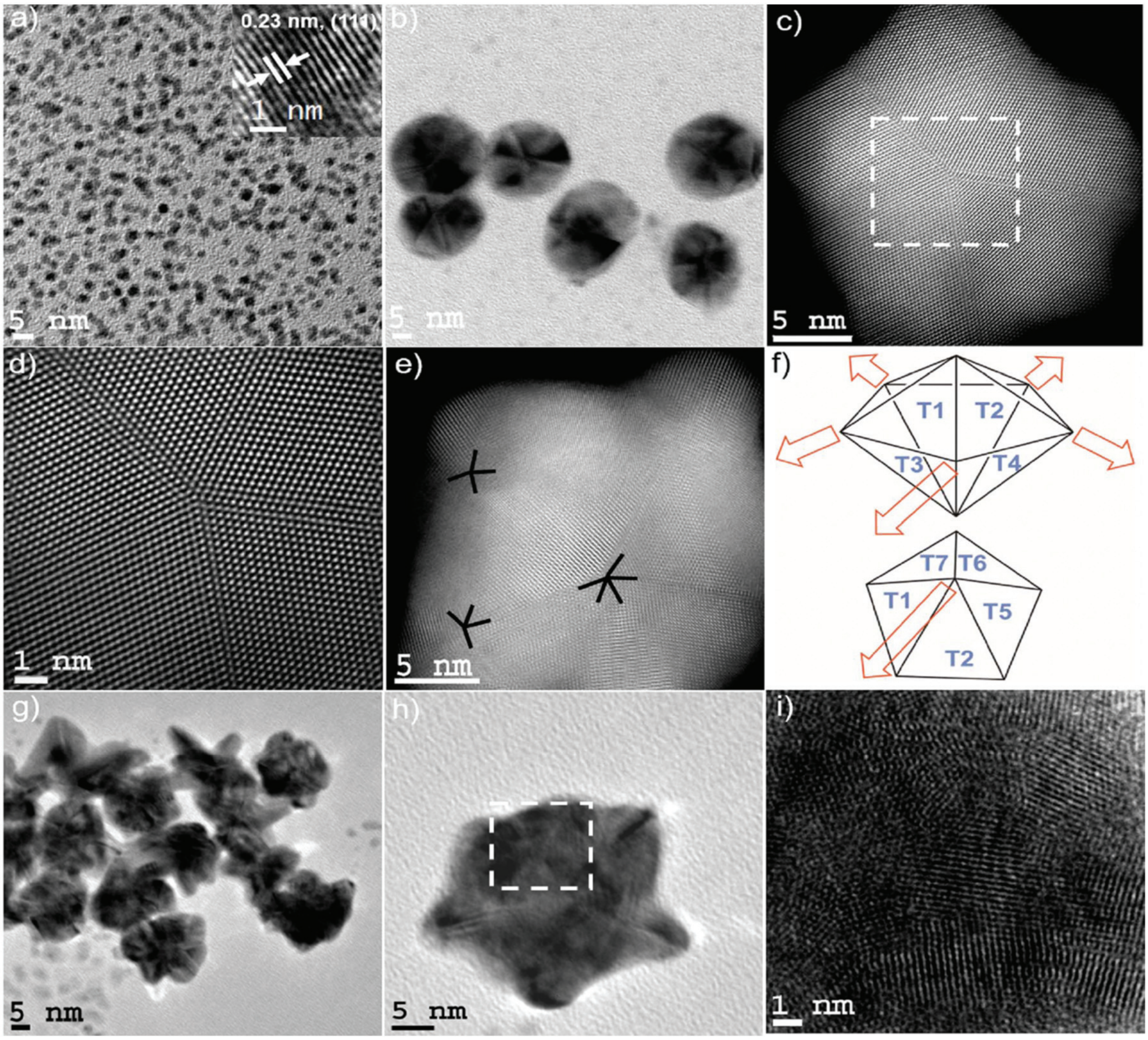

Figure 8.3: (a) TEM micrographs of the seeds with an average diameter of 3 nm. The HRTEM micrograph (inset) shows the single crystalline morphology of the seed, with an interplanar spacing characteristic of the 111 plane in FCC gold. (b, c) TEM and STEM micrographs of penta-twinned intermediate seeds isolated within the first instance of growth of the 6-branched stars. (d) High resolution STEM image (FFT analysis shown in Fig. S2†) of the selected area of Fig. 2c exhibiting a fivefold symmetry. (e) STEM image of a typical penta-twinned intermediate seed showing one five-fold symmetry and two four-fold symmetry defects, which correlates with the 3D construction of the decahedral morphology of the penta-twinned intermediate seeds. (f) Representation of spike growth from decahedral seeds. Top image: Schematic side view identifying the spike growth directions on seeds such as that shown in Fig. 2e. A maximum number of five spikes can grow along the equatorial directions identified by the red arrows, which are determined by four neighbouring facets (T1, T2, T3, and T4). Bottom image: Schematic top view representing five neighbouring facets are shown (T1, T2, T5, T6, and T7). (g–i) TEM and HRTEM images of multiply twinned intermediate seeds isolated within the first instance of growth of the multibranched stars.

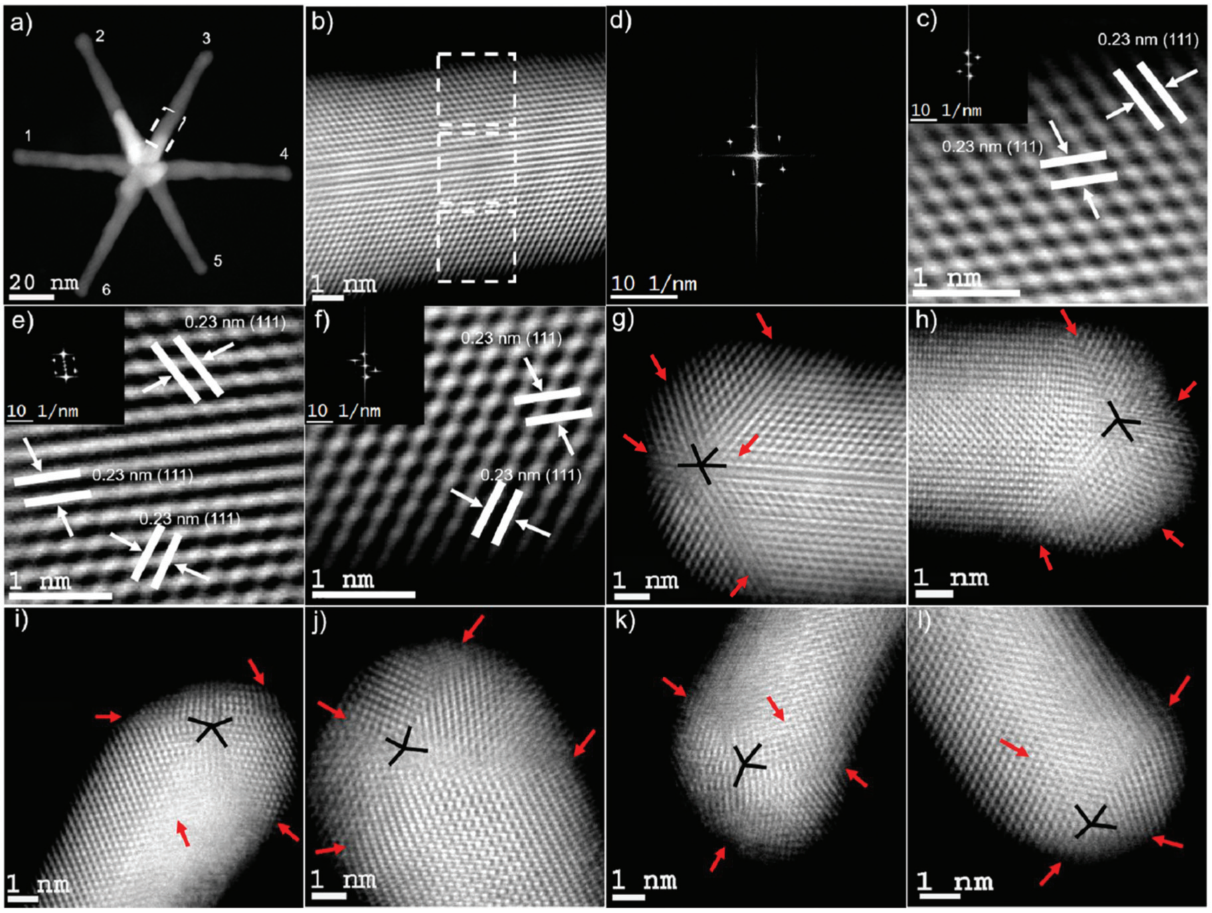

Figure 8.4: 4 (a) STEM image of a typical 6-branched star. (b–f) High resolution STEM images with FFT analysis on the selected area of the spike in Fig. 3a showing the presence of only a twin boundary where the FFT (inset) and lattice fringes represent 111 planes reversely oriented with respect to a common twin plane. (g) STEM micrograph of the tip showing five twinning planes, which indicates that the spike is formed on the twinning axis of a pentagonal unit. (h–l) STEM micrographs of the tips show four twinning planes, indicating that the spike is formed on the twinning axis of a tetrahedral unit. Red arrows show the twin planes.

To study the fate of silver and its role on the evolution of the spike morphology, we first monitored the branch sharpness, which is the ratio between the spike widths at the core and the tip, observing that it increased from 1.2 to 1.9 (Fig. S8†) on increasing the $AgNO_3$ concentration from 30 µM to 100 µM, possibly due to the migration of gold atoms from the tip toward the core. This result further motivated us to study the evolution of the spike morphology. Spike growth was investigated in detail by arresting the reaction at different time points and examining the intermediates via TEM to correlate morphology evolution to the LSPR position, when the concentrations of Triton X, ascorbic acid, and $AgNO_3$ were 0.15 M, 1.6 mM, and 30 µM, respectively (Fig. 6 and Fig. S9†). TEM micrographs (Fig. 6a–l and Fig. S9a–l†) at different time intervals reveal that the branches grew gradually and reached the maximum length (100 nm) after 5 minutes. After that, they shrank, and the process was completed after 12 hours, with an overall shrinkage in the spike length by 30 nm, from 100 nm (5 min) to 70 nm (12 hours). The time-dependent evolution of this reaction was monitored by UV-Vis spectrophotometry (Fig. 6m), which elucidated that the LSPR band gradually red shifted as the spike length increased between 30 seconds and 5 minutes. The LSPR band reached its maximum redshift to 1071 nm after 5 min, and then blue shifted from 1071 nm to 734 nm after 12 hours. The blue shift was associated with the migration of gold atoms from the high energy sites on the tip toward the lower energy sites at the core, resulting in a decrease in the spike length from 100 nm to 70 nm. The LSPR shift was also accompanied by a visual color change in the solution from blue to green to brown to blue, as previously observed for the growth of multibranched gold nanostars and gold nanorods when the spike length was reduced in the late stages of the reaction.[4,20,25,40]

The nanostar morphology at 30 µM $AgNO_3$ concentration for a given growth time was further investigated by STEM (Fig. 6n–p) to assess the spike morphology in detail. STEM micrographs revealed that the gold nanostars grown for 5 minutes contained spherical penta-twinned tips where twin boundaries having 111 facets bridging the sides with the tips can be observed (Fig. 6n). However, after 6 hours, the tip appeared less spherical (Fig. 6o) and it became oblate after 12 hours, with no clearly distinguishable facets, as the pentatwinned morphology of the tips disappeared after 6 hours (Fig. 6o and p). We believe that the driving force for these morphological changes is the surface energy minimization that is achieved by removing reactive edge atoms located at the twin boundaries of highly faceted penta-twinned spikes.[18,41]

To gain further insight into the evolution of the spikes, we have investigated in detail the changes in overall nanostar morphology at the 5-minute (Fig. S10†) and 12-hour (Fig. 5b–d, f, and h) marks, by varying the concentration of $AgNO_3$, starting from the observation that the maximum spike length is reached after 5 minutes and the minimum after 12 hours, for reactions with 30 µM $AgNO_3$. We have used five different additional concentrations of $AgNO_3$ (40 µM, 50 µM, 60 µM, 80 µM, and 100 µM), and observed that the spike length is maximized after 5 minutes (100 nm)

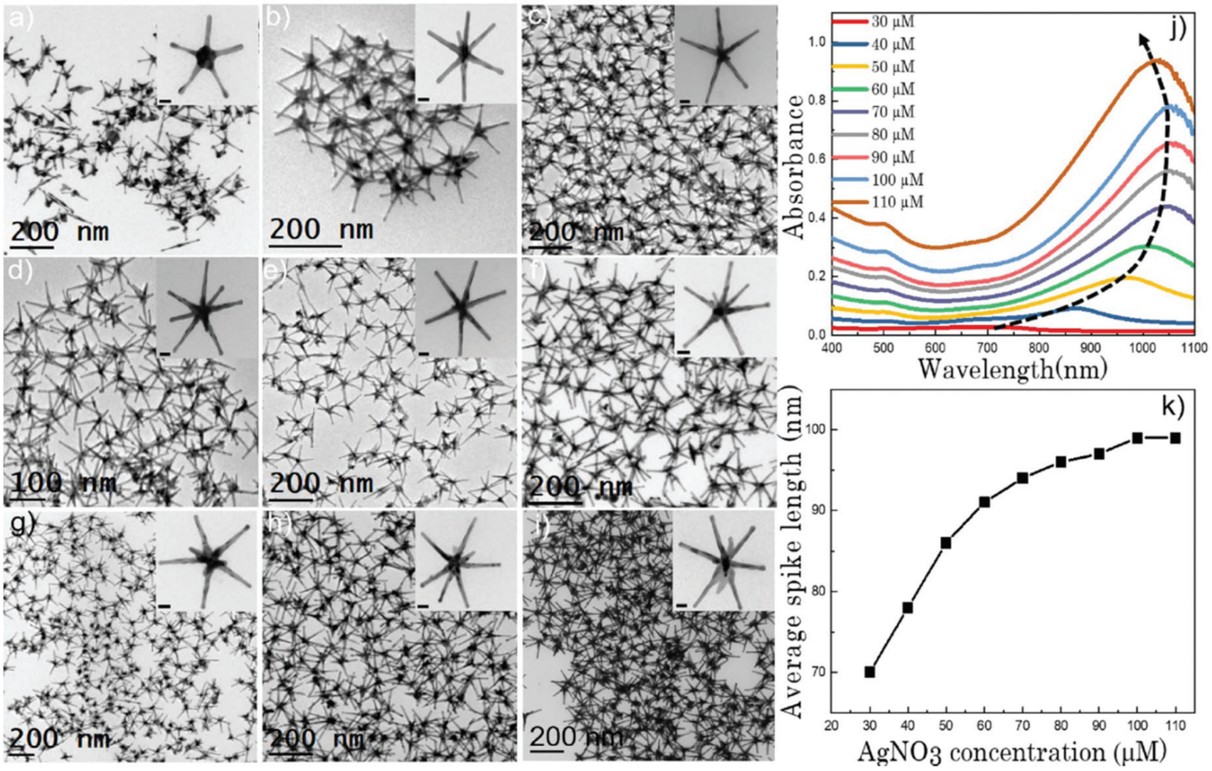

Figure 8.5: (a–i) TEM micrographs of nanostars formed at different $AgNO_3$ concentrations: 30 µM (a), 40 µM (b), 50 µM (c), 60 µM (d), 70 µM (e), 80 µM (f), 90 µM (g), 100 µM (h), and 110 µM (i). The concentration of the other two chemical variables (ascorbic acid and Triton-X) was 1.6 mM and 0.15 M, respectively. Scale bars are 20 nm (inset). (j) UV-vis spectra (normalized) for each of the colloidal dispersions show a gradual red shift with increasing $AgNO_3$ concentration as the spike length is increased, and a blue shift after 100 µM $AgNO_3$ as silver is deposited at the core. (k) Evolution of the average spike length as a function of $AgNO_3$ concentration.

for all $AgNO_3$ concentrations, with additional substantial shape reconstruction occurring at the 12 hour time point. For nanostars synthesized with 30 µM $AgNO_3$, the shape reconstruction was substantial, with a spike length reduction from 100 nm to 70 nm and a loss of the sphere at the tip (Fig. 6n–p). However, the extent of deformation decreased on increasing the concentration of $AgNO_3$ from 30 µM, becoming the lowest for nanostars synthesized at 100 µM $AgNO_3$ (Fig. S10a–f†). For instance, while a 341 nm blue shift was observed for 30 µM $AgNO_3$ stars, only a 6 nm blue shift was observed for 100 µM $AgNO_3$ stars (Fig. 7a–f). We also observed visually that the color did not change from brown to blue when the concentration of $AgNO_3$ was maintained at 100 µM. These results led us to postulate that the 5-minute morphology might be a kinetically trapped version of the thermodynamically stable 12-hour morphology, and that the deposited Ag atoms might significantly reduce the atom diffusion typically observed for the highly energetic gold facets on gold nanoparticles. These observations also established the added important role for $AgNO_3$ (i. e., to stabilize the nanostar shape and size) beyond the well-known shape-inducing role. We attribute the shape reconstruction observed at longer reaction times for low $AgNO_3$

concentration to the fact that the highly energetic gold atoms at the tips can easily diffuse along the spike migrating to more energetically favorable positions on the nanostar, such as the base of the spike. However, when the concentration of $AgNO_3$ was 100 µM, the Ag atoms appeared to stabilize the highly energetic gold atoms, thus inhibiting their diffusion toward the core. A similar result was reported by Tong et al., who observed a blue shift of the longitudinal plasmon peak of gold nanorods when they were kept from 2 h to 13 weeks.[18] The possible reason behind the stability gained with a $AgNO_3$ concentration above 30 µM is the presence of a monolayer of silver atoms that stabilizes the underlying gold atoms on the surface of the nanoparticles with a Au–Ag(UPD)–Cl type of interaction.[42,43] While other interactions may be present, this appears to be the most plausible based on previous reports[23,24,42] and our preliminary voltammetric identification of both Ag(0) and Ag^+ in the nanostar suspension after purification (data not shown).

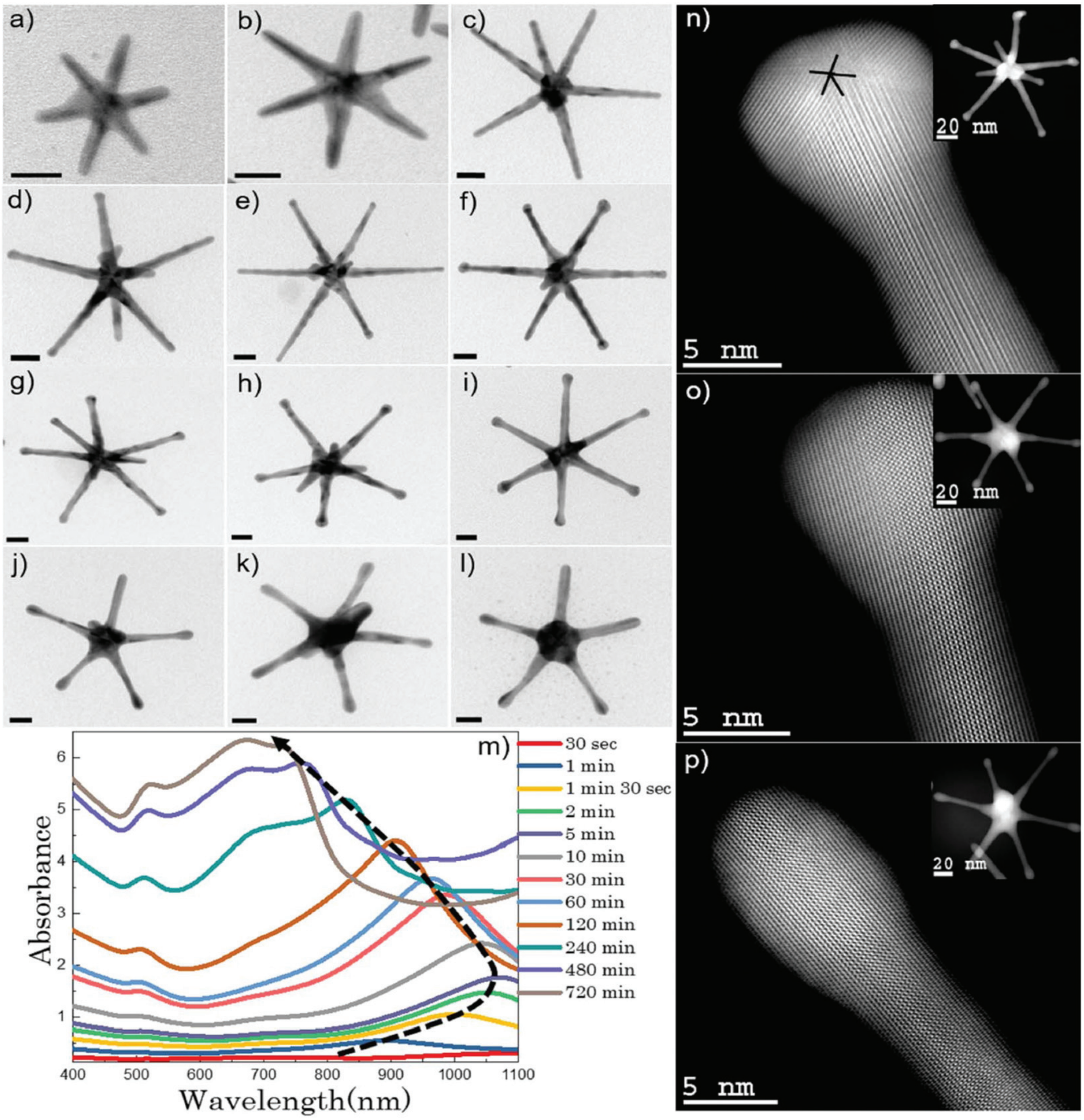

Figure 8.6: (a–l) TEM micrographs of gold nanostars when the concentrations of the growth solution are as follows: Triton-X: 0.15 M, ascorbic acid: 1.6 mM, and $AgNO_3$: 30 µM, for which growth was arrested at the indicated reaction times (30 s (a), 1 min (b), 1 min 30 s (c), 2 min (d), 5 min (e), 10 min (f), 30 min (g), 60 min (h), 120 min (i), 240 min (j), 480 min (k), and 720 min (l)). (m) Corresponding UV-vis spectra (normalized) taken from each aliquot sample indicate that an initial red shift of the longitudinal plasmon peak occurred, which reversed after 5 minutes, and was followed by a permanent blue shift. Scale bars are 20 nm. (n–p) STEM micrographs of the spike at 5 min (n), 240 min (o), and 720 min (p) showing the morphology from the twinned spherical tip to the oblate tip.

We have further investigated the role of Ag by using scanning transmission electron microscopy energy dispersive X-ray spectroscopy (STEM-EDS), to determine whether or not Ag exists as adsorbed species on the Au surface or becomes fully alloyed to Au on the nanostar spike. We also wanted to ascertain whether or not the deposition of increasing amounts of silver at high concentrations of $AgNO_3$ is responsible for the observed morphology stabilization and LSPR blue shifts. Fig. 8 shows the STEM image of 6-branched gold nanostars having three different $AgNO_3$ concentrations (30, 100, and 110 µM) along with a corresponding STEM-EDS map showing the gold signal (red scale) and the silver signal (blue scale), which reveal that silver was alloyed with gold in the nanostars. Moreover, we have observed that the relative silver signal increased with increasing $AgNO_3$ concentration, going from 3.86 % (2.21 % at core, and 5.51 % at spike) to 14.66 % (13.87 % at core, and 15.45 % at spike) when the concentration of $AgNO_3$ was increased from 30 µM to 100 µM, and even further increased to 16.45 % (18.94 % at core, and 13.97 % at spike) when the concentration of $AgNO_3$ was 110 µM. Interestingly, the line-scanned EDS elemental profiles of the spike and the core of 30 µM $AgNO_3$ showed that the amount of Ag was uniform throughout the spike and the core (Fig. 8a' and b'), while it was higher at the side wall of the spike for 100 µM $AgNO_3$, which supports our hypothesis that a monolayer of silver stabilizes the surface Au atoms (Fig. 8c' and d'). Moreover, silver deposition increased at the core at high $AgNO_3$ concentration (110 µM, Fig. 8e'). This growth mechanism also supports the observed patterns in gold nanorod growth, where silver deposits on the side wall of the rod rather than the tips.[23] We further carried out an area scanned analysis of the EDS map to obtain more information about the amount of Ag present in the gold nanostars (Table S1†). The area scan results of the spike at 30 µM $AgNO_3$ show 3.28 % (A1), 8.84 % (A2), and 4.12 % (A3) of Ag present in the tip, side wall, and middle portion of the spike, respectively, which reveals that the amount of Ag present in the spike was almost uniform. On the other hand, the amount of Ag was significantly lower at the core (A4, 2.46 % Ag). However, we have seen an increase in the amount of Ag on the side wall of the spike of the stars at 100 µM and 110 µM $AgNO_3$ (36.87 % for 100 µM (A7) and 33.70 % for 110 µM (A15)) compared to the middle portion of the spike (23.61 % for 100 µM (A8) and 13.78 % for 110 µM (A16)). Interestingly, we have seen that the amount of Ag increased at the core when the concentration increased from 100 µM (8.34 % Ag (A10)) to 110 µM (25.05 % Ag (A13)) which supports our hypothesis that the observed LSPR blue shift is also due to the Ag deposition at the core (Fig. 5i).

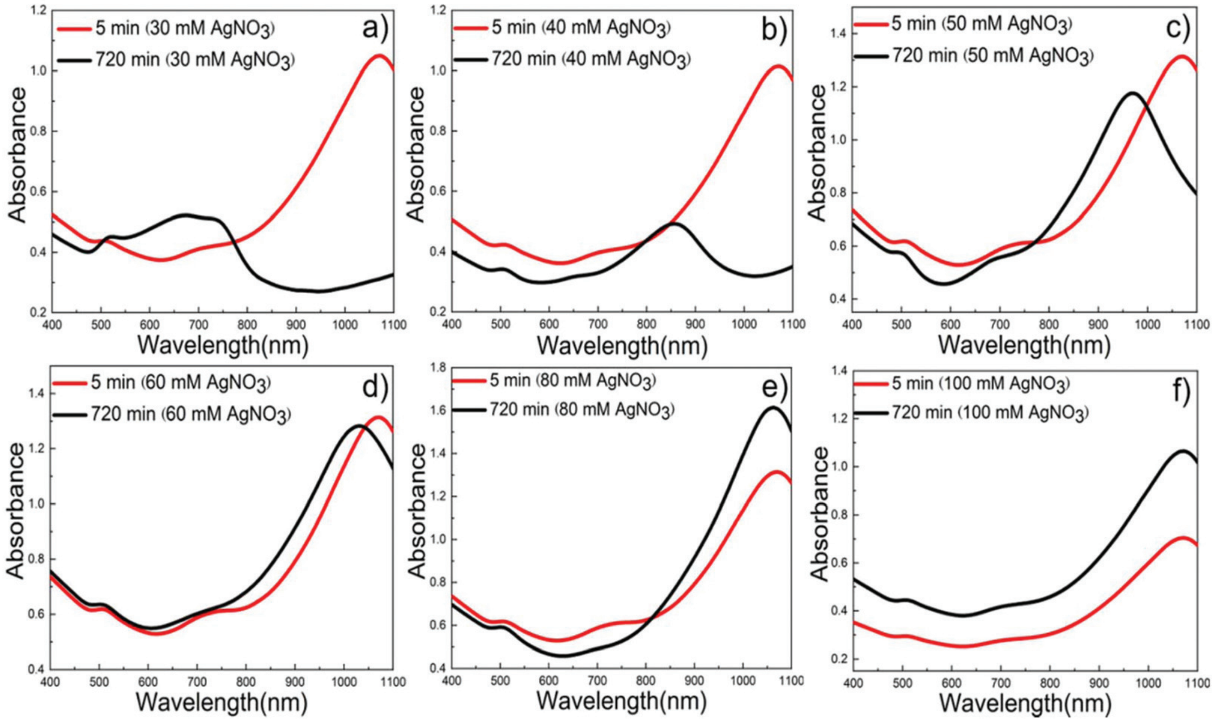

Figure 8.7: (a–f) UV-Vis spectra of 6-branched gold nanostars formed after 5 min and 720 min reaction times at different $AgNO_3$ concentrations: 30 µM (a), 40 µM (b), 50 µM (c), 60 µM (d), 80 µM (e), and 100 µM (f). UV-Vis spectrum shows a 341 nm, 212 nm, 99 nm, 42 nm, 12 nm, and 6 nm blue shift for 30 µM, 40 µM, 50 µM, 60 µM, 80 µM, and 100 µM $AgNO_3$ respectively

The concentration of seeds to be added to the growth solution is also a very important parameter that needs to be monitored, as the seed is the primary nucleation center from which the spikes are formed. Moreover, it is reported that multibranched hollow gold nanostars can be formed in the absence of seeds.[10] We have determined the concentration of seeds following a reported method,[44] and investigated their effect by increasing their concentration from 0.02 nM to 0.14 nM, in 0.04 nM increments (Fig. 9a–d and Fig. S11†). We determined that 0.14 nM is the smallest concentration of seeds necessary to achieve 6-branched stars with high monodispersity (Fig. 9d), which is associated with both spike number and spike length reduction (Fig. 9a–d). In contrast, multibranched stars were formed at 0.02 nM seed concentration (Fig. 9a). Interestingly, the spike number never increased above six on increasing the concentration of seeds above 0.1 nM (Fig. 9c). The high sample monodispersity achieved for 0.14 nM seeds was evidenced in the UV-Vis spectra as shown in Fig. 8e in the form of narrower LSPR bands (green curve) compared to those observed at lower seed concentrations. During the growth process, the availability of free gold atoms is very high when the concentration of seeds in the growth solution is low. These gold atoms can easily associate with the seeds and generate nucleation centers in high numbers, thus leading to the formation of multibranched stars. However, the availability of free gold atoms saturates at or above 0.1 nM seed concentration, thus leading to nanostars with fewer spikes and shorter spike lengths, as larger amounts of seeds at equal Au concentration create more primary growth centers. A similar observation was reported by Barbosa et al. who noted that the branching of PVP-capped gold nanostars increased by decreasing the seed concentration in the growth solution.[45]

One of the most interesting aspects of this synthesis is the possibility of leveraging the interplay between Triton X, ascorbic acid, and seeds to modify the number of branches in the nanostars. For instance, in Fig. 1 we have seen that the number of branches can be increased by either decreasing Triton X (Fig. 2c and f) or increasing ascorbic acid (Fig. 2g and h) at constant seed concentration. In Fig. 9(a–d), the number of branches was increased by decreasing the seed amount when the other variables were kept constant. To examine how these three variables are connected to each other, we ran two additional control experiments starting from the multibranched stars shown in Fig. 9a and b. These nanoparticles were synthesized under conditions ideal to specifically obtain multibranched stars (0.15 M Triton X, 1.6 mM ascorbic acid, 100 µM $AgNO_3$, and either 0.02 nM or 0.06 nM seeds). In our first control, we increased the concentration of Triton X from 0.15 M to 0.3 M, while the other concentrations were kept constant, and observed that in both cases, the morphology changed from multibranched to 6-branched stars (Fig. 9f and g). In the second control experiment, we decreased the concentration of ascorbic acid from 1.6 mM to 0.8 mM, while keeping the other variables constant. Under these conditions, we did observe a decrease in the number of branches with decreasing ascorbic acid concentration (Fig. 9h and i), but this was not sufficient to produce 6-branched nanostars at 0.02 nM seed concentration (Fig. 9h). These

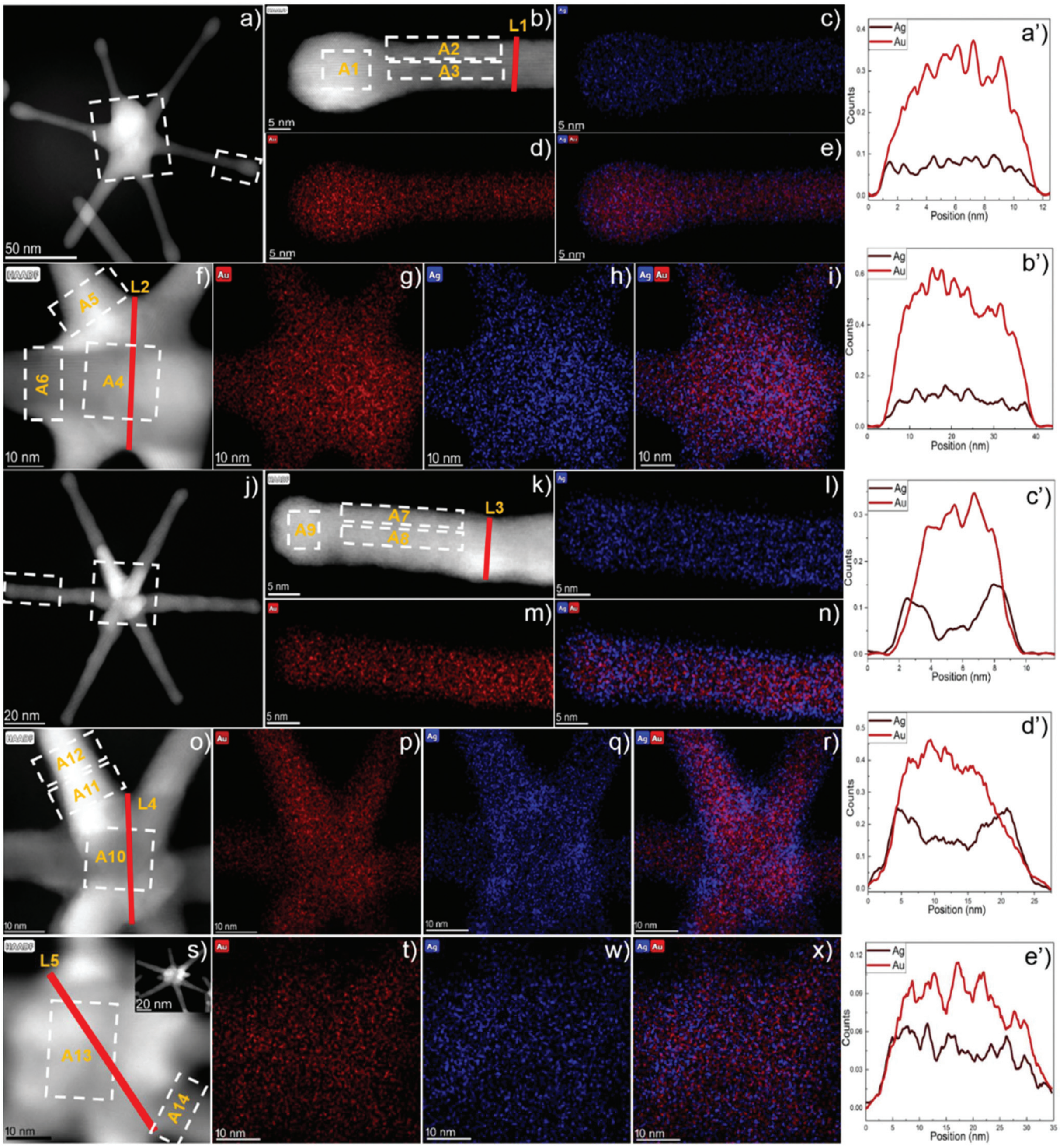

Figure 8.8: (a) TEM micrograph and (b–i) HAADF-STEM micrograph and elemental maps of the spike (b–e) and the core (f–i) of 30 µM $AgNO_3$ after 12 hours. (j) TEM micrograph and (k–r) HAADF-STEM micrograph and elemental maps of the spike (k–n) and the core (o–r) of 100 µM $AgNO_3$ after 12 hours. (s–x) HAADF-STEM micrograph and elemental maps of the core of 100 µM $AgNO_3$ after 12 hours. (a'–e') Line scan elemental profiles of 6-branched nanostars at 30 µM (spike a', and core b'), 100 µM (spike c', and core d'), and 110 µM (core e') which reveal that Au and Ag are miscible in all samples. At increasing $AgNO_3$ concentrations, metallic Ag first saturates the deposition sites along the side wall of the tips, and then proceeds to deposit at the core.

results show that the basic process of forming 6-branched stars can be tweaked by independently modifying the concentration of Triton X, ascorbic acid, and seeds, which provides a useful knob to rationally tune morphology.

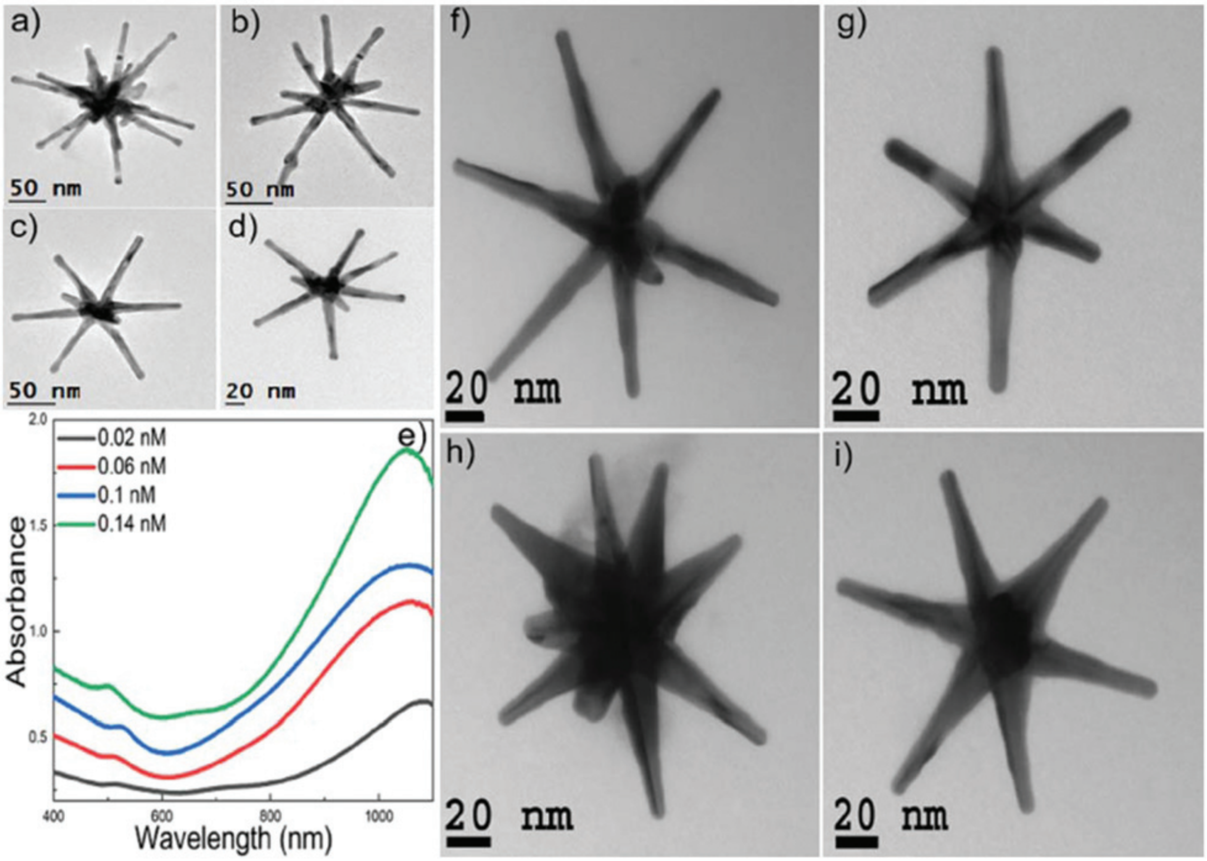

Figure 8.9: (a–d) TEM micrographs of gold nanostars synthesized by the addition of different amounts of seeds (0.02 nM (a), 0.06 nM (b), 0.1 nM (c), and 0.14 nM (d)) to the growth solution containing 0.15 M Triton X, 1.6 mM ascorbic acid, and 100 µM of $AgNO_3$. (e) UV-Vis spectra (normalized) of the nanostars at different concentrations of seeds showing a blue-shifted narrower LSPR band with increasing seed concentration, which indicates that lower branching and higher monodispersity of the stars can be achieved at 0.14 nM seed concentration. (f, g) TEM micrographs of gold nanostars synthesized by the addition of different amounts of seeds (0.02 nM (f), and 0.06 nM (g)) to the growth solution containing 0.3 M Triton X, 1.6 M ascorbic acid, and 100 µM of $AgNO_3$. (h, i) TEM micrographs of gold nanostars synthesized by the addition of different amounts of seeds (0.02 nM (h), and 0.06 nM (i)) to the growth solution containing 0.15 M Triton X, 0.8 mM ascorbic acid, and 100 µM of $AgNO_3$. A decrease in the spike number from (a) and (b) is evident. At low ascorbic acid concentrations (h and i), 6-branched nanostars cannot be obtained at low seed concentration, as opposed to the other conditions.

8.4 Conclusion

In this study, we have reported a detailed systematic study of the seed-mediated growth mechanism of 6-branched gold nanostars. The interplay of various synthetic parameters (Triton X, ascorbic acid, $AgNO_3$, and seed concentrations) is shown to influence the growth and final morphology of the nanostars. After extrapolating the fundamental growth parameters, and identifying the ideal parameter space for Triton X, ascorbic acid, $AgNO_3$, and seeds to yield the expected 6-branched products, we explored in detail the role of the nature of the seeds and the concentration of $AgNO_3$. Analysis of the kinetic data and microscopic images reveals that during this synthesis the single crystalline seeds transform into two different types of intermediate seeds: multiply-twinned intermediate seeds for multibranched stars and penta-twinned intermediate seeds for 6-branched stars. Moreover, the evolution of the spikes of the 6-branched stars shows that the shape and size of the spikes are highly dependent on $AgNO_3$ concentration, proceeding via a common intermediate having the maximum spike length (100 nm), with the final spike length determined by the amount of $AgNO_3$ in solution. We have demonstrated the important role of silver in the stabilization of the evolving crystal, confirmed by the observation that at low $AgNO_3$ concentrations, kinetically trapped nanostars, at 5-minute time points, evolve substantially before reaching thermodynamic equilibrium at 12 hours. Most importantly, the presence of metallic silver both at the side walls of the spikes (at low $AgNO_3$ concentration) and also at the core (at high $AgNO_3$ amounts) reveals in detail the importance of this reagent in tuning the nanostar morphology: increasing amounts of deposited silver appear to stabilize the five-fold twinned morphology, which would instead be lost at low Ag concentrations due to the substantial strain present in highly curved twinned regions. These nanostars display high monodispersity, batch-to-batch reproducibility, and plasmon tunability between the visible and the short-wave infrared, which could prove to be extremely useful in several quantitative applications or fundamental studies for which the rational design of multibranched nanoparticles is necessary. Looking ahead, it is possible to envision how this synthesis could lend itself as a model for the implementation of machine learning tools in materials design. In particular, the simple nanoparticle morphology characterized by a limited number of branches, the high shape anisotropy, the dependence of the LSPR band position on the tunable morphology of the branches, and the straightforward synthetic conditions, could be leveraged to implement highly parallelized automated syntheses. In turn, the thousands of samples produced could be employed to train and test machine learning algorithms to explore and understand uncharted multidimensional parameter spaces and thus lead to the discovery of novel nanoparticle morphologies that would otherwise remain untapped.

8.5 Experimental Section

Materials

Gold(III) chloride trihydrate ($HAuCl_4 \cdot 3\,H_2O$), silver nitrate ($AgNO_3$; 99.995 %), L(+)-ascorbic acid, sodium borohydride ($NaBH_4$), and Triton X-100 were purchased from Sigma-Aldrich. All these chemicals were used without further purification. Ultrapure MilliQ water (18.2 MΩ cm) was used in all syntheses. All glassware was cleaned with aqua regia before each synthesis.

Instrumentation

Absorption spectra were collected on a Thermo Scientific Evolution 300 UV-Visible spectrophotometer using a quartz cuvette with a 1 cm path. The nanoparticle morphology was determined using a Topcon 002B TEM. HRTEM analysis was performed on a JEOL 2010 F high-resolution transmission electron microscope. The particle sizes (spike length and spike width) were analyzed using ImageJ. The particle morphology was analyzed using Gatan DigitalMicrograph (TM) 3.11.1 for GMS 1.6.1. The values of averaged spacing were obtained from Fourier transform analysis of high-magnification images.

Scanning transmission electron microscopy (STEM) was carried out using a FEI Titan Themis transmission electron microscope (TEM) operated at 200 kV. Energy dispersive X-ray spectroscopy maps (EDX maps) were obtained in the scanning mode of TEM (STEM). The point resolution in this aberrationcorrected mode is 0.08 nm. 1 nm resolution EDX maps with an average beam current of 100 pA are routinely used with this microscope.

STEM tomography was obtained collecting a tilt series (from –60° to +60° in 10° steps) using a FEI Titan Themis 60–300 operated at 300 kV. Tomographic reconstruction was carried out using software based on TomToolbox for Matlab.[46] Alignment of the tilt series was carried out via TomoJ.[47] Masked SIRT and DART were performed according to Zürner et al.[48] A discrete tomography of demanding samples was based on a modified SIRT algorithm.[48]

Synthesis of 6-branched gold nanostars

The synthesis of 6 branched gold nanostars was first proposed by Pallavicini et al.[31] However, their nanoparticles did not display sufficient purity and monodispersity. We, therefore, modified and varied the synthetic parameters to achieve high monodispersity and tunable morphology. Briefly, the seed solution was prepared by the addition of a freshly prepared ice-cold solution of $NaBH_4$ (0.6 ml, 0.01 M) into a solution mixture of $HAuCl_4$ (10 ml, 0.25 mM) and Triton X, whose concentration ranged from 0.01 to 0.3 M. The solution immediately turned from pale yellow to orange after the addition of $NaBH_4$. The mixture was stirred for 2 minutes and aged for 10 minutes at 4°C before use.

The growth solution was prepared by adding 0.4 ml of 25 mM $HAuCl_4$ solution to a 20 ml Triton-X solution where the concentration of Triton-X was the same for both the seed and growth solutions. This step was followed by the addition of ascorbic acid (ranging from 0.8 to 3.9 mM), $AgNO_3$ (ranging from 30 to 110 µM), and Au seeds (ranging from 0.02 nM to 0.14 nM) to the growth solution. The solution was stirred for 12 hours and then centrifuged at 4000g for 10 min and dispersed with 5 ml of Ultrapure MilliQ water (18.2 MΩ cm).

Arrested growth studies

We have observed that n-pentanethiol works best to trap reaction intermediates compared to the more commonly used mPEG-SH (MW 5000), as we observed surface modifications and nanoparticle restructuring using the latter. Briefly, an aliquot (1 ml) of growth solution at the desired time was added to the solution of 1 ml 8.4 mM n-pentane in ethanol. Then, the solution was mixed well and centrifuged at 8000g for 10 minutes. UV-Vis and TEM analyses of the particles were performed immediately after the re-dispersion of the particles in 500 µL of MilliQ water.

Bibliography

[1] A. S. D. S. Indrasekara, S. Meyers, S. Shubeita, L. C. Feldman, T. Gustafsson & L. Fabris. *Nanoscale*, **2014**. *6*(15), 8891–8899.

[2] Y. Wang, A. B. Serrano, K. Sentosun, S. Bals & L. M. Liz-Marzán. *Small*, **2015**. *11*(34), 4314–4320.

[3] A. Kedia & P. S. Kumar. *Journal of Materials Chemistry C*, **2013**. *1*(30), 4540.

[4] C. G. Khoury & T. Vo-Dinh. *The Journal of Physical Chemistry C*, **2008**. *112*(48), 18849–18859.

[5] S. Trigari, A. Rindi, G. Margheri, S. Sottini, G. Dellepiane & E. Giorgetti. *Journal of Materials Chemistry*, **2011**. *21*(18), 6531.

[6] H. Yuan, C. G. Khoury, H. Hwang, C. M. Wilson, G. A. Grant & T. Vo-Dinh. *Nanotechnology*, **2012**. *23*(7), 075102.

[7] S. Atta, T. V. Tsoulos & L. Fabris. *The Journal of Physical Chemistry C*, **2016**. *120*(37), 20749–20758.

[8] G. Kawamura, Y. Yang, K. Fukuda & M. Nogami. *Materials Chemistry and Physics*, **2009**. *115*(1), 229–234.

[9] P. Ndokoye, X. Li, Q. Zhao, T. Li, M. O. Tade & S. Liu. *Journal of Colloid and Interface Science*, **2016**. *462*, 341–350.

[10] A. J. Blanch, M. Döblinger & J. Rodríguez-Fernández. *Small*, **2015**. *11*(35), 4550–4559.

[11] W. Niu, Y. A. A. Chua, W. Zhang, H. Huang & X. Lu. *Journal of the American Chemical Society*, **2015**. *137*(33), 10460–10463.

[12] J. D. Ramsey, L. Zhou, C. K. Almlie, J. D. Lange & S. M. Burrows. *New Journal of Chemistry*, **2015**. *39*(12), 9098–9108.

[13] A. Guerrero-Martínez, S. Barbosa, I. Pastoriza-Santos & L. M. Liz-Marzán. *Current Opinion in Colloid & Interface Science*, **2011**. *16*(2), 118–127.

[14] M. Sajitha, A. Vindhyasarumi, A. Gopi & K. Yoosaf. *RSC Advances*, **2015**. *5*(119), 98318–98324.

[15] N. Ahmad, G. Wang, J. Nelayah, C. Ricolleau & D. Alloyeau. *Nano Letters*, **2017**. *17*(7), 4194–4201.

[16] Y. Pu, Y. Zhao, P. Zheng & M. Li. *Inorganic Chemistry*, **2018**. *57*(14), 8599–8607.

[17] H. Yuan, W. Ma, C. Chen, J. Zhao, J. Liu, H. Zhu & X. Gao. *Chemistry of Materials*, **2007**. *19*(7), 1592–1600.

[18] W. Tong, H. Katz-Boon, M. J. Walsh, M. Weyland, J. Etheridge & A. M. Funston. *Chemical Communications*, **2018**. *54*(24), 3022–3025.

[19] W. Tong, M. J. Walsh, P. Mulvaney, J. Etheridge & A. M. Funston. *The Journal of Physical Chemistry C*, **2017**. *121*(6), 3549–3559.

[20] B. Nikoobakht & M. A. El-Sayed. *Chemistry of Materials*, **2003**. *15*(10), 1957–1962.

[21] F. Hubert, F. Testard & O. Spalla. *Langmuir*, **2008**. *24*(17), 9219–9222.

[22] M. Liu & P. Guyot-Sionnest. *The Journal of Physical Chemistry B*, **2005**. *109*(47), 22192–22200.

[23] C. J. Orendorff & C. J. Murphy. *The Journal of Physical Chemistry B*, **2006**. *110*(9), 3990–3994.

[24] S. R. Jackson, J. R. McBride, S. J. Rosenthal & D. W. Wright. *Journal of the American Chemical Society*, **2014**. *136*(14), 5261–5263.

[25] T. K. Sau & C. J. Murphy. *Langmuir*, **2004**. *20*(15), 6414–6420.

[26] J. Xie, J. Y. Lee & D. I. C. Wang. *Chemistry of Materials*, **2007**. *19*(11), 2823–2830.

[27] O. M. Bakr, B. H. Wunsch & F. Stellacci. *Chemistry of Materials*, **2006**. *18*(14), 3297–3301.

[28] G. H. Jeong, Y. W. Lee, M. Kim & S. W. Han. *Journal of Colloid and Interface Science*, **2009**. *329*(1), 97–102.

[29] P. S. Kumar, I. Pastoriza-Santos, B. Rodríguez-González, F. J. G. de Abajo & L. M. Liz-Marzán. *Nanotechnology*, **2007**. *19*(1), 015606.

[30] T. V. Tsoulos, S. Atta, M. J. Lagos, P. E. Batson, G. Tsilomelekis & L. Fabris. **2018**.

[31] P. Pallavicini, A. Donà, A. Casu, G. Chirico, M. Collini, G. Dacarro, A. Falqui, C. Milanese, L. Sironi & A. Taglietti. *Chemical Communications*, **2013**. *49*(56), 6265.

[32] A. B. Mandal, B. U. Nair & D. Ramaswamy. *Langmuir*, **1988**. *4*(3), 736–739.

[33] Y. Takenaka, Y. Kawabata, H. Kitahata, M. Yoshida, Y. Matsuzawa & T. Ohzono. *Journal of Colloid and Interface Science*, **2013**. *407*, 265–272.

[34] H. Zhou, H. Jia, A. Zhang, L. Zhang, C. Jia & L. Zheng. *Journal of Molecular Liquids*, **2015**. *208*, 27–33.

[35] W. Ahmed, E. S. Kooij, A. van Silfhout & B. Poelsema. *Nanotechnology*, **2010**. *21*(12), 125605.

[36] C. Novo & P. Mulvaney. *Nano Letters*, **2007**. *7*(2), 520–524.

[37] C.-H. Kuo & M. H. Huang. *Langmuir*, **2005**. *21*(5), 2012–2016.

[38] T. K. Sau, A. L. Rogach, M. Döblinger & J. Feldmann. *Small*, **2011**. *7*(15), 2188–2194.

[39] A. M. Fales, H. Yuan & T. Vo-Dinh. *The Journal of Physical Chemistry C*, **2014**. *118*(7), 3708–3715.

[40] H. A. Keul, M. Möller & M. R. Bockstaller. *Langmuir*, **2007**. *23*(20), 10307–10315.

[41] D. Alpay, L. Peng & L. D. Marks. *The Journal of Physical Chemistry C*, **2015**. *119*(36), 21018–21023.

[42] M. R. Langille, M. L. Personick, J. Zhang & C. A. Mirkin. *Journal of the American Chemical Society*, **2012**. *134*(35), 14542–14554.

[43] M. L. Personick, M. R. Langille, J. Zhang & C. A. Mirkin. *Nano Letters*, **2011**. *11*(8), 3394–3398.

[44] X. Liu, M. Atwater, J. Wang & Q. Huo. *Colloids and Surfaces B: Biointerfaces*, **2007**. *58*(1), 3–7.

[45] S. Barbosa, A. Agrawal, L. Rodriguez-Lorenzo, I. Pastoriza-Santos, R. A. Alvarez-Puebla, A. Kornowski, H. Weller & L. M. Liz-Marzan. *Langmuir*, **2010**. *26*(18), 14943–14950.

[46] S. Nickell, F. Förster, A. Linaroudis, W. D. Net, F. Beck, R. Hegerl, W. Baumeister & J. M. Plitzko. *Journal of Structural Biology*, **2005**. *149*(3), 227–234.

[47] C. MessaoudiI, T. Boudier, C. Sorzano & S. Marco. *BMC Bioinformatics*, **2007**. *8*(1), 288.

[48] A. Zürner, M. Döblinger, V. Cauda, R. Wei & T. Bein. *Ultramicroscopy*, **2012**. *115*, 41–49.

9 Colloidal plasmonic nanostar antennas with wide range resonance tunability

This chapter is based on the following publication:

Colloidal plasmonic nanostar antennas with wide range resonance tunability, T. V. Tsoulos, S. Atta, M. J. Lagos, M. Beetz, P. E. Batson, G. Tsilomelekisf, L. Fabris, *Nanoscale*, **2019**, 11, 18662 – 18671.

9.1 Abstract

Gold nanostars display exceptional field enhancement properties and tunable resonant modes that can be leveraged to create effective imaging tags, phototherapeutic agents, and hot electron-based photocatalytic platforms. Despite having emerged as the cornerstone among plasmonic nanoparticles with respect to resonant strength and tunability, some well-known limitations have hampered their technological implementation. Herein we tackle these recognized intrinsic weaknesses, which stem from the complex, and thus computationally untreatable morphology and the limited sample monodispersity, by proposing a novel 6-spike nanostar, which we have computationally studied and synthetically realized, as the epitome of 3D plasmonic nanoantenna with wide range plasmonic tunability. Our concerted computational and experimental effort shows that these nanostars combine the unique advantages of nanostructures fabricated from the top-down and those synthesized from the bottom-up, showcasing a unique plasmonic response that remains largely unaltered on going from the single particle to the ensemble. Furthermore, they display multiple, well-separated, narrow resonances, the most intense of which extends in space much farther than that observed before for any plasmonic mode localized around a colloidal nanostructure. Importantly, the unique close correlation between morphology and plasmonic response leads the resonant modes of these particles to be tunable between 600 and 2000 nm, a unique feature that could find relevance in cutting edge technological applications.

9.2 Introduction

Gold nanostars have been shown to possess plasmonic properties with potential to enable technological breakthroughs in various fields, such as imaging,[1] sensing,[2] and catalysis.[3] Importantly, their limited cytotoxicity[4] promises to enable their use in vitro and in vivo. With respect to their applicability, their most appealing features are the tunability of the resonant modes associated with the spikes well into the near infrared (NIR) and the generation of intense scattered electric fields at the tips of the spikes upon interaction with impinging radiation. These features, in addition to the unique tridimensional morphology that these nanoparticles possess when synthesized colloidally, render gold nanostars a very promising nanomaterial onto which assembly-free 3D plasmonic antennas are implemented. Substantially hampering this development is however the well-known multi-spiked complex morphology, which is difficult to rationally control during synthesis or to fundamentally study with computation, and the largely poly-dispersed batches that are obtained even following seed-mediated protocols, notwithstanding some recent progress.[5] Recently we have shown6 that spike length tunability, sample monodispersity, and batch-to-batch reproducibility can be achieved for gold nanostars when following a seedmediated method employing both $AgNO_3$ and Triton X as the shape inducing reagents. In our work we have also shown that the morphological stability (especially of the tips) can be furthered by increasing the relative amounts of $AgNO_3$, which appears to be stabilizing the as-synthesized nanostar by depositing as a monolayer of metallic Ag throughout the nanostructure, as demonstrated by high resolution STEM-EDX. With further improvements upon our initial results, this novel, 6-spiked nanostar is well poised to become a useful plasmonic nanoantenna with intrinsic 3D tunability and with relevance not only from the applied standpoint but also as a model nanoparticle for fundamental studies. The rationale behind this claim is two-fold: (1) separated spikes will likely only weakly couple within a single nanostar, rendering their resonances easy to study and interpret, and (2) spikes with high shape anisotropy should display multiple narrow harmonics of a fundamental plasmonic mode, as our calculations predict[6] (and as observed in long nanorods and nanowires).[7] Motivated by these appealing features, in this work, referring back to the 2007 seminal paper by Hao et al.,[8] we investigate in detail, with a holistic computational-experimental approach, the relationship between nanostar morphology and relevant plasmonic properties, focusing in particular (1) on determining how structural modulation is reflected into the tunability of the various LSPR modes and (2) on colloidally synthesizing nanostars whose ensemble optical response matches, within a narrow range of variability, their single particle characteristics. In doing so, we aim to prove this nanostar as the missing link between bottom-up and top-down nanomaterials, providing (in 3D) the low cost and ease of fabrication that are unique from the former, and the refined tunability and monodispersity that characterize the latter. As added bonuses, these nanostars display (vide infra) plasmonic resonances within a wide range spanning the visible, the NIR, and the short wave infrared (SWIR), and a first harmonic mode that extends in space much farther than that observed with any resonances in other plasmonic nanomaterials, rendering them uniquely suited for applications in which mode coupling is sought on large scale arrays.

In contrast to nanostar systems, which have until now only found minimal technological relevance, gold nanorods and nanowires have been successfully studied and understood, and they are now well-established nanomaterials leveraged for technological applications. The clear structure–property relationships that describe their plasmonic behavior have led to their use for the study of localized and propagating plasmons[9,10] and to demonstrate the concept of wave-particle duality.[11] Regardless of the notable improvement in the synthetic protocols, that now achieve monodisperse nanorods with high tunability,[12] and the decrease in plasmon bandwidth through post-synthetic manipulations,[13] the 1D morphology of nanorods and nanowires limits their ability to probe the tridimensional space, unless 3D self-assembly protocols are employed.[14] By realizing that nanostars represent the epitome of a 3D plasmonic antenna and by taking as example the progress achieved over the years with nanorods, we herein carried out single-particle and ensemble characterization to validate structure–property predictions enabled by our 3D finite element modeling method. In particular, we demonstrate numerically the presence of an intense fundamental mode in the SWIR regime and its higher harmonics at lower energy, and we demonstrate its existence on highly monodisperse nanostar samples obtained with our synthetic protocol. Furthermore, we show that this fundamental mode can be accurately measured via ATR-FTIR in dense nanostar samples, if 3D interparticle coupling of tips and cores is taken into account. Importantly, we prove that the existence of this mode via STEM-EELS at resonant energies almost unaltered from what was spectrophotometrically measured in ensemble, offering some interesting insight into the opportunity to compare plasmon mode excitation mediated by photons or electrons in aloof-beam configurations. Finally, we determine that the position of the various harmonic modes linearly depends on the length of the spikes, a dependence that is maintained both at the single particle and the ensemble level. Importantly, by tomographically reconstructing the 3D morphology of an almost ideal and a rather defective nanostar, and by inserting the topographic elements in the finite element model, as we reported before, [15] we prove that it is indeed only by synthesizing highly monodisperse nanostars that we can experimentally confirm in ensemble the results obtained computationally and experimentally at the single particle level. We believe that this work, with the thorough insight it offers, could provide the necessary knowledge basis to achieve an improved understanding of the plasmonic properties of these highly anisotropic nanomaterials and promote their implementation in technologically-relevant applications.

9.3 Results and Discussion

By employing 3D finite element optical simulations via Comsol Multiphysics software (see the ESI† for details), we have implemented a computational framework to study the plasmonic properties of gold nanostars in which the core and the spikes are considered to resonate as inseparable units, thus contributing interactively to the number, position, and intensity of the resulting LSPR modes. [6] We focused on the study of our recently reported 6-branch gold nanostars, [16] i. e. 3D colloidal nanostructures characterized by conical spikes with high shape anisotropy and lengths between 70 and 100 nm, radially grown on decahedral cores via a Triton X 100-based seed-mediated protocol, and decorated by small hemispherical tips (Fig. 1). These morphologically simple systems reveal some interesting plasmonic properties, in particular the role of the long spikes in the overall plasmonic response, which can be confirmed experimentally both at the ensemble and single particle level. Importantly, the exquisite morphological tunability and batch monodispersity lend themselves well to establish these nanostars as 3D colloidal nanoantennas with a unique plasmonic response that can be studied both at the single particle and ensemble level without loss of information, if not for minor peak broadening.

Our model of the optical response predicts, for idealized models of these nanostars, the existence of an intense resonant band at wavelengths longer than 1000 nm (at positions that depend on the

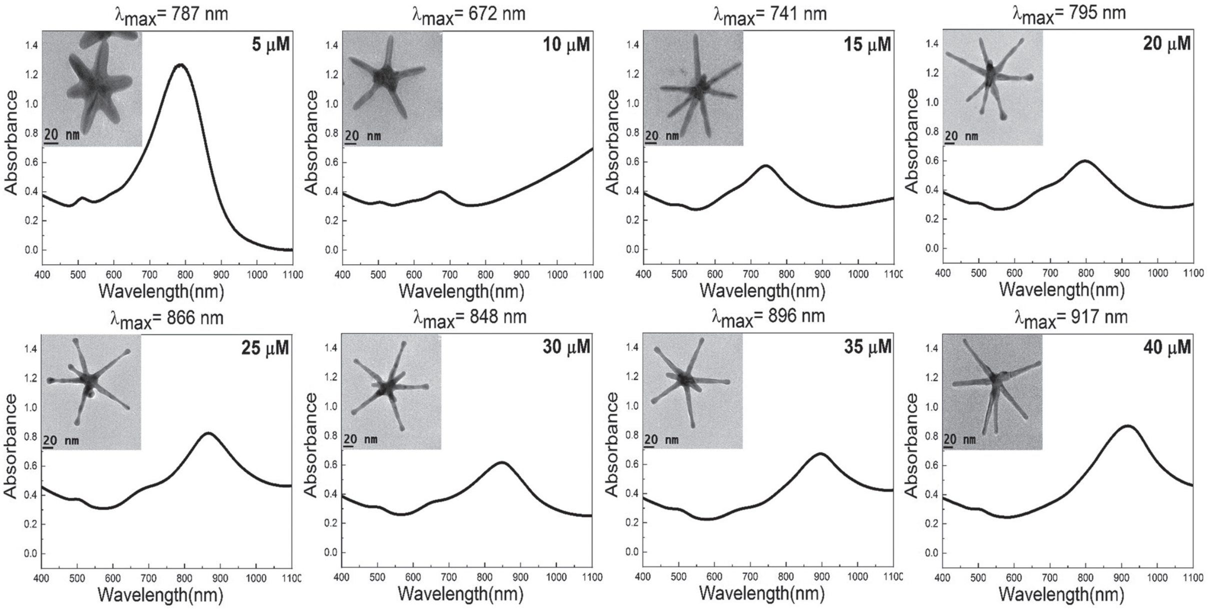

Figure 9.1: Transmission electron micrographs and UV-Vis-NIR spectra of gold nanostar samples obtained by increasing the amount of $AgNO_3$ between 5 and 40 µM as described in the Methods section. The resulting UV-Vis-NIR spectra are characterized by a prominent LSPR mode that shifts between 672 nm (at 10 µM $AgNO_3$ concentration) and 917 nm (at 40 µM $AgNO_3$ concentration) and can be described as the second harmonic of the primary dipolar mode, which resonates above 1100 nm and thus cannot be observed in these spectra. For the 5 µM $AgNO_3$ concentration case, the observed prominent band is the first harmonic mode, which in this case appears at higher energies because of the shorter spike length obtained at this $AgNO_3$ concentration. It is important to observe how the morphology of the nanostars, and of the spikes in particular, changes in close correlation to the amount of $AgNO_3$ added. Scale bars at 20 nm.

specific nanostar morphology), that can be assigned to the first harmonic of the localized surface plasmon resonance (LSPR) spike mode. As expected, higher order harmonics (i. e. second and third) are also predicted, that resonate between 600 and 1000 nm, with spacing between the three that depends on the slant length of the conical spikes. Our model also predicts a linear dependence between the position of the harmonic modes and the spike length. In order to test our model on real gold nanostar samples and corroborate its predictions, we synthesized 6-branch gold nanostars employing our seed-mediated protocol in which the concerted action of Triton X, ascorbic acid, and silver nitrate enables the synthesis of gold nanostars with spike lengths between 70 nm and 100 nm (which we will later also refer to as the average size) and characterized by LSPR bands that can be tuned, through the addition of increasing amounts of $AgNO_3$ (see Fig. 1),[17] from 600 to 2000 nm. The possibility of bridging the gap between computation and experiment with a truly 3D model that does not make constraining structural assumptions promises to lead to a complete understanding of structure–plasmonic property relationships in these complex nanomaterials. We have investigated in depth the size and shape dependence of the plasmon resonances for the synthesized 6-branched nanostars, showing in Fig. S1† the results for particles with spike lengths between 70 nm and 100 nm. Size and shape can be tuned by rationally varying the relative concentrations of $AgNO_3$, ascorbic acid, Triton X, and seeds, as well as reaction time (Fig. S2†). Furthermore, detailed dimensional analysis over samples larger than 100 particles revealed substantial monodispersity (both within and among batches), with maximum standard deviations of $\pm 4\,\%$, as reported in the representative histograms shown in Fig. S1(i–l).† Analysis of nanostar morphology has also shown that, although some of the nanostars possess five or seven spikes, the majority of them are characterized by six branches, as confirmed by detailed TEM tomography reconstruction.[15]

UV-Vis-NIR-SWIR spectrophotometry was employed to optically characterize ensemble 6-branch nanostar samples with spike lengths of 70 nm, 80 nm, 90 nm, and 100 nm (Fig. 2), showing excellent agreement between the results predicted by our optical model on ideal nanostars (Fig. 2a–d); in particular, the very good agreement between the position and normalized intensity of the bands modeled and measured (Fig. 2e and Fig. S3†) confirms the validity of our model. Importantly, the experimental validation corroborates our generalized vision[6] of plasmonic resonances in gold nanostars as harmonics of the main LSPR mode, whose appearance as distinct bands can be achieved only in the presence of long spikes with high shape anisotropy. When nanostars with shorter and thicker spikes are studied, the higher harmonics, being less intense and more closely spaced compared to the case of nanostars with high aspect ratio spikes, seemingly disappear giving rise to the well-known broad LSPR bands observed for surfactant free gold nanostars.[18,19] In reality these resonances become simply enveloped within the more intense fundamental mode. Interspike coupling, common in the case of multi-spike nanostars (again observed in surfactant free gold nanostar syntheses) also causes them to slightly blue shift, further broadening the LSPR band. Importantly, disruptions in nanostar morphology lead to substantial modifications in plasmonic response, as shown in Fig. S4.† We confirmed this computational prediction by collecting TEM tomograms of two individual gold nanostars of 72 and 76 nm spike length, one of which is characterized by a close-to-ideal morphology (72 nm), and the other (76 nm) being rather imperfect (Fig. 3), and transferring the topographic elements into Comsol Multiphysics, as we reported before.[15] Correct reconstruction was confirmed through ortho slices in the x, y, and z directions, as shown in Fig. S5.† The approach allowed us to simulate the absorption cross sections and scattered E-fields for the real nanostars in broad LSPR band. The similarity between the calculated spectra between ideal and real nanostars reinforces the validity of our computational calculations on ideal 6-branch nanostars as an effective predictor of the resonances of real nanostars, provided that a reproducible and tunable synthetic method for the growth of the nanostar is employed to ensure sufficient monodispersity. Our study, proposing a more generalized approach to the interpretation of LSPR bands in gold nanostars, predicts very well the position of the harmonics based on the detailed morphology of the nanostar under examination. The core dimensions, the length, and the sharpness of the spikes, along with the tip morphology (Fig. S6†), dictate the position and distance between the harmonics. The relative

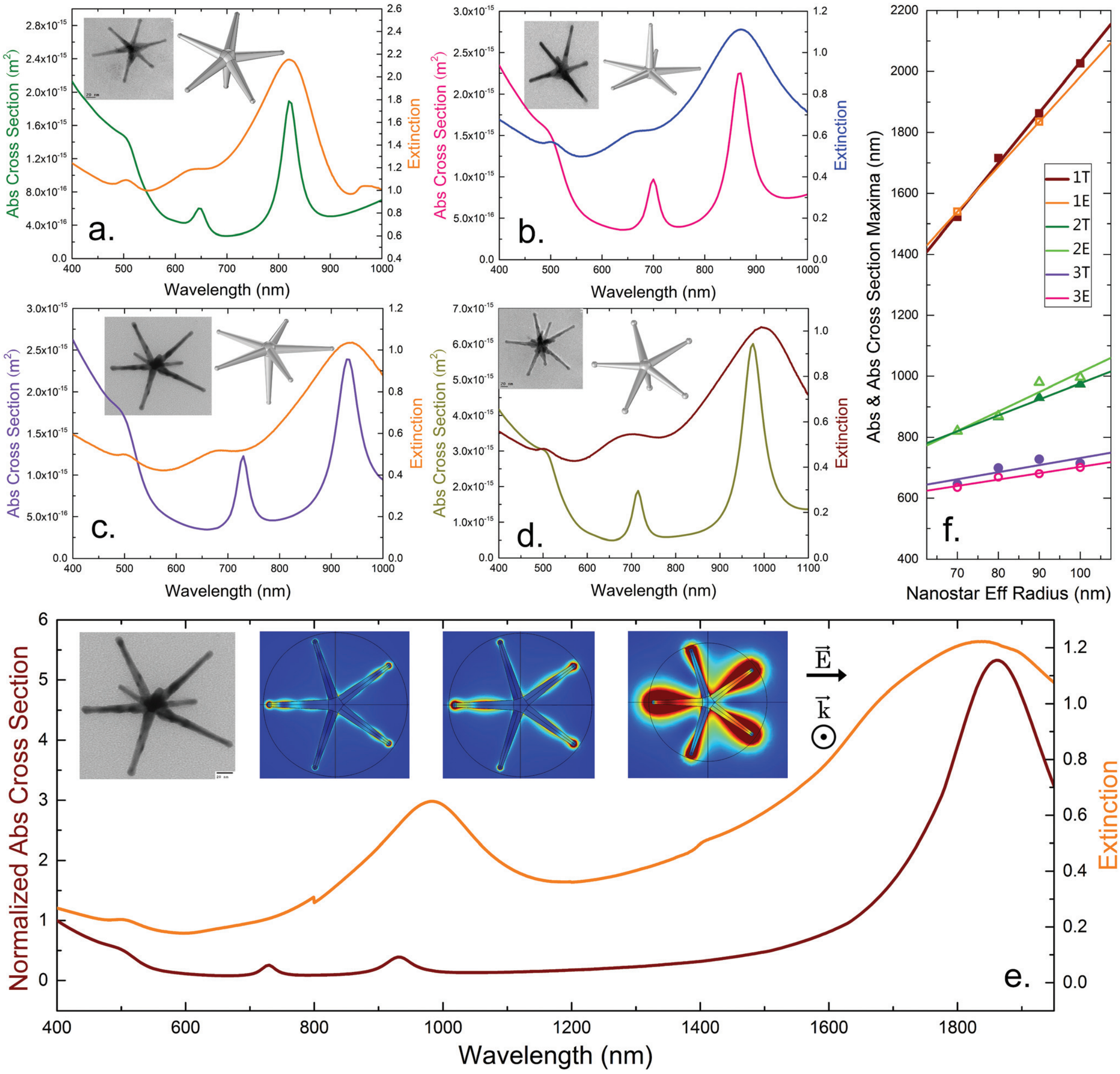

Figure 9.2: Experimental and computational spectra of 6-spike nanostars of (a) 70, (b) 80, (c) 90, and (d) 100 nm spike lengths. (e) Long range theoretical and experimental spectra of 90 nm radius 6-spike nanostars. E-field norm (calculated via eqn (5) in the ESI†) maps of the first, second, and third harmonic modes at 1865 nm, 930 nm, and 730 nm, respectively. Spectra normalization was carried out with respect to the photon energy of each wavelength compared to the photon energy at 400 nm. FWHM for first and second harmonics are 242 nm and 65 nm, respectively, for the calculated spectra, and 500 nm and 190 nm, respectively, for the experimental ones. (f) Linear dependence (actual fits) between the harmonic modes resonant maxima (1, 2, and 3) and the nanostar spike lengths. Note the decreasing slope as we move towards higher harmonics and the very good matching between theoretical (T) predictions and experimental (E) results. Details on the normalization in Fig. 3e are reported in Fig. S3.†

position of the bands governs the linear relationship shown in Fig. 2f, and follows a simplified rule in agreement with antenna theory.[20] In the long range 400–1950 nm spectrum in Fig. 2e we report both the Vis-NIR-SWIR spectrum and the calculated normalized absorption cross section of a 90 nm nanostar, along with three E-field maps highlighting the spatial distribution of the field at the position of the maxima for the three observed harmonics. The very good agreement between position and intensity modeled and experimentally measured provides a solid experimental proof of the validity of our computational approach, which is further supported by the ATR-FTIR and EELS results presented onwards. Interestingly, our optical model suggests that the first harmonic mode, in addition to displaying substantially higher intensity compared to its higher harmonics, appears to extend in space much farther from the surface than the other two, which could be leveraged in techniques such as surface enhanced Raman scattering (SERS) where E-field enhancements lead to higher signal intensity and assay sensitivity.

Fig. 2 also highlights a very unique aspect of the nanostars we report, that is the extension of their resonant window well into the SWIR. We thus hypothesized that a linear dependence between the resonance wavelength and nanostar spike length could be measured also employing FTIR. A validation of this hypothesis would render these particles extremely powerful as plasmonic nanoantennas for applications in medical imaging, sensing, or catalysis, in addition to potentially acting as fiducial marks for the resonance alignment of UV-Vis-NIR spectrophotometry and FTIR. In Fig. 4, we present the ATR-FTIR spectra of highly concentrated aqueous solutions of gold nanostars with spike lengths spanning between 70 nm and 100 nm. The full spectral range, 700–7500 cm^{-1}, is shown in Fig. S7.† In the 4000–6500 cm^{-1} spectral range, we observe the peak maxima for the first harmonic to be centered at ≈5700 cm^{-1}, 5180 cm^{-1}, 4930 cm^{-1}, and 4830 cm^{-1} for 70, 80, 90, and 100 nm respectively. The peak positions of the four different samples fit nicely the E-field norm introduced by the numerical predictions and the Vis-NIR-SWIR spectroscopy measurements. A noticeable shift in the observed first harmonic peaks can be attributed to interparticle coupling effects (Fig. S8†), since the FTIR measurements took place in concentrated solutions as compared to the Vis-NIR spectrophotometric measurements, as supported by our recent computational work on 3D nanostar antenna coupling.[6] Interestingly, the observed center of each peak appears to be linearly dependent on the average size of the gold nanostars in solution, demonstrating the strong dependence of this plasmonic mode on the length of the spike, as described in the previous section and plotted in Fig. 4d and e.

The results obtained from the ATR-FTIR spectra further underscore the ability and reliability of the developed protocol for the synthesis of colloidal nanostars with plasmonic properties that can be rationally tailored for specific applications. It is worth mentioning here that contrary to the well-defined, Gaussian-type peaks predicted by the model, in our ATR-FTIR spectra the first harmonic appears to be a convolution of more than one contribution in the overall spectral envelope. To address this issue, all the spectra were deconvoluted using Gauss functions based on the Levenberg–Marquardt algorithm as shown elsewhere.[21–24] The deconvoluted spectra show two or three major peaks separated by approximately 800 cm^{-1}. To further investigate the latter, in Fig. 4b and c we show the comparison between the deconvoluted ATR-FTIR spectrum and the calculated absorption cross section for 90 nm-spike nanostars. The distinct peaks in ATR-FTIR can be attributed to the same plasmonic mode under different geometrical configurations (Fig. 4f). Numerical results (Fig. 4c and f) show that changing the distance as well as the configuration between two adjacent nanostars can both blue shift and red shift the plasmonic mode. The computational treatment to nanostar coupling aims to outline the importance of considering multiple geometric configurations between randomly dispersed adjacent nanostars at high concentrations when interpreting the experimental results. We have investigated three of these numerous possible configurations and reported the shifts of the first harmonic with respect to the distance between nanostars (Fig. S8†).

After demonstrating that our calculations can accurately predict, given the spike length, the resonances of real 6-branch gold nanostars employing an idealized 6-branch model nanostar, and demonstrating that the predicted resonances can be validated by measuring them in ensemble by simply employing UV-Vis-SWIR spectrophotometry or ATR-FTIR, we confirmed, at the single particle level, the observed results by carrying out electron energy loss spectroscopy (STEM-EELS) measurements on an individual 90 nm-spike nanostar. While single particle scattering data could be in first principles proposed to assess the plasmonic response, the presence of the substrate, coupling anisotropically to the nanostars, would have further complicated the experimental response, and was therefore not deemed accurate to assess the LSPR bands in this particular study.

Fig. 5 shows EELS spectra acquired on a 6-spike nanostar with the electron beam probing the nanostructure in nonintersecting and intersecting geometries. Since the plasmon coupling between spikes is very weak due to their large physical separation, [25] one can in principle analyze their plasmonic behavior considering an isolated spike coupled to the star core. This approach allows us to probe a single spike and then repeat the process for the other spikes of the stars. It is important to mention that in this experiment the examined nanostar was supported by an amorphous carbon film with 15 nm thickness; under these conditions it is expected that the interference of the C film on the EELS response will be minimal, especially in the energy regime probed. We obtained the same findings for all the spikes, as illustrated in Fig. 5 (left side–spike 1; right side–spike 2). Note that the spectra can exhibit up to two resonances associated with the first (670 meV) and second (1360 meV) harmonic excitations, depending on the beam location (the third harmonic mode is not intense enough to be measured). The resonant energies are similar to those found by optical techniques (UV-Vis-NIR and ATR-FTIR, Fig. 3 and 4 respectively) and match well the computational simulations of the optical response. While we recognize that comparing mode excitation via electron beam and plane wave illumination involves different physical phenomena, we can consider the connection between electron and photon excitation to be valid in the aloof mode for large input parameters (i. e., when the electron beam does not intersect the nanostructure). In the intersecting geometry, on the other hand, two phenomena occur: (a) the electron beam can probe coupled core-spike resonances with sufficient sensitivity to measure shifts due to the varying electron density, which increases as we move from the tip to the base of the spike; (b) the electron beam perturbs the local electron density leading to resonant mode damping. When the electron beam is located in regions near/within the tip (positions 1 and 3) the excitation of the first harmonic dominates the EELS spectra. This is expected due to the dipolar configuration of that mode in rod-like structures,[26] which is highly efficiently excited in the non-intersecting configuration (position 1). It is also important to note that there is a slight shift to lower energies of the characteristic resonance of the first harmonic, as we move along the axis of the spike (position 3). We also probed the middle regions of the spikes producing an additional excitation at around 1290 meV, which corresponds to the excitation of the second harmonic. A blue-shift trend can be observed for the resonances excited, as we move from the middle regions of the spikes to their extremities and to the aloof mode. When the beam intersects with the spikes it disturbs the local charge distribution, which gives rise to the mentioned damping of the spike modes, leading to a red shift, notable in the case of the first harmonic as the beam moves from the aloof mode to the inner part of the spikes.

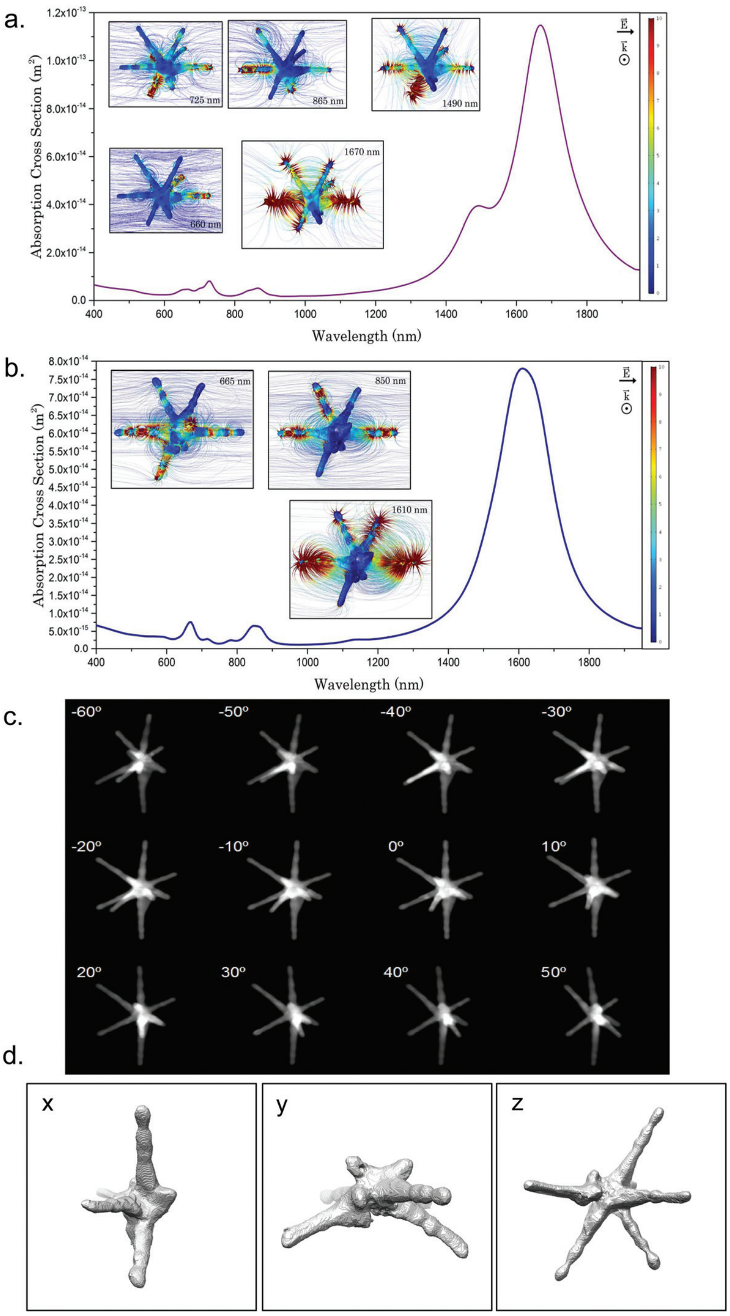

Figure 9.3: Numerical solutions for the E-field norm of two different 3D nanostars reconstructed from TEM tomograms. (a) A highly defective one with spikes of variable lengths and a more ideal nanostar in (b) with spikes of equal length (despite the presence of a short unformed spike). Presented at the eigenvalues of the main resonant modes, these real 3D reconstructed nanostars exhibit a behavior that solidifies our approach. A slightly imperfect nanostar in the (a) case exhibits additional resonances in all of the three reported harmonic cases, two of which, i.e. a secondary 1st and secondary 3rd harmonic, are depicted in the E-field norm plots. Streamline plots allow us to visualize the resonances in real particles like these. In both cases small protrusions on the volume of the stars contribute to broadenings and slight asymmetries on the peaks, although the spectral response is clear for the more ideal nanostar in (b), corroborating our approach and supporting our computational data for disrupted geometries (Fig. S4†). Interestingly, very small differences in spike lengths result in clear secondary resonances, which stands as a proof that our synthetic method yields highly monodisperse and reproducible samples and our numerical approach successfully describes even slight disruptions in the geometry and the resulting spectral profile. In (c) STEM tilt series collected for nanostar in (b) for tomographic reconstruction. The topographic elements were then employed to transfer the real nanostar morphology into Comsol Multiphysics and model absorption cross sections and scattered E-fields in 3D, as we reported before.[15] (d) Projections in x, y, and z directions of the 3D tomographic reconstruction realized from the tilt series reported in (b).

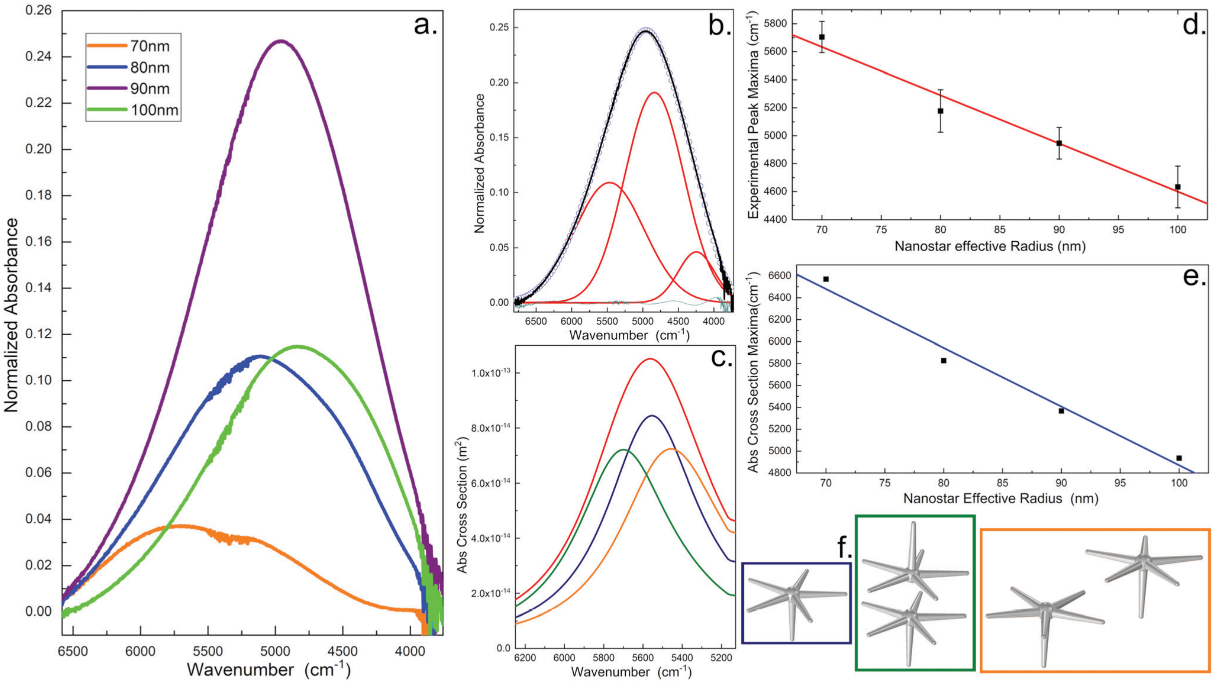

Figure 9.4: FTIR spectra collected on nanostars with 70 nm, 80 nm, 90 nm, and 100 nm spike lengths. Normalization carried out with respect to the area under the curve of each spectrum (a). Spectrum of a suspension of nanostars with 90 nm spike length deconvoluted with the Gauss function (b). Theoretical absorption cross section spectra of (1) a single 90 nm nanostar, (2) two nanostars with their in-plane spikes kept parallel at 50 nm distance, (3) two nanostars aligned tip-to-tip at 50 nm, along with the average of these three spectra shown in red (c and f). Linear fitting of the observed FTIR peak maxima shows a strong interdependence between the first harmonic resonances and the spike length experimentally (d) and theoretically (e). Error bars in (d) calculated from peak deconvolution, as reported in Fig. S9.†

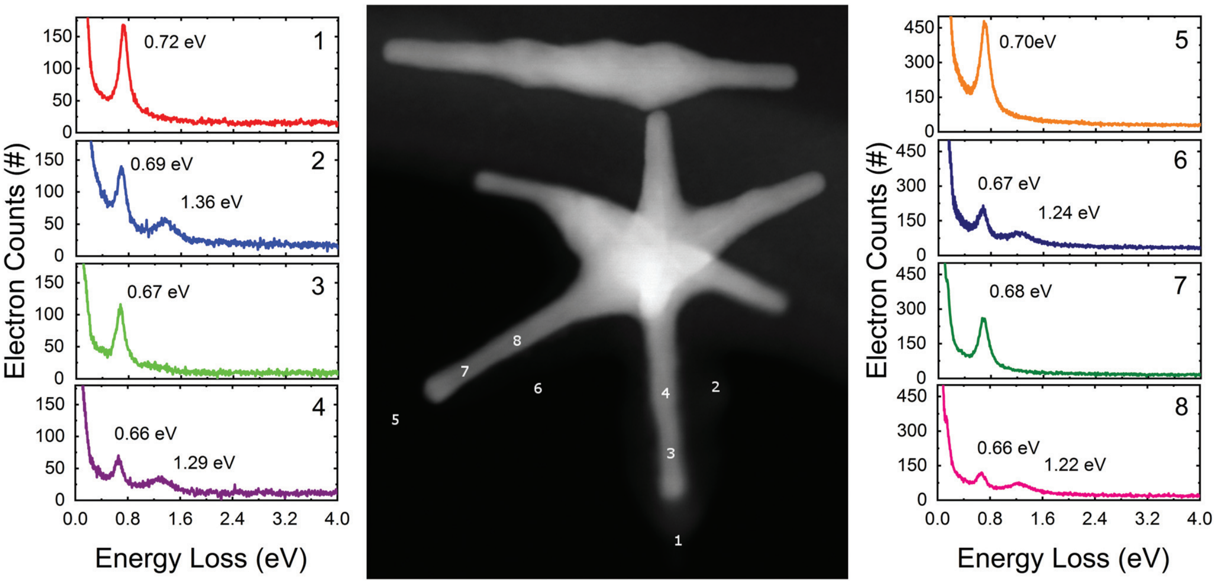

Figure 9.5: EELS spectra collected at the positions depicted in the STEM micrograph presented in the middle. Up to two resonances associated with the first (670 meV) and second (1360 meV) harmonic excitations can be observed, with slight energy shifts that depend on the proximity to the core of the position probed by the electron beam. This nanostar was chosen for EELS analysis because the two probed spikes were observed to be oriented almost perpendicularly with respect to the carbon-coated TEM grid, thus ensuring that the interference of the substrate, although substantially smaller in the NIR compared to the UV-visible region, would be further minimized.

9.4 Conclusions

In conclusion, the 6-branched nanostars reported herein offer an example of highly anisotropic, colloidally-synthesized plasmonic material in which the optical properties of the nanostructure can be predicted computationally and observed experimentally owing to their high monodispersity. While other non-spherical nanoparticles (e. g. nanorods) have been synthesized with a high degree of monodispersity and synthetic control, the morphology of these nanostars is substantially more complex to achieve. However, the opportunity to leverage them as true 3D nanoantennas is a powerful rationale to further our understanding of their properties. In-depth multi-technique characterization has shown that the peak positions of the plasmonic resonances linearly depend on the length of the spikes, with slight variations originating from the specific tip- and spike-morphologies. The proposed model has predicted a strong plasmonic mode, along with its higher order eigenmodes, in excellent detail. EELS data, collected on isolated spikes, have confirmed the influence of the electrons of the core on the spectral position of the various harmonics; in addition, they have underscored the importance of taking into consideration the effect of the electron beam in intersecting probing geometries. From the single particle level to the highly interacting ensemble, the agreement between the optical model and experiment advocates the need for a combined approach towards a rational and effective evolution of plasmonic materials and methods. The high monodispersity and batch-to-batch reproducibility of the samples, ensured by our synthetic protocol, suggest that these 6-branched nanostars might be ideal testbeds for the experimental validation of plasmonics theory or for the implementation of plasmonicsbased technology in medical imaging, sensing, or catalysis.

9.5 Methods

9.5.1 Synthesis of 6 branched stars with tunable plasmon resonance

6-Branched stars with tunable plasmon resonance were synthesized by modifying the concentration of $AgNO_3$, starting from the general protocol, described as follows. A seed solution was prepared by the addition of a freshly prepared icecold solution of $NaBH_4$ (0.6 ml, 0.01 M) into a solution mixture of $HAuCl_4$ (10 ml, 0.25 mM) and 0.15 M Triton X. The solution immediately turned from pale yellow to orange after the addition of $NaBH_4$. A 14 µL aliquot of seeds was added to the growth solution containing 20 ml of 0.15 M Triton-X, 0.4 ml of 25 mM $HAuCl_4$, 0.04 ml of 0.788 M ascorbic acid, and a $AgNO_3$ solution whose concentrations ranged from 5 to 40 µM (Fig. 1). The reaction mixture was gently stirred at room temperature for 10 minutes. The final nanostar suspension was purified by centrifugation at 4000g for 10 min and re-dispersed with 5 ml of Ultrapure MilliQ water (18.2 MΩ cm).

9.5.2 Nanostar Synthesis

Materials. Gold(III) chloride trihydrate ($HAuCl_4 \cdot 3\,H_2O$), silver nitrate ($AgNO_3$; 99.995 %), L(+)-ascorbic acid, sodium borohydride ($NaBH_4$), and TritonX-100 were purchased from Sigma-Aldrich. All these chemicals were used without further purification. Ultrapure MilliQ water (18.2 MΩ cm) was used in all syntheses. All glassware was aqua regia cleaned before each synthesis.

Synthesis of 6 branched gold nanostars. 6-Branched gold nanostars were synthesized following a modified seedmediated method first developed by Taglietti and coworkers.[17] Briefly, the seed solution was prepared by adding 0.6 ml of fresh, ice-cold 0.01 M $NaBH_4$ solution to a mixture containing 0.1 ml of 25 mM $HAuCl_4$ and 10 ml of 0.15 M Triton X. After the addition of $NaBH_4$ the solution immediately turned from pale yellow to orange-red. The mixture was stirred for 2 minutes and aged for 10 minutes at 4°C before use. The growth solution was prepared by adding 40 µl of 0.788 M ascorbic acid to a solution containing 0.4 ml of 25 mM $HAuCl_4$ and 20 ml of 0.15 M Triton-X. A variable amount of $AgNO_3$ solution was added to the growth solution to obtain a precise spike length: for instance, 45, 50, 60, and 100 µM $AgNO_3$ were used for the synthesis of nanostars with 80, 70, 90, and 100 nm spike length, respectively. After that, a variable amount of seeds were added to the growth solution. Specifically, nanostars with 70 nm spike length were synthesized by the addition of 24 µl (14 µl for the other three spike lengths) seed solutions to the growth solution. The color of the solution turned from colorless to green after the addition of the seeds, with the color becoming more intense after 5 minutes. The solution was gently stirred at room temperature for 12 hours. The conical spike morphology with a spherical tip was obtained when 25 µM $AgNO_3$ were added to the growth solution, and the reaction time was 10 minutes. The rod morphology was obtained when 15 µM $AgNO_3$ was added to the growth solution, and the reaction time was 10 minutes. The solution was purified via centrifugation at 4000g for 10 min and redispersed with 5 ml of Ultrapure MilliQ water (18.2 MΩ cm).

Case example: synthesis of 80 nm spike length stars. 6-Branched gold nanostars with 80 nm spike length were synthesized by the addition of a 14 µL aliquot of seed solution to the growth solution containing 20 ml of 0.15 M Triton-X, 0.4 ml of 25 mM $HAuCl_4$, 0.04 ml of 0.788 M ascorbic acid, and 45 µM $AgNO_3$ solution. An intense brown color appeared immediately after the addition of the seeds. The solution was gently stirred at room temperature for 12 hours until it became green in color. The suspension was purified by centrifugation at 4000g for 10 min and re-dispersed with 5 ml of Ultrapure MilliQ water (18.2 MΩ cm).

Spike length measurement of gold nanoparticles. The core diameter, spike length, and aspect ratio of nanostars were measured via ImageJ software. The spike length was measured from the center of the core to the tip of the spike. We have measured 150 spikes for each different type nanostar to generate the reported statistics.

Bibliography

[1] M. W. Rotz, K. S. B. Culver, G. Parigi, K. W. MacRenaris, C. Luchinat, T. W. Odom & T. J. Meade. *ACS Nano*, **2015**. *9*(3), 3385–3396.

[2] A. S. D. S. Indrasekara, S. Meyers, S. Shubeita, L. C. Feldman, T. Gustafsson & L. Fabris. *Nanoscale*, **2014**. *6*(15), 8891–8899.

[3] A. Sousa-Castillo, M. Comesaña-Hermo, B. Rodríguez-González, M. Pérez-Lorenzo, Z. Wang, X.-T. Kong, A. O. Govorov & M. A. Correa-Duarte. *The Journal of Physical Chemistry C*, **2016**. *120*(21), 11690–11699.

[4] M. Bhamidipati & L. Fabris. *Bioconjugate Chemistry*, **2017**. *28*(2), 449–460.

[5] A. S. D. S. Indrasekara, S. F. Johnson, R. A. Odion & T. Vo-Dinh. *ACS Omega*, **2018**. *3*(2), 2202–2210.

[6] T. V. Tsoulos & L. Fabris. *The Journal of Physical Chemistry C*, **2018**. *122*(50), 28949–28957.

[7] O. Nicoletti, M. Wubs, N. A. Mortensen, W. Sigle, P. A. van Aken & P. A. Midgley. *Optics Express*, **2011**. *19*(16), 15371.

[8] F. Hao, C. L. Nehl, J. H. Hafner & P. Nordlander. *Nano Letters*, **2007**. *7*(3), 729–732.

[9] C. Rewitz, T. Keitzl, P. Tuchscherer, J.-S. Huang, P. Geisler, G. Razinskas, B. Hecht & T. Brixner. *Nano Letters*, **2011**. *12*(1), 45–49.

[10] E. K. Payne, K. L. Shuford, S. Park, G. C. Schatz & C. A. Mirkin. *The Journal of Physical Chemistry B*, **2006**. *110*(5), 2150–2154.

[11] L. Piazza, T. Lummen, E. Quiñonez, Y. Murooka, B. Reed, B. Barwick & F. Carbone. *Nature Communications*, **2015**. *6*(1).

[12] N. Ortiz, B. Zoellner, S. J. Hong, Y. Ji, T. Wang, Y. Liu, P. A. Maggard & G. Wang. *ACS Applied Materials & Interfaces*, **2017**. *9*(31), 25962–25969.

[13] G. González-Rubio, P. Díaz-Núñez, A. Rivera, A. Prada, G. Tardajos, J. González-Izquierdo, L. Bañares, P. Llombart, L. G. Macdowell, M. A. Palafox, L. M. Liz-Marzán, O. Peña-Rodríguez & A. Guerrero-Martínez. *Science*, **2017**. *358*(6363), 640–644.

[14] C. Hamon, M. Postic, E. Mazari, T. Bizien, C. Dupuis, P. Even-Hernandez, A. Jimenez, L. Courbin, C. Gosse, F. Artzner & V. Marchi-Artzner. *ACS Nano*, **2012**. *6*(5), 4137–4146.

[15] T. V. Tsoulos, L. Han, J. Weir, H. L. Xin & L. Fabris. *Nanoscale*, **2017**. *9*(11), 3766–3773.

[16] S. Atta, M. Beetz & L. Fabris. *Nanoscale*, **2019**. *11*(6), 2946–2958.

[17] P. Pallavicini, A. Donà, A. Casu, G. Chirico, M. Collini, G. Dacarro, A. Falqui, C. Milanese, L. Sironi & A. Taglietti. *Chemical Communications*, **2013**. *49*(56), 6265.

[18] H. Yuan, C. G. Khoury, H. Hwang, C. M. Wilson, G. A. Grant & T. Vo-Dinh. *Nanotechnology*, **2012**. *23*(7), 075102.

[19] M. Chirea, S. S. E. Collins, X. Wei & P. Mulvaney. *The Journal of Physical Chemistry Letters*, **2014**. *5*(24), 4331–4335.

[20] P. Biagioni, J.-S. Huang & B. Hecht. *Reports on Progress in Physics*, **2012**. *75*(2), 024402.

[21] D. Fischer, P. Pötschke, H. Brünig & A. Janke. *Macromolecular Symposia*, **2005**. *230*(1), 167–172.

[22] A. Kalampounias, G. Tsilomelekis & S. Boghosian. *Journal of Molecular Liquids*, **2014**. *198*, 299–306.

[23] A. G. Kalampounias, G. Tsilomelekis & S. Boghosian. *The Journal of Chemical Physics*, **2015**. *142*(15), 154503.

[24] P. Pötschke, H. Brünig, A. Janke, D. Fischer & D. Jehnichen. *Polymer*, **2005**. *46*(23), 10355–10363.

[25] S. Mazzucco, N. Geuquet, J. Ye, O. Stéphan, W. V. Roy, P. V. Dorpe, L. Henrard & M. Kociak. *Nano Letters*, **2012**. *12*(3), 1288–1294.

[26] M. Bosman, E. Ye, S. F. Tan, C. A. Nijhuis, J. K. W. Yang, R. Marty, A. Mlayah, A. Arbouet, C. Girard & M.-Y. Han. *Scientific Reports*, **2013**. *3*(1).

10 Conclusions

Efficient and sustainable hydrogen production remains one of the greatest challenges facing society today. This thesis explored several approaches to overcome limitations in such processes, including improving the stability of electrochemically active materials, prolonging the lifetime of catalysts, and enhancing their overall performance and activity.

In the first two projects, extensive corrosion studies of photoelectrochemically active materials were carried out on the anode and cathode sides for oxygen and hydrogen evolution, respectively. The dissolution and corrosion of photoelectrochemically active materials are not yet fully understood, so in-depth electrochemical and electron microscopic studies were conducted to monitor dissolution processes and phase transitions under operating conditions. The results showed that ultrathin and amorphous niobium-doped titanium dioxide films deposited by atomic layer deposition provide excellent protection for photoelectrochemical catalysts while maintaining their catalytic activity. Furthermore, additional oxygen evolution co-catalysts or hydrogen evolution co-catalysts applied on top of the protective layer exhibited unprecedented activities for more than 16 hours under harsh operating conditions.

All the photoelectrochemical catalysts investigated in this thesis are affordable, easy to produce, and have moderate electrolyte requirements. However, their stability still has limitations with regard to the requirements of industrial applications. Thus, further improvements of the material, protective layers, and co-catalysts need to be made for large-scale application.

In the third to fifth chapters, advanced electrochemical catalysis in the dark is highlighted using new approaches. Since iridium dioxide has been one of the most active and stable catalysts, known so far, sustainability improvements must be made by reducing the amount of iridium required or by finding new materials that are as active and stable as iridium dioxide but occur in much larger quantities.

One approach was to use microporous antimony doped tin oxide nanoparticles homogeneously loaded with a thin layer of iridium oxide nanoparticles, which drastically reduced the amount of required iridium while maintaining high catalytic activity. The desired homogeneous loading was confirmed using electron tomography. Another approach involved using vanadium-doped nickel oxide as a catalyst material for electrochemical water splitting, where it was found that doping of nickel oxide with vanadium ions using a simple synthesis at room temperature, inhibits the formation of a less active nickel oxide phase, stabilizing the more active α-$Ni(OH)_2$ phase, thus making it a cheap and abundant water splitting catalyst material.

Both of these approaches reduce the need for noble metal iridium while still maintaining high electrochemical activity for water splitting. These approaches hold the potential for significantly reducing the cost and environmental impact of electrochemical catalysis.

In the last two chapters, a highly tunable synthesis for gold nanostar antennas was demonstrated, and deep insights into computational simulation of the plasmonic resonance behavior of nanoparticles were provided using electron tomographic reconstructions as a model system to simulate the plasmonic response of the gold nanostar antennas.

In conclusion, this thesis establishes innovative and new approaches for (photo-)electrochemical water splitting catalysts, as well as solutions for dissolution and corrosion processes under harsh operational conditions. The thesis also shows that electron tomography is an effective and powerful method to provide new insights into nanostructured materials and to deliver needed three-dimensional spatial information for plasmonic resonance simulation. These findings hold significant potential for advancing the field of electrochemical catalysis and enabling more sustainable hydrogen production.

11 Publications and Conference Contributions

11.1 Publications

15. Ultra-thin Protective Coatings for Improved Durability and Water Oxidation on Mo:BiVO$_4$, **M. Beetz**, S. Häringer, P. Elsässer, J. Kampmann, L. Sauerland, F. Wolf, A. Fischer, T. Bein, Advanced Functional Materials, 2021, 31(45), 2011210.

14. Fast-Switching vis-IR Electrochromic Covalent Organic Frameworks, D. Bessinger, K. Muggli, **M. Beetz**, F. Auras, Journal of the American Chemical Society. 2021, 143(19), 7351 – 7357.

13. Highly conductive titania supported iridium oxide nanoparticles with low overall iridium density as OER catalyst for large-scale PEM electrolysis, D. Böhm, **M. Beetz**, C. Gebauer, M. Bernt, J. Schröter, M. Kornherr, T. Bein and D. Fattakhova-Rohlfing, Applied Materials Today, 2021, 24, 101134.

12. Nanocellulose mediated transition of lithium-rich pseudoquarternary metal oxide nanoparticles into lithium nickel cobalt manganese oxide (NCM) nanostructures, P. M. Zehetmaier, F. Zoller, **M. Beetz**, M. A. Plaß, F. Friedrich, S. Häringer, B. Böller, M. Döblinger, T. Bein, D. Fattakhova-Rohlfing, Chemistry of Nanomaterials for Energy, Biology and more, 2020, 6(4), 618 – 628.

11. How Photocorrosion can trick you: A detailed study on low-bandgap Li doped CuO photocathodes for solar hydrogen production, J. Kampmann, S. Betzler, H. Hajiyani, S. Häringer, **M. Beetz**, T. Harzer, J. Kraus, B. V. Lotsch, C. Scheu, R. Pentcheva, D. Fattakhova-Rohlfing, T. Bein, Nanoscale, 2020, 12(14), 7766 – 7775.

10. V(III) Doped Nickel Oxide-Based Nanocatalysts for Electrochemical Water Splitting: Influence of Phase Composition and Doping on the Electrocatalytic Activity, D. Böhm, **M. Beetz**, C. Kutz, S. Zhang, C. Scheu, T. Bein, D. Fattakhova-Rohlfing, Chemistry of Materials, 2020, 32(24), 10394 – 10406.

9. [Cover Adv. Funct. Mater. 1/2020] Efficient OER Catalysts: Efficient OER Catalyst with Low Ir Volume Density Obtained by Homogeneous Deposition of Iridium Oxide Nanoparticles on Macroporous Antimony-Doped Tin Oxide Support, Daniel Böhm, **Michael Beetz**, Maximilian Schuster, Kristina Peters, Alexander G. Hufnagel, Markus Döblinger, Bernhard Böller, Thomas Bein, Dina Fattakhova-Rohlfing.

8. Efficient OER Catalyst with Low Ir Volume Density Obtained by Homogeneous Deposition of Iridium Oxide Nanoparticles on Macroporous Antimony-Doped Tin Oxide Support, D. Böhm, **M. Beetz**, M. Schuster, K. Peters, A. G. Hufnagel, M. Döbliner B. Böller, T. Bein, D. Fattakhova-Rohlfing, Advanced Functional Materials, 2019, 30(1), 1906670.

7. Colloidal Plasmonic Nanostar Antennas with Wide Range Resonance Tunability, T. V. Tsoulos, S. Atta, M. J. Lagos, **M. Beetz**, P. E. Batson, G. Tsilomelekis, and L. Fabris, Nanoscale, 2019, 11, 18662 – 18671.

6. Understanding the role of $AgNO_3$ concentration and seed morphology in the achievement of tunable shape control in gold nanostars, S. Atta, **M. Beetz** and L. Fabris, Nanoscale, 2019, 11, 2946 – 2958.

5. Carbon-templated conductive oxide supports for oxygen evolution catalysis, A. G. Hufnagel, S. Häringer, **M. Beetz**, B. Böller, D. Fattakhova-Rohlfing and T. Bein, Nanoscale, 2019, 11, 14285 – 14293.

4. Solvatochromic covalent organic frameworks, L. Ascherl, E. W. Evans, M. Hennemann, D. D. Nuzzo, A. G. Hufnagel, **M. Beetz**, R. H. Friend, T. Clark, T. Bein and F. Auras, Nature Communications, 2018, 9, 3802.

3. Accelerated fuel cell tests of anodic Pt/Ru catalyst via identical location TEM: New aspects of degradation behavior, K. Hengge, T. Gänsler, E. Pizzutilo, C. Heinzl, **M. Beetz**, K.J.J. Mayrhofer, C. Scheu, International Journal of Hydrogen Energy, 2017, 42(40), 25359 – 25371.

2. Titanium Doping and Its Effect on the Morphology of Three-Dimensional Hierarchical $Nb_3O_7(OH)$ Nanostructures for Enhanced Light-Induced Water Splitting, S.B. Betzler, F. Podjaski, **M. Beetz**, K. Handloser, A. Wisnet, M. Handloser, A. Hartschuh, B.V. Lotsch and C. Scheu, Chemistry of Materials, 2016, 28(21), 7666 – 7672.

Book chapter:

1. The Chemistry of Metal–Organic Frameworks: Synthesis, Characterization, and Applications, **Michael Beetz**, Andreas Zimpel, Stefan Wuttke, Wiley, 2016, Volume 1, Chapter 16: Nanoparticles, pages 491-521, (DOI:10.1002/9783527693078).

11.2 Contributions to Conferences and Oral Presentations

Invited Talk: Max-Planck-Institut für Eisenforschung GmbH 07/16 Düsseldorf, Germany	Parameter Analysis and Performance Improvement of Discrete Iterative Reconstruction Techniques in Electron Tomography
18th European Symposium on Fluorine Chemistry 08/16 Kiev, Ukraine	Nitramines in Superacids. Where does the Proton go?
Kopernikus-Meeting 2018 01/18 Frankfurt am Main	Development of Nanosized OER Catalysts and High Surface Area Conductive Oxide Supports
NanoGe Fall Meeting 2018 10/18 Torremolinos, Spain	Structure-activity Relations in Transition Metal Doped Nickel Oxide-based Nanocatalysts for Electrochemical Water Oxidation
Kopernikus-Meeting 2019 01/19 Frankfurt am Main, Germany	Development of Nanosized OER Catalysts and High Surface Area Conductive Oxide Supports
Bunsen-Discussion-Meeting 2019 04/19 Taormina, Italy	An In-depth EELS Study on the Photocorrosion of Li_xCuO Cathodes for Photoelectrochemical Water Splitting
Bunsen-Discussion-Meeting 2019 04/19 Taormina, Italy	Structure-activity Relations in Vanadium-doped Nickel Oxide-based Nanocatalysts for Electrochemical Water Oxidation
Kopernikus-Meeting 2020 01/20 Frankfurt am Main, Germany	Development of Nanosized OER Catalysts and High Surface Area Conductive Oxide Supports
SolTech 2020 10/20 Online-Conference	In-depth Electron Microscopy Studies on Photoelectrochemical Water-splitting Materials
Kopernikus-Meeting 2021 02/20 Online-Conference, Germany	Development of Nanosized OER Catalysts and High Surface Area Conductive Oxide Supports